Multiscale modeling of gas transport in partially saturated heterogeneous media assisted by machine learning

A thesis submitted to the University of Manchester for the degree of
Doctor of Philosophy
in the Faculty of Science and Engineering

2021
Arash Rabbani
Department of Chemical Engineering and Analytical Science

Contents

Abstract

In this research, gas transport, diffusion and adsorption through micro–structured porous materials with the help of data–driven methods are investigated. Different types of the geological porous media from organic–rich shale to tight carbonate and clays have been digitally analysed and simulated to characterize various fluid–solid interactions. Considering the heterogeneous structure of the many nature–made porous materials, a multi-scale pore network modeling approach has been presented which couples the effects of micro–pores, meso–pores and fractures at the same time. Considering the high computational cost of the multi–scale multi–physical systems, machine learning (ML) is employed to make statistical surrogate models with minimal accuracy losses. Several physical features of the porous material have been predicted using deep convolutional neural networks based on the segmented images as input. Properties like absolute permeability, gas permeability, gas storage capacity, and capillary pressure have been successfully predicted by the proposed machine learning model with averaged r–squared of around 0.9. In some of the cases like permeability, ML predicted values have been compared to the micro–scale laboratory experiments and relative error of 13 % has are reported which is reasonable considering 3 to 4 orders of magnitude lower computational cost. The outcome of this study is to equip researchers with a series of ML–assisted tools to accelerate numerical simulations of several fluid–solid interactions in porous materials. As an example, the proposed methodology can be used in screening of the suitable CO_2 subsurface storage sites based on analysis of the pore scale images of shale–deposits.

Declaration

No portion of the work referred to in the thesis has been submitted in support of an application for another degree or qualification of this or any other university or other institute of learning.

Copyright

The following four notes on copyright and the ownership of intellectual property rights must be included as written below: i. The author of this thesis (including any appendices and/or schedules to this thesis) owns certain copyright or related rights in it (the "Copyright") and s/he has given The University of Manchester certain rights to use such Copyright, including for administrative purposes. ii. Copies of this thesis, either in full or in extracts and whether in hard or electronic copy, may be made only in accordance with the Copyright, Designs and Patents Act 1988 (as amended) and regulations issued under it or, where appropriate, in accordance with licensing agreements which the University has from time to time. This page must form part of any such copies made. Presentation of Theses Policy You are required to submit your thesis electronically Page 11 of 25 iii. The ownership of certain Copyright, patents, designs, trademarks and other intellectual property (the "Intellectual Property") and any reproductions of copyright works in the thesis, for example graphs and tables ("Reproductions"), which may be described in this thesis, may not be owned by the author and may be owned by third parties. Such Intellectual Property and Reproductions cannot and must not be made available for use without the prior written permission of the owner(s) of the relevant Intellectual Property and/or Reproductions. iv. Further information on the conditions under which disclosure, publication and commercialisation of this thesis, the Copyright and any Intellectual Property and/or Reproductions described in it may take place is available in the University IP Policy (see http://documents.manchester.ac.uk/DocuInfo.aspx?DocID=2442 0), in any relevant Thesis restriction declarations deposited in the University Library, The University Library's regulations (see http://www.library.manchester.ac.uk/about/regulations/) and in The University's policy on Presentation of Theses.

Acknowledgement

I want express my sincere thanks to my caring supervisor, Dr. Masoud Babaei, for his unconditional help and generous support to this project. In Addition to be a great leader, I found him as a passionate friend and a colleague with high level of professional ethics.

Also, I want to thank the University of Manchester for awarding President's Doctoral Scholarship 2018 to carry out this research. In addition, special thanks to Dr. Vahid Niasar for his thoughtful consultancy, instructive collaboration, and for sharing some of the used data in the present study. Furthermore, thanks to Dr. Farzam Javadpour for his valuable comments and suggestions that have enhanced the applicability of the present study. Also, I wish to thank Dr. Xiaolei Fan, my first year referee for his constructive suggestions and warm encouragement which led to improve the scope of the present study. Additionally, Dr. Majid Sedighi, the second year referee who has truly helped to elevate the work through his valuable and considerate comments. Furthermore, I'd like to thank Dr. Morteza Aminnaji for his great help, support, and consultancy during this project. Also, I wish to extend my gratitude to my great friends Dr. Reza Vakili and Dr. Hamidreza Erfani, for their helpful comments and clever instructions through the rough patches.

Special thanks to my great collaborators from the University of New South Wales (UNSW), Dr. Ryan Armstrong, Dr. Ying Da Wang, Dr. Yu Jing, Dr. Ankita Singh, Dr. Traiwit Chung, and especially Dr. Peyman Mostaghimi for his patient guidance, invaluable encouragement, and eye–opening advice throughout my studies and great hospitality during my research visit at the UNSW.

Then, I would like to thank my parents who endured my absence for several long years with patience, while keeping their encouraging support to me following my dreams.

Finally, I wish to express my deepest gratitude to my wife who stood by me through this journey, and non of this would have been possible without her selfless support and sacrifice.

Chapter 1

Introduction

1.1 Preface

In this section, a brief general introduction to the porous material concepts and data–driven approaches such as machine learning is presented to familiarize the readers from different disciplines with the main discussed subjects.

1.1.1 What is porous media?

To put it simply, a piece material that contains distributed void chambers can be called a porous medium. Most of the nature–made structures from lifeless objects and particles to living beings that surround us are porous at some level in a closer look. That's a reason why porous material research is fundamentally beneficial for many engineering, scientific, and biomedical fields from geoscience, water resources [1] and fuel cells [2] to bone marrow and cardio–vascular studies [3, 4, 5]. Most of the nature–made porous materials have an uneven distribution of void spaces in both size and spatial domains which are called heterogeneous porous media. Several physical properties can be defined for porous material as characterization criteria. Porosity, pore size distribution, hydraulic permeability and adsorption capacity are some of the most discussed properties in the literature. Porosity is the fraction of the porous material material occupied by void space to its bulk volume. Pore size distribution is a probability density function that represents the abundance of each pore sizes and it is commonly obtainable via pore–scale image analysis as well as adsorption tests [6]. Hydraulic permeability, is a measure of fluid flow capacity through the connected pathways of porous media with the unit of m^2 or *Darcy*. Higher the permeability values indicates an easier fluid passage or equivalently lower fluid pressure gradient. Finally, adsorption capacity of the porous material indicates the mass of a fluid that can be attached to the surface sites of a porous material in a relatively stable manner. Considering the fact that porous materials have significantly higher surface area compared to the solid materials with the same volume, they are frequently used in the processes which demands high surface area for better a mass transfer such as chemical catalysis, sub-surface gas storage, fluid filtering and etc. In this thesis, fluid transport and storage within heterogeneous geo–porous materials are discussed.

1.1.2 What are data–driven methods?

As a broader concept of data–driven methods, data science is becoming a powerful tool to solve a wide range of problems [7]. Dhar [8] has famously defined data science as *"study of the generalizable extraction of knowledge from data"*. Data science can be viewed as a combination of classical disciplines, namely, statistics, data mining, and image analysis with more recent artificial intelligence approaches like deep machine learning to create additional value from the abundantly available data [7]. In another definition, Data science is the mutual overlapping of mathematics, computer science, and a real–world field of expertise which the data originates from and applies to it [9, 10, 11]. The two main data–driven modeling approaches are known as statistical methods and machine learning [12]. Statistical methods can be named as linear regression, auto–regression, multivariate regression, k-means clustering and many other classic approaches. On the other hand, machine learning methods are relatively more recent and flexible to model complex and highly non-linear phenomena. The common machine learning methods can be named as regression trees, support vector machines and artificial neural networks (ANNs).

ANNs have been initially designed and inspired by the learning pattern of a natural neural cell [13]. An illustration of a neuron and a corresponding artificial perception are exhibited in Figure 1.1–a and b. In such a structure, the dendrites receive the inputs and the cell body is the computational hub of the neuron where it is essentially mimicked by the hidden layers of the ANN. The output is transmitted through the axon which is subsequently received by other nearby neurons. Although, this simple operation is virtually a linear transformation, when large number of neural structures are connected to each other, they are able to process highly non–linear problems especially by adding the activation functions[14]. Generally, ANN data-feed is split into three distinct assortments, namely, training, validation and the test sets [13]. Each dataset is composed of x and y values which correspond to an input (e.g. pore size) and output (e.g. permeability). During the training phase of the ANN model, the inputs are compared with the outputs and the corresponding relationships are determined in terms of weights and biases of the network using back propagation of the errors. In the meanwhile, the amount of model loss on validation dataset is recorded to provide an unbiased criteria for the training performance. Once the validation error reach an acceptable level, the model is considered to be ready for prediction on the test set [15]. The accuracy levels are user defined and the robustness of the model is highly contingent on the available data points [16]. The model is subsequently subjected to the test set, which evaluates the accuracy and overfitting criteria [17]. The test set is not a part of the initial model training phase, thus becomes ideal in evaluating the generality of the trained model. Upon the convergence to an acceptable error on the test set, the model can be employed on the unknown data, whereby predictions are made [18]. Sometimes, an additional fraction of the dataset is often reserved as the validation dataset. This is an optional step to evaluate the trained dataset and to propose certain optimisation algorithms to enhance the accuracy of the model [19, 20].

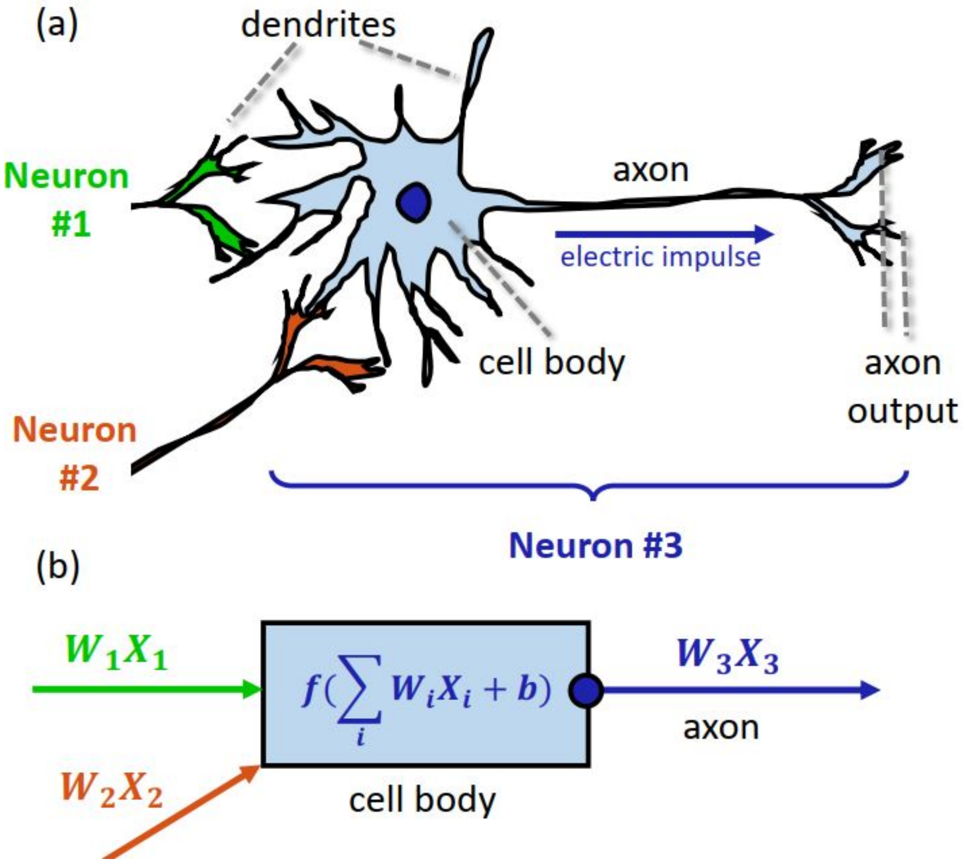

Figure 1.1: Analogy of the biological neuron (a) and the mimicked ANN (b).

1.1.3 Interface of porous media research and data–driven methods

Data–driven methods can be very suitable candidates to tackle porous material modeling tasks considering the fact that random–like structures of such material cannot be easily described using analytical methods. There have been several interdisciplinary studies in the literature utilizing the power of machine learning to characterize, classify, or reconstruct pore–scale images.

Data regression

A plethora of regression methods are reported in pore scale research which primarily revolve around porosity and permeability determination [21, 22]. These two properties dictate the transport and storage characteristics of the porous material and they are useful in many engineering fields from determining the oil and gas recovery in the petroleum industry, to CO_2 sequestration modeling, geothermal plants, and radioactive waste management schemes [23, 24, 25, 26, 22, 27]. Over the years, many experimental techniques have been developed to accurately quantify these two properties [28]. However, the precision of these primary parameters is hampered by the complexity and heterogeneity of the studied porous media. Besides, the classical techniques through experiments are expensive and time intensive [29, 22]. Therefore, machine learning techniques are adopted by a multitude of researchers to benefit from a large dataset of imagery data to predict the porous media properties [30, 31, 32].

Data classification and clustering

In the regression analysis, the variability of a particular parameter such as permeability is determined with respect to several other properties [33]. In contrast, classification techniques are employed to distinguish a distinct data class, which does not necessarily represent a value [34]. A data class is typically an assortment of several parameters contained together as a representative entity. Both regression and classification techniques belong a larger family of the statistical models known as supervised models in which target labels or values are predefined in the training process. Conversely, unsupervised models does not dictate specific labels to the data and tries to reveal the inherent or natural divisions within the data [35]. As an example, clustering, as implied by the term itself, groups the data according to the distribution in an n-dimensional space without knowing the exact corresponded labels [36]. The clustering and classification processes are routinely encountered in applications, where image analysis and data grouping are a requisite. For instance, in porous media research, image analysis is widely practised for mineral identification studies and clustering is employed for identifying specific facies such as lithofacies and environmental facies in the subsurface geology [37, 38].

Image reconstruction

To appraise the morphological, topological, statistical, and flow properties of porous media, we need accessing various reliable realizations of porous media at pore scale [39]. While direct acquisition high–resolution tomography images of porous material can generally be costly and non–practical, reconstruction techniques can provide a shortcut to obtain realistic–look imagery data [40]. Among the traditional reconstruction methods, we may encounter stochastic, process–based, hybrid and data mining methods, which are mostly time consuming and in some cases overestimate or underestimate the statistical and dynamical properties [5, 41]. However, deep machine learning as a modern approach shows more realistic reconstruction in a reasonable computing cost and in an intelligent manner [42, 43, 38].

Among the introduced data–driven techniques, in the present study, shallow ANNs and deep neural networks have been employed for characterization and regression of porous materials which will be discussed in chapters 2, 4, and 5.

1.2 Motivation

Subsurface gas–rich structures are becoming more important in the past decade due to the two main benefits they can provide; supplying natural gas as a cleaner form of fossil fuel, and application as a storage site of the unwanted gases like CO_2. Both of these applications can have positive impacts to approach the net–zero emission pledge as planned by many developed countries to achieve by 2050[44, 45].

A major part of the subsurface sediments are composed of heterogeneous porous media with complex micro-structures. Shale, coal, and tight carbonates are well-known examples of these type of sediments with coexistence of different levels of porosity from nano to micron scale coupled with natural fractures. In such media, in addition to the regular gas transport models, we need to take into the account the effects of gas slippage, surface diffusion, adsorption, and desorption. This phenomena would be more complicated if the medium is partially saturated with a secondary component which is a frequently observed condition in a majority of the porous sediments. Conventional direct simulation methods such as finite volume method, finite element method, or Lattice Boltzmann might become computationally unaffordable in multi-physical problems. In such situation, application of the surrogate models using Machine learning (ML) techniques can be highlighted to cut down the computational costs of a physically complicated model. Such an integrated nano to micrometer approach for modeling gas transport within the complex porous material in the presence of a secondary component, would have several applications in different engineering and geoscience fields such as shale gas resources, coal bed methane, tight carbonated reservoirs, and subsurface carbon storage.

Recent advances in multiscale 3D/2D imaging techniques have brought us a new insight and opportunity to understand the governing mechanisms more clearly. In the heterogeneous media we are dealing with a wide range of pore sizes embedded in different types of material each of which can behave in a different manner during the gas transport. Due to a high surface area, micro–pores are able to adsorb gas and gradually release it when the pressure of the system drops. Also, Knudsen and bulk diffusion can cause a noticeable deviation from the classical gas transport models such as the Darcy's law. Considering the multi–scale/multi–physical aspects of the gas transport behaviour in the heterogeneous media, there is a demand for an integrated modeling of micro and meso scales, which is at the same time computationally efficient.

1.3 Chapters summary

As mentioned, considering the fact that the simulation of fluid flow models with diversified conductive components and multiple physics can be computationally expensive, we have employed machine learning techniques to make surrogate models able to predict numerical simulation outputs. This emulation concept, has been utilized in different chapters of the present study.

- In **chapter #2**, a hybrid pore network model is presented which uses Lattice Boltzmann (LB) flow simulation to calculate the pressure drop in pore throats. Then using a shallow neural network model, pressure drop in pore throats, is modeled based on the geometrical characteristics of the throat cross-sections to emulate the LB calculations and speed up the fluid flow modeling.
- In **chapter #3**, a triple porosity network model is presented to predict steady state gas flow behaviour in heterogeneous geo–porous materials like tight carbonate rocks. The presented workflow is capable to simulate meso pores, micro pores and fractures simultaneously. To evaluate the accuracy of the presented model we have compared its predictions with the results from analytical solutions.
- In **chapter #4**, a deep learning workflow is introduced to comprehensively characterize the physical features of naturally–occurred porous materials. A large dataset of 17700 porous samples have been generated and 30 different pore–scale properties and features have been extracted from them to feed into a machine learning model named as DeePore. Some of the predictions from this model were in close agreement with experimental outcomes adopted from the literature.
- In **chapter #5**, pieces of information from the previous chapters have been combined to build a comprehensive model of gas transport, diffusion and adsorption in organic-rich shales for the purpose of carbon subsurface storage. The presented model which is

equipped with machine learning for faster predictions can be used for quick evaluation of the carbon storage sites and find the proper locations based on the pore–scale images of the shale samples.

1.4 Publications

The presented journal format thesis is comprising four peer-reviewed papers as direct outcomes of the PhD. project. The first three papers which form chapters #2 to #4 have been published and available online, while the fourth paper that is presented in chapter 5 is still under review.

1. **Hybrid pore-network and Lattice-Boltzmann permeability modelling accelerated by machine learning**, Rabbani, A. and Babaei, M. (2019) *Advances in Water Resources 126, 116 - 128.*

   Also, this paper has been presented in an invited talk for London SPE Evening 26 Feb, 2019 under this topic: **Accelerating pore-scale flow simulations with a machine learning approach**.
   Public repository: `github.com/ArashRabbani/PaperCodes`.

2. **A triple pore network model (T–PNM) for gas flow simulation in fractured, micro-porous, and meso-porous media** Rabbani, A., Babaei, M., & Javadpour, F. (2020). *Transport in Porous Media, 1-34.*

3. **DeePore: a deep learning workflow for rapid and comprehensive characterization of porous materials.** Rabbani, A., Babaei, M., Shams, R., Da Wang, Y., & Chung, T. (2020). *Advances in Water Resources, 146, 103787.*
   Public repository: `www.github.com/ArashRabbani/DeePore`.

4. **Image-based modeling of carbon storage in fractured organic–rich shale with deep learning acceleration.** Rabbani, A., Babaei, M.(2021). *Fuel, 299, 120795.*

   Also, a preliminary version of this paper has been presented as poster in PGR Conference 2019, on 17th of May, Department of Chemical Engineering and Analytical Science, at the University of Manchester, and has been awarded the second best poster in class of 2018. The title of the poster is: **A coupled pore network model of methane desorption, diffusion, and flow in shale**.

1.5 Secondary publications

In addition to the main publications listed above as the chapters of the present study, there are secondary publications that are closely related to the thesis subject but are not included due to the fact the author have not been the lead researcher but have made a contribution.

1. **Computer vision and unsupervised machine learning for pore-scale structural analysis of fractured porous media**, Singh, A., Rabbani, A., Regenauer-Lieb, K., Armstrong, R. T., & Mostaghimi, P. (2021). Advances in Water Resources, 147, 103801.

2. **Hybrid fracture-micropore network model for multiphysics gas flow in coal**, Jing, Y., Rabbani, A., Armstrong, R. T., Wang, J., & Mostaghimi, P. (2020). A. Fuel, 281, 118687.

3. **Gas Flow Models of Shale: A Review** Javadpour, F., Singh, H., Rabbani, A., Babaei, M. and Enayati, S., (2021), Energy and Fuels.

Chapter 2

Hybrid pore-network and Lattice-Boltzmann permeability modelling accelerated by machine learning

2.1 Abstract

In this paper, a permeability calculation workflow is presented that couples pore network modeling (PNM) with a Lattice Boltzmann Method (LBM) to benefit from the strengths of both approaches. Pore network extraction is implemented using a watershed segmentation algorithm on 12 three-dimensional porous rock images. The permeabilities of all throats are calculated using the LBM and substituted in the pore network model instead of using the cylindrical formulation for throat's permeability based on the Hagen–Poiseuille equation. Solving the LBM for every throat results in an accurate representation of flow but the algorithm is computationally expensive. In order to minimize the computational costs, LBM is used to model the steady-state incompressible fluid flow through 9,333 different throat images and an Artificial Neural Network (ANN) is trained to mimic the trend of throat's permeabilities based on the cross–sectional images. To this end, we extract several morphological features of the throats cross–sectional images and search for the best describing feature. It is found that the averaged distance map of the throat images is highly correlated with the LBM-based permeability of throats to the extent that even a simple empirical correlation can reasonably describe the relationship between these two parameters. Finally, we compare the absolute permeability of samples obtained by full LBM with the presented hybrid method. Results show that the proposed method provides an accurate estimation of permeability with a considerable reduction in the computational CPU time.

Keywords: Lattice Boltzmann Method, Pore Network Modeling, Machine Learning, Permeability, Distance Map.

2.2 Introduction

2.2.1 Permeability calculation

Microscale computed tomography has triggered a series of advances in porous media studies by revealing accurate interior structures non-destructively [46, 47, 48, 49, 50]. Knowledge of microscopic porous structure provides a better understanding of porous media properties, for example, hydraulic conductivity or absolute permeability. In many research areas from material science to hydrology and geoscience, hydraulic conductivity and permeability of porous materials have been subjects of research during the past decades [51, 52, 53, 54, 55, 56, 57]. Existing approaches for estimating the pore-level permeability using computed tomography images can be categorized as direct and indirect methods. "Direct" refers to the fact that in these methods realistic geometry of the porous media is taken into account and governing equations are written to be solved on the exact structure. Finite Volume [58, 59, 60, 49], Finite Element [61, 62, 63, 64] and Lattice Boltzmann [65, 66, 67, 68, 69, 70, 71] are the most prominent direct simulation methods in the literature. Conversely, indirect methods do not consider the exact geometry of porous media and the equations are solved on a simplified proxy model that behaves similarly to the original geometry. Pore Network Modeling [72, 73] and Bundle-of-Tubes [74, 75, 76] are two indirect methods that have been widely used for modeling and simulation of several transport phenomena in porous media.

2.2.2 Direct simulation methods

As mentioned, these methods are able to be implemented for the exact geometry of porous media with a minimal amount of simplification. As a result, they could be accurate if the governing equations and boundary conditions are selected and solved properly. The main limitation of direct methods is the high computational cost [46], which could be a major obstacle when we are dealing with large-sized and high-resolution volumetric images of porous material. As a solution to this size and time limitation, domain decomposition and parallel computation have been comprehensively hired to increase the models efficiency and scalability [77, 78, 79, 80, 81]. Additionally, as another solution to deal with computational limitations, machine learning can be employed to mimic the behaviour of the complex solid/fluid systems. The main idea is to save the computational sources by solving a series of typical/representative problems and extend the results to all similar cases [82, 83, 84]. For this purpose, we need to break down a large problem into several small independent pieces and try to find computationally inexpensive features which are statistically related to the original problem.

As one of the most trending approaches in pore-scale flow modeling, Lattice Boltzmann method has been initiated by Frisch et al. [85] under the name of lattice-gas automata in 1986. Later in 1988, Boltzmann equation was plugged into the method proposed by McNamara and Zanetti [86] and named as LBM. This direct simulation method can be easily implemented by computer programming [87] and it's a versatile tool to consider multiple physics in a parallelized fashion [88]. So, in addition to the single phase flow modelling, more advanced processes such as multiphase flow including the effect of variable wettablity can be implemented by LBM [89, 90, 91]. Classic LBM [85] uses a uniform lattice grid for simulation and this could reduce the simulation performance by avoiding local coarsening/refinement of the grid, while modern approaches have coupled the finite volume and finite element schemes with LBM calculations to increase the performance of the method by adopting multi-domain/unstructured grid which can catch more complex geometries [92, 93, 94]. However, LBM could be computationally expensive. In a comparison published by Manwart et al. [95] it was claimed that LBM demands 2.5 times more memory than the amount required by finite difference on the same porous geometry and similar CPU time.

2.2.3 Indirect methods

Indirect methods such as pore network modeling assume several geometrical simplifications to reduce the computational costs, but lead to error in the simulation results [73, 96]. As an example, in the classical pore network models, the pressure drop is neglected in pore bodies and throat cross-sections are considered as definitive geometrical shapes such as circle, square and triangle [73]. Also, in order to make the PNM's more realistic, complicated throat shapes have been investigated by coupling a series of mathematical curves and defining an analytical shape factor for throats [97]. In comparison, none of these assumptions are made in the direct simulation methods and the realistic geometry with many of its morphological details are used to build a mesh and initiate the numerical simulation. Considering the relentless advances in the 3D imaging techniques [98, 99] and large size of the recorded images, low–cost computational methods such as PNM are becoming popular. However, the level of simplifications in PNM should be minimized to avoid compromising the accuracy.

2.2.4 Coupling direct and indirect methods

In recent years, there have been several efforts to couple different direct and indirect simulation methods to increase the performance of permeability models [100, 101, 102]. Miao *et al.* [100] extracted 3,292 pore elements and simulated the single-phase permeability of the pore elements using COMSOL Multiphysics software by solving the Navier-Stokes equation. They used 3 image-based features to train an Artificial Neural Network (ANN) as a means to predict the throat absolute permeability as well as shape factor, solidity, and aspect ratio of the images. In a similar but improved approach in terms of image-based features, here, we couple both direct and indirect methods for calculation of porous media permeabilities. Furthermore, in addition to features extracted by Miao *et al.* [100], we study four more image-based features from 9,333 pore-throats and substitute the throat permeabilities in a pore network model to calculate the overall permeability of rock samples.

2.3 Methodology

2.3.1 Synopsis

Based on the definition, pore throat is referred to the locations of the porous elements in which the opening of the pathway reaches to its minimum. Thus, the permeability of such tight openings play as a bottleneck for the rest of the structure and will be critical in determination of the macroscopic properties.

As opposed to the classical pore network modeling that describes throat cross–sections analytically [50, 97], we assemble a workflow to handle any arbitrary throat shape with minimal computational costs. As an illustration, a 3-D image of Berea Sandstone, obtained from [39], is modeled and absolute hydraulic permeability is calculated with both classical and proposed PNM–LBM methods (Fig. 2.1a). As we will show in Section 2.4, the PNM–LBM (Fig. 2.1b) method can calculate the absolute permeability of the porous samples with a higher accuracy than the classical PNM (Fig. 2.1c).

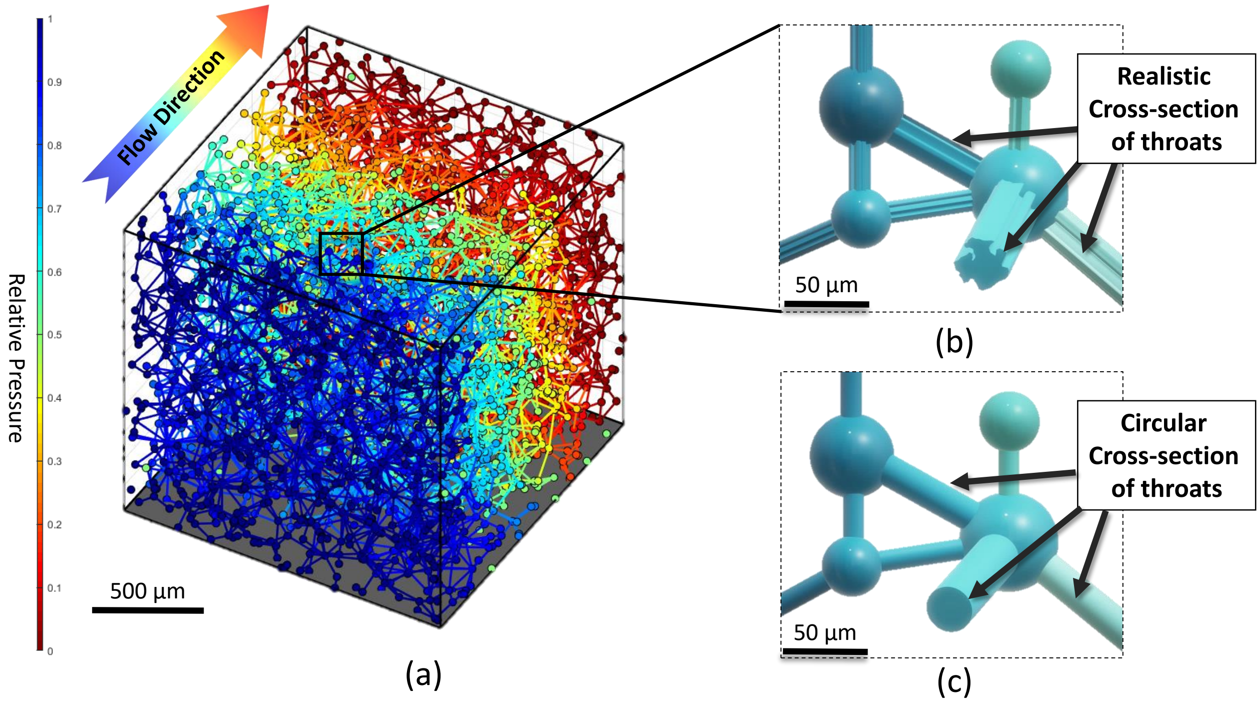

Figure 2.1: Visual comparison of modified (PNM–LBM) and classical PNM approaches, (a) single–phase steady–state pressure drop in a pore network of Berea Sandstone (raw data obtained from [39]) with relative pressures between 0 and 1, (b) the PNM–LBM approach with realistic throat cross–sections, and (c) the classical PNM approach with circular throat cross–sections.

In this study, instead of the hydraulic radius, we use D3Q19 Lattice Boltzmann modeling with Bhatnagar-Gross-Krook (BGK) approach [103] to estimate the throat's permeability. In order to reduce the computational costs of LBM simulations, we introduce Image–Based Throat Permeability Model (ITPM)[1]. The workflow of building this model is described step by step in Fig. 2.2. The process starts with preparation of micro–CT images including noise filtering and binarization. Next, the pore network is extracted by help of the watershed algorithm and cross–sectional images of throats are recorded in a database. Additionally, several morphological features of the throat images are extracted and stored in the database. Next, we run a series of relatively time consuming LBM simulations on throat images to determine their absolute permeability and relate them to the permeabilities of the database [2].

---

[1] Image–Based Throat Permeability Model is available in the Supplementary information as well as on on GitHub: `https://github.com/ArashRabbani/PaperCodes`

[2] CPU times will be discussed in the results and discussion section.

Using the database and by training two ANN's and one empirical correlation we build a set of ITPM's that are able to predict the permeability of the throats with minimal computational cost.

Next, ITPM is used to find the hydraulic properties of the pore networks in a hybrid approach that couples both PNM and LBM. In this regards, Fig. 2.3 presents the simplified workflow in a stepwise manner. A 3–D binary pore–level image is taken as an input of the workflow. At the first step, we need to extract the pore network. This is done in a subsidiary workflow (Fig. 2.3a) comprising noise removal, distance transform, Gaussian filtering, watershed segmentation, labeling and connectivity detection. A brief description of pore network extraction is presented in the next subsection. The extracted pore network is used in the next step of the main workflow (Fig. 2.3b) for feature extraction from throat cross–sections. This step, similarly is shown in a subsidiary workflow (Fig. 2.3c) and comprises of projecting 3–D image of throat surfaces on a 2–D plane and then calculating the average value of its distance map. The extracted feature goes back to the main workflow as an input for ITPM. This process should be repeated for all throats of the network. Finally, the ITPM permeabilities are substituted in the classical PNM.

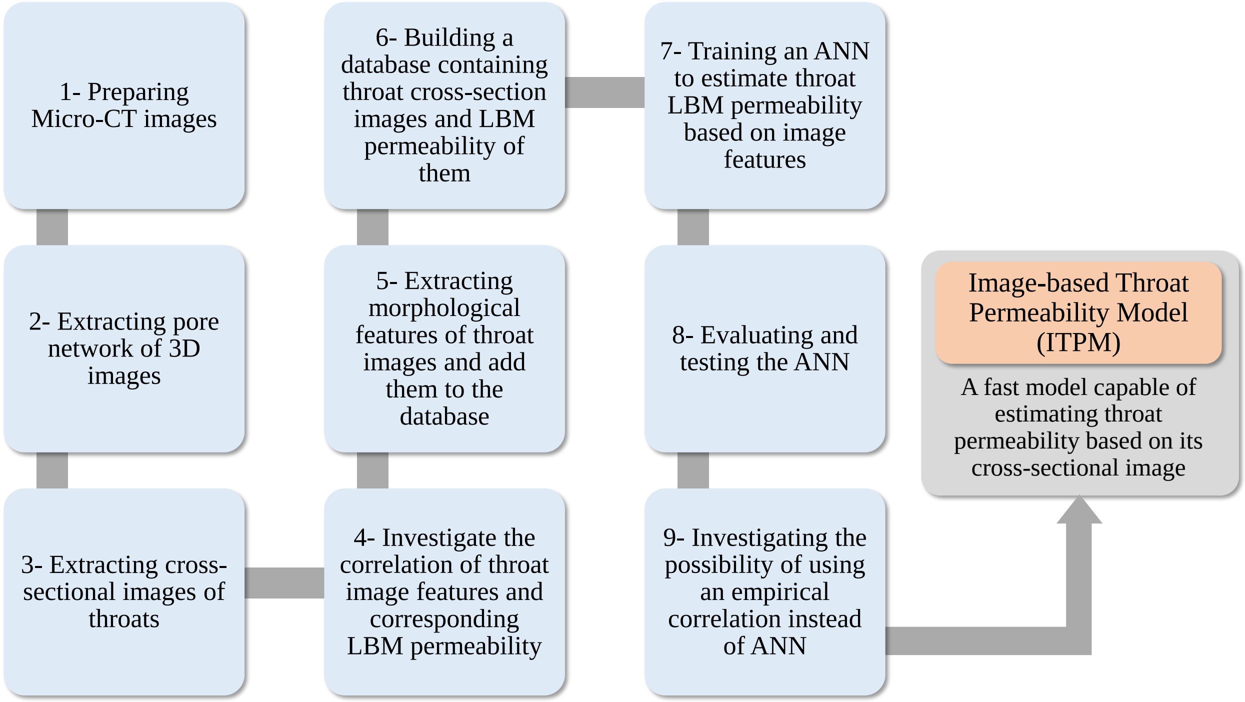

Figure 2.2: Workflow of building the Image–Based Throat Permeability Model (ITPM).

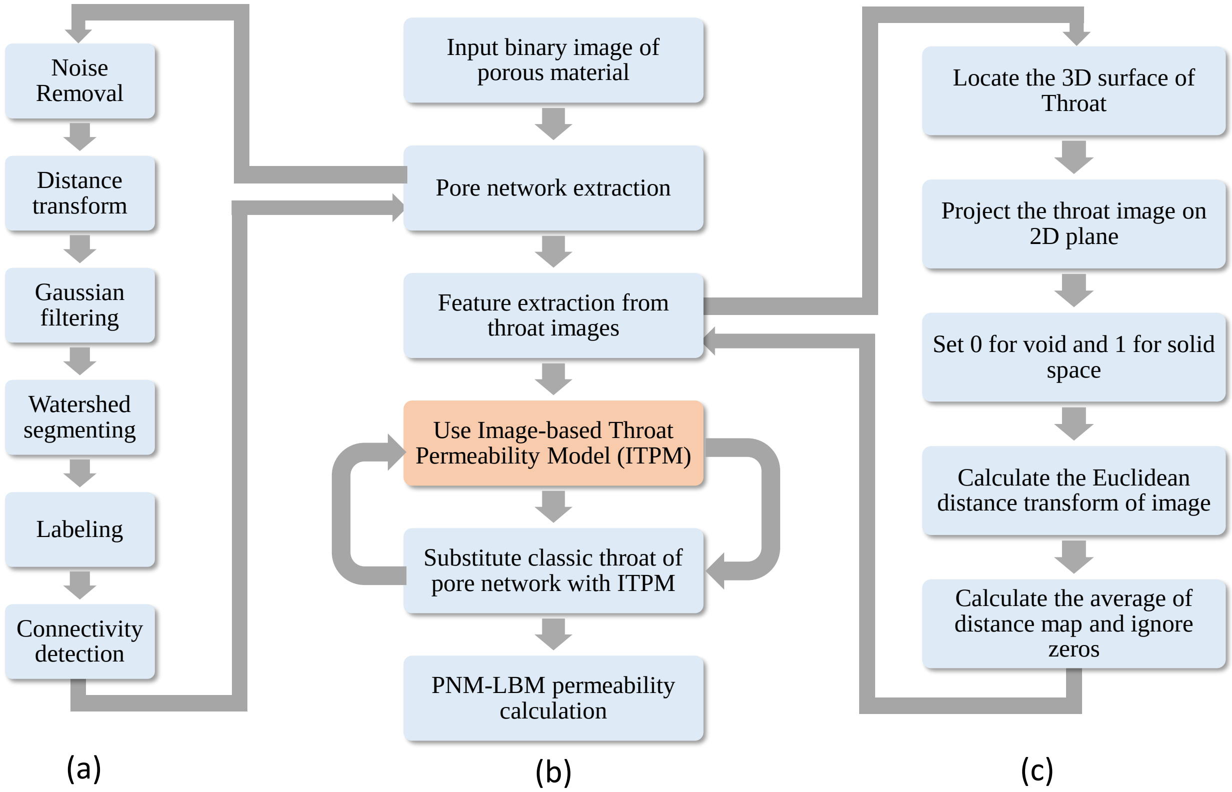

Figure 2.3: Workflow of the hybrid PNM–LBM approach for calculation of the pore–level permeability, (a) subsidiary workflow of pore network extraction, (b) main workflow of the PNM–LBM permeability calculation, and (c) subsidiary workflow of throat features extraction.

2.3.2 Pore network extraction

A brief procedure for extracting pore networks is illustrated in Fig. 2.3(a). Watershed segmentation algorithm is used for pore network extraction. This method is computationally efficient and sufficiently accurate for auto–detection of pore bodies and pore throats [104, 105, 106, 107]. Watershed algorithm utilizes the distance transform of the pore space to find out the narrowest pathways of porous media and introduces them as network throats [108, 109, 110]. In order to have more stabilized results and avoid over–segmentation, 3D Gaussian filtering is implemented on the distance transform [104, 111]. The output of the watershed segmentation is an image with isolated segments each of which represents a unique pore body. This image goes under labeling process to identify all isolated spaces. Finally, by searching the whole image voxel by voxel, we detect and record adjacent pore spaces with unique labels to build a connectivity matrix which represents the extracted pore network.

In this workflow of pore network extraction, throats are curved surfaces at the interface of two adjacent pores (Fig. 2.4a). In this study, we do not simplify the throat cross–section to circles and preserve their original shape to compute a more realistic permeability using a Lattice Boltzmann method. We extract the throat surfaces along the line that connects the centers of two adjacent pores and forms a prism with arbitrary base shape (Fig. 2.4b).

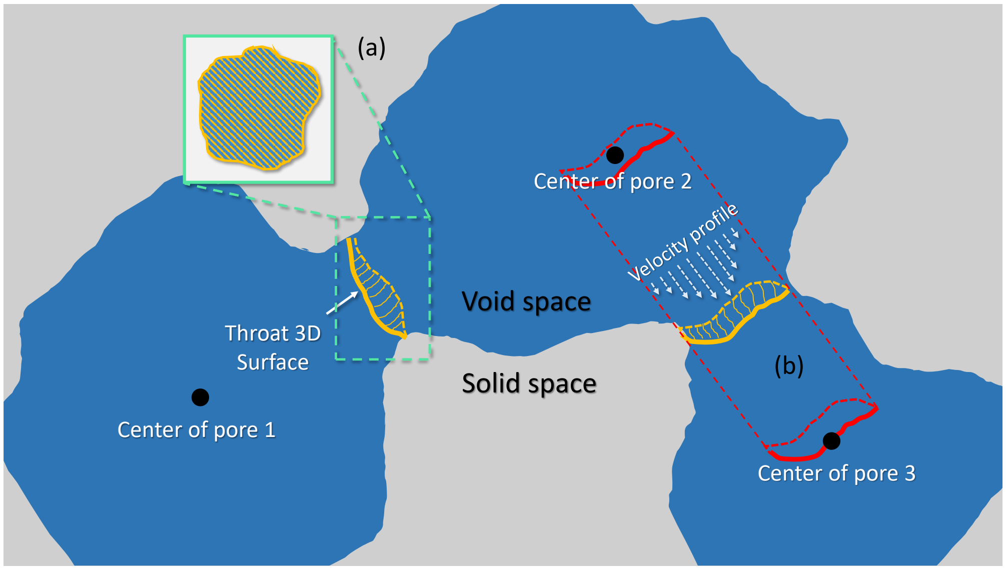

Figure 2.4: Throats definition in the model, (a) a projected image of 3–D throat surface on 2–D plane which is used for feature extraction, and (b) extruded geometry of the throat cross–section which is considered as the flow pathway between the pore centers.

2.3.3 Extraction of features

As mentioned, throats are considered to be the interfaces where two adjacent pores touch each other [108]. These interfaces may have slight curvatures based on the morphology of the original volumetric image of porous media. In order to effectively extract the image features, we project the throat images in the direction of a line that connects the centers of two adjacent pores. Thus, 3D slightly curved surfaces will be converted to flattened 2D binary images which represent the cross–section of the tightest pathway between two adjacent pores (Fig. 2.4a). Next, we use MATLAB Image Processing Toolbox to extract multiple morphological features that may be correlated with hydraulic conductivity of the throats.

Table 2.1 presents a list of features we extract from 2–D images of throats in addition to their definitions.

Although most of these features have been extensively discussed in the literature for characterization of porous structures, amongst these, average distance map needs more clarifications. Thus, consider a throat with circular cross–section as shown in Fig. 2.5(a). Assign zero to the void space and one to the solid space of the image. Then instead of each zero pixel, put the Euclidean distance between that pixel and the nearest non–zero pixel in the image (Fig. 2.5b). Consequently, this distance value will be equal to zero for all the pixels located in the solid space. This transform is known as the distance transform and it is available in most of major open–source or commercial image processing packages. The final feature that we are using to correlate with the throat's LBM-based permeability is "non–zero average of the distance map". A physical justification will be presented in Section 2.4 to explain the relationship between this feature and the throat permeabilities.

No.	Feature	Feature Description
1	Cross–section area ($pixel^2$)	Surface area of the 2–D projection of throat
2	Wetted perimeter ($pixel$)	Perimeter of the 2–D projection of throat
3	Axes ratio	Ratio between the major and minor axes of the throat which is always equal or greater than 1
4	Equivalent diameter ($pixel$)	Diameter of the circle with the same area as the throat
5	Solidity	Area of the throat convex hull divided by the throat area
6	Hydraulic radius ($pixel$)	Throat area multiplied by two divided by throat wetted perimeter
7	Mean distance ($pixel$)	Non–zero average of the throat distance transform

Table 2.1: Extracted throat features and their description.

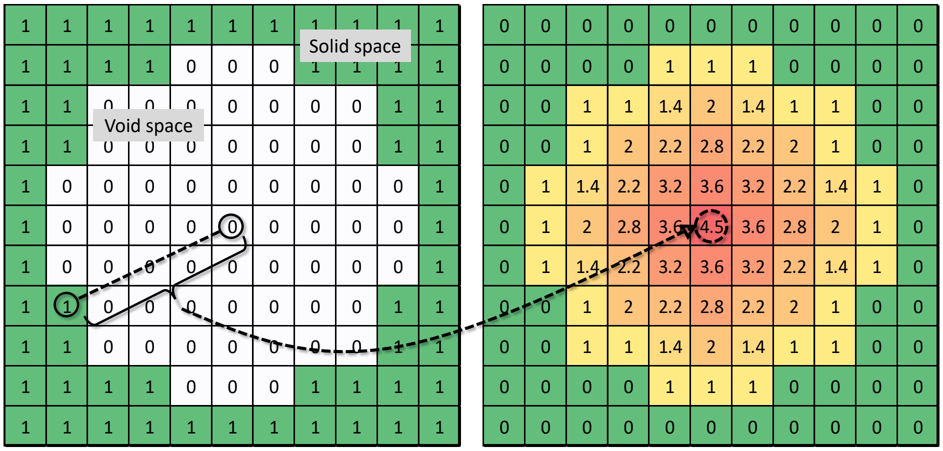

1	1	1	1	1	1	1	1	1	1	1
1	1	1	1	0	0	0	1	1	1	1
1	1	0	0	0	0	0	0	0	1	1
1	1	0	0	0	0	0	0	0	1	1
1	0	0	0	0	0	0	0	0	0	1
1	0	0	0	0	0	0	0	0	0	1
1	0	0	0	0	0	0	0	0	0	1
1	1	0	0	0	0	0	0	0	1	1
1	1	0	0	0	0	0	0	0	1	1
1	1	1	1	0	0	0	1	1	1	1
1	1	1	1	1	1	1	1	1	1	1

(a)

0	0	0	0	0	0	0	0	0	0	0
0	0	0	0	1	1	1	0	0	0	0
0	0	1	1	1.4	2	1.4	1	1	0	0
0	0	1	2	2.2	2.8	2.2	2	1	0	0
0	1	1.4	2.2	3.2	3.6	3.2	2.2	1.4	1	0
0	1	2	2.8	3.6	4.5	3.6	2.8	2	1	0
0	1	1.4	2.2	3.2	3.6	3.2	2.2	1.4	1	0
0	0	1	2	2.2	2.8	2.2	2	1	0	0
0	0	1	1	1.4	2	1.4	1	1	0	0
0	0	0	0	1	1	1	0	0	0	0
0	0	0	0	0	0	0	0	0	0	0

(b)

Figure 2.5: Definition of the distance transform on a circular cross–section, (a) throat cross–section in which zero indicates the void space and one indicates the solid space, (b) values are equal to the Euclidean distance between the current pixel and the nearest non–zero pixel.

2.3.4 Throat flow simulation with the LBM

In order to model single–phase steady–state flow in a throat, we consider it as a tube with an arbitrary cross–section with a uniform shape along the throat length. We assume that the single–phase flow in throats is steady–state and fully developed. So, technically it is not required to simulate the whole length of the throat from the center of one pore to the center of the adjacent pore to find out its permeability (Fig. 2.6a). We take the 2D cross–section of a throat (Fig. 2.6b) and stack 6 layers of that cross–section (Fig. 2.6d) to build the simulation geometry. A D3Q19 scheme (Fig. 2.6c) is considered for the LBM which means there are 18 possible directions for fluid flow within each block. Considering the small size of the 2D throat images, image voxels are considered to be the simulation blocks without any upscaling.

We adopt an open–source LBM code in MATLAB to predict the permeability of the tube section (throat), originally developed by Haslam *et al.* [112]. A Newtonian fluid with BGK collision model [103] is used. Also, it is assumed that bounce–back is only in the direction normal to the geometry boundary. Particle distribution function f_i evolves in the directions of the distribution vectors e_i at each time step $(t + \Delta t)$ and location (x) as [112]:

$$f_i(x + e_i + \Delta t) - f_i(x, t) = -1/\tau(f_i(x, t) - f_i^{eq}(x, t)) \tag{2.1}$$

where f_i^{eq} is a truncated Maxwell–Boltzmann equilibrium distribution that can be expressed as a function of local velocity (v) in all possible directions and τ is the equilibrium state time. Also i is the distribution function index for different neighbours. Equilibrium function is [112]:

$$f_i^{eq} = w_i(1 + 3e_i.v)\sum_{i=1}^{r} f_i \tag{2.2}$$

where r is the number of particle density distribution vectors which is equal to 19 in the current 3-D derivation, w_i indicates neighbour weights and its values are 1/3, 1/18, and 1/36 for stationary, nearest and next–nearest vectors, respectively (Fig. 2.6c). Please refer to [112] for more details.

We start the flow simulation by imposing uniform distribution vectors (velocities) to the inlet blocks of the geometry. Periodic boundary condition is assumed in the direction of flow which means that during the LBM simulation, velocity distribution in the outlet face of geometry are assigned to the geometry inlet velocity distribution. It is known that the absolute permeability of tubes in laminar flow is calculated as $k = r_t^2/8$ [113], in which r_t is the tube radius. Considering that this formulation is independent of the tube length, periodic boundary condition is a valid assumption for the geometry considered.

The LBM simulation continues until a convergence is reached in the magnitude and direction of the distribution vectors at each block. This equilibrium state can be expressed in terms of permeability convergence by keeping the relative error smaller than a specified value. The convergence criterion we use to detect the density equilibrium is

$$\text{error} = \frac{k_{old} - k_{new}}{k_{old}} < 10^{-6} \tag{2.3}$$

where k_{old} and k_{new} are two consecutive values obtained for permeability during iterations. In order to calculate the permeability of throat tubes at each iteration, Darcy's law is rearranged as:

$$k = -\frac{\mu \bar{U}}{\frac{dp}{dx}} \tag{2.4}$$

where $\bar{U}$ is the averaged velocity vector in the direction of pressure drop, k is absolute permeability, dp/dx is the pressure gradient that similar to the velocity vector is obtained from LBM simulation results, and μ is the fluid viscosity which is calculated as:

$$\mu = \frac{\frac{1}{\omega} - 0.5}{3} \tag{2.5}$$

where ω is a relaxation frequency used in LBM. We assume that it is equal to 1 to ensure convergence of the LBM densities and minimize the error [114, 115].

After running several time steps in an explicit manner, permeability values converge to a value which is recorded as the absolute permeability of the simulated throat geometry. As an illustration, the permeability calculation method discussed above is applied on some throats' images with arbitrary shapes. Velocity maps at the outlet surface are visualized in Fig. 2.7. In this figure, sections (a) to (f) present the exiting velocity maps for throats with circular, star–shape, square, triangular, sample convex and sample concave cross–sections, respectively. In all images, as it was expected, velocity has higher values where node is farther away from the throat wall. Also, for the circular cross–section (Fig. 2.7a), the analytical and numerical permeabilities match with the value of 25 μm^2.

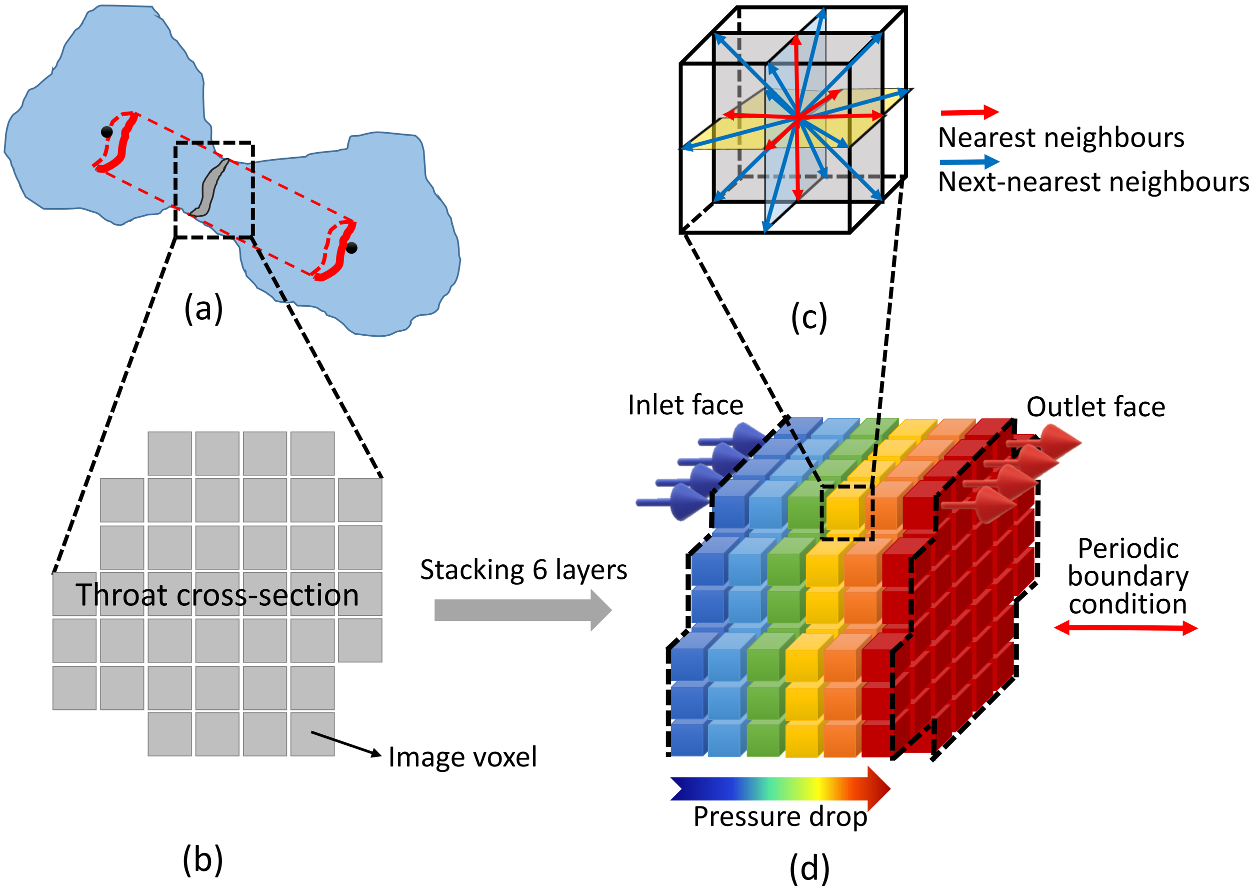

Figure 2.6: Extraction and construction of the equivalent throat geometry used for LBM simulation, (a) equivalent throat geometry used in the pore network model and its cross–section, (b) cross–section of the throat acquired from image processing, (c) D3Q19 scheme of LBM comprised of nearest and next–nearest neighbour vectors, and (d) schematic pressure drop during the flow and periodic boundary condition in the direction of flow.

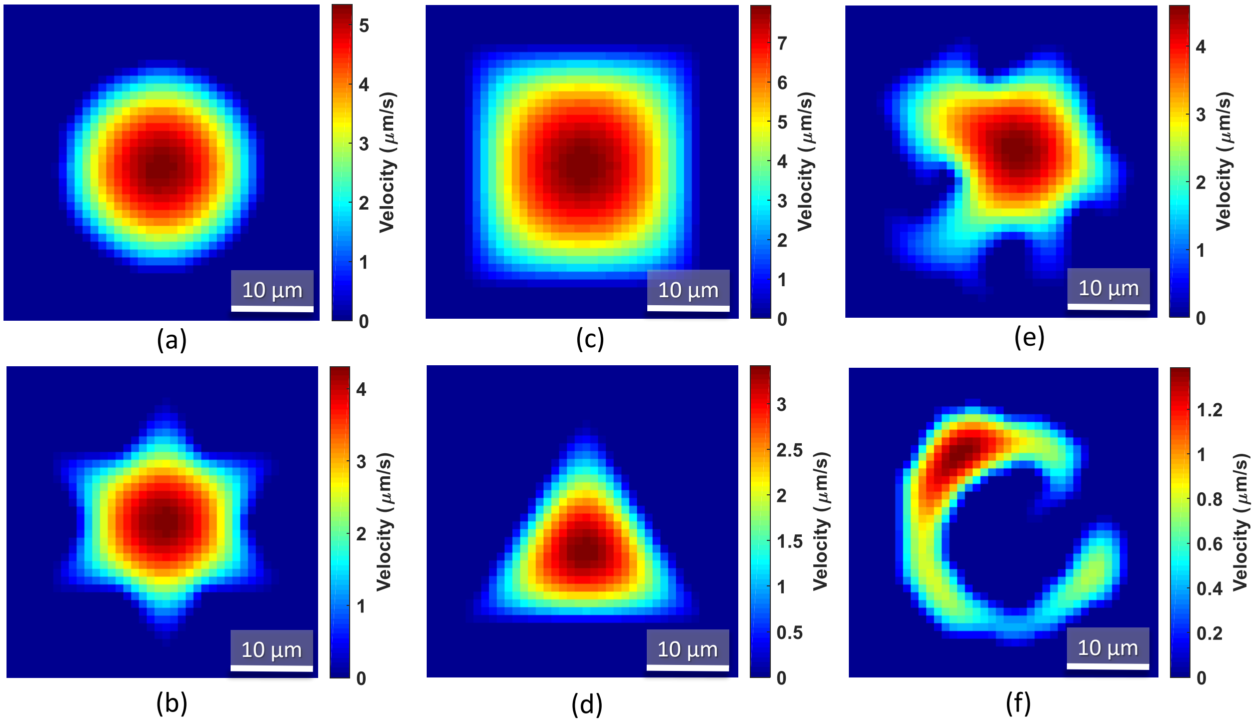

Figure 2.7: Exiting velocity map for different throat cross–sections obtained by LBM, (a) circular, (b) star–shape, (c) square, (d) triangular, (e) arbitrary and convex, and (f) arbitrary and concave cross–section.

2.3.5 Machine learning

We use machine learning to avoid repetitive calculation of the LBM-based permeability in all throats. Machine learning methods inherently classify the input samples into self–similar categories and develop a unique matrix–based relationship for each category to predict the best accurate outputs [116]. In this study, we use Levenberg-Marquardt method to train two ANN's in order to predict the throat's permeability based on the image–extracted features. Levenberg-Marquardt is an iterative algorithm to find the minimum value of a function that depends on the sum of squares of a series of nonlinear functions [117]. This algorithm is a common tool to optimize weights and biases of an ANN in a reasonable time scale [118]. From the two trained ANNs, the first ANN (Fig. 2.8a) takes 7 input parameters and has 6 nodes in the hidden layer and one output parameter. The input parameters are cross–sectional area, wetted perimeter, axes ratio, equivalent diameter, solidity, hydraulic radius, and mean distance. In order to avoid over–fitting, size of the hidden layer is set –based on a rule of thumb– equal to the 2/3 of input parameters plus the number of output parameters.

Neural network training is performed using the functions existing in *Neural Fitting Toolbox* of MATLAB.

The second ANN (Fig. 2.8b) is simpler and composed of one input parameter which is the mean distance, three nodes in the hidden layer and one output parameter. We train the second ANN to check out the effect of omitting probably less significant input parameters and present a simpler model. Variable selection for this ANN model will be described later in the results and discussions.

In order to train these ANN's, we build a database composed of 9,333 entries using the throat images extracted from 12 porous samples used in this study (Table 2.2).

From total number of analyzed throats, we take 65% of them for training, 15% for validation and 20% for testing. Then mean squared error (MSE) and coefficient of determination (R^2) are calculated to check the performance of training, validation and testing processes. Using the trained networks, we are able to calculate the throat's permeability without running the LBM.

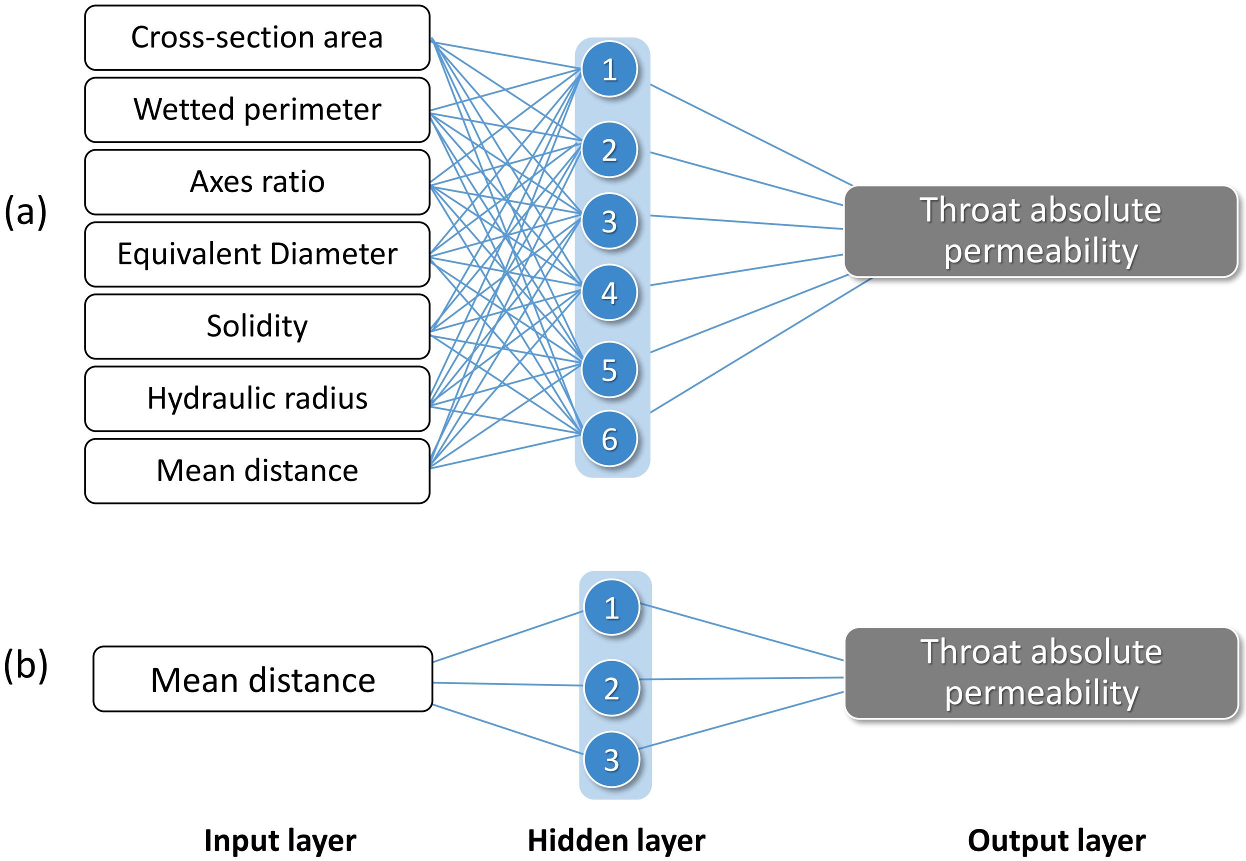

Figure 2.8: Illustration of two ANN's employed to model the permeability of throats based on the image features and previously calculated LBM-based permeabilities which are stored in a database, (a) the first ANN with 7 features as input and hidden layer with 6 nodes, and (b) the second ANN with 1 feature as input and 3 nodes in the hidden layer.

2.3.6 Empirical correlation for throat's permeability

Machine learning is typically applied in systems with complicated/non–linear relationships between the inputs and outputs [119]. ANN's are powerful and versatile tools for these purposes, however, they cannot be easily transferred to or replicated by other researchers, as they would need all nodal weights and biases. Thus, we aim to present an empirical correlation which relates the throat's LBM-based permeability and the best fitted feature which is extracted from throat images. A general form will be considered for the correlation based on the trial and error. Then using an optimization method we minimize the error of prediction by assigning values to the correlation constants. It is noteworthy that this empirical correlation is virtually an alternative to Hagen Poiseuille [120] equation which assumes an ideal cylindrical shape for the flow pathway.

2.3.7 Samples studied

In this study, we use 12 micro–CT images to investigate the permeability prediction accuracy of the proposed method. The samples are imaged at Imperial College London [50, 121] and their size and resolution are listed in Table 2.2. Samples C1 and C2 are carbonate rocks and rest of the samples are sandstone including Br sample (Berea Sandstone). These samples have been thoroughly studied in the literature [122, 46, 108, 121, 123].

Name	Resolution (μm/voxel)	Size (voxel)
S1	8.68	300^3
S2	4.96	300^3
S3	9.10	300^3
S4	8.96	300^3
S5	4.00	300^3
S6	5.10	300^3
S7	4.80	300^3
S8	4.89	300^3
S9	3.40	300^3
C1	2.85	400^3
C2	5.35	400^3
Br	5.35	400^3

Table 2.2: List of studied porous rock samples.

In order to avoid the effect of different spatial image resolutions, we temporarily change all spatial image resolutions to one micrometer per pixel. Then, after calculation of throat's permeability, we undo this change by multiplying the obtained value by the second power of the real spatial resolution provided in Table 2.2.

2.4 Results and Discussions

2.4.1 Pore network extraction

Pore network extraction is implemented on 12 porous samples (Table 2.2) studied in this research to provide the throat images needed for the LBM-based permeability simulation. In addition, these networks will be used to calculate the total permeability of the samples by assuming throat permeabilities derived by ITPM. The properties of extracted pore networks are provided in Table 2.3.

The throat radius reported is obtained by assuming equivalent circles with same surface area. In the current modeling, the pore radius of the network does not directly affect network permeability. Pore radius is just used to calculate and match the network porosity. Also, we have not taken into the account the pressure drop of pores. This is because of the fact that pressure drop in porous elements are mainly controlled by throats which are the narrowest openings rather than the pore bodies. In the extracted networks, we define the length of throats as the distance between centroids of two adjacent pores.

Samples	Mean pore radius (μm)	Mean throat radius (μm)	Mean throat length (μm)	Mean pore connectivity
S1	49.18	24.88	207.04	2.64
S2	30.64	16.22	120.13	3.80
S3	32.55	14.26	143.84	2.49
S4	32.68	15.49	133.83	2.07
S5	26.07	21.85	128.81	2.45
S6	33.33	26.73	145.57	3.23
S7	35.11	18.95	138.38	4.11
S8	27.16	21.24	126.60	3.56
S9	29.91	17.57	115.83	3.00
C1	11.39	11.99	62.49	2.12
C2	18.00	15.10	94.29	1.55
Br	26.22	14.70	112.98	2.90

Table 2.3: Properties of the classical pore networks extracted using watershed segmentation algorithm.

2.4.2 Features statistics

Total number of 9,333 throats are analyzed from 12 extracted networks and 7 morphological features are extracted from each throat image. This database includes a wide range of porous rocks with diverse fabric and morphological properties. We have statistically analyzed these features to measure the dependency of the permeability on each of them. In this line, stepwise regression coefficients of the features are calculated and shown in Table 2.4 relative to the absolute permeability. Stepwise regression is an automated method for fitting regression models and find the explanatory variables [124]. A higher regression coefficient means that the function value is more correlated to the corresponding variable [124]. According to Table 2.4, it can be concluded that mean distance is the best correlated variable which is also physically justified in section 2.4.5. Also, the hydraulic radius of the throat is reasonably correlated to the LBM-based permeability. Considering the higher correlation of mean distance, we have selected this feature to be used as single input of the second ANN. In addition, the proposed empirical correlation for throat's permeability will utilize the mean distance as input variable to have the best performance in permeability estimation.

Fig. 2.9 illustrates the scatter plots of 7 image-extracted features vs. absolute permeabilities. In order to remove the effect of different image resolutions, we consider "*pixel*" unit for length and "$pixel^2$" for area. Thus, in these figures permeability values are shown with "$pixel^2$" unit. By visual comparison of the scatter plots from Fig. 2.9(a) to (g), it can be concluded that absolute permeability of throats has a more significant relationship with the mean distance (Fig.2.9g). This conclusion is previously verified considering the higher value of stepwise regression coefficient corresponding to mean distance (Table 2.4).

Feature	Stepwise regression coefficient
Cross-section area	0.017
Wetted perimeter	0.013
Axes ratio	−0.003
Equivalent Diameter	−0.627
Solidity	−1.391
Hydraulic radius	0.572
Mean distance	4.399

Table 2.4: Stepwise regression coefficients between the extracted features of throats and their corresponding LBM-based permeability.

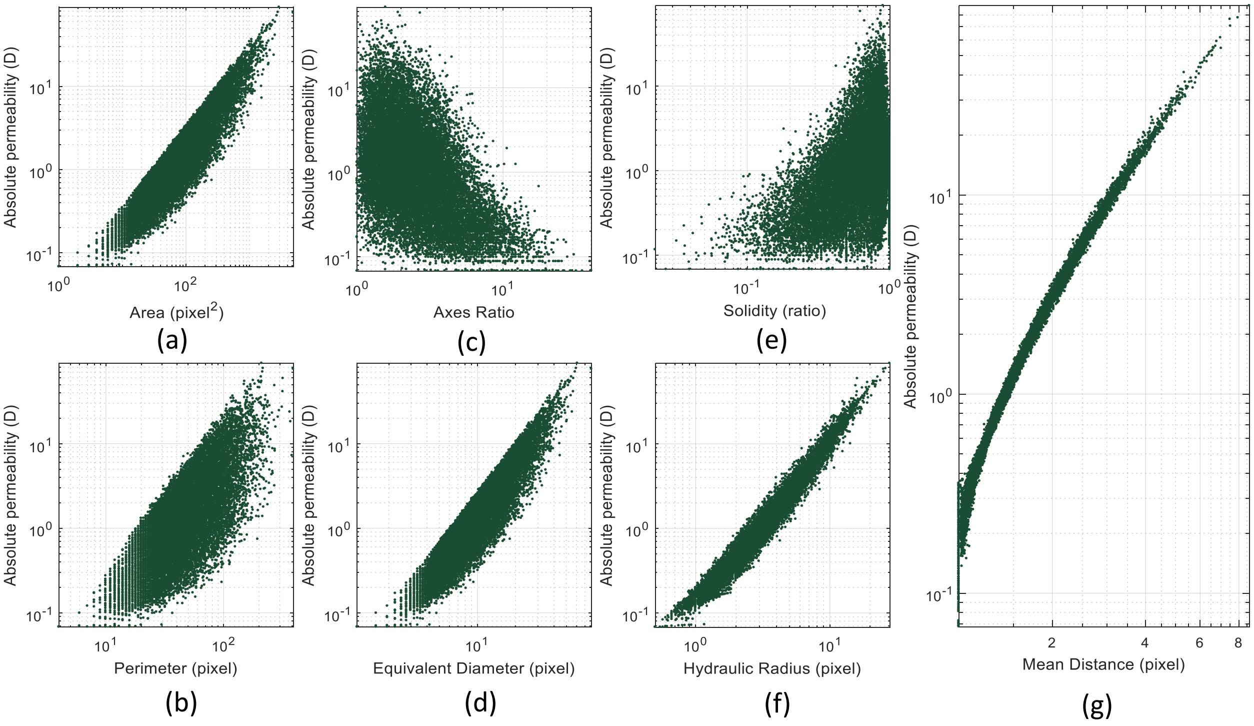

Figure 2.9: Scatter plot of LBM absolute permeability vs. values of 7 extracted features of throats: (a) cross-sectional area, (b) wetted perimeter, (c) axes ratio, (d) equivalent radius, (e) solidity, (f) hydraulic radius, and (g) mean distance.

2.4.3 Machine learning

Visual comparison between the cross-plots of Fig. 2.9 leads to the mean distance as the selected well-correlated input parameter to be used for the single-parameter ANN. The points of Fig. 2.9g are less scattered and apparently follow a predictable trend. Both 7- and single-parameter ANN's are trained to be able to predict throat's permeability. The learning performance of both ANN's are provided in Table 2.5 in terms of mean squared error (MSE) and coefficient of determination (R^2). Although, generally higher number of input parameters will enhance the ANN's predictions, parsimony and simplicity of the model will be affected. Consequently, the single-parameter ANN is able to estimate the LBM-based permeability with a reasonably high coefficient of determination (Testing $R^2 = 0.9982$), as such it would be more practical to use single-parameter ANN than to use the 7-parameter ANN.

Fig. 2.10(a) and (b) illustrate the original and predicted throat permeabilities by single- and 7-parameter ANN's , respectively. As it is expected, the predictions of single-parameter ANN is more scattered than the 7-parameter ANN.

Data Set	7-Param. MSE	7-Param. R^2	1-Param. MSE	1-Param. R^2
Training	0.0142	0.9998	0.1436	0.9984
Validating	0.0193	0.9997	0.1281	0.9980
Testing	0.0264	0.9996	0.1971	0.9982

Table 2.5: Learning performance of both 7- and single-parameter ANN's in terms of coefficient of determination (R^2) and mean squared error (MSE).

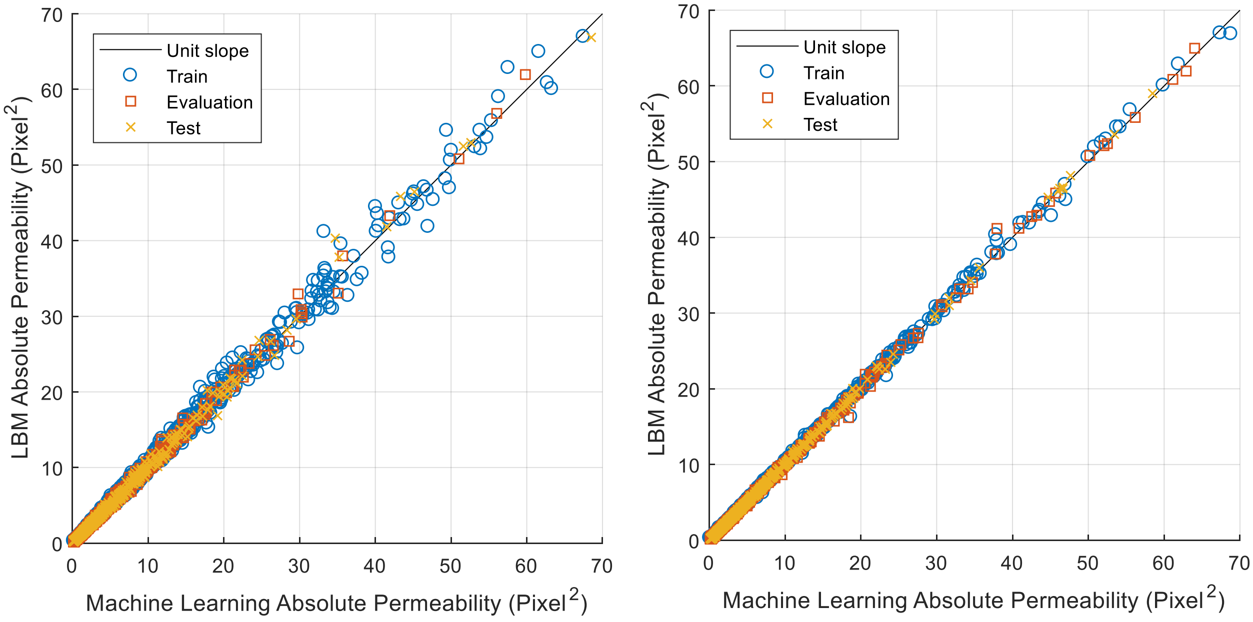

(a)

(b)

Figure 2.10: The capability of ANN's to predict LBM-based permeability of throats including training, evaluation and testing data, (a) single-parameter ANN, (b) 7-parameter ANN.

2.4.4 Empirical correlation for throat's permeability

In order to improve simplicity of the coupling method, we use empirical correlations beside neural networks. The developed correlation will estimate the LBM-based permeability of throat using mean distance of the throat image. By testing several forms of empirical correlations, a quadratic form is accepted because of a low magnitude of MSE:

$$k_{throat} = a\bar{D}^2 + b\bar{D} + c \tag{2.6}$$

where k_{throat} is throat's permeability with $pixel^2$ unit, and $\bar{D}$ is mean distance of the throat image. Optimization of the correlation constants is carried out by linear least squares method. The constants obtained for the empirical formula and the 95% confidence interval for those constants are provided in Table 2.6. Fig.2.11 illustrates the original and estimated LBM-based permeabilities using the proposed formula. The overall R^2 and MSE of the empirical correlation results are 0.996 and 0.146, respectively. These values are in the same order of magnitude as R^2 and MSE of single-parameter ANN. Thus it is reasonable to use the proposed empirical correlation when ANN's are not available. Finally, the proposed empirical formula for throat's permeability can be written as:

$$k_{throat} = 1.342\bar{D}^2 - 0.913\bar{D} - 0.381 \tag{2.7}$$

Model constants	Mean value	Lower boundary	Upper boundary
a	1.342	1.338	1.345
b	-0.9127	-0.9376	-0.8878
c	-0.3814	-0.4131	-0.3498

Table 2.6: Constants in the empirical formula and their 95% confidence intervals.

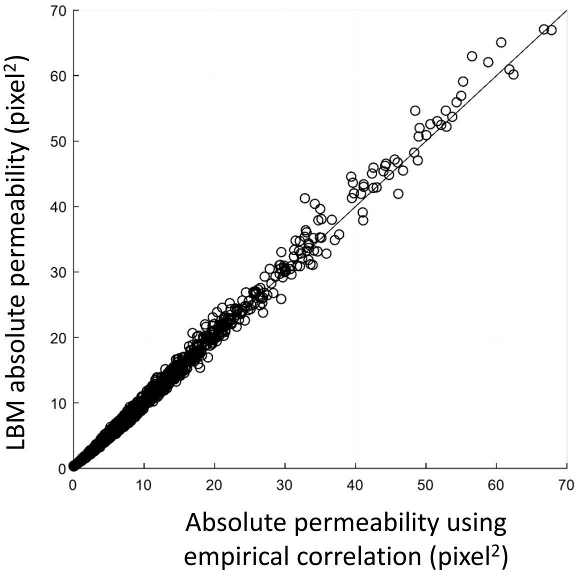

Figure 2.11: Original LBM-based throat permeabilities and predicted values using the proposed empirical formula ($R^2 = 0.996$).

2.4.5 Physical justification

We showed statistically that mean distance is the best image feature to estimate the LBM-based permeability of a throat. Here, we explain the physical concept behind this observation. Based on the distance map definition, we know that the distance value of a pixel in a void space is higher for the pixel that is far from the solid walls (Fig. 2.5). Similarly, for a steady-state incompressible laminar flow through a tube, fluid velocity reaches its maximum at the center of the tube since fluid is far from the tube walls (Fig. 2.7a). So, distance map mimics the trend of the velocity profiles in the tubular laminar flow. In order to illustrate this statement, Fig. 2.12 is presented. The top row of the figure, shows the relative velocity maps obtained from the LBM simulations and the bottom row is the relative distance map of the throat cross-sections. For the sake of comparison, we have divided all values of both map types over their maximum values to generate the maps with relative intensities. In addition, the non-zero average and non-zero standard deviation of both groups of maps are inscribed in the figure. Based on these three pairs of examples, the difference is not more than 25% between the LBM velocity maps and the distance maps. By the term “non-zero average” we mean that the zero values (dark blue portion of the maps) are not considered in averaging.

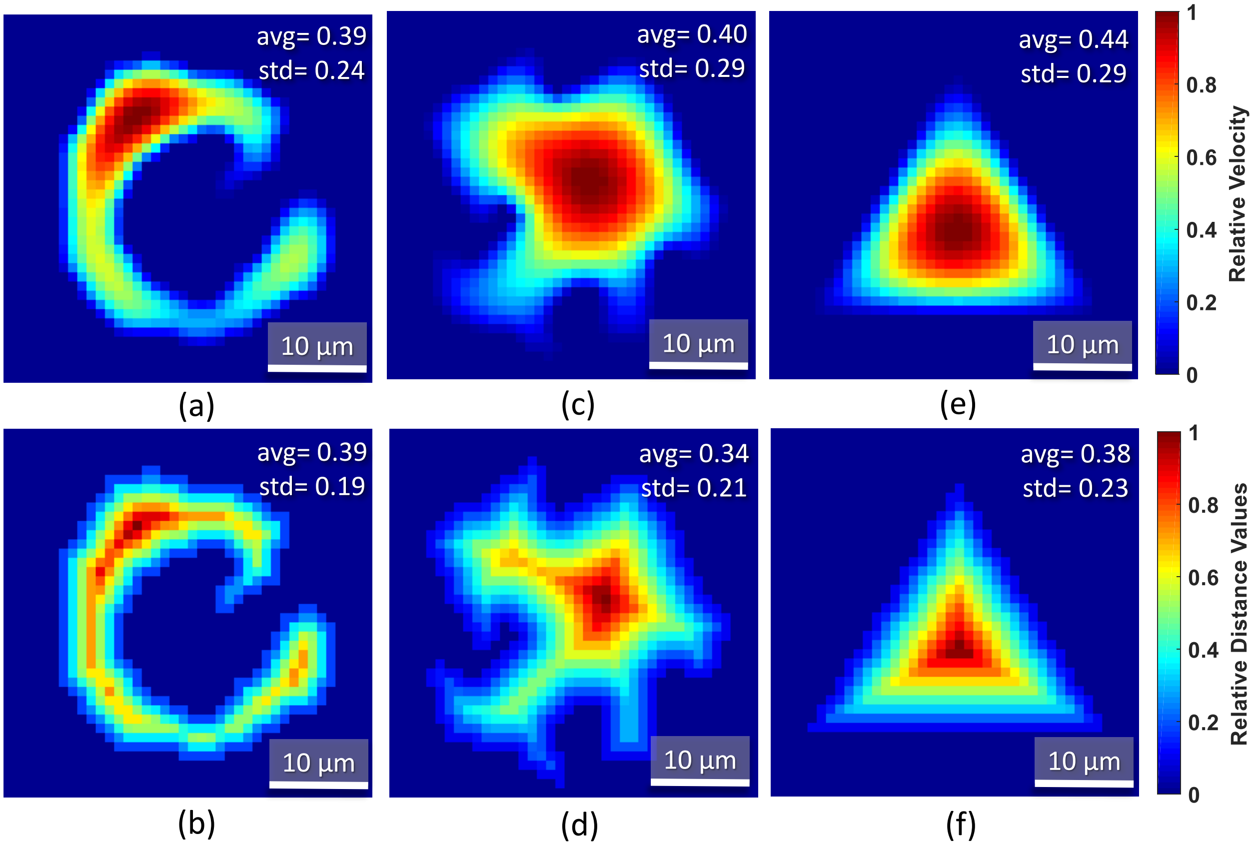

Figure 2.12: Comparison of velocity maps and distance maps obtained by the LBM simulation in three different throats: (a) and (b) concave cross-sections, (c) and (d) convex cross-sections, (e) and (f) triangular cross-sections.

2.4.6 Permeability calculation

When the permeability of all network throats is estimated using ITPM, there is one step remaining to calculate the permeability of the whole pore network. For this step, we assume a pressure difference between two sides of the network so that the pressure at the center of the pores are unknown. In the next step, the continuity equation is written for each pore for a steady-state single-phase flow of an incompressible fluid. Then we rearrange the continuity equation in terms of throat permeability, length and pore pressures. Since throat's permeability and length are previously known, the only unknown parameters are the pressure of each pore. This leads to a linear system of equation which can be numerically solved to find the pressures. After determination of all pressures, the overall flow rate is calculated and total absolute permeability of the network is obtained using Darcy's law. We call the final value "hybrid PNM-LBM permeability" since both methods are used. Here, we compare three different options for throat's permeability calculation and compare the total permeability of our 12 samples for each option. The three options for throat's permeability are as follow:

a) **Hagen-Poiseuille permeability with equivalent radius**
   In this option, throat's permeability is calculated as $r^2/8$ in which r is throat radius and it is equal to the radius of a circle with the same surface area as the throat.

b) **Hagen-Poiseuille permeability with hydraulic radius**
   In this option, throat's permeability is calculated as $r^2/8$ in which r is hydraulic radius of the throat and can be calculated as $2A/P$, that A is throat cross area and P is the wetted perimeter of throat.

c) **LBM-based permeability**
   In this option, permeability of throats is calculated using the LBM simulation and by means of Eq. 2.7.

In addition, the total permeability of the studied samples when running LBM on the whole geometry is available in the literature [122]. Consequently, we are able to compare our calculated permeabilities with total LBM-based permeability of the samples. This comparison is illustrated in Fig. 2.13 by averaging the absolute permeability of samples in x, y and z directions. Fig. 2.13(a) (for Option a) shows the PNM permeability considering equivalent radius for throats vs. the total LBM-based permeability of the sample. It is clear that the predicted values are over-estimated. This could be due to ignoring the wetted perimeter of the throats in permeability calculation. Larger wetted perimeter causes more friction during fluid flow and reduces the throat's permeability. As an example, angular throat shapes are less permeable than the circular ones, although they have the same cross-sectional area. Fig. 2.13(b) presents results for Option b. The difference is that for this option, we are calculating the throat's permeability using the hydraulic radius concept and this is a more realistic approach than option a. For option b, the accuracy of the model increases to R^2=0.9689, but still some deviations from the unit slope line are visible, especially for the higher permeability values. Finally, Fig. 2.13(c) (for Option c) illustrates the permeabilities obtained by the PNM-LBM approach vs. the values obtained by the LBM. We reach to R^2=0.9973 for permeability estimation which is an improved accuracy. This shows that the presented hybrid model is adequately capable of estimating direct simulation permeabilities by coupling PNM and LBM approaches.

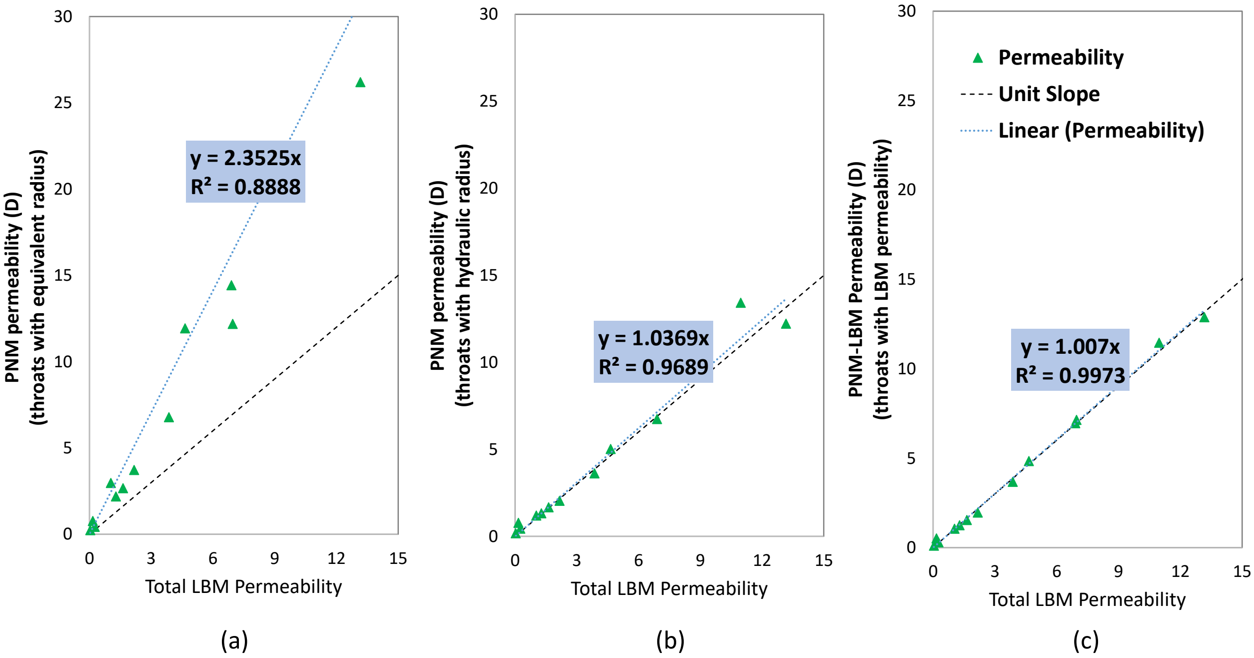

Figure 2.13: Comparison of network permeability values if using three different options for throat's permeability, (a) throats with permeability based on the equivalent radius concept, (b) throats with permeability based on the hydraulic radius concept, and (c) throats with permeability estimated using LBM by means of Eq. 5.1.

2.4.7 Computational costs

Here, we present the CPU times of the simulation machine while running different permeability modelling techniques. The results are presented in Fig. 2.14. CPU times of the full LBM are adopted from Mostaghimi *et al.*[122] who performed LBM on a sandpack image (LV60) with spatial resolution of 10 micrometer per voxel. CPU times of the classical PNM and the PNM-LBM methods are measured in the present study. All simulations are performed using a 3.0 GHz CPU with no parallel processing. As it can be seen in Fig. 2.14, the PNM-LBM method is not computationally efficient and its CPU time is increasing with a steep trend relative to the other methods. The accelerated PNM–LBM which uses Eq. 2.7 for the throat's permeability, is virtually as fast as the classical PNM approach but as we have shown in Fig. 2.13, it is more accurate. It is noteworthy that for the PNM-based methods, CPU time of pore network extraction is included in total times. Finally, it can be stated that using the CPU configuration mentioned and with PNM–LBM approach, the absolute permeability of a sample (in the size of 400^3 voxels) can be calculated in around 200 seconds.

In addition to the CPU time saving, the PNM-LBM approach demands less computational memory. The amount of peak memory usage for full LBM-based permeability model on the discussed 300^3 sample is 3.5 GB. For the tested PNM–based methods, memory needed is around 1 GB when running on the same sample. Additionally, it is possible for the PNM–based methods to use even less amount of memory if using domain decomposition approach for running pore network extraction. This part of the presented code has been shown to be a memory bottleneck [80].

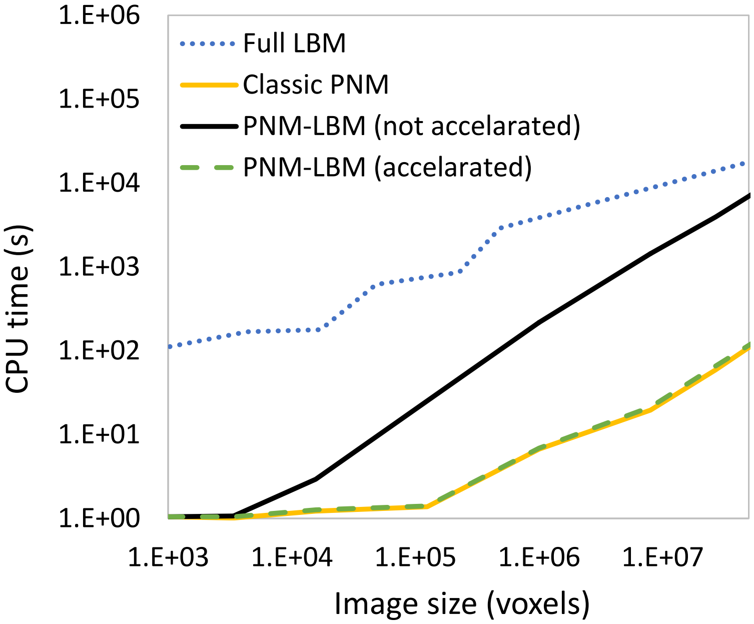

Figure 2.14: CPU times of the different methods for calculating the absolute permeability of a sandpack image [122]. Tested methods are full LBM (CPU times from [122]), the classical PNM [106], the PNM–LBM without machine learning acceleration, and the PNM-LBM with machine learning acceleration.

2.5 Conclusions

In this study, we coupled PNM and LBM approaches to estimate the hydraulic permeability of porous rock samples. In this regards, a classic pore network model is extracted from micro-tomography images and throat permeabilities are simulated using LBM. Then, in order to reduce the computational cost of the LBM simulation, we utilized some image-based features to estimate LBM throat permeabilities in an efficient manner.

The main conclusions and findings of this study are as follow:

- Two ANN's and one empirical formula were presented capable of estimating the throat's

LBM-based permeabilities with coefficient of determination (R^2) higher than 0.99.

- The "mean distance" was found to be an image-based feature highly correlated with LBM throat permeabilities. It was defined as non-zero average of the throat distance map.
- The empirical quadratic formula for estimating the throat's LBM-based permeability employed mean distance as the input variable and this simple equation predicted the throat's permeability with coefficient of determination around 0.996.
- The throat permeabilities obtained were substituted within the classical pore networks of 12 rock samples and overall network permeabilities were calculated successfully. PNM-LBM absolute permeabilities with pure LBM-based permeabilities of the samples are compared and it has been found that the proposed model is capable of predicting the overall permeability of the rock samples with coefficient of determination around 0.997.
- The proposed PNM-LBM approach was capable of predicting the permeability with higher accuracy than the classical PNM and with considerably less computational cost than the classic LBM.

Chapter 3

A triple pore network model (T–PNM) for gas flow simulation in fractured, micro-porous, and meso-porous media

3.1 Abstract

In this study, a novel triple pore network model (T–PNM) is introduced which is composed of a single pore network model (PNM) coupled to fractures and micro–porosities. We use two stages of the watershed segmentation algorithm to extract the required data from semi–real micro–tomography images of porous material and build a structural network composed of three conductive elements: meso–pores, micro–pores, and fractures. Gas and liquid flow are simulated on the extracted networks and the calculated permeabilities are compared with dual pore network models (D–PNM) as well as the analytical solutions. It is found that the processes which are more sensitive to the surface features of material, should be simulated using a T–PNM that considers the effect of micro–porosities on overall process of flow in tight pores. We found that, for gas flow in tight pores where the close contact of gas with the surface of solid walls makes Knudsen diffusion and gas slippage significant, T–PNM provides more accurate solution compared to D–PNM. Within the tested range of operational conditions, we recorded between 10 to 50 % relative error in gas permeabilities of carbonate porous rocks if micro–porosities are dismissed in the presence of fractures.

3.2 Introduction

3.2.1 Single pore network model

A pore network model (PNM) is a simplified proxy model to simulate various transport phenomena in porous materials. PNMs can be statistically generated [125, 126] or extracted from realistic tomography images of porous media [127, 108, 128]. Despite PNM simplifications, it is still interesting due to the low computational cost, especially with the growing size and resolution of the tomography images of porous materials [129]. Single PNM has been initially introduced by Fatt [130] in 1956 (Fig. 3.1a). He discussed several approaches to tackle the porous media transport problems from single–size capillary tube to dynamic displacement of two phase fluids. Since then many developments have been accomplished by researchers to enhance the capability and reliability of PNMs [131] to realistically simulate and predict the properties of porous materials [132, 133, 134], from hydraulic permeability [127] and mass diffusivity [135, 136] to electrical [137] and thermal conductivities [138].

In the present study, the main focus of PNM is on simulation of gas transport in porous media. One of the first applications of PNM for gas flow simulation was presented by Millington and Quirk in 1961 [139]. They used the physical concept of capillaries network demonstrated by Fatt [130] and studied the effects of Knudsen diffusion [140] on gas permeability of the porous solids. From 1960s to 1990s, most of the gas PNM studies were dedicated to chemical processes and catalysis applications [141, 142, 143], while the gradually rising role of the natural gas in world energy market [144] has led to many petroleum–oriented studies emerged in the literature [145, 146, 147]. Specifically, in the past decade, the prosperity of unconventional natural gas resources such as shale gas, tight gas, and coal–bed methane triggered a significant research trend to model and simulate gas transport in these irregular materials [148, 149, 147, 150, 151, 152, 153, 154]. As a prominent example, shale gas is pioneering among the unconventional gas research subjects and many numerical studies have been recently presented to include a wide range of physics into a gas transport model such as adsorption [155, 156], multiple gas components [157], multi–level of porosity[158, 159], super critical condition [158], and arbitrary pore shapes[160]. Furthermore, in parallel to the natural gas PNM studies, many fuel cell researchers started to use PNMs as a tool to model gas diffusion in porous membrane of proton exchange cells [161, 162] even with capability of including micro–porosities in the network [163] which is one of the main focuses of the present study.

3.2.2 Dual pore network model (D–PNM)

Meso–pore and micro–pore coupling

A single continuum pore network model defines a void-solid structure in which the granular portion of the material does not contribute to the fluid flow [164]. In the more recent pore network studies, many researchers have started to consider an implicit contribution for the solid phase assumed in the transport properties of porous media [165, 166, 167, 168, 169, 170, 171, 172]. The main logic behind this assumption is the fact that in the heterogeneous material, micro–pores residing in the solid section can affect the macroscopic properties of porous material in certain physical conditions. In some physical processes such as gas transport and two–phase imbibition, micro-pores can make a statistically significant change in the simulation results as well as in the experiments [148, 170].

Many geometrically different structures for dual pore network of meso and micro-pores have been suggested by researchers. Bekri *et al.* [166] presented a D–PNM with lattice-like networks of micro-pores embedded between the neighbouring meso-pores (Fig. 3.1b). Then they predicted relative permeabilities with a quasi-static assumption and compared them with experimental values. In another effort, Bauer *et al.* [167] considered that some portion of the meso-pores are connected to the adjacent pores with both meso and micro-throats in a paralleled way (Fig. 3.1c). Using an approach similar to Bekri *et al.* [166], they compared their relative permeability results obtained from modelling and experiment. Jiang *et al.* [171] presented the next comprehensive work on D–PNMs and developed a fully connected PNM with two scales of pores and throats to consider the effect of unresolved porosities on PNMs constructed based on micro-tomography images. They studied the effects of changing the density of micro-throats on two-phase properties of porous media such as relative permeability. Inspired by their work, Bultreys *et al.* [170] used micro-CT images of several tight and heterogeneous porous carbonate rocks to extract a pore network that in addition to the meso-throats, utilizes some micro-throats to connect adjacent meso-pores (Fig. 3.1e). Some of their non-fractured raw images of porous carbonated rocks with multi-levels of porosity are used in this paper as case studies.

Meso–pore and fracture coupling

Similar to the smaller-scale features such as micro-porosities that can be plugged into pore networks, some larger-scale features like fractures can be coupled to regular PNMs. Researchers must answer two important questions when coupling these components: how should they specify a void section as a fracture or simply a pore body, and what network properties, such as hydraulic permeability, should those sections exhibit? To answer the second question, it is commonly assumed that a pore throat's hydraulic permeability obeys the Hagen-Poiseuille law [173, 113], and equals $r^2/8$, where r is the throat hydraulic radius. Similarly, we can calculate the absolute permeability of an ideal fracture segment using $h^2/12$ where h is the distance between two planes of the fracture [174, 175].

Hughes and Blunt [176] presented one of the first studies to simulate fluid flow through the fractures using PNM. They arranged several box-shaped conductors in a row to simulate the aperture variation of a fracture which is in contact with a regular porous space (Fig. 3.1f). Erzeybek and Akin [177] studied different arrangements of such fracture nodes in different pore and fracture configurations to evaluate the contribution of each element in the fluid flow simulations.

Jiang *et al.* [178] presented a more versatile approach to calculate the absolute permeability of a pore-fracture system. They utilized the medial axis method to extract the regular PNM then devised a shrinking algorithm to locate the fractures, answering the important question of how to specify a void section as a fracture or a pore body. In this shrinking algorithm, they removed non-planar structures in a stepwise manner to obtain the remaining fracture body and simulated it with a virtual network of locally variable throats (Fig. 3.1i). As mentioned, this virtual network for simulating fracture behaviour has been introduced by Hughes and Blunt [176], and it is used in the present study with modifications. Details of fracture modelling and method validation will be discussed later in this paper.

In another effort to couple fractures and porous space, Weishaupt *et al.* [179] used a Navier–Stokes model for free flow and a PNM for the porous domain to simulate pressure drop and velocity map of a porous–fractured system in two dimensions. They studied the mass transport of a component in the porous-space due to the free flow in fractures for different Reynolds numbers. Their developed method is dynamic, robust and flexible for modeling of unstructured networks coupled with fractures, however, it could become computationally intensive for complex 3D geometries.

3.2.3 Triple pore network model

To the best of our knowledge, there is no previous study to couple micro–pores, meso–pores and fractures at the same time in a triple pore network model (T–PNM). Here, we present an approach to extract a triple pore network model based on the semi–real micro-tomography images of heterogeneous porous material. Then by simulating liquid and gas flow through the porous–fractured geometries of the selected samples, we demonstrate the capability of the proposed method and justify the conditions that a T–PNM would give more accurate results than single PNMs or D–PNMs. The diagram of the previous D–PNM structures in the literature and the presented triple structure are illustrated in Fig. 3.1. Some of the illustrations in this figure are inspired by Tahmasebi and Kamrava [165].

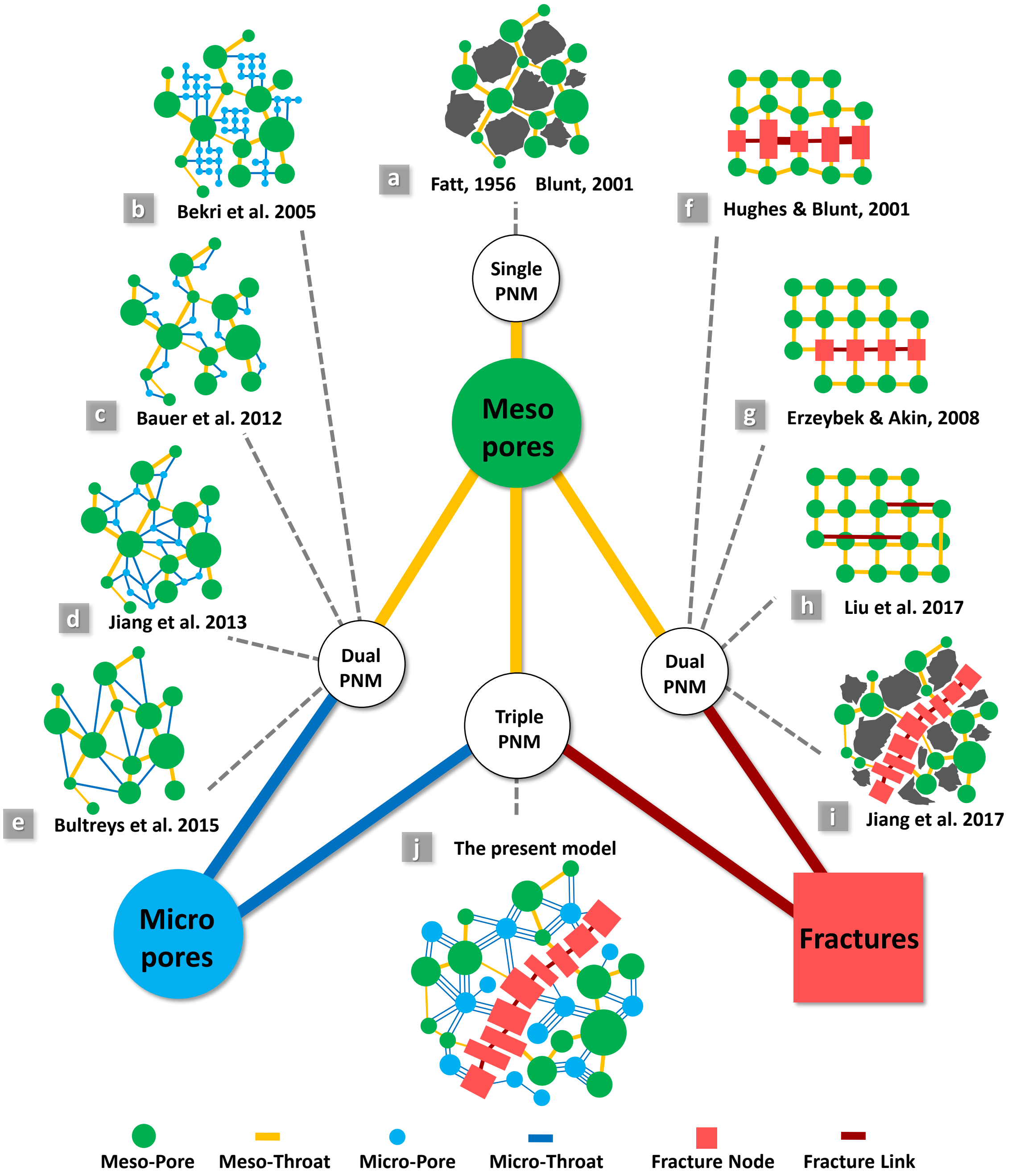

Figure 3.1: Network structure of the previous single PNMs and D–PNMs compared to the presented T–PNM, (a) single PNM [164, 130], (b) D–PNM with meso-pores coupled to a lattice micro–pores [166], (c) dual with meso-pores and parallel micro-pores and throats [167], (d) a fully two–scale PNM with micro and meso-pores [171], (e) dual with extra micro-throats to connect the meso-pores [170], (f) dual with meso-pores and fractures with variable aperture [176], (g) dual with meso-pores and fractures with fixed aperture [177], (h) D–PNM with extra bypassing fracture links [180], (i) dual with unstructured network and variable geometry of fracture [178], (j) the presented T–PNM which includes meso and micro-pores, meso and micro-throats, fracture nodes, and fracture links.

3.3 Methodology

In this research we extract a T–PNM from micro-tomography images of heterogeneous porous media and simulate steady-state liquid and gas flow through the network to investigate the viability/applicability/advantages of the proposed method. For this purpose, we describe the porous material preparation and image processing techniques that lead to extracting a PNM consisting of (1) meso-pores, (2) micro-pores which are unresolved in the images, and (3) fractures which have been generated synthetically on the volumetric images of porous carbonated rocks. We define micro–pores as pores so small that they are not explicitly visible in the tomography images. However, a population of the micro–pores causes local density reduction that locally decreases the intensity of the X–ray tomography image [181]. On the other hand, based on our definition, meso–pores are clearly visible in the images, and pore boundaries can be distinct from the solid or partially solid background. After extracting the regular PNM, we need to include fractures and micro-pores. Finally, we clarify the equations that we use to simulate steady–state liquid and gas flow through the proposed T–PNM by assuming no surface reaction or physical adsorption.

3.3.1 Materials

The International Union of Pure and Applied Chemistry (IUPAC) defines meso–pores as between 2 nm and 50 nm in size [182], and states that size of micropores should not exceed 2 nm. However, in the present study, we assume a dynamic threshold level for distinguishing between the micro–pores and meso–pores. This dynamic threshold is equal to the imaging spatial resolution (see Table 3.1), in which pores with sizes less than spatial resolution are considered as *micro–pores* and larger ones are assumed to be *meso–pores*.

Three carbonate porous rocks are selected as case studies. These samples are heterogeneous with two scales of porosity imaged and published by Bultreys *et al.* in the public domain [170]. Several artificial fractures are created though these samples to mimic the conditions of a triple–pore system. These fractures are carved into the samples with a cost–minimizing random walk approach inspired by Mhiri *et al.* [183] and coded for our specific application. The method dictates the fracture pathway to grow in the direction with highest porosity and consequently with less mechanical strength. This approach is physically plausible, considering the fact that breaking a material at loose connections requires less amount of energy [184]. Details of generating fracture realizations are beyond the scope of this study, however, more information is provided in Appendix A. Estaillades, Savonnieres and Massangis are the conventional names of three types of carbonated porous rocks that we use as the raw material (Fig. 3.2a, b and c, respectively). Dimensions and spatial resolution of the porous samples studied are provided in Table 3.1.

Fig. 3.2 illustrates the 3D map of CT numbers for the porous–fractured samples studied and the corresponding porosity map of each sample. We assume that mineralogy and consequently mineral density remain constant throughout various sections of the samples. Based on this assumption, bulk density of a section is the major factor that controls the energy of the photons received during the tomography process [185, 186]. Bulk density of the pure materials is inversely related to porosity [187]. Consequently, we can roughly assume that any increase in porosity, linearly decreases the local CT number of the material [188]. Therefore, in order to obtain a porosity map for the unresolved part of the image we simply consider a linear relationship with a unit slope between the normalized CT number and micro–porosity. Then, the darkest portion of the CT number map is considered to be completely void and the lightest parts of the geometry are assumed to be completely solid.

The segmentation between the void space and porous space of the samples is conducted using Otsu algorithm [189] which is based on the minimization of standard deviation in each segment of the data. So, in Fig. 3.2-d to f, the pure yellow segments of the samples are assumed to be completely porous and the porosity of other parts of the samples varies between 0 to 1. In addition to tomography images, an experimental curve for the pore size distribution of each porous material has been obtained by mercury intrusion porosimetry. These curves are adopted from Bultreys *et al.*[170], Gibeaux *et al.* [190], and Neveux *et al.* [191], respectively, for Estaillades, Savonnieres and Massangis samples. Dashed part of the curves in Fig. 3.2g represent the size distribution of the sub–resolution pores.

No.	Name	Voxels	Resolution (μm/voxel)
1	Estaillades	$500 \times 500 \times 150$	6.83
2	Savonnieres	$500 \times 500 \times 150$	7.61
3	Massangis	$500 \times 500 \times 150$	4.54

Table 3.1: Dimensions and spatial resolution of the porous samples.

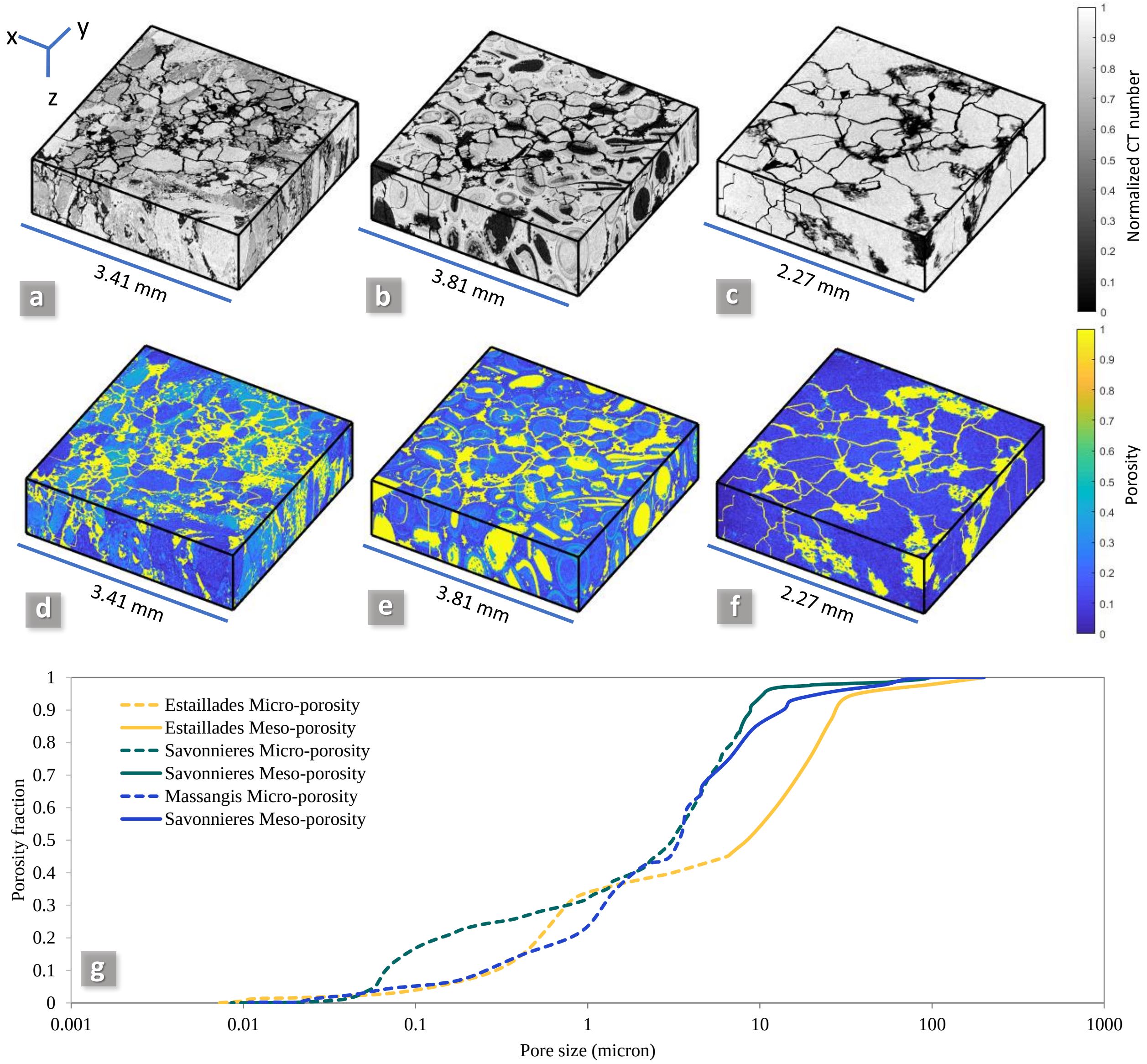

Figure 3.2: Fractured realizations of porous samples and corresponding porosity map of each sample, (a) normalized CT number of Estaillades Carbonate Rock, (b) normalized CT number of Savonnieres Carbonate Rock, (c) normalized CT number of Massangis Carbonate Rock, (d) porosity fraction map of Estaillades, (e) porosity map of Savonnieres, and (f) Porosity map of Massangis, (g) pore size distribution of all three samples with distinction between macro and micro–porosity based on image spatial resolution

3.3.2 Extraction of the single pore network model

Extraction of a single–continuum pore network model is a routine procedure reported in the literature of modeling fluid flow in porous materials [134]. In order to extract the regular PNM, we use the watershed segmentation algorithm [192] which has been extensively employed to segment objects with morphological connections or overlapping [107, 128, 193]. It has been shown in the literature that watershed segmentation is reasonably accurate and computationally efficient for extraction of the pore bodies and pore throats [128, 107]. This algorithm takes the distance transform of the pore space to locate the narrowest pathways of pore network and record them as pore throats [108, 109, 110]. Distance transform gives the minimum distance of a zero voxel to the nearest non-zero voxel [194] (Fig. 3.3b). This transform is a function available in most of the image processing libraries and packages. We used MATLAB 2018a Image Processing Toolbox to analyse 2D and 3D images. In order to avoid over–segmentation of the structure, it is recommended to apply a smoothing transform such as Gaussian filtering or image opening on the distance map [128, 195, 131, 32].

Fig. 3.3 illustrates a simple workflow for extracting single PNMs (a to d), D–PNMs (e to h), and T–PNMs (i to l). Initially, we consider a simple bed of spherical solids (Fig. 3.3a). Applying the distance transform on this geometry generates a map visualized in Fig. 3.3b. After smoothing, watershed algorithm uses this map to generate the distinct map of the pore bodies labelled with random shades of grey in Fig. 3.3c. This algorithm simulates a hypothetical flooding process starting from the local maximum values of the distance map. In a step–wise manner, the algorithm dilates the central nuclei of each pore while in the meantime keeps track of the distinct bodies. Each time that two dilating nuclei from neighbouring pores touch, the intersection voxel is recorded as a throat. This process continues until all voxels of the domain of interest are flooded by the dilating nuclei [196, 192, 197]. Watershed segmentation inherently calculates the labelled map of pore bodies. In Fig. 3.3c we have assigned random shade of grey to each pore body to demonstrate the segmentation. Now, using a 3×3 sliding window we scan the whole area of the image and detect connections between different pore labels. Consequently, a pore network can be constructed based on the inter–pore connections (Fig. 3.3d).

To simulate fluid flow within the extracted single PNM, we should determine the magnitude of pressure drop occurring when fluid is moving between a pair of connected pore bodies. If we ignore the pore body pressure drop, the major element that controls the fluid transport will be the pore throat that has minimal opening area compared to its connected pores. Hydraulic permeability in a throat can be simply calculated by Hagen-Poiseuille law

[173], and it is equal to $r^2/8$ that r is the throat hydraulic radius. A more realistic approach to calculate the absolute permeability of a throat with an arbitrary cross–sectional shape is presented by Rabbani and Babaei [198] and it is based on the Lattice–Boltzmann method (LBM) to simulate a steady–state single–phase flow through the throat. They showed that numerical results obtained for permeability of arbitrary–shaped throats are highly correlated with averaged distance map of the throat image and permeability can be obtained as the following quadratic form:

$$K_p = 1.342\bar{D}^2 - 0.913\bar{D} - 0.381 \tag{3.1}$$

where K_p is the absolute permeability of the porous space links such as a meso–throat with pixel^2 unit, and $\bar{D}$ is the mean distance of the throat cross-sectional image. This approach for obtaining absolute permeability of a single throat is referred to as Image–based Throat Permeability Model (ITPM) [198] and its code is available in the public domain [1]. As mentioned previously, a distance map shows the minimum distance between a zero voxel to the nearest non-zero voxel (Fig. 3.3b) and to obtain $\bar{D}$, we perform an averaging on the non–zero values of a distance map. More details of statistical and physical justifications for this empirical equation are provided in [198]. Also, the basics and modelling assumptions of LBM simulation used in [198] and extended to the current study are described in Appendix B. By describing the hydraulic behaviour of the links in a single continuum PNM, we are able to model fluid flow through the extracted networks that consist of meso–pores and meso–throats.

---

[1] The code for "Image–Based Throat Permeability Model" is available online at GitHub: `https://github.com/ArashRabbani/PaperCodes`

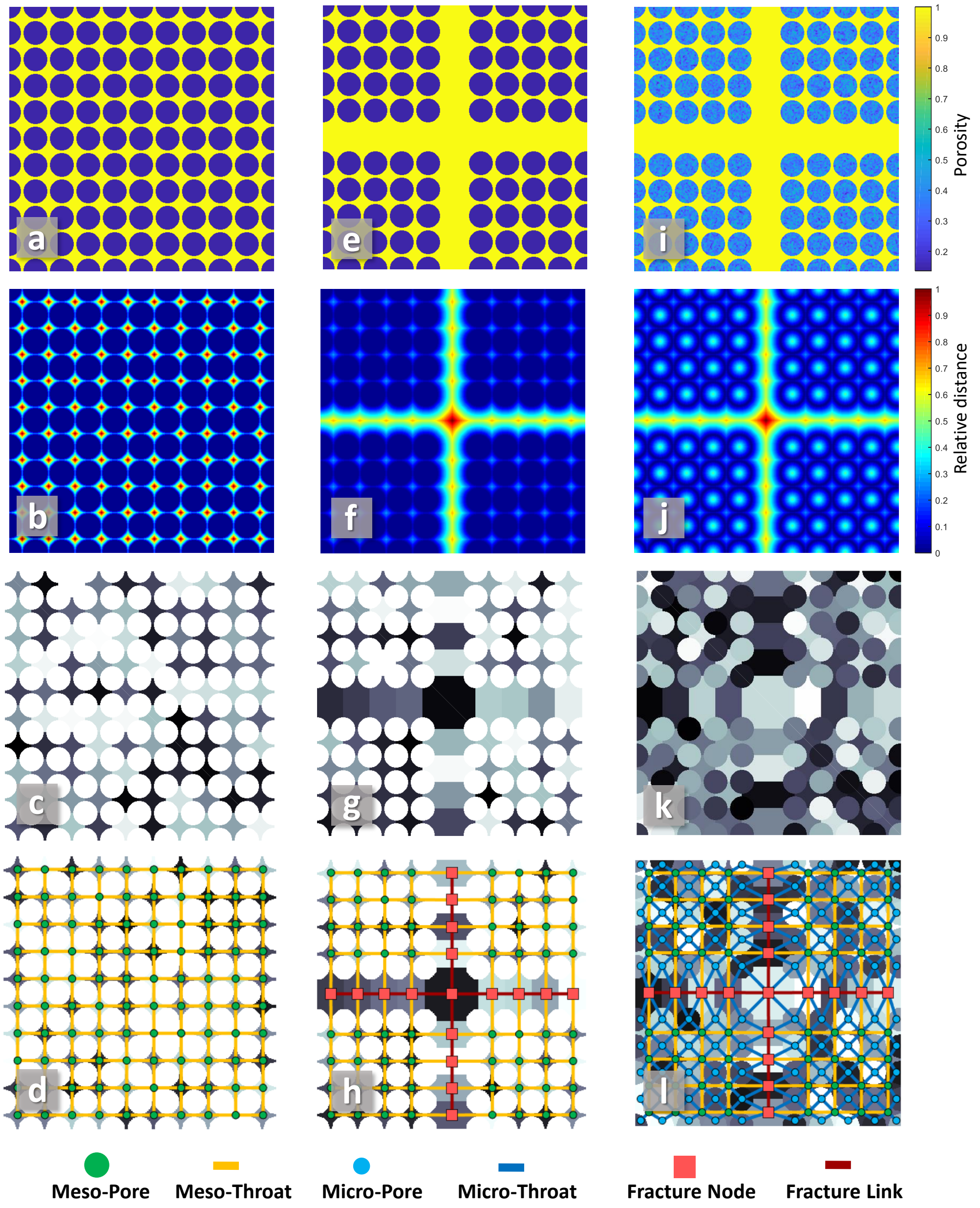

Figure 3.3: A simplified illustrative workflow for extracting single PNMs(a to d), D–PNMs (e to h), and T–PNMs (i to l), (a) porosity map of a single continuum sample, (b) distance map of the single continuum sample, (c) labelled nodes of the single continuum sample, (d) extracted pore network of the single continuum sample, (e) porosity map of a dual continuum sample with meso–pores and fractures, (f) distance map of the dual continuum sample, (g) labelled nodes of the dual continuum sample , (h) extracted pore network of the dual continuum sample, (i) porosity map of a triple continuum sample, (j) distance map of the triple continuum sample, (k) labelled nodes of the triple continuum sample, (l) extracted pore network of the triple continuum sample.

3.3.3 Fracture inclusion

The common approach to model a D–PNM containing meso–pores and fractures is to separate the single PNM from fracture elements and then use different flow equations for each type of the elements [178]. Various morphological operations can be used to specify the location of fracture elements [178], however, this distinction could become difficult in cases with complicated morphologies. For instance, a meso–throat can have a fracture–like elongated cross-sectional shape that casts shadow on the distinct definition of the elements. In order to avoid this issue, we present a unified permeability model for both meso–scale and fracture networks. A fracture network is assumed to be composed of an inter–connected structure of nodes and links. As a similar definition to the meso–scale network, fracture–links represent geometrical bottlenecks between fracture–nodes so that these bottlenecks create a pressure drop when fluid is moving between two connected nodes.

Shape issues

In this subsection, the capability of ITPM (Eq. 5.1) to calculate the absolute permeability of meso–throats as well as fracture links will be investigated. In this regard, we generate a set of cross-sectional images with a wide range of elongations from 1 to 10 and different roundnesses from 0.1 to 1 (Fig. 3.4). Elongation is the ratio between the major axis and the minor axis of the shape, and roundness is a measure that shows the deviation of the shape radii from a perfect circle, thus a shape with pointy corners will have less roundness [199]. By analyzing the sets of geometries, we observed that the hydraulic permeability values obtained by LBM simulation and ITPM are consistent and averaged relative error is around 3.3%. Relative error percentage does not necessarily increase or decrease when objects are more elongated. This observation is validated by performing Student's t–test between the relative errors and elongation for 20 different cross-sections illustrated in Fig. 3.4. The obtained Student's t–test p–value is 1.5×10^{-4} that verifies the independence of these two variables.

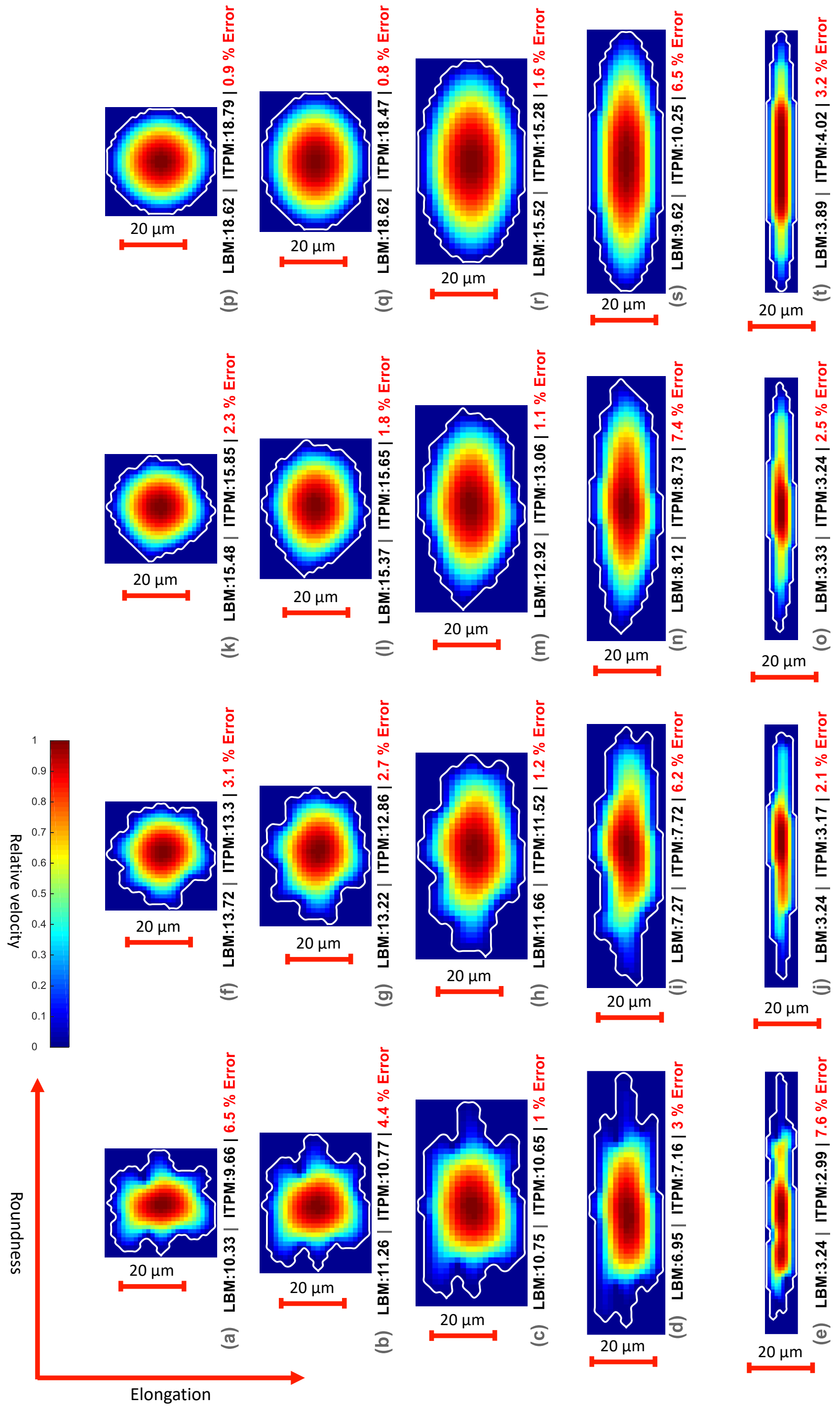

Figure 3.4: Relative velocity map obtained by LBM and permeability prediction for various range of conductive elements with different roundness and elongation, (a to e) elongation increases from 1 to 10, (a to p) roundness gradually increases to 1. Averaged relative error of ITPM results is 3.3% compared to the LBM permeabilities. Permeability unit is Darcy.

Lateral segments

Another issue when we are extracting a fracture–included porous material is unfavourable lateral segments. Consider a channel cross–section as visualized in Fig. 3.5a with flow direction perpendicular to the image surface. If our pore segmentation method mistakenly divides this elongated channel into 3 sections, its permeability is likely to be under–estimated due to the added unrealistic zero–velocity boundaries as shown in Fig. 3.5b. Considering that we are using averaged distance values of throat images ($\bar{D}$) for calculating their permeability (Eq. 5.1), Fig. 3.5b exhibits a lower permeability compared to Fig. 3.5a. The simple solution to avoid the aforementioned issue is to calculate the distance map prior to the pore network segmentation. Thus, the distance map will not be affected in the case that lateral segmentation occurs (Fig. 3.5c).

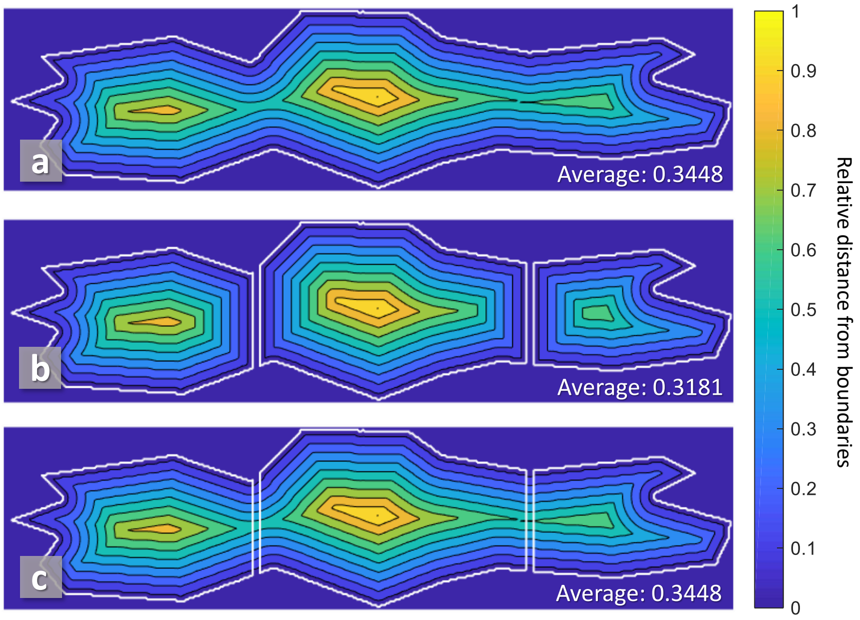

Figure 3.5: Visualizing the issue related to the lateral segments that are not perpendicular to the flow direction, (a) a fracture distance map without lateral segments, (b) an under–estimated fracture distance map due to the lateral segments, (c) a fracture element with is segmented after performing a 3–D distance transform, thus the distance values are not affected by the extra boundary lines

Coupling to the meso-pore network

We showed that ITPM can be used for permeability estimation of both meso–throats and fracture–links. So these elements are effortlessly coupled to each other with no extra calculation to distinguish each of them. Fig. 3.3e to h, illustrates the steps of network extraction process for our defined D–PNMs and as it can be seen, the workflow is similar to the single PNMs.

3.3.4 Micro-porosity inclusion

As described, the solid elements of the porous material could contain micro–porosities. As mentioned in Section 3.3.1, we are able to generate an approximated porosity map for micro–pores based on the mineralogy and normalized CT numbers. In this section, we describe the hydraulic properties of partially solid elements by knowing their approximated porosity and pore size distribution. Our proposed configuration of T–PNM is illustrated in Fig. 3.6a in which two micro–pores are connected to a pair of meso–pores and one fracture–node. We define two types of micro–throats: (1) micro–throats that connect two micro–pores (Fig. 3.6c), and (2) micro–throats that connect a micro–pore into a meso–pore or fracture–node (Fig. 3.6b and d). Each micro–throat is consisted of a bundle of micro–tubes with different range of radii. These micro–tubes intersect at the center of the solid element that is called main micro–pore (Fig. 3.6b-2). Also, some isolated cavities could exist within the solid element and they affect the image–based porosity we obtain from CT numbers while not contributing to fluid flow (Fig. 3.6b-1). If we assume that the radial density of micro–tubes is constant, based on a probabilistic permeability model of a bundle of tubes developed by Juang and Holtz [200], the absolute radial permeability of the solid elements (K_s) are:

$$K_s = \alpha\phi_m \int_0^{\infty} f(r_m)\frac{r_m^2}{8}\, dr_m \tag{3.2}$$

where ϕ_m is micro–porosity of the solid element, r_m is the radius of the micro–tubes with a distribution described by $f(r_m)$, $f(r_m)$ is a function that gives the void fraction of the solid element occupied by micro–tubes with the radius of r_m. Parameter α is porosity correction factor between 0 to 1 that subtracts the portion of the total micro–porosity occupied by isolated pores. In other words, when α is 0 it means that we have no interconnected micro–porosity in the solid element and when it is 1, it means there is no isolated micro–porosity within the solid element. This parameter can be obtained from nano–tomography, high–resolution FIB–SEM images [201], or by density analysis of the crushed particles of the porous sample [202]. Here we have simply assumed that α is 0.95. The term $\frac{r_m^2}{8}$ which is used in Eq. 3.2 represents the absolute permeability of a single micro–tube based on Hagen-Poiseuille law [173, 113]. The integral used in Eq. 3.2 can be simply solved by numerical discretization. Considering that the overall pore size distribution of samples is experimentally obtained by mercury intrusion, we only need to extract and normalize the sub–resolution part of the pore size curve ($f(r_m)$) (Fig. 3.2-g). Then by descretizing $f(r_m)$ over different values of r_m, the integral will be converted to a set of summations.

Then, to calculate the absolute permeability of the micro–throats type 1 (Fig. 3.6c), we use Eq. 3.2 but instead of a single value for micro–porosity (ϕ_m), we put the averaged value of micro–porosities from two adjacent solid elements. This averaging needs to be weighted relative to the radii of the elements, which means that the larger size of the solid elements makes them more significant in permeability averaging for micro–throats type 1. Additionally, in order to calculate the absolute permeability of the micro–throats type 2, we ignore the pressure drop happening in the void section of the micro–throat (Fig. 3.6b-4 and Fig. 3.6d-4). Considering that the absolute permeability of a series of elements is mainly controlled by the smallest permeability value [203], this assumption is reasonable.

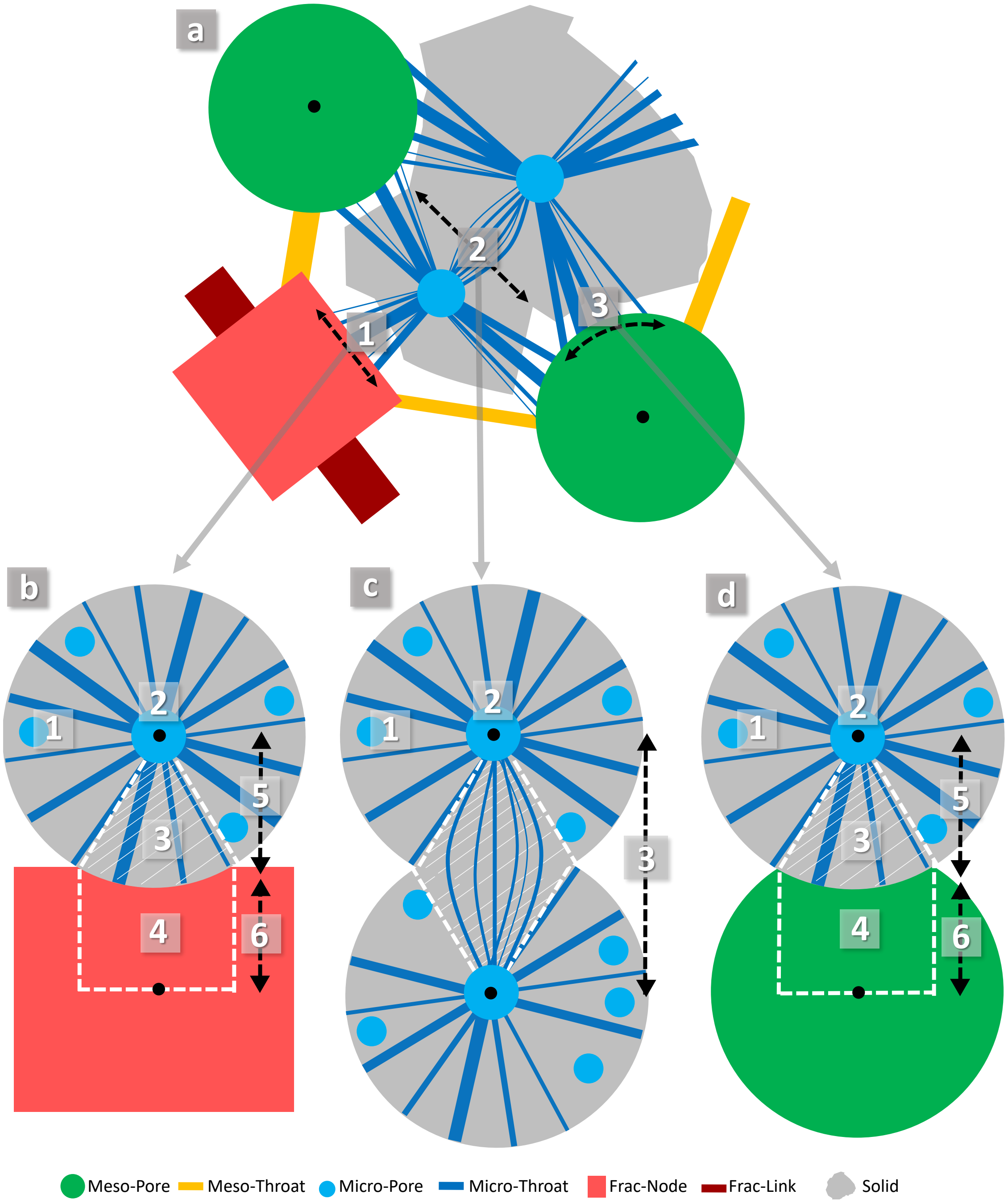

Figure 3.6: Different configurations of micro–porosities in connection with other elements in a T–PNM, (a) a system of two micro–pores in connection with two meso–pores and one fracture–node, (b) the structure of a micro–throat type 2 in connection with a fracture–node, (c) the structure of a micro–throat type 1, (d) structure of a micro–throat type 2 in connection with a meso–pore (details of figure elements are described in Table 3.2)

Part	Element	Description
Fig. 3.6a	1	Interface area between a micro–pore and a fracture–node in which a bundle of micro–tubes with variable sizes represents a type 2 micro–throat;
	2	Interface area between two micro–pores in which a bundle of micro–tubes with variable sizes represent a type 1 micro–throat;
	3	Interface area between a micro–pore and a meso–pore in which a bundle of micro–tubes with variable sizes represents a type 2 micro–throat;
Fig. 3.6b	1	An isolated cavity that does not contribute to fluid flow;
	2	The main micro–pore that all micro–tubes are connected to it;
	3	A part of the micro–throat that is located within the solid element and contains several micro–tubes with different sizes;
	4	A part of the micro–throat type 2 that is located outside the solid element and does not have any micro–tubes;
	5	Length of the micro–tubes;
	6	Length of the micro–throat without micro–tubes;
Fig. 3.6c	1 and 2	Same as Fig. 3.6b-1 and 2;
	3	The length of the micro–tubes that form the micro–throat type 1;
Fig. 3.6d	1 to 6	Same as Fig. 3.6b-1 to 6.

Table 3.2: Description of the triple network elements in Fig. 3.6.

Coupling to the dual pore network model

In the previous sections, we developed a D–PNM consisted of meso–pores and fractures. Now, in order to couple micro–pores into that D–PNM, we need to revise the pore network extraction method. In order to clarify the workflow of T–PNM extraction, Fig. 3.3i to l is presented. Fig. 3.3i illustrates the porosity map of a system with three types of porosities: micro–pores, meso–pores and fractures. In the next step, we apply Euclidean distance transform on both void and solid spaces separately. then, the obtained distance maps are summed as follow:

$$DM = DT(PM < 1) + DT(PM = 1) \tag{3.3}$$

That DM is the overall Euclidean distance map (Fig. 3.3j), DT is the distance transform function that takes a binary map and gives back its distance map, and PM is porosity map of the media as appears in Fig. 3.3i. Consequently, $PM < 1$ implies a binary map in which all the pixels with porosities less than 1 are set to one and other pixels are set to zero. Similarly $PM = 1$ represents a binary map in which all the pixels that are completely porous, are set to 1 and the rest of the pixels are set to zero. On the basis of the obtained overall distance map, we apply watershed segmentation and generate the node map that includes all three types of aforementioned nodes (Fig. 3.3k). Finally, based on the generated node map, we detect the neighbour nodes and interfaces between them. Then by determining the types of micro–throats, we assign proper hydraulic properties to them. Finally, the T–PNM could be visualized as in Fig. 3.3l.

3.4 Results and Discussion

In this section, we first verify the developed method using simplified geometries. Then, statistics of the T–PNMs will be compared to D–PNMs in order to provide a more quantitative measure of differences. Next, steady-state gas flow (formulation presented in Appendix C) through the extracted PNMs will be simulated to investigate the effects of micro–porosity presence on the governing flow mechanisms. Finally, the results of gas flow simulation will be extended to a wide range of pressure, temperature, and molecular mass conditions and the observed trends in the apparent permeability of the samples will be discussed.

3.4.1 Method verification

In order to measure accuracy of the proposed methodology, we have constructed six idealized geometries that contain a combination of the three porous elements: meso–pores, micro–pores and fractures (Fig. 4.11a). Then absolute permeability of each geometry is calculated using the developed methodology and analytical equations. The analytical absolute permeability of the geometries is calculated based on expressions $r^2/8$ and $h^2/12$, respectively for permeabilities of capillary tubes and ideal fractures as discussed before. Also, analytical permeability of the partially solid section is obtained by assuming ideal micro–tubes with an identical radius. The size of all cubic geometries is 200^3 μm and spatial resolution is 1 μm per voxel. Four of the geometries (Fig. 3.7a-2, a-4, a-5 and a-6) contain six capillary tubes with the diameter of 20 μm, equally distributed and aligned to the direction of flow. Similarly, in four of the geometries (Fig. 3.7a-1, a-3, a-5 and a-6), an ideal fracture with no roughness is present in the middle section with the aperture of 10 μm. Additionally, in geometries a-3, a-4, and a-6, we have considered 30 % of micro–porosity in the shape of parallel micro–tubes with diameter of 2 μm (Fig. 3.7d).

Watershed segmentation cannot be used to extract the pore network of these simplified geometries due to their idealized shapes. The reason is that, most of the pore network extraction methods including watershed is useful to detect the pathways with minimal cross–sectional area, while in an idealized uniform geometry, there is no minimal cross–sectional area in the capillary tubes nor in the fracture. Consequently, to generate the node map we have divided the void–space and solid–space into equal cubic segments with the size of 10 μm (Fig. 3.7c) and then we have superimposed these maps to generate a complete node map which includes all flow domains. As can be seen in the magnified part of Fig. 3.7c, each node is labelled with a random colour.

Considering the porous elements mentioned in this paper, we investigate six types of geometries that include a combination of the different elements, and then using the developed pore network model, we calculate the absolute or liquid permeability of each geometry as presented in Fig. 3.7a. We assumed 1 Pa pressure gradient between two opposite faces of the PNM to calculate the absolute permeability of the system. The average relative error between the estimated permeability using the present method and the analytical solution is less than 2%. Fig. 3.7b illustrates the pore pressure obtained by simulating single–phase steady–state flow on the geometry with triple porosity.

As can be seen in the magnified section of Fig. 3.7c, capillary tubes contain lateral segments. These segments did not affect the permeability calculations (Fig. 3.7a) because we have calculated the distance transform of the geometry prior to the segmentation. To calculate the analytical permeability of the whole geometry, we assume a system of parallel conductors with the same length. Thus, the equivalent analytical permeability of the whole geometry (K_e) is [203]:

$$K_e = K_s\phi_s + K_f\phi_f + K_p(1 - \phi_s - \phi_f) \tag{3.4}$$

where ϕ_s is the volume fraction of the geometry occupied by the partially or fully solid elements, K_f is the absolute permeability of the fracture, ϕ_f is the volume fraction of the geometry occupied by the fracture, K_s is the permeability of the partially solid parts, and K_p is the overall permeability of the six capillary tubes.

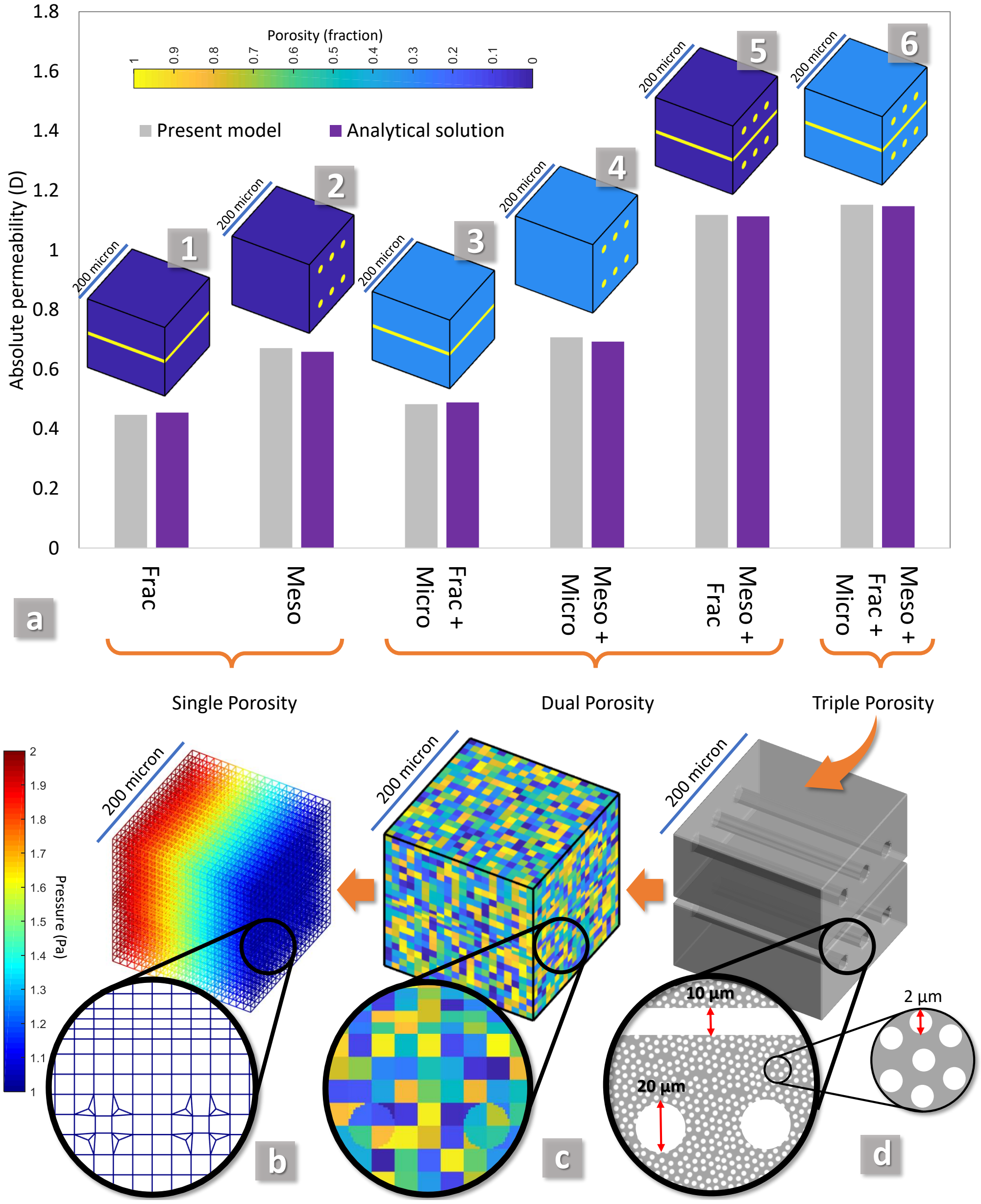

Figure 3.7: Verification of estimated absolute permeabilities on a simplified geometry, (a) comparison of absolute permeabilities obtained by the present model and analytical solution for six combinations of porosity types with an average relative error less than 2%, (b) pore pressure distribution in a single-phase steady-state flow modelling with 1 Pa pressure difference between two opposite faces of the T–PNM, (c) extracted node map with a random colour for each node, (d) original geometry of the medium with a fracture, six capillary tubes, and 0.3 porosity at the solid sections.

3.4.2 Network statistics

In this subsection, we discuss the statistics of the extracted triple pore networks and compare them with D–PNMs that contain only meso-pores and fractures. In other words, the effects of including micro–porosities on the statistical features of the PNMs are investigated. Some statistics of these networks, including network porosity, average link permeability, specific surface, number of links, and number of nodes are presented in Table 3.3. As it can be seen, T–PNM shows higher porosity up to two times higher than the D–PNM which does not contain micro–porosity. On the contrary, the average link permeability in a T–PNM is commonly four to five times lower than the D–PNM due to the effect of multitudes of low permeable micro–throats which are present in a T–PNM. This ratio is virtually the same as the number of links of the T–PNMs compared to the D–PNMs. It is notable that micro–throats can contain up to thousands of micro–tubes with minuscule radii. Therefore, the actual number of links can be two or three orders of magnitude larger than the reported values.

Specific surface of the pore network is defined as the ratio between total internal surface area and the bulk volume of the whole geometry. As it can be seen in Table 3.3, specific surface of the T–PNM can be up to 20-40 times greater than a D–PNM. This property is significant in the simulation of the surface processes such as reactions or diffusion layers [204, 205].

Property	Network	Estaillades	Savonnieres	Massangis
Network porosity (fraction)	Dual	0.236	0.248	0.206
	Triple	0.429	0.408	0.310
Average link permeability (D)	Dual	97.265	170.694	83.795
	Triple	24.773	39.971	25.494
Specific surface (1/mm)	Dual	12.681	8.892	11.453
	Triple	411.655	338.548	230.621
Number of links	Dual	16187	9116	5616
	Triple	64123	39359	18557
Number of nodes	Dual	5877	3352	1901
	Triple	9586	5933	2978

Table 3.3: Comparing pore pore network statistics between T–PNMs and D–PNMs.

Additionally, distributions of two pore network parameters are illustrated in Fig. 3.8 for the triple and dual approaches. Fig. 3.8a shows the distribution of the node connectivity in both networks of Estaillades sample. T–PNM has considerably higher coordination number due to the presence of partially solid elements which are in touch with many adjacent nodes and increase the maximum number of connections per node up to 50. The other effect of micro–porosities is shown in Fig. 3.8b that presents the distribution of node surface area of both PNMs. The presence of partially solid elements exhibit nodes with surface area with two to three orders of magnitudes larger than the regular nodes. Consequently, simulation of the surface dependant processes can give significantly different results by using a T–PNM instead of a dual or single PNM.

In order to provide more insight into the physical features of the extracted PNMs, Fig. 3.9 is presented for Estaillades sample. Fig. 3.9a illustrates the top view of the original volumetric image in which the level of darkness intuitively indicates the porosity. Fig. 3.9b and Fig. 3.9c shows two halves of the plan view with the left–hand half displayed as a D–PNM and the right–hand half displayed as a T–PNM for providing a concise illustration. The T–PNM half is denser and contains many large size nodes that indicate the presence of the large partially solid elements, while the D–PNM half is less dense with relatively smaller size of nodes. Large nodes of the triple side are highly connected to the neighbouring nodes and this is the source of high coordination number shown in Fig. 3.8a. In terms of the surface area, we expect to see large values for partially solid elements (Fig. 3.9d and e) due to the presence of hundreds to thousands of micro–tubes in each of the links. Finally, if we calculate the absolute permeability of each link based on Eq. 5.1 and Eq. 3.2, the distribution of this parameter is visualized in Fig. 3.9f and g. As it can be seen, despite the large sizes of the partially solid nodes, their connected links have low permeability. However, due to the large number of connections, their role can become significant in some cases. Roughly, it can be stated that the highest absolute permeabilities of both PNMs belong to fractures by comparing the original geometry (Fig. 3.9-a) and permeability network of Fig. 3.9f and g.

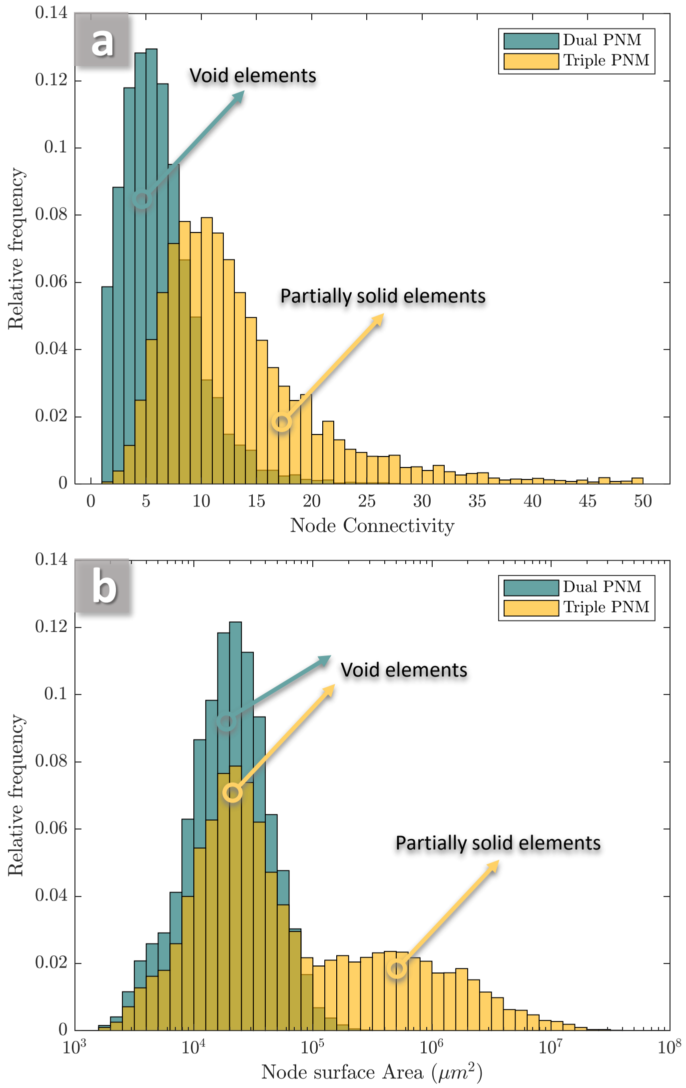

Figure 3.8: Distribution of the node connectivity (a), and node surface area (b) in T–PNM and D–PNM of the Estaillades sample.

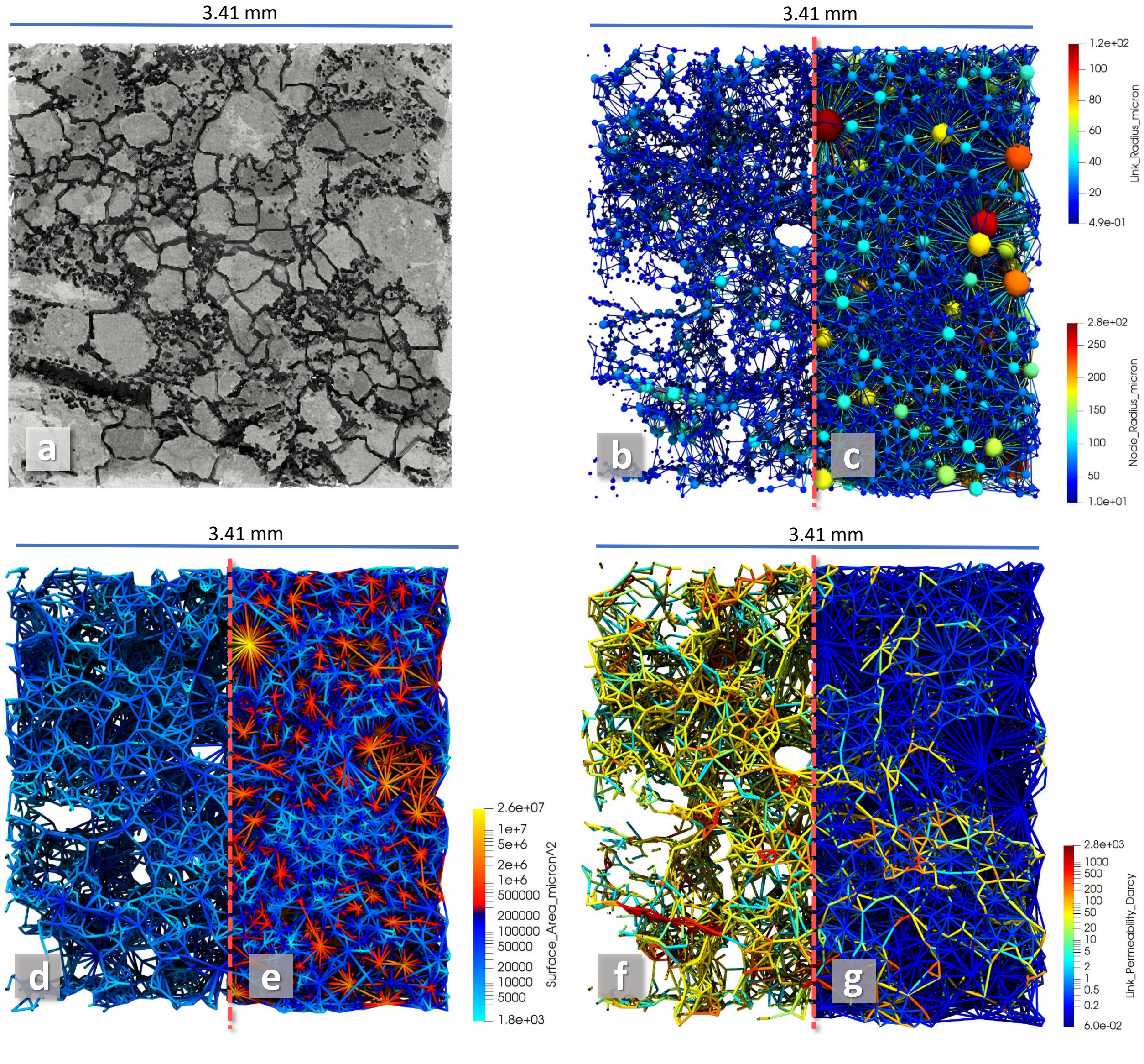

Figure 3.9: Structure of D–PNMs and T–PNMs of the Estaillades sample partially imposed on each other, (a) top view of the original geometry of the Estaillades sample with dark void spaces and partially dark micro–porous zones, (b and c) Radii of the nodes and links respectively in D–PNM and T–PNM, (d and e) internal surface area of the network respectively in D–PNM and T–PNM, (f and g) link absolute permeability respectively in D–PNM and T–PNM.

3.4.3 Gas flow simulation

In this subsection, we present the gas flow simulation results (formulation presented in Appendix C). Initially, effective flow mechanisms are investigated and then flow pattern is discussed among D–PNMs and T–PNMs. Finally, we present a sensitivity analysis for conditions with different pressure and temperature, followed by a discussion on the effect of gas molecular mass.

Flow mechanisms

As discussed in Appendix C, three main types of gas transport mechanisms happen in porous media: Knudsen, slippage and viscous flow. Each of these mechanisms could become significant in a specific range of Knudsen number. This sensitivity of gas flux ratio to Knudsen number is plotted for each type of the mechanisms and their combinations in Fig. 3.10a. In order to calculate the gas flux fractions, we have assumed an ideal tube geometry and then by gradual changing of the tube radius, flux fractions are obtained in a wide range of Knudsen number. In Fig. 3.10a, non–Knudsen flux denotes the summation of the viscous and slippage fluxes. Similarly, non–viscous flux is the summation of the slippage and Knudsen fluxes and finally, non–slip flux is the summation of the Knudsen and viscous fluxes. Assuming the definition of the Knudsen number which is the ratio of the gas mean free path to the tube radius, it is reasonable that the viscous flux fraction decreases in higher Knudsen numbers under conditions where gas molecules frequently collide with tube walls rather than other gas molecules. When Knudsen number is greater than 1, Knudsen flux and slippage are dominant flow mechanisms. On the other hand, when Knudsen number is smaller than 0.01, non–viscous fluxes are minimal. It is noteworthy that the fraction of the slip-flux is always less than the Knudsen flux at any Knudsen number range.

In order to investigate the effective flow mechanisms in a more complex geometry, we have considered four sets of gas flow mechanisms to simulate the full pore network model of three porous materials. Fig. 3.10b shows the ratio between the triple and dual gas permeabilities calculated with different mechanistical assumptions for three rock samples at the standard temperature–pressure condition. Simulated gas is methane and we have considered 1 Pa pressure difference between two opposite faces of the pore network model in the x direction. As readers can see in Fig 3.10b, the ratio between triple– and dual–porosity permeabilities increases as we integrate more flow mechanisms into our model. The final columns indicates the condition that all three mechanisms have been applied and it is found that triple permeability can be 1.3 to 1.55 times larger than the dual permeability which ignores the micro–porosities. Also, for the simulated conditions, it can be concluded that Knudsen flux, is more significant compared to slippage, since the major jump in permeability ratio happens when Knudsen flow is added to the system (Fig. 3.10b).

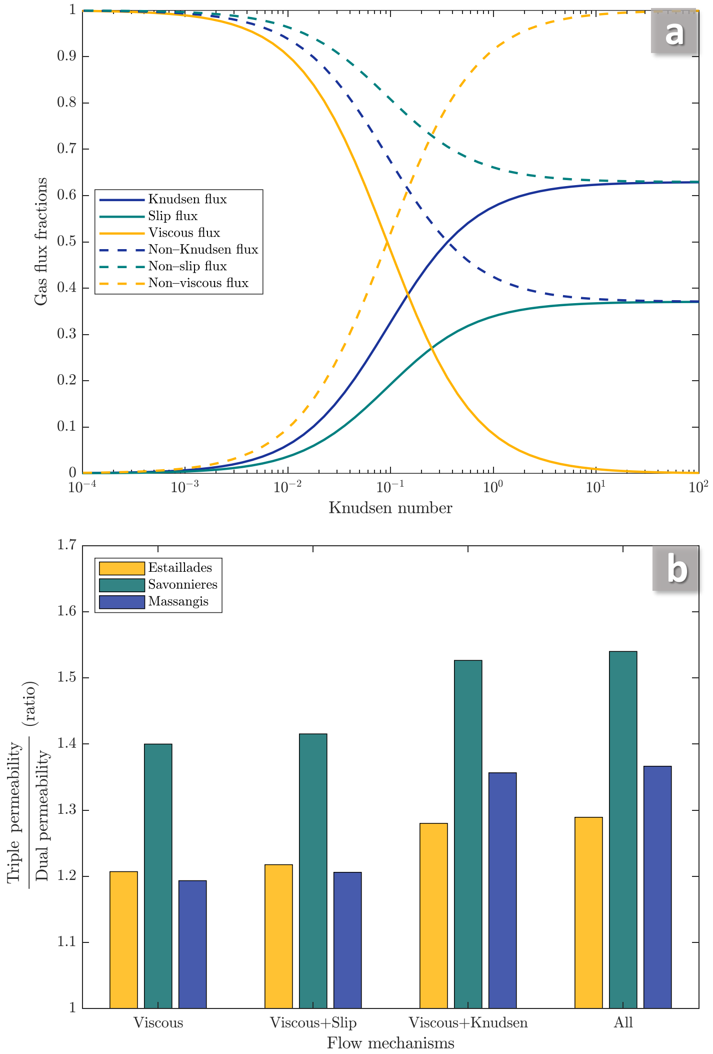

Figure 3.10: Comparing the effect of considering different gas transport mechanisms in the model, (a) gas flux fraction for six types of flow mechanisms composed of a combination of viscous, Knudsen and slippage fluxes, (b) comparing the ratio between gas permeability of T–PNMs and D–PNMs calculated using 4 sets of flow mechanisms for three different rock samples.

Flow pattern

Considering a steady–state condition we have simulated gas flow in the direction of Y axis through D–PNM and T–PNM of Estaillades sample. The pressure map and flow rate distribution are visualized in Fig. 3.11. Pressure difference between two opposite faces of the PNM is 1 Pa and we have assumed that in this short range of pressure, the gas density and viscosity remains constant. The average pressure for calculating gas properties is 101 kPa and the temperature is 25 °C. As it can be inferred from Fig. 3.11a and b, iso–pressure lines do not show sharp changes when changing the geometry from a T–PNM to a D–PNM. Fig. 3.11c and d illustrates the flow rates of links within D–PNM and T–PNM partly imposed on each other. Despite the pressure distribution, flow pattern is significantly different between two PNMs and many micro–throats are contributing in fluid transport. Due to the numerous connections, micro–throats make a difference in the overall permeability results, while each single of them does not pass a significant amount of flow compared to the meso–throats or fractures.

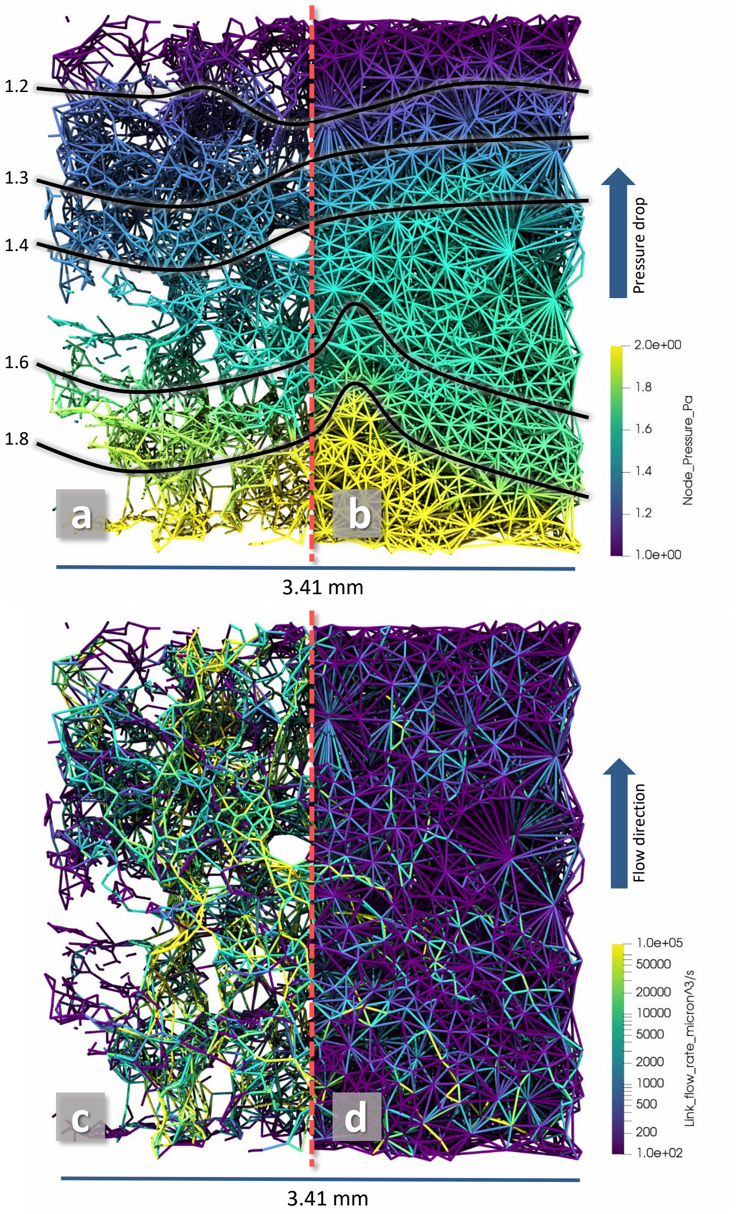

Figure 3.11: Pressure and flow rate distribution in Estaillades pore networks stacked on each other, (a & b) pressure distribution respectively in D–PNM and T–PNM, (c & d) flow rate distribution respectively in in D–PNM and T–PNM.

Sensitivity analysis

In order to provide an insight into the application of a T–PNM and clarify the conditions that ignoring the partially–porous part of the media could create a significant error, we analyze the sensitivity of gas permeability by changing three independent parameters: average pressure, temperature, and gas molecular mass while keeping the flow pressure drop of the whole sample equal to 1 Pa. We simulate gas flow in D–PNMs and T–PNMs of all three porous samples for a wide range of each parameter by keeping the other two as constant. The results are presented in Fig. 3.12.

Fig. 3.12a shows the gas permeability changes in different average pressures for methane gas and constant temperature of 25°C. Low pressures could dramatically increase the gas permeability of T–PNMs, while D–PNMs are relatively less sensitive to the pressure change. For the tested range of average pressure, lowering the pressure two orders of magnitude increases the gas permeability of T–PNMs up to two times. This is mainly due to the increment of gas mean free path in low pressures and consequently higher Knudsen flow rates. Gas permeability is relatively less sensitive to the temperature variations compared to the pressure (Fig. 3.12b).

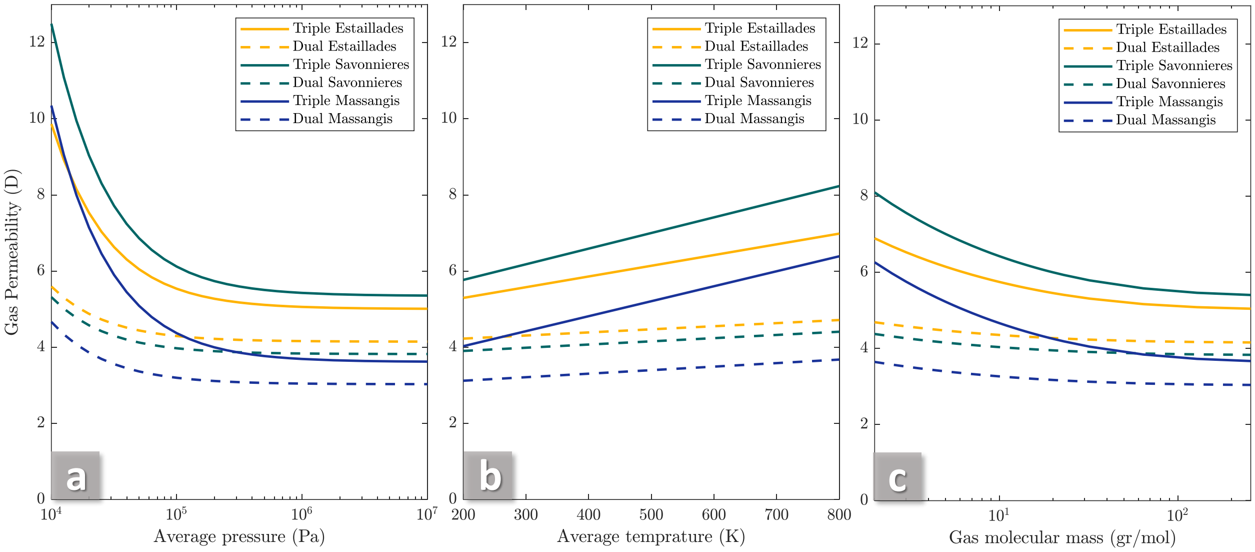

Figure 3.12: Sensitivity analysis of gas permeability due to changes in average pressure, temperature and molecular mass, (a) sensitivity to pressure for methane in 25°C, (b) sensitivity to temperature for methane in 101 kPa pressure, (c) sensitivity to molecular mass in 101 kPa pressure and 25°C.

By increasing the average temperature of the gas and keeping constant pressure of 101 kPa, methane permeability linearly increases. This change is more significant for T–PNMs compared to D–PNM. However, the change hardly exceeds 20 % for 500 degrees of temperature variation. It should be noted that in the case of subsurface flow modelling in heterogeneous porous material such as the case in tight carbonate reservoirs or gas shales, due to the higher range of environmental pressure, the effect of micro–pores in permeability will become less significant. In contrary due to a higher subsurface temperature, molecules will have more interaction with solid walls and non–viscous flow mechanisms will be still important.

Finally, we have examined the effect of changing the gas molecular mass which is hypothetically equivalent to changing the gas type (Fig. 3.12c). It has been found that for lighter gases in the standard temperature and pressure condition, T–PNM permeability is around 20 % higher than the heavy gases with molecular mass above 100 gr/mol. This change is less significant in D–PNMs and its almost less than 10 %. Gas permeability gradually approaches to a constant value when molecular mass increases and this means that mean free path of the molecules becomes so small that they less frequently interact with the solid walls of the throats compared to interacting with themselves.

Computational trade–off

While including micro pores can improve the accuracy of the flow model, the computational cost of the model increases which should be considered as a trade–off. Considering that at least two stages of pore space segmentation are required for building a T–PNM, it is observed that the overall computational cost can increase up to three times. However, based on the fact that PNMs are computationally inexpensive compared to the direct simulation method, three times increment would not affect the applicability of the presented method. As an example, pore network extractions and steady–state flow simulation of the studied Estaillades D–PNM sample takes around 1 minute using a regular desktop computer with an i7-9750H CPU at 2.60GHz without parallelization. Adding micro porosities to the model, increases the computational time up to 2 minutes which is still attractive compared to direct simulation costs which could be greater than 100 times as we have seen in chapter 2.

3.5 Conclusions

In this study, we introduced the concept of triple pore network models that incorporated a meso–pore network coupled with fractures and micro-porosities. The proposed triple pore network presents a more detailed model of a porous material in which two levels of porosity exist in connection with fracture or channel–like elements. After describing the method for developing these networks, we simulated steady–state gas flow through three porous samples in different ranges of pressure, temperature and gas molecular masses. The developed method was validated by comparing the gas permeability results obtained in simple geometries and analytical solutions.

We showed that using a T–PNM to model a fractured porous media with two scales of porosity made substantive differences compared to a D–PNM. Concisely, the main conclusions and findings of this research can be drawn as follow:

- Triple pore network models are introduced and constructed based on the semi–real tomography images in order to simulate gas and liquid permeabilities.
- A unified approach is invented to simulate fluid flow within a network with both meso–pores and fractures. In this approach we used distance map of the channels with arbitrary cross–sections and estimated the LBM permeabilities using an empirical correlation. The benefits of using this approach are that we bypass the lateral segmentation problem in pore network extraction as well as no requirement to locate the fracture elements explicitly.
- A hypothetical micro–network structure is presented for taking into the account the hydrodynamical effects of micro–porosities in liquid and gas flow through porous samples with dual scales of porosity.
- Effects of micro–porosities on gas permeability are investigated and operational conditions in which ignoring the presence of micro–porosities make a significant error are discussed.
- Within the tested range of operational conditions, we have recorded between 10 to 50 % relative error in gas permeabilities if micro–porosities are dismissed in the presence of the fractures.

Chapter 4

DeePore: a deep learning workflow for rapid and comprehensive characterization of porous materials

4.1 Abstract

DeePore is a deep learning workflow for rapid estimation of a wide range of porous material properties based on the binarized micro–tomography images. By combining naturally occurring porous textures we generated 17700 semi–real 3–D micro–structures of porous geo–materials with size of 256^3 voxels and 30 physical properties of each sample are calculated using physical simulations on the corresponding pore network models. Next, a designed feed–forward convolutional neural network (CNN) is trained based on the dataset to estimate several morphological, hydraulic, electrical, and mechanical characteristics of the porous material in a fraction of a second. In order to fine–tune the CNN design, we tested 9 different training scenarios and selected the one with the highest average coefficient of determination (R^2) equal to 0.885 for 1418 testing samples. Additionally, 3 independent synthetic images as well as 3 realistic tomography images have been tested using the proposed method and results are compared with pore network modelling and experimental data, respectively. Tested absolute permeabilities had around 13 % relative error compared to the experimental data which is noticeable considering the accuracy of the direct numerical simulation methods such as Lattice Boltzmann and Finite Volume. The workflow is compatible with any physical size of the images due to its dimensionless approach and can be used to characterize large–scale 3–D images by averaging the model outputs for a sliding window that scans the whole geometry.

4.2 Introduction

Data science is becoming an essential tool to analyze the structural features of porous materials based on the tomography images [206, 207, 208]. The behavior and performance of porous materials are strongly related to the characteristics of its internal micro–structure. In order to discover the descriptive features and the process–structure–property relationships in a porous material, we need to achieve a reliable representation of the internal structure of the porous materials [206, 209, 210, 211]. Spatial description of such micro–structures have created added–value in diverse fields of studies, from composite material engineering [212, 213, 214] and food processing [215, 216], to the petroleum and petrochemical industries [39, 5]. For instance, during the past two decades, the field of digital rock physics grew rapidly and showed outstanding advances owing to the power of imaging and analysis techniques [39, 40]. Based on the captured images, we are able to build realistic simulation models and run many digital measurements and experiments on porous material such as pore and throat sizes, hydraulic and electric conductance, two–phase displacement, and mechanical deformations [217, 218]. Direct calculation of the abovementioned physical properties based on the tomographic data could be a complicated and computationally expensive task especially in the case of large images [219, 220, 129]. In this regard, machine learning approaches can be utilized to make hybrid [198] or full artificially intelligent models [32] which are able to reduce the computational costs significantly while maintaining the level of accuracy.

In this regard, shallow neural networks are powerful tools for modeling moderately complex problems in a timely and efficient manner [221, 222, 41] while they are not very suitable to predict high orders of non–linearity [223]. On the contrary, deep learning models are capable of estimating a highly non–linear behaviour if they are trained on an adequately diversified and large set of input and output data [224, 225]. Convolutional neural networks (CNNs) as a particular type of deep neural networks can be used for analyzing data with a recognized grid-like topology, similar to image data [226, 227, 228]. A typical CNN uses several filters to extract higher level features from the input data or images and gradually narrows it down to the specified output features [229]. CNNs have been mostly used for image segmentation, recognition, classification, and regression [226, 228, 230]. In mathematical terms, convolution is a spatial operation to transform an original function or data into a secondary realization using an operating kernel [231]. Convolution on an input image could lead to generating negative values which are not usually favorable considering the physical meaning of the output layer in that specific problem. At each level of convolution, we can use a down–sampling method such as maximum or average pooling to condense the volume of data without losing noticeable amount of information [232]. In many cases CNNs can be followed by some fully–connected dense layers of nodes to give more flexibility to the model [233]. CNNs have been used in many recent porous material studies for different purposes including segmentation of porous media images [234, 43], image quality improvement [235], super resolution, reconstruction [236, 237], classification [238], and regression [239, 21]. Here we briefly describe a background of these applications and narrow the topic down to the specific approach of the present study.

4.2.1 Image improvement and reconstruction

Considering the multi–scale nature of many of the porous micro–structures, it is necessary to have plenty of details in images while covering a large volume of the object at the same time. In this regard, super resolution techniques powered by CNNs are valuable tools to be trained on pairs of low and high resolution images. There are plenty of recent studies that have presented quantitative methods to obtain a high resolution tomography image of porous material using images with lower spatial resolution [237, 240, 241, 242, 243, 244]. As a recent example, Kamrava *et al.* [235] have used a cross–correlation–based simulation to generate an augmented dataset of porous shale images and make a CNN that is able to improve the image quality of similar porous textures.

The resolution enhancement can go further to a level that we are able to generate a detailed realization of the porous material based on the simple input of noise maps through a specific type of CNNs known as Generative Adversarial Networks (GAN) [245, 246, 247, 248]. As an example, Mosser *et al.* [245] presented a workflow to train a GAN based on the available 3–D tomography images and to reconstruct similar realizations of the original images, while not making an exact copy of them. Then by looking at the hydrodynamic properties of the constructed porous material, they have evaluated the similarity of the realizations.

4.2.2 Classification of porous materials

CNNs are good tools to classify images based on texture, visible elements, or objects [228]. This texture recognition has several applications in material and geological sciences to classify or cluster a dataset of porous material images. Additionally, some other researchers utilized the CNN framework for recognition of the materials texture [249, 238]. For instance, in geoscience, classifying different types of rocks in terms of mineralogy and micro–structure could be a time consuming and biased task if done by hand, while CNNs have widely been used in the past three years to automate these processes in a timely and efficient manner [250].

4.2.3 Image–based regression models

Many diverse physical properties of porous materials have been estimated using CNNs in recent years; from thermal to hydraulic and mechanical features [251, 252]. Wei *et al.*[253] proposed a CNN to predict the effective thermal conductivities of composite materials and porous media with more than 0.98 accuracy (R^2) on 100 testing image samples while training on 1400 samples. Additionally, permeability and porosity have been heavily investigated through CNNs [254, 255, 256, 257]. CNNs are able to take both binary or gray–scale images of porous materials to estimate porosity and permeability with an acceptable error. Alqahtani *et al.*[21] used CNNs to estimate porosity, average pore size and specific surface of the porous rocks based on both types of 2–D tomography images and found that binary images could give a more accurate estimation of porous material characteristics compared to the gray–scale ones. However, the morphology of the binarized images is highly dependent on the thresholding technique and it suffers from the inherent uncertainty [258]. In another attempt, Cang *et al.*[259] designed a CNN for prediction of physical properties of heterogeneous materials and successfully predicted the Young modulus, diffusion and permeability of the porous material with more than 90% of certainty on their testing data. Recently, Karimpouli and Tahmasebi [260] developed a CNN model to estimate P-wave and S-wave velocities based on the cross-sectional images of porous material. They were able to estimate these parameters with coefficients of determination around 0.65, and 0.74, respectively. A recent extension of the Karimpouli and Tahmasebi [260] work is published by Kamrava *et al.* [251] to investigate the link between the absolute permeability and morphology of the porous materials. They have used a cross–correlation–based simulation technique to augment an image dataset of sandstones and enriched it with hundreds of synthetic and digital images. Then a CNN structure followed by a dense layer is trained to estimate the absolute permeability values that have been obtained by solving the Stokes equation using Avizo commercial software. The range of permeability variations in their work is around one order of magnitude which could be a subject of improvement.

Considering the above-mentioned categories of CNN applications in porous material research, the present study can be considered as an image–based regression model. In order to improve the applicability of the proposed model, a dimensionless and size–independent approach is introduced to calculate porous material features that enables us to analyze images with a wide range of spatial resolutions.

4.3 Methodology

In this study, we use an augmented set of semi–realistic tomography images of geological porous material to train a convolutional neural network (CNN). The aim of this artificial intelligence model is to predict multiple physical properties of a porous material based on its pore scale images. We refer to this deep learning model of porous material characterization as *DeePore*. In this section, the devised data augmentation technique, assumptions and methods for building the ground truth data, and the utilized deep learning approach are discussed.

4.3.1 Input data augmentation

The original core of the image dataset is composed of 60 real micro-tomography images which their detailed information and corresponding references are available in Appendix D. Considering the fact that it is critical for CNNs to be trained on a large dataset of images, and due to the limited availability of the diverse and realistic tomography data of porous material, data augmentation is required. Several different methods have been used in the literature for augmentation of the training data [261] such as elastic deformation [262], mixing images [263], cross–correlation–based simulation [251], and adversarial reconstruction [264].

Inspired by the mixing image method [263], we have adopted a previously developed algorithm to generate more realizations of such data by transforming the existing ones [265]. For each augmentation, we select two different images out of the 60 samples and interpolate a hybrid texture among them by weighted averaging of the normalized distance maps. A simplified example of the interpolation technique is illustrated in Fig. 4.1. In this example, two initial grayscale images with different textures (Fig. 4.1-a and h) are binarized using a locally adaptive Otsu algorithm [266] (Fig. 4.1-b and i). Then, normalized maps of the Euclidean distances are calculated (Fig. 4.1-c and j) and combined by weighted averaging to mimic an interpolated texture (Fig. 4.1-e). Then, we can set the threshold level on the obtained hybrid map to reach any desired amount of porosity (Fig. 4.1-d, g and k).

As a more realistic example, Fig. 4.2 illustrates the texture interpolation results over only two real tomography images (Fig. 4.2-c and w). In this figure, by going from top to the bottom rows, texture is gradually changing from sample #1 to #2. Meanwhile, by moving from left to right side of the matrix, porosity is increasing by manipulating the threshold level mentioned above.

It is noteworthy to highlight that the distance maps should be normalized prior to averaging in order to avoid large elements of one image from cloaking the smaller ones in the other image. In order to generate the hybrid realizations of each pair of the real images, we have assumed 10 uniform random numbers between 0 to 1 as interpolation weights, as well as 10 uniform random numbers between 0.1 to 0.45 as final porosity fractions. Then each of the interpolated textures are translated to a randomly selected direction with a random shift within the range of one third of the image width. This random translation process helps to diversify the created dataset and avoid two similar samples which may eventually end up in training and test subgroups and harm the evaluation process by giving a false high performance. After directional shifting of the images, the empty space created is filled by the mirror image of the remaining parts of the micro–structure to maintain the image texture. Based on the data augmentation method described above, the total number of the images in the dataset would be $\binom{60}{2} \times 10$ that yields 17700. However, considering that we aim to calculate several physical properties of these materials, it is expected to filter out outlier geometries with non–physical or null properties that cannot be modelled through the regression techniques. For example, in the case that there is no percolating pathway from one side to the other side of the sample, hydraulic permeability, will be zero and formation factor which indicates electrical resistivity of the void space approaches to infinity. Also, tortuosity will have a null value in such cases.

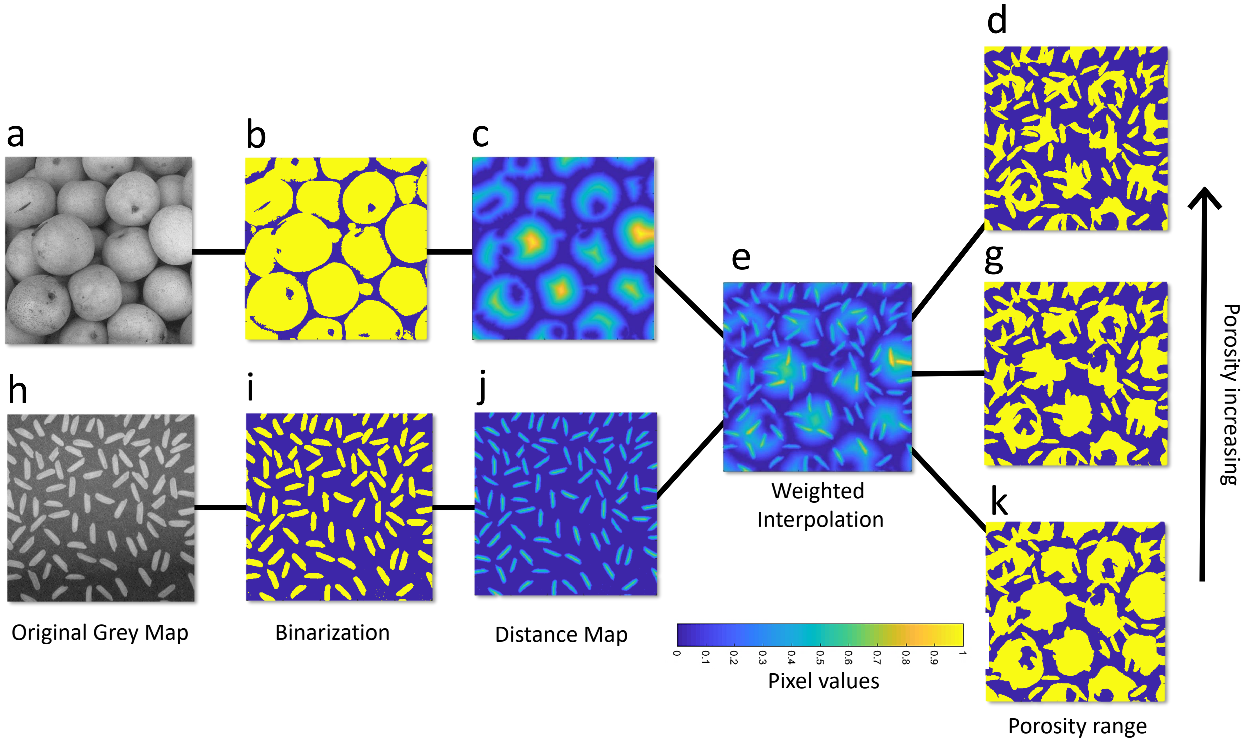

Figure 4.1: Texture interpolation by weighted averaging of the normalized distance maps, (a and h) original gray maps, (b and i) binarized geometries, (c and j) normalized distance maps of the solid space, (e) equally–weighted average of the distance maps, (d, g and k) three realizations made by changing the threshold level that controls the porosity.

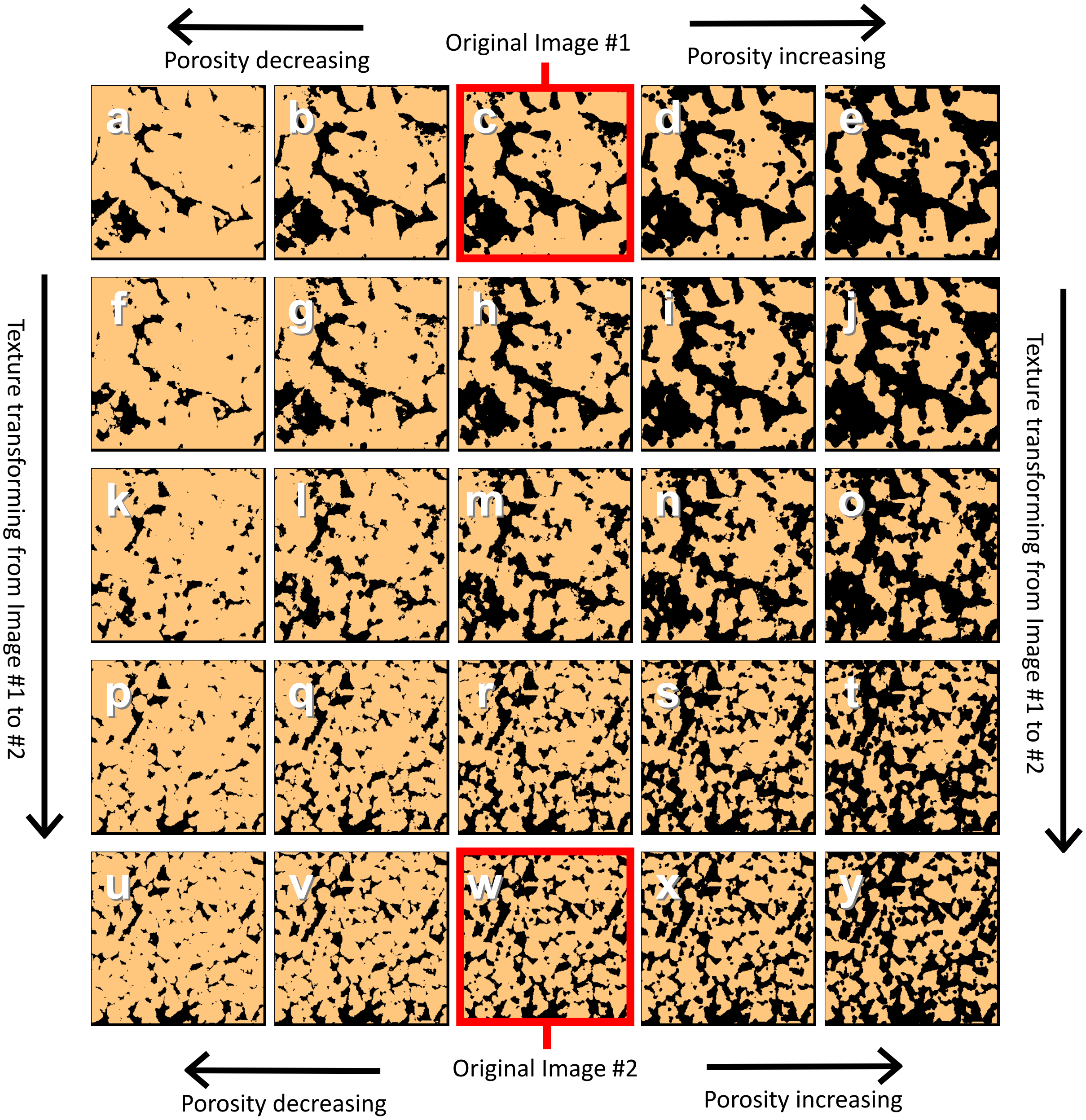

Figure 4.2: Texture interpolation results based on two real tomography images with a wide range of porosity and texture distributed between two original samples (d and w), porosity of the samples increases from left to right and texture is transforming from c to w when moving downwards.

4.3.2 Building the ground truth data

After construction of the augmented set of image data, we use a series of in–house codes developed based on the available literature to analyze the micro–structures of the porous material. In this regard, we have used several pore network modeling (PNM) techniques [134] to simulate different physics and processes on the 3–D porous samples and the results obtained are assumed to be the ground truth for training the DeePore CNN. In addition to the pore space characterization, we analyze the solid portion of the images which are defined as a solid network model to enable studying its mechanical behaviour similar to approach presented by Herman in 2013 [267] but with 3 dimensions. A solid network model describes the contact area, direction and length between different grains of a porous structure and assimilate the porous structure to a truss which makes it possible to solve finite element equations in a coarse grid model and obtain some mechanical properties of the micro–structures[268, 267]. A sample realization of the solid and pore networks of a porous material are visualized in Figure 4.3-d and g. In order to construct these networks, initially we need a 3–D binarized image (Fig. 4.3-a) that is segmented to the void and solid spaces which are respectively shown in Figure 4.3-b and e. Then using watershed segmentation algorithm we break down an interconnected micro–structure into a separately labelled map of nodes as can be seen in Figure 4.3-c and f. The color gradient in these illustrations indicates the relative equivalent radius of the nodes extracted for both void (pore) and solid networks. When we have detected location and boundaries of each node, then by analyzing the node map connectivities, two networks can be extracted for both void and solid spaces (Fig. 4.3-d and g). Watershed segmentation algorithm which is used to break down the micro-structures into a mathematically describable 3–D network, has been widely employed for porous material characterization from tomography images [269, 128, 108]. This algorithm uses the Euclidean distance transform of a binary object to detect the narrowest parts of the connections between different nodes. More details on the methodology and validation of watershed segmentation algorithm can be found in [128, 108].

Now in order to build the ground truth data for training DeePore CNN, we investigate the constructed pore and solid networks by measuring several morphological features and running physical simulations (Fig. 4.3-h). In this section, we briefly describe the simulation techniques employed and some assumptions made to generalize the analysis of outcomes. As an example, we have illustrated 3 simulation results on a sample pore network model in Fig. 4.3-g. These simulation results are fluid saturation in a 2–phase drainage process, electricity flow through the saturated pore–space, and pore pressure of the single–phase fluid flow, respectively depicted in Fig. 4.3-h1 to h3 to give some insight on the ground truth generation.

The list of the physical properties and features that have been obtained for each of the samples within the dataset is provided in Table 4.1. As can be seen, we report 15 single–value features that comprehensively describe the morphological, hydraulic, mechanical and electrical properties of porous material. Additionally, 4 functions and 11 distribution curves are extracted for each porous sample to describe its characteristics (Fig. 4.3-i). Here is a brief introduction to the calculated set of properties and more details regarding the methodology of extracting each of the features is available in the corresponding references in Table 4.1.

Morphological properties

Based on the extracted network models, probability distribution in addition to the average values are reported for pore body radius, pore throat radius, throat length, grain radius, and pore connectivity [108] which is also known as the network coordination number [39]. In addition, pore density that indicates the number of pores per unit volume of the geometry, grain sphericity [270], and specific surface are calculated for each of the 3–D images in the dataset. Furthermore, we have used Dijkstra's algorithm [271, 272] to find the shortest path from one face to the other face of the pore networks and calculate tortuosity. In this regard, the shortest path between each two random pairs of the pores from inlet to the outlet of the pore network is calculated for several times and average value of all shortest paths is reported as tortuosity. Finally, as a morphological property of porous material we have calculated the two–point correlation function of the binarized images which shows how well–correlated are the porosity of two random points selected with a specified distance between them [273]. For more details regarding the calculation methodology for each of the properties please refer to the references provided in Table 4.1.

Hydraulic properties

Absolute and relative permeabilities are calculated based on the extracted pore networks. For calculating the fluid conductance in each pore throat, realistic cross–sectional shapes of the throats are used to provide better results [198]. Additionally, for calculation of the two–phase flow functions, we have assumed zero contact angle in the case that two immiscible fluids are present within the porous media. Also, smooth spherical curvatures are assumed for pores and throats to simplify the displacement process. A thin layer of the wetting phase fluid is present at the wall surface to maintain the phase connectivity but it does not contribute to the hydraulic conductivity of the throats. The procedure we use to model two–phase displacement in a pore network is a quasi–static approach with stepwise increment of the non–wetting phase pressure and domination of the capillary forces over the viscous forces. The quasi–static approach is fully described by Valvatne and Blunt [274]. The capillary pressure curve is another important hydraulic property of the porous material and as discussed, we require a technique to remove the pressure unit of this parameter. To this end, we have used the concept of Leverett J-function curve [275] which is a dimensionless version of the capillary pressure normalized for different porosities, permeabilities, contact angle and interfacial tension between the two displacing fluids in porous media.

Electrical properties

Formation and cementation factors are two electrical properties of porous material that have been calculated using the extracted pore network models [276, 277]. These parameters are critical in Archie's equation [278] and helps to describe the electrical behaviour of a porous medium saturated with a conductive fluid. Formation factor is the ratio of the electrical resistance of the fully saturated porous media to the electrical resistance of the pure fluid [279]. In order to calculate this feature, we solve a resistor network assuming conductive fluid inside the pore space using finite difference method. Also, with a similar approach, this value remains the same when we are measuring the ratio of the mass diffusivity of a component in a bulk fluid relative to its diffusivity through the fully–saturated porous media [280, 281].

Mechanical property

In addition to many pore–dependent properties, we have modelled relative Young modulus of the material which is a solid phase feature. For this purpose, we assume that the extracted solid network is a truss–like structure and by applying normal compressional force on each side of the geometry, the directional Young modulus is calculated by dividing the normal stress over the strain ratio [282, 283]. Then arithmetic average of the directional values is calculated and divided by the Young modulus of the pure non–porous material to obtain the relative Young modulus which is a dimensionless number [284].

Dimensionless approach

It is noteworthy that we have removed the original spatial resolution of the data and defined a unified unit of length which is equal to the physical size of each voxel. For example, the unit of absolute permeability which is area has become px^2 which means that we need to multiply the resulted permeability by the spatial resolution to the power of two in order to retrieve the re–scaled permeability value. Here, we used px as a short form for pixel or voxel size which is our unit of length. In the same manner, all other reported features are dimensionless or described only in length unit which is convertible to voxel size. The list of all alternative units is presented in Table 4.1. For features that can be calculated directionally such as permeability, we have assumed an isotropic structure and reported the arithmetic average of the values in x, y, and z directions. Although in some cases this averaging does not have explicit physical meaning, but it is used to cover directional non–conformities in the porous structures that can affect the extensibility of the model.

Num.	Output indices	Feature	Data type	Reference
1	1	Absolute permeability (px^2)	Single value	[198]
2	2	Formation factor (ratio)	Single value	[276]
3	3	Cementation factor (ratio)	Single value	[277]
4	4	Pore density ($1/px^3$)	Single value	[285]
5	5	Tortuosity (ratio)	Single value	[271, 272, 286]
6	6	Average coordination number	Single value	[108]
7	7	Average throat radius (px)	Single value	[287]
8	8	Average pore radius (px)	Single value	[287]
9	9	Average throat length (px)	Single value	[287]
10	10	Average pore inscribed radius (px)	Single value	[288]
11	11	Specific surface ($1/px$)	Single value	[289, 290]
12	12	Average throat inscribed radius (px)	Single value	[288]
13	13	Grain sphericity (ratio)	Single value	[270]
14	14	Average grain radius (ratio)	Single value	[193]
15	15	Relative Young module (ratio)	Single value	[282, 283, 291]
16	16-115	Leverett J–function (ratio)	Function	[275]
17	116 - 215	Wetting relative permeability (fraction)	Function	[274]
18	216 - 315	Non-Wetting relative permeability (fraction)	Function	[274]
19	316 - 415	Two-point correlation function ($1/px$)	Function	[273]
20	416 - 515	Pore radius distribution (px)	Distribution	[195, 131]
21	516 - 615	Throat radius distribution (px)	Distribution	[195, 131]
22	616 - 715	Throat length distribution (px)	Distribution	[195, 131]
23	716 - 815	Pore inscribed radius distribution (px)	Distribution	[288]
24	816 - 915	Throat inscribed radius distribution (px)	Distribution	[288]
25	916 - 1015	Throat average distance (px)	Distribution	[198]
26	1016 - 1115	Throat permeability distribution (px^2)	Distribution	[198]
27	1116 - 1215	Coordination number distribution	Distribution	[108]
28	1216 - 1315	Pore sphericity distribution (ratio)	Distribution	[292]
29	1316 - 1415	Grain sphericity distribution (ratio)	Distribution	[270]
30	1416 - 1515	Grain radius distribution (px)	distribution	[193]

Table 4.1: List of the physical features of porous material which are considered to be the outputs of the model in addition to the corresponding units and references that describe the methodologies in detail.

4.3.3 Deep learning method

We have generated the dataset of semi–realistic micro–structures of porous material and a wide range of 30 physical properties are calculated for each of the samples. The aim is to build a machine learning model that is able to estimate these properties purely by analyzing input images and learning an implicit knowledge of the underlying physics. It should be noted that this *implicit* knowledge is different than the physics-informed machine learning models that *explicitly* embed physical equations in the structure of their network layers [293].

As discussed, CNNs have proved to be efficient in image classification, segmentation, and regression. So, we have designed a CNN structure combined with two dense layers of neurons to make a regression model that is able to estimate all physical properties of porous material mentioned above in a supervised manner. Data workflow and CNN structure are presented in Fig. 4.3 and Table 4.2. Here, we are providing more details regarding the structure of the network and the training process.

Network input layer

Initially, we take a 3–D image from the dataset with the size of 256^3 voxels and extract three perpendicular mid–planes of the volumetric data (Fig. 4.3-k to l). Then, the distance transform of the solid and void spaces is calculated for each of the images and is deduced to make an initial feature map (M) as follows:

$$M = \left\lfloor \frac{8}{S} f_d(1 - A) - \frac{8}{S} f_d(A) \right\rfloor \tag{4.1}$$

Where S is side size of the image which is 256 voxels in our case, and $\lfloor x \rfloor$ is the floor operator that rounds down the decimal points to the closest smaller integer, f_d is the Euclidean distance transform and A is the a 2–D plane cut through the 3–D volume perpendicular to one of the major axes (Fig. 4.3-k). As a matter of fact, variable A is an array that contains 0 representing pore space and 1 for solid voxels. The reason to multiply distance maps by the ratio of $\frac{8}{S}$ is to ensure all the calculated values will be mainly between -1 and 1 which is suitable to be used as CNN input. The distance maps are not only able to deliver information about the original binary map, but also, describe the Euclidean distances between each point of that binary map to the nearest boundary. This additional information enriches the model input layer with more data compared to passing a simple binary array.

Now, based on the three maps generated using Eq. 4.1, we generate a fictitious RGB image by stacking them into each other and make an initial feature map to be used as the input for the CNN (Fig. 4.3-n). The term RGB refers to a color space for image quantization composed of three channels of red, green, and blue. The reason to mimic an RGB image is the common use of these image formats as input of a CNN. In addition, RGB images are easy to store and read from hard disk and there are plenty of lossless compression methods invented to minimize their size when stored on disk [294]. Use of the whole 3–D data as the input of the CNN instead of the perpendicular mid–planes could increase the accuracy of the results, while it can significantly increase the computational expenses which are not desirable. Also this defeats the purpose of this research to propose an efficient while adequately accurate model.

Network hidden layers

At the first layer of CNN, we initially run a 2 by 2 max–pooling filter to reduce the size of the input data without losing too much information (Fig. 4.3-o2). Then, 3 convolutional layers are designed to gradually decrease the size of the information while maintaining the main geometrical features by applying different sequential filters on the input images (Fig. 4.3-o3 to o5). Each convolutional layer is followed by a 2 × 2 max–pooling filter to finally make data small enough to be fitted into a fully–connected dense layer. The first dense layer is activated by ReLU, while the second one uses sigmoid (Fig. 4.3-o6 and o7). This network architecture is designed by testing a range of different structures and monitoring the performance of each training scenario in terms of accuracy. The selected training scenario has three convolution kernels with the size of 3 × 3 with stride equal to 1 × 1. More details on the structure of the proposed CNN is provided in Table 4.2.

Network output layer

As it can be seen in Table 4.2, the output layer of the network is a one dimensional array of 1515 elements (Fig. 4.3-o8). The first 15 elements of the array are 15 single–value features calculated for each of the porous samples as described in Table 4.1, rows 1 to 15. The next 1500 elements of the output array describe 4 functions and 11 distribution curves each of which occupies 100 elements of the array. The range of the array indices for each of the output parameters is described in Table 4.1. In order to fit the wide range of variables and functions into an array of 1515 elements, certain reshaping and interpolation operations are required for the raw results of pore scale modelling. The four functions that occupy indices from 16 to 415, are Leverett J-function, wetting relative permeability, non–wetting relative permeability and two–point correlation function. The first three are functions of wetting phase saturation which is a fraction between 0 to 1. So, in order to summarize each of these three curves into 100 elements, we have divided the whole curve into 100 pieces each of which with 0.01 distance from each other in terms of wetting phase saturation. Similarly, for two–point correlation function, we have split the curve into 100 segments each of which with 0.5 voxel distance to the next one, in order to cover a total lag distance of 50 voxels in 100 elements. For more details regarding this function please refer to [273]. Next, in order to fit each of the 11 distribution curves into 100 elements, we are using the cumulative format of the probability distributions (CDF) that pack a full range of variable changes into a sigmoid–like curve between 0 and 1. Consequently, we have divided the CDF curve into 100 pieces with 0.01 distance between every two consecutive points in Y axis and embedded the corresponding values of X axis into the output array. For more clarification, a sample set of the described functions and distribution curves will be presented in the Results and Discussion section (Table 4.4 and Fig. 4.7).

Model training

Development and training of the DeePore CNN is implemented in Python using Keras with TensorFlow backend [295]. Additionally SciPy, Numpy and Matplotlib [296] as open–source packages of Python are used for data pre– and post–processing. Back–Propagation RMSprop algorithm [297] with the learning rate of 10^{-5} is used for training the CNN by minimizing the prediction loss in terms of mean squared error. We have used 80 % of the data samples for training the network, 10 % for validation and 10 % are kept outside of the workflow for independent and un–biased testing of the results obtained. We have trained the model for 100 epochs with batch size of 100 samples per each updating of the model gradient. The input and output data are fed into the model using large size Hierarchical Data Format (HDF) files. A Python Generator method, reads the data batch by batch from the HDF file to avoid occupying a large amount of machine memory.

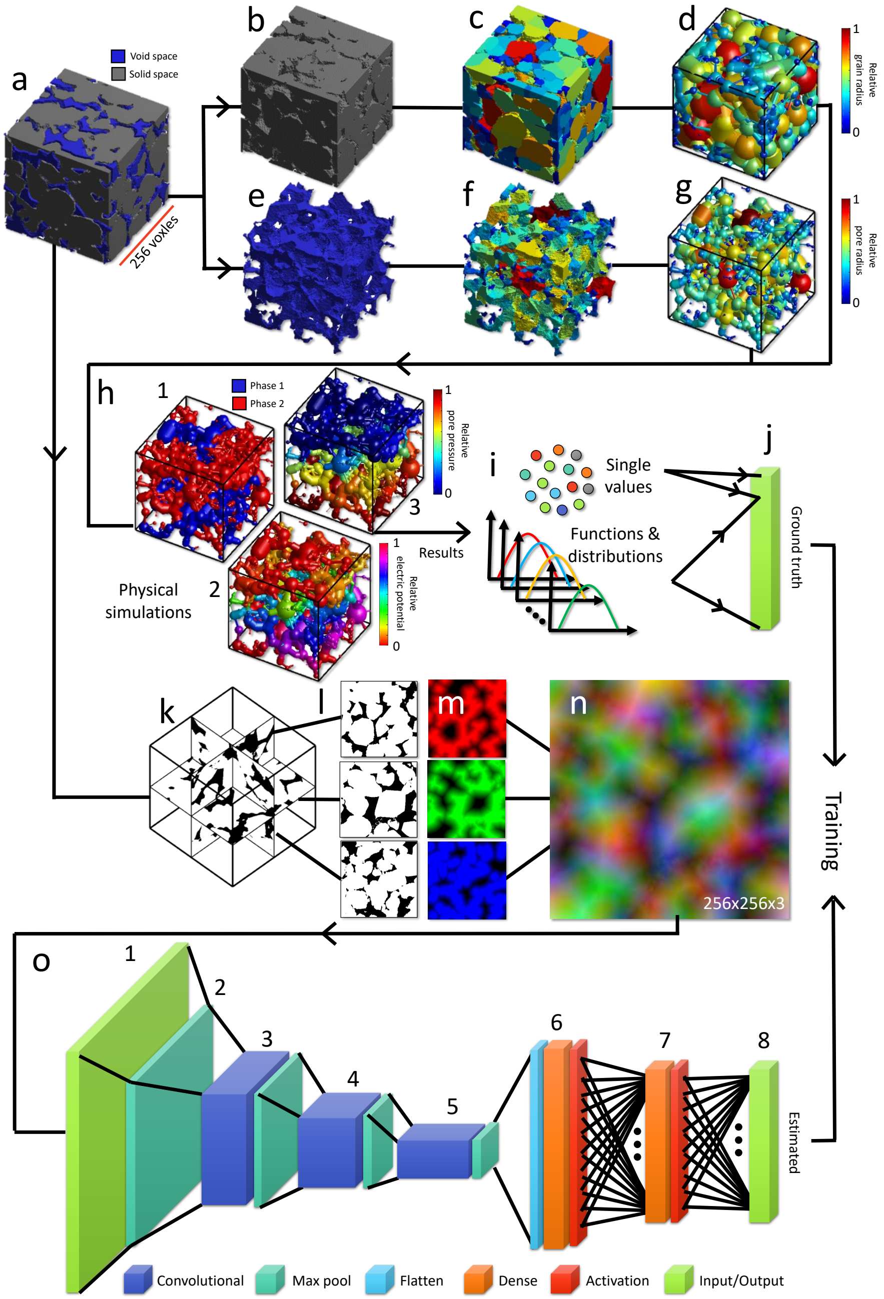

Figure 4.3: DeePore data workflow for generating the ground truth data and training the CNN based on that, original binary geometry (a), solid and void spaces (b and e), labelled map of nodes (c and f), solid and pore network models (d and g), some of physical simulations on the pore network (h1 to h3), calculated single–value features, as well as the functions and distributions (i), flatten array of ground truth data (j), three perpendicular mid–planes out of the 3–D volumetric data (k), structure of three selected planes with one as solid and zero as void space (l), three differential distance maps of the solid space which mimics red, green, and blue channels of a synthetic RGB image (Eq. 4.1) (m), input feature map of the porous media as a fictitious RGB image (n), (o) structure of the designed CNN with 8 layers each of which are described in Table 4.2.

Layers	Type	Input size	Kernel	Options	Trainable parameters
1	Input	256×256×3	-	Normalization	0
2	Pooling	128×128×3	-	Max Pool 2×2	0
3	Convolutional	64×64×6	3×3	Max Pool 2×2	336
4	Convolutional	32×32×12	3×3	Max Pool 2×2	2616
5	Convolutional	16×16×18	3×3	Max Pool 2×2	7812
6	Fully-connected	1×1×9217	-	ReLU Activation	9217×1515
7	Fully-connected	1×1×1515	-	Sigmoid Activation	1516×1515
8	Output	1×1×1515	-	Denormalization	0
Total	-	-	-	-	16,271,259

Table 4.2: Structure of the designed CNN including type, size, option, kernel and trainable parameters of each layer.

4.3.4 Direct numerical simulations

In order to provide an insight towards the performance of the proposed method compared to the direct numerical simulation approaches, we have used Lattice Boltzmann method (LBM) and pore–scale finite volume solver (PFVS) to calculate the absolute permeability of 3 realistic test samples. Here, we aim to briefly describe the methodology of these numerical methods.

Pore–scale finite volume solver (PFVS)

The PFVS method solves an elliptic diffusion equation to obtain the spatial pressure distribution in micro–CT images, hence it estimates the absolute permeability of micro–CT images [298]. This method is CPU time efficient as it does not require time-stepping to converge to a solution. The conservation of mass can be expressed as:

$$\nabla.\vec{v} = q \tag{4.2}$$

where $\vec{v}$ is the velocity vector and q represents source and sink terms, which is assumed to be zero. We assign each voxel a local conductivity w, calculated as outlined by Chung *et al.* [298] to relate the velocity to the pressure gradient:

$$\vec{v} = -w\nabla P \tag{4.3}$$

where P is pressure. Combining equations 4.2 and 4.3 gives an elliptic equation:

$$-\nabla.(w\nabla P) = 0 \tag{4.4}$$

This equation is solved with prescribed constant pressure (Dirichlet) boundary conditions on the inlet and outlet by using Two Point Flux Approximation (TPFA) [299, 300] and Finite Volume Methods with an Algebraic Multi-Grid (AMG) solver. All solid voxels are removed from the system of equations, resulting in a smaller system matrix. Once the spatial pressure distribution and velocity profile (and subsequently, the flow rate) are calculated by equations 4.3, the absolute permeability is estimated from:

$$K = \frac{N_x}{N_y N_z R} \frac{Q\mu}{\Delta P} \tag{4.5}$$

The length of the system is expressed as the voxels multiplied by the resolution of the image (R). Hence, the number of voxels in the main flow direction can be defined as N_x and the other two directions are N_y and N_z, Q is flow rate (m^3/s), μ is fluid viscosity ($Pa.s$), ΔP is pressure difference across the image (Pa), imposed as a boundary condition. Under the assumptions of laminar incompressible flow and no–slip boundary condition, local conductivity (w) is defined as a weighting function representing the conductivity of a voxel for fluid flow. Local conductivity is a function of two variables, the largest inscribed radius of the flow channel (r_{max}) and the distance from the solid wall (r):

$$w = \alpha R^2 \frac{\rho}{8\mu}(2d_{max}d - d^2) \tag{4.6}$$

where w is local conductivity, α is the shape factor, R is resolution of image (m), d_{max} is digital equivalent of the largest inscribed radius, d is digital equivalent of radial distance from the inner wall, and ρ is fluid density (kg/m^3).

Lattice Boltzmann method (LBM)

In another direct numerical simulation approach, flow within the pore space is calculated by the Lattice Boltzmann Method (LBM) using a Multi-Relaxation Time scheme [301, 302, 303] in D3Q19 quadrature space in order to eliminate spurious parameter coupling between viscosity and permeability that occurs with Single Relaxation Time and improve stability in high velocity pore throats. LBM reformulates the Navier-Stokes Equations by numerically estimating the resulting continuum mechanics from underlying kinetic theory. The kinetics of a bulk collection of particles within a control volume is estimated with a vector velocity space ξ_q and velocity distributions f_q. For each velocity space vector ξ_q, the velocity component in the specified direction is given by f_q. The momentum transport equation at location $\vec{x_i}$ over a timestep δt relies on a collision operation J which recovers the Navier Stokes Equation, and outlined in detail by McClure *et al.* [302].

$$f_q(\vec{x_i} + \vec{\xi_q}\delta t, t + \delta t) = f_q(\vec{x_i}, t) + J(\vec{x_i}, t) \tag{4.7}$$

Single phase flow is simulated within the pore space of the segmented test samples until steady state conditions are reached. In the present study we continue the simulations until the change in permeability over 1,000 LBM timesteps is less than 1e−5. All samples are simulated with a constant pressure drop between the inlet and outlet, and wall boundary conditions are imposed along the other sides to avoid geometric inconsistencies associated with periodic boundary conditions.

4.4 Results and Discussions

In this section, three main outcomes of this study are discussed. Initially we describe the significance and applications of the present dataset of the porous material and then we focus on the statistical lessons learned by examining cross–correlations of the dataset features. Finally, the accuracy of the features estimated by the model will be checked on the testing samples to demonstrate the capability of DeePore workflow for rapid characterization of the porous material.

4.4.1 Porous material dataset

In this research we have generated a comprehensive dataset of semi–real micro–porous structures with 17700 samples and a wide range of morphological, hydraulic, electrical and mechanical features are calculated for each of the samples. The main application of this dataset is to be used as the raw material for more advanced machine learning studies on porous materials. In addition to the raw 3-D geometries, Python codes, extracted pore networks and all calculated characteristics are available in the public domain for replication and improvements in future studies [1].

4.4.2 Statistical lessons learned

Considering the large number of analyzed samples of porous material, we have created a rich dataset to investigate the existing trends and relationships among the calculated features. Binary correlation coefficients of 15 single-value features are visualized in Fig. 4.4 as a heat map to summarize the statistical significance of cross-parameter relationships. Pure blue color at the intersection of two parameters indicates strong correlation and pure red color shows a strong inverse correlation between them. As an example, absolute permeability of

---

[1] GitHub Repository: `https://github.com/ArashRabbani/DeePore`

porous media is well correlated with average pore–throat radius which is expected based on the available literature [304], while it does not have a significant relationship with average grain radius and finally it has an inverse relationship with relative Young modulus of the porous material. This relationship is physically justifiable considering that large values of relative Young modulus indicate a tight and consolidated structure of porous material [291] which leads to lower permeability. Although, many of these relationships have been widely investigated in the literature [305, 306, 307], having a diverse range of them in a single map (Fig. 4.4), could provide a concise but broad insight about porous material characteristics.

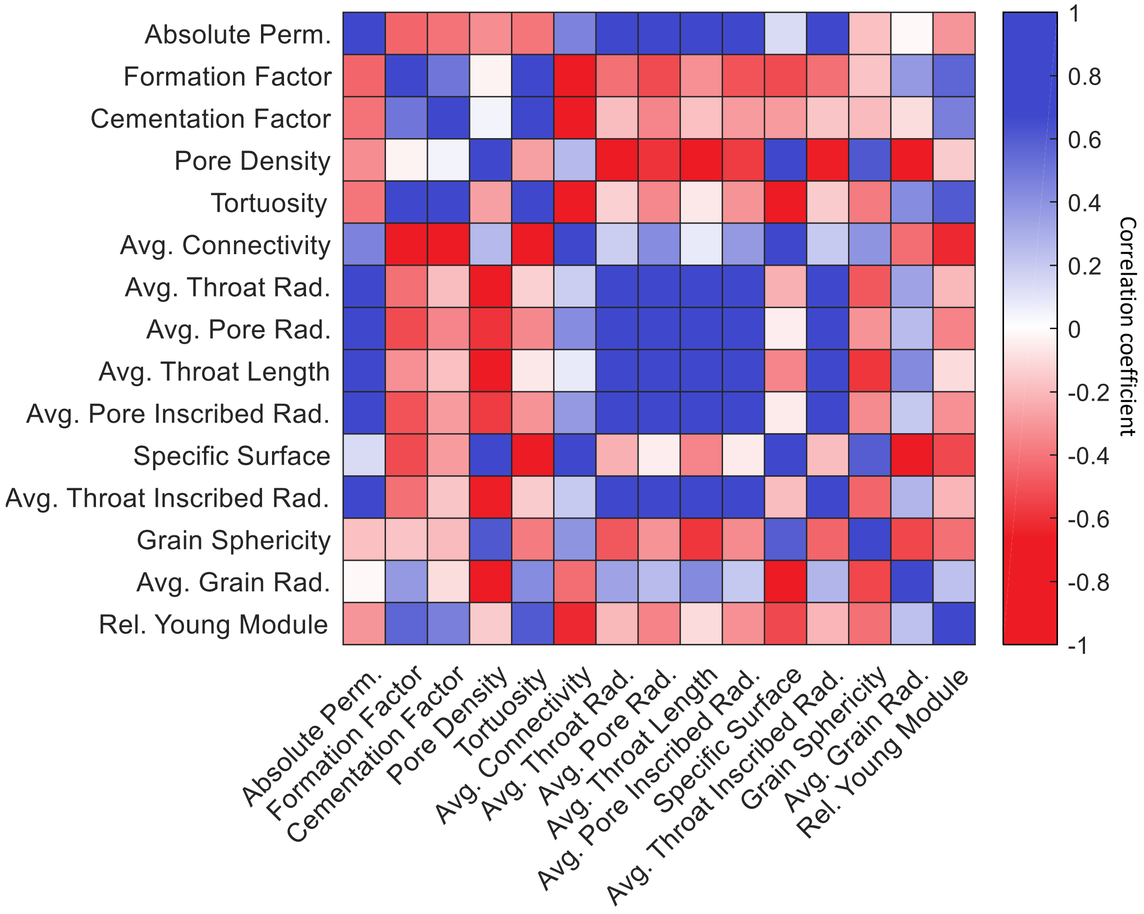

Figure 4.4: Heatmap of the cross–correlations between the physical properties of the porous material, blue color indicates that two variables are highly correlated, white color indicates that variables are not statistically related and red color denotes a strong inverse correlation.

4.4.3 Data distribution

The data is randomly split by shuffling into three sections with the proportions of 80 %, 10 %, and 10 % respectively for training, validation, and testing processes. Relative frequency distribution of the training, validation, and test data are plotted in Fig. 4.5 to demonstrate similarity/difference of the data statistics. We have run two–sample Kolmogorov–Smirnov

(K–S) test to check if the distributions of training and validation/test data are statistically similar. K–S distances of the tests are provided in Appendix E and if the value is closer to 1, it indicates that the two compared distributions are dissimilar. Based on the obtained results, 97 % of the K–S distances are below 0.03 which shows that data shuffling and sample selection are unbiased which is favourable in terms of the training robustness. Fig. 4.5 illustrates the three distributions of training, validation and testing datasets for 15 single–value features modelled in this study.

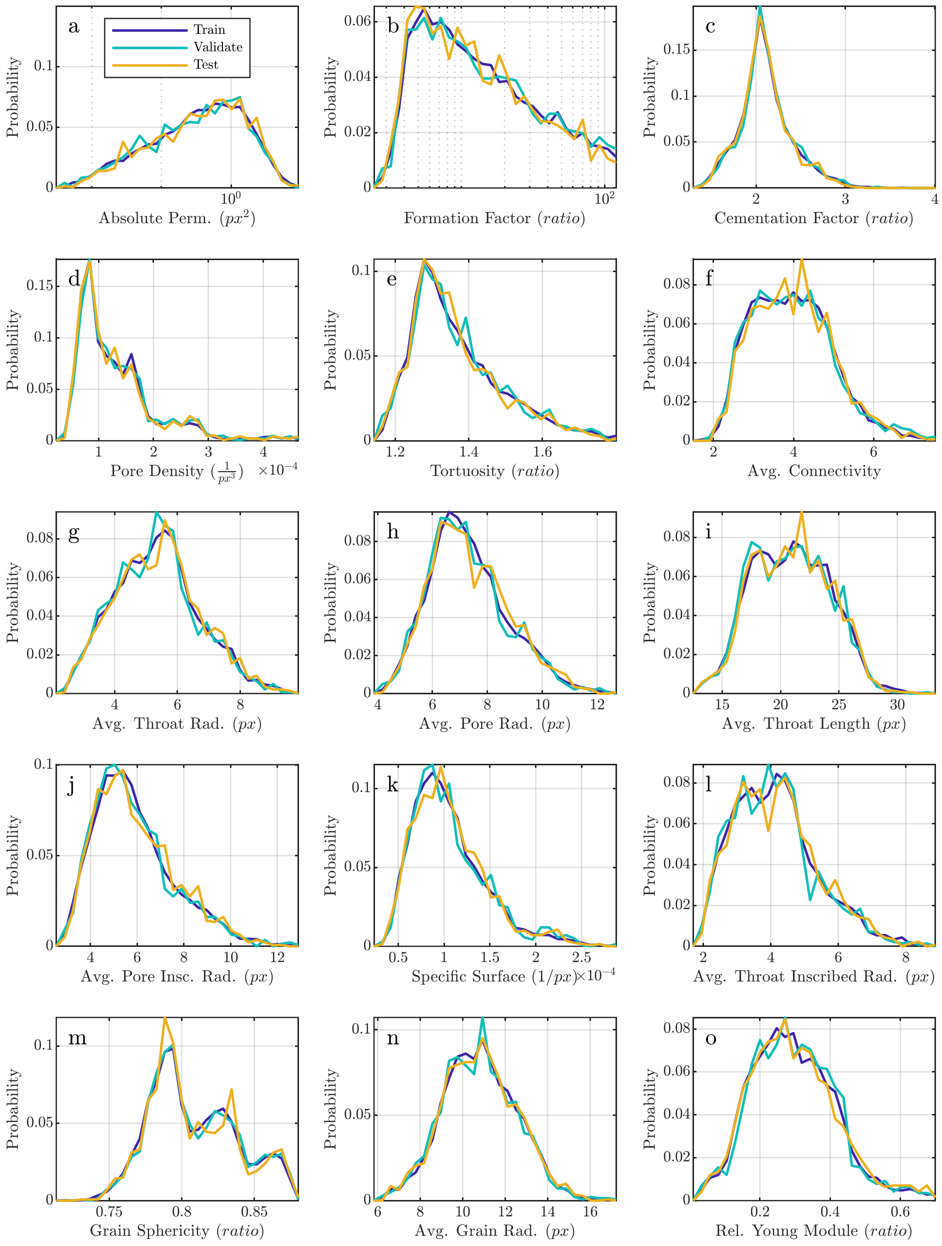

Figure 4.5: Relative frequency distribution of 15 single–value features for each bundle of the training, validation and testing data.

4.4.4 Alternative models

In order to fine–tune the model structure and select the best options, we have tested 9 training scenarios of which they were more likely to fit the purpose. Different number of filters in each convolution layer, corresponding kernel sizes, optimizers, and loss functions used for each scenario are presented in Table 4.3. Additionally, the total averaged $R2$ of the models based on the testing dataset is calculated to be used as evaluation criterion. Also, the averaged $R2$ is calculated for both group of single–value features and functions illustrated in Fig. 5.10–a. It has been found that the accuracy of the models is dependant to both loss function and network structure. Four different loss functions have been tested through 9 scenarios:

- **Mean squared error (MSE)**: this is the simplest version of loss function and by using it we assume that all the 1515 elements of the CNN output array share the same weight in the training process.

  $$Loss = \frac{1}{1515}\sum_{i=1}^{1515}(y_i - {y'}_i)^2 \tag{4.8}$$

  where, y_i is the actual value and y'_i is the predicted value of the i_{th} elements of the output array.

- **Weighted MSE**: this type of loss function indicates that the 15 single–value outputs should have same weight as the 15 functions and distributions each of which with 100 elements. Thus, MSE is calculated for each of the function elements then it is averaged over the 100 elements and summed up with the 15 single–value errors as follows:

  $$Loss = \frac{1}{15}\sum_{i=1}^{15}(y_i - {y'}_i)^2 + \frac{1}{15}\sum_{i=16}^{30}\frac{1}{100}\sum_{j=1}^{100}(y_{ij} - y'_{ij})^2 \tag{4.9}$$

- **Binary cross entropy**: This loss function is regularly used for evaluating the accuracy of a binary classification, while it has been found in this paper to be effective for the functions and numbers that revolve around the values between 0 and 1. This loss function performs a maximum likelihood estimation based on the Kullback–Leibler divergence [308] and it performs better than MSE in the cases with large difference in the order of magnitude due to the logistic formulation as follows:

  $$Loss = \frac{1}{1515}\sum_{i=1}^{1515} y_i(-\log({y'}_i)) + (1 - y_i)(-\log(1 - {y'}_i)) \tag{4.10}$$

- **Weighted binary cross entropy**: this loss function behaves similar to the regular binary cross entropy, but it is normalized over 100 elements of the 15 functions and distributions to avoid unnecessary additional influence of them in model training due to the higher quantity compared to the single–value outputs. The formulation is presented as follows:

$$
\begin{aligned}
Loss = \frac{1}{15}\sum_{i=1}^{15} y_i(-\log({y'}_i)) + (1-y_i)(-\log(1-{y'}_i)) \\
+ \frac{1}{15}\sum_{i=16}^{30}\frac{1}{100}\sum_{j=1}^{100} y_{ij}(-\log(y'_{ij})) + (1-y_{ij})(-\log(1-y'_{ij})) \quad (4.11)
\end{aligned}
$$

In addition to the loss functions discussed above, two types of optimizers have been utilized in the alternative scenarios namely Adam and RMSprop. These are two adaptive gradient-based optimization methods for stochastic objective functions [309, 310]. These methods store an exponentially decaying average of past squared gradients to utilize it for future estimations. The advantage of Adam is the fact that it also keeps the momentum of past gradients which helps it for better estimation of higher order behaviours [311]. We have used learning rates of 10^{-5} and 10^{-3} for RMSprop and Adam optimizers, respectively.

Based on the model performances presented in Table 4.3 and Fig. 5.10–a, it can be concluded that a simple mean squared error is suitable to be used as the loss function for the present dataset. Also, the comparison shows that weighted MSE underperforms the simple MSE in terms of coefficient of determination. ($R^2 = 0.885$ among the alternative models). In addition to the r–squared comparison, we have illustrated the MSE of the validation and training datasets at the end of each epoch (Fig. 5.10–b and c). As it can be seen, training and validation curve of Scenarios 3 are stable when approaching to 100 epochs. In addition, they are converging almost to a same MSE while in Scenarios 2, 8, and 9 overfitting are observed. Considering all discussed criteria, Scenario 3 is recommended and we use it as the predictor model for results presented hereafter.

Another alternative approach to perform this modeling is the use of separated CNNs for each of the 30 output features. Theoretically, this approach can lead to a better performance while for the purpose of this study, it is not without flaws. Use of 30 different CNNs not only increases the storage size and computational burden of the model up to several times, but also it offers an unnecessary level of accuracy which is beyond the accuracy of the dataset. Considering the fact that the PNM–obtained ground truth data such as the one for permeability contains around 5 to 30 % of simplification error [131], the present commingled structure of CNNs is sufficiently accurate. In addition, the present light implementation of the model makes the online and client–side predictions more viable.

Scenarios	Number of filters	Kernel sizes	Optimizer	Loss function	Averaged R^2
1	6,12,18	8^2,4^2,2^2	RMSprop	MSE	0.832
2	6,12,18,24	8^2,4^2,2^2,2^2	RMSprop	MSE	0.824
3	12,24,36	3^2,3^2,3^2	RMSprop	MSE	0.885
4	6,12,18	8^2,4^2,2^2	RMSprop	Weighted MSE	0.775
5	6,12,18,24	8^2,4^2,2^2,2^2	RMSprop	Weighted MSE	0.781
6	12,24,36	3^2,3^2,3^2	RMSprop	Weighted MSE	0.782
7	6,12,18	8^2,4^2,2^2	Adam	Binary cross entropy	0.791
8	6,12,18	3^2,3^2 ,3^2	Adam	Binary cross entropy	0.749
9	6,12,18	3^2,3^2 ,3^2	Adam	Weighted binary Cross entropy	0.818

Table 4.3: Comparing 9 different training scenarios in terms of filter number and kernel sizes, optimizer, loss and coefficient of determination (R^2). Scenarios 3 show the best performance and have been selected to be used as the DeePore ANN structure.

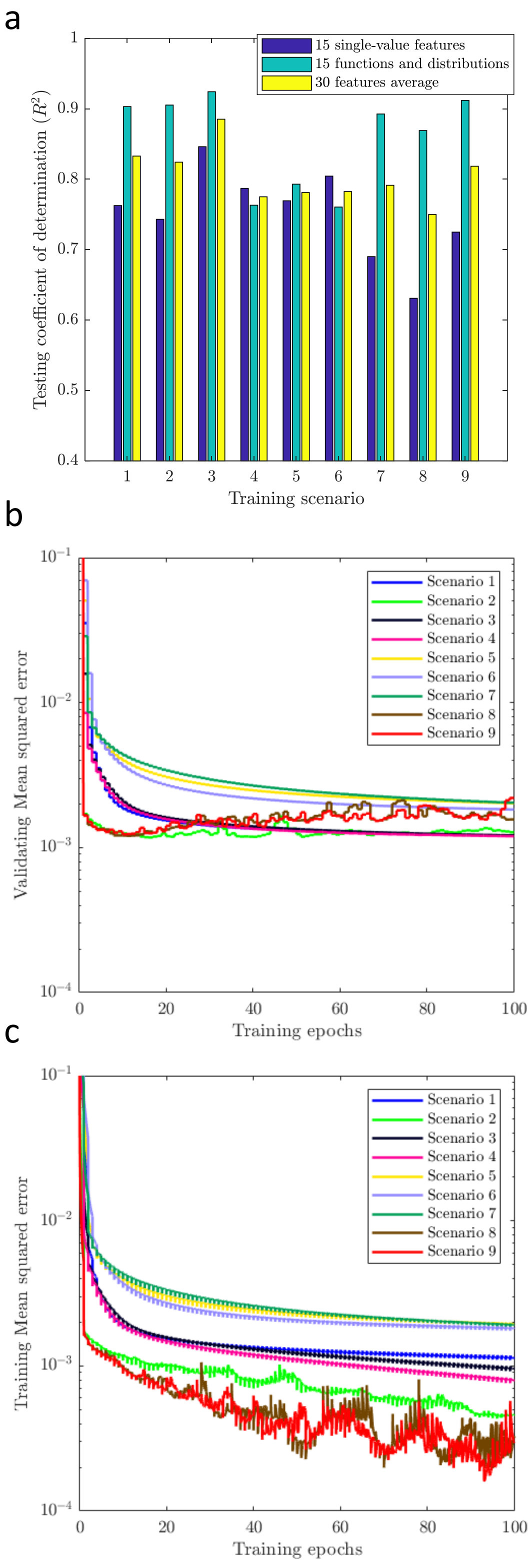

Figure 4.6: Comparing 9 training scenarios in terms of testing coefficients of determination (r-squared) (a), validating mean squared error per epoch (b), and training mean squared error per epoch (c).

4.4.5 Model performance

Model training is performed both in CPU and GPU architectures. CPU–based computations are done on a machine with four 3.2 GHz. Intel Xenon processors and 32 GB of memory. This arrangement enables the model to be trained in 3 to 4 minutes per epoch. In addition, prediction of the porous media features based on the trained model takes 9.23 ms per sample on average which is 4 to 6 orders of magnitude faster if the features are to be extracted by physical simulations whether PNM or direct numerical simulation methods [198].

Using GPU to accelerate the training and prediction stages can make this workflow even faster. Using an Nvidia GeForce GTX 1660 Ti with Max-Q Design Graphic Card with Compute Capability of 7.5 and 6 GB of memory, we are able to train the model around 4 times faster, in which each epoch would take around 45 s to finish. Also prediction of the test dataset can be performed with the speed of 0.379 ms per sample on average which is 24 times faster than the CPU–based instance and it is a considerable improvement.

At each epoch of training the validation and training losses are measured in terms of mean squared error to ensure that over–fitting is not occurring and training has reached an optimum point (Fig. 4.6–b and c). In our case, increasing the number of epochs to more than 100, it hardly reduces the validation loss less than 10^{-3} in a stable manner. So, we have stopped the training at 100 epochs as visualized in Fig. 4.6–b and c.

Using the trained CNN model we have estimated a wide range of porous material characteristics on the 10% of the data which are not used in the training or validation processes. The average determination coefficients (R^2) of the reference and estimated features for the test data are 0.846 and 0.924, respectively, for single–value features (rows number 1 to 15 of Table 4.1), and function/distribution features (rows number 16 to 30 of Table 4.1). Also, the average determination coefficient of all 30 features is 0.885. This overall level of accuracy is reasonably good considering the wide range of porous structures and variety of the predicted features.

In order to provide an insight into the sample outputs of the model, we have presented Table 4.4 and Fig. 4.7 for discussing single–value features and functions, respectively. In Table 4.4, reference values and estimated values are matching with a low level of average relative error at only 5.4%. If the real spatial resolution of this sample image is assumed to be 5 microns per voxel, consequently, in order to scale the values with the unit of length (px) we simply multiply them by 5. Similarly for the area (px^2), values are multiplied by 5^2. This approach gives us the flexibility to predict porous material characteristics in a wide range of spatial resolutions without changing or re–training the model. A similar approach is used for functions and distribution curves which are depicted in Fig. 4.7. The average determination coefficient of all 15 curves shown in this figure for sample #1 is 0.9417.

Additionally we have compared the distribution probability of all single–value features to check the correspondence between the reference and estimated data (Fig. 4.8). This data has been visualized for 1418 testing samples and in the most of the cases both two distributions follow the same pattern, while for parameters like relative Young module and , some deviations are observed (Fig. 4.8-o). Also, in grain sphericity reference curve, a trimodal behavior is observed while the estimated distribution has failed to match that trend accurately (Fig. 4.8-m). This distributed data are also visualized in the form of scattered plots in Fig. 4.9. These charts carry the same R^2 values as the distribution curves in Fig. 4.8, while unit–slope lines in Fig. 4.9 could give better insight regarding the over or under–estimation of the parameters. We have observed a degree of underestimation for larger values especially in tortuosity, grain sphericity and average connectivity data (Fig. 4.9-e and f). This is probably due to the skewness of the distribution of these parameters in which a long but thin tail toward the larger values do not lead the model to sacrifice its accuracy on the middle–range data for better coverage on the whole domain. In other words, during the training process, model prefers to have higher accuracy for the majority of the data points instead of less accuracy but better coverage on the whole set of points.

Finally, we have plotted the predicted functions and distributions versus reference values for 100 randomly selected samples from the testing pool of data (Fig. 4.10). Also, we have calculated R^2 coefficients for each of the plotted lines and the average values are presented in Fig. 4.10. We have found that the data which are directly calculated from the geometrical features of the porous samples such as pore radius distribution (Fig. 4.10-e) are easier to estimate compared to more complicated functions, such as throat permeability distribution (Fig. 4.10–k) that are obtained from a higher level simulation.

Num.	Feature	Reference Value	Estimated Value	Relative Error (%)
1	Absolute permeability (px^2)	0.544	0.573	5.39
2	Formation factor (ratio)	6.541	5.542	15.28
3	Cementation factor (ratio)	2.000	1.980	1.00
4	pore density ($1/px^3$)	1.48E-04	1.43E-04	3.25
5	Tortuosity (ratio)	1.244	1.264	1.62
6	Average coordination number	4.566	4.584	0.40
7	Average throat radius (px)	4.797	5.008	4.40
8	Average pore radius (px)	6.952	6.965	0.18
9	Average throat length (px)	19.722	19.602	0.61
10	Average pore inscribed radius (px)	5.379	5.722	6.37
11	Specific surface (1/px)	1.39E-04	1.36E-04	1.98
12	Average throat inscribed radius (px)	3.585	3.836	7.01
13	Grain sphericity (ratio)	0.807	0.819	1.49
14	Average grain radius (ratio)	8.575	9.039	5.41
15	Relative young module (ratio)	0.219	0.160	26.66
	Average	-	-	5.4

Table 4.4: Example comparison of the reference and estimated values of 15 single–value features for one of the image samples in the dataset (test sample #1).

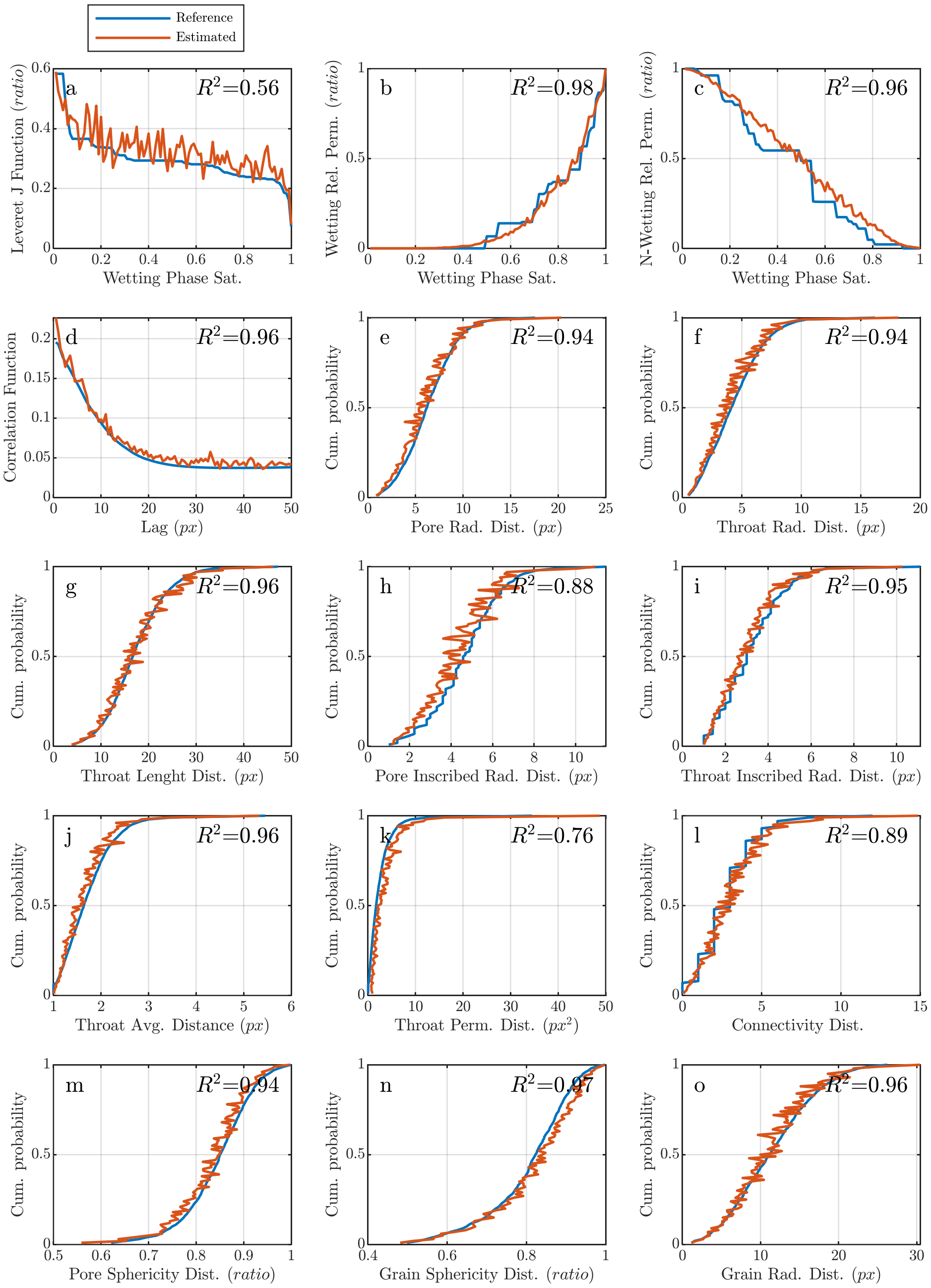

Figure 4.7: Example comparison of the reference and estimated values of 15 functions and distribution for one of the image samples in the dataset (sample #1). The average correlation coefficient of the reference and estimated curves is 0.9616.

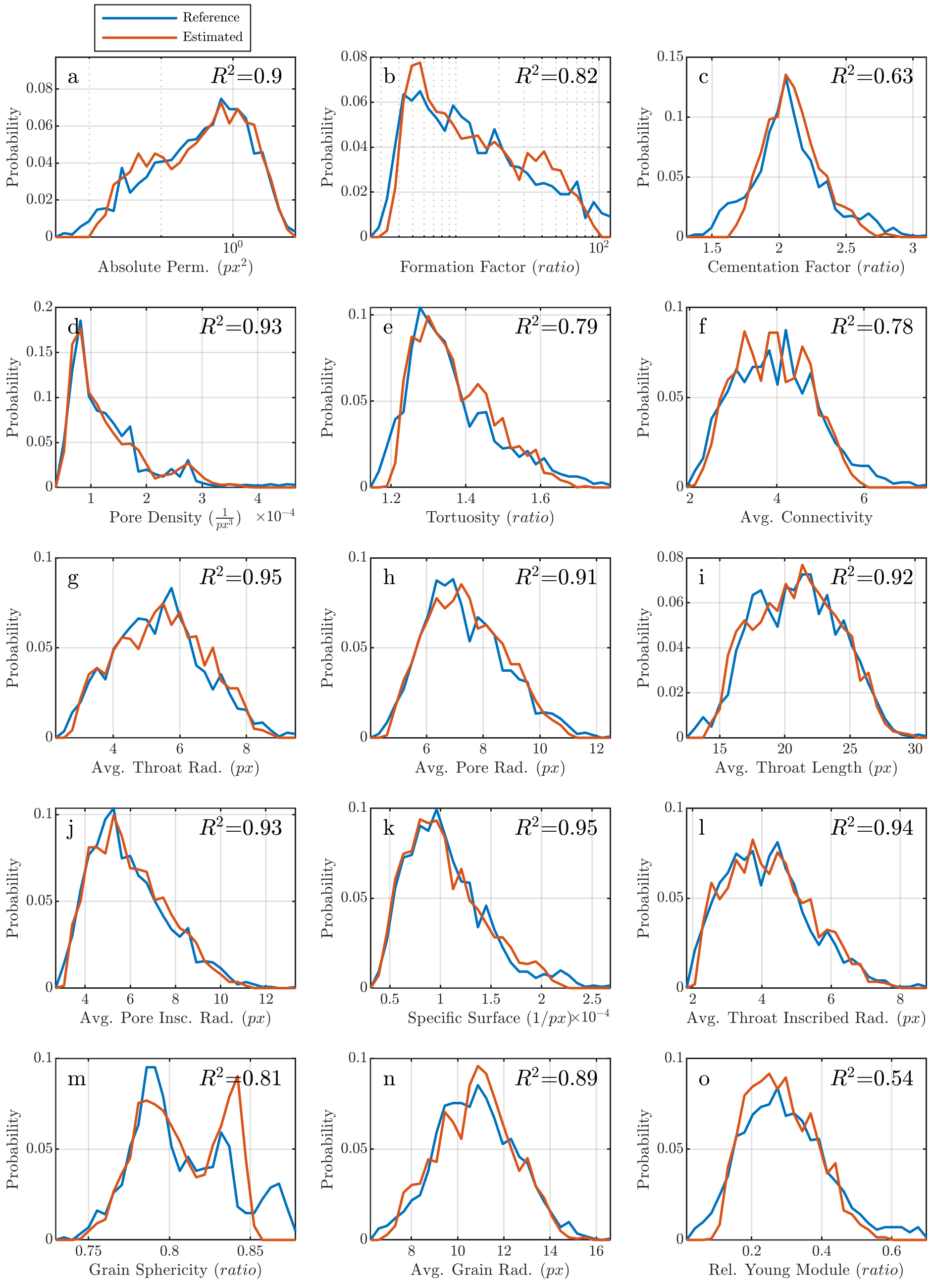

Figure 4.8: Comparison between the reference and estimated distributions of the 15 single–value features, a to o charts correspond to the features inscribed in Table 4.1 rows from 1 to 15.

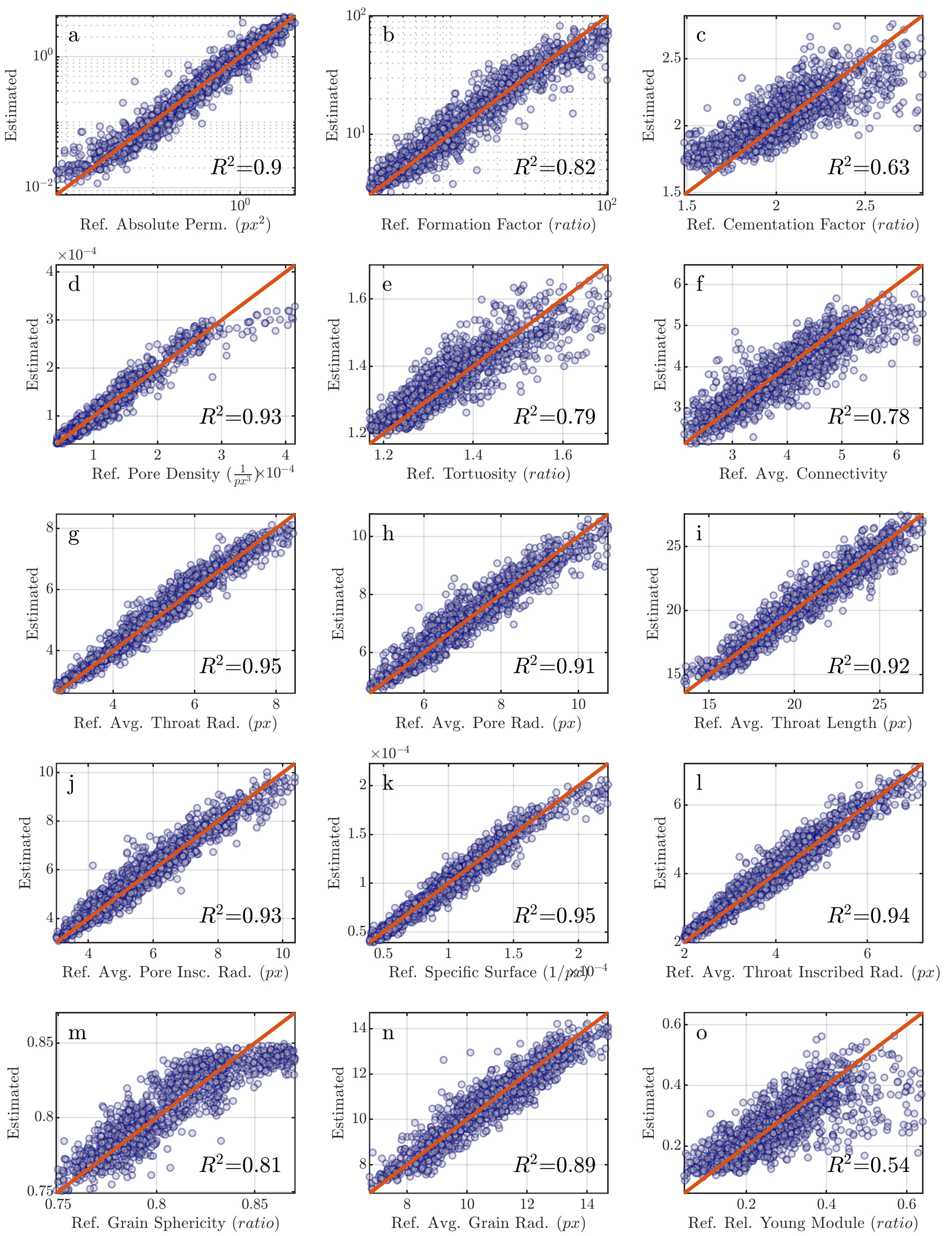

Figure 4.9: Comparison between the reference and estimated values for 15 single–value features and their correlation coefficients, a to o charts correspond to the features inscribed in Table 4.1 rows from 1 to 15.

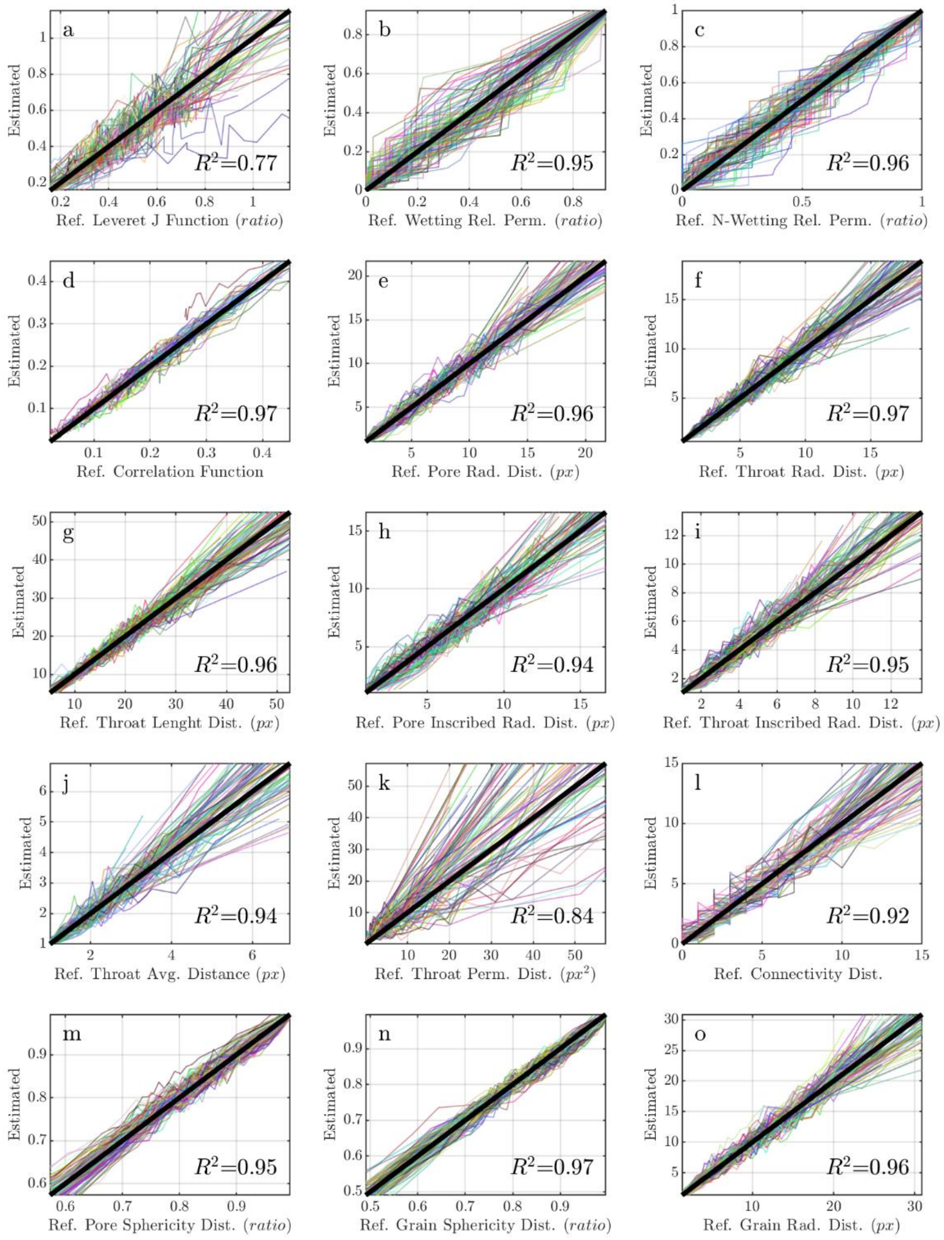

Figure 4.10: Comparison of the reference and estimated curves for 15 functions and distributions that correspond to the rows of 16 to 30 in Table 4.1 (plotted for randomly selected 100 samples and labeled with random colors).

4.4.6 Independent model verification

In order to ensure that the model is not over–trained with the augmented dataset of semi–realistic images, we have created three fundamentally different and independent images with no similar structure inside the dataset to check if the model has implicitly learned the physics instead of only memorizing different textures and corresponding features. In Fig. 4.11 we have visualized three porous samples: (a) the medium is made up of overlapping cubes with no offset limitation, (b) a packing of spheres with overlapping length limited by the half of the spheres' radii, and (c) a fibrous medium made by straight cylindrical rods with 10 voxels radius. It has been found that the model predictions on the shown out–of–the–box samples are almost as good as the testing dataset used to check the model performance in the previous subsection in terms of r–squared. By lumping 15 single–value features of 3 verification images, r–squared of 0.916 is obtained which shows that the DeePore predictions are noticeably similar to the pore network modeling simulations. To provide some examples of the estimated features, we have compared the absolute permeability, average pore radius and Leverett J function of three constructed samples simulated by PNM and estimated by DeePore (Fig. 4.11–d to f, respectively). Averaged relative error of the permeabilities obtained is around 34 % which is reasonable considering the wide range of variation of this variable. Also, for average pore size this error is around 8.1% that is not out of expectation due to the high predictability of pore size from images. Finally, Leverett J function of three samples has been reasonably accurately estimated by DeePore, although a high level of noise is observed in the prediction. The shape of the fluctuations in Fig. 4.11–f are visually similar to the white unbiased noise which can be easily cancelled by performing a moving average or Gaussian filter.

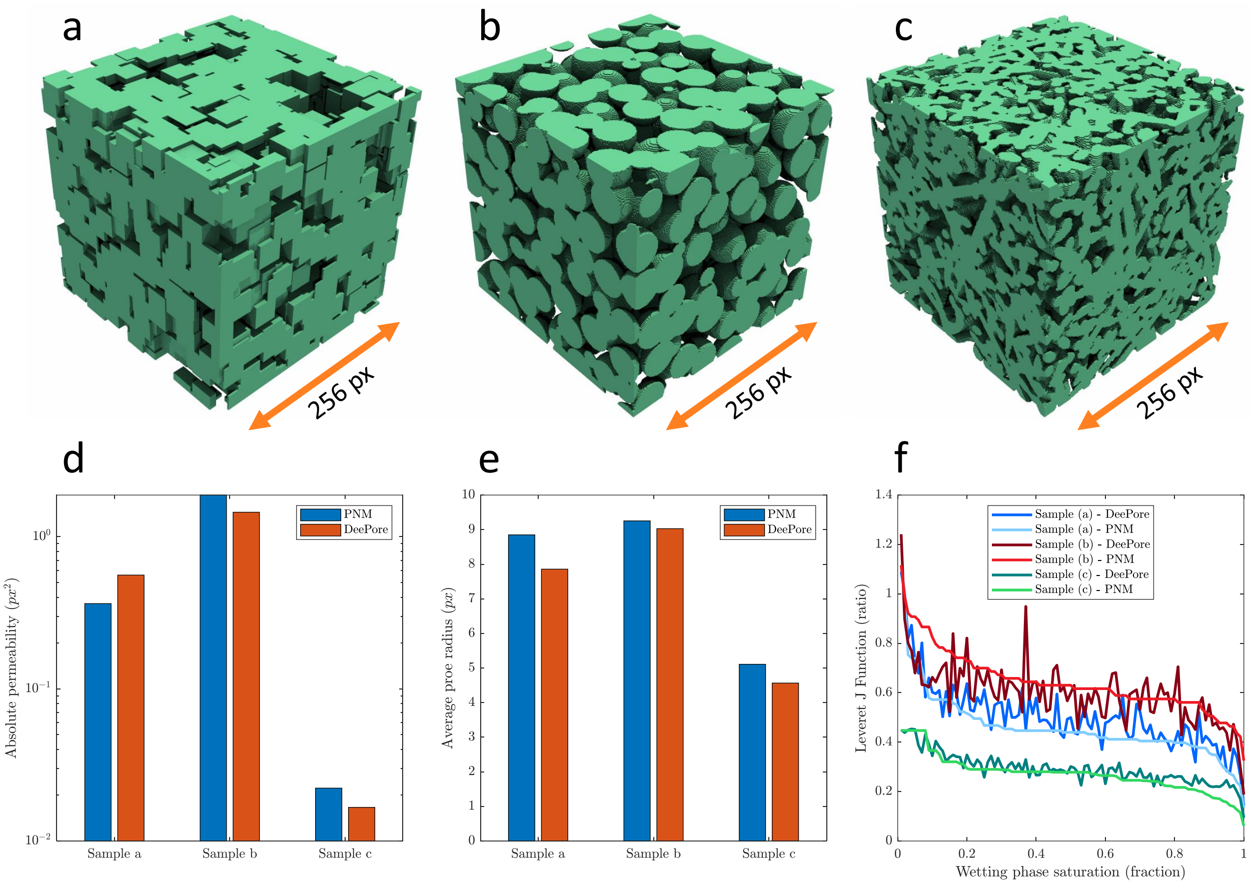

Figure 4.11: Independent verification of model using three artificial porous structures completely outside the training, validation and testing dataset. (a) overlapped pack of cubes, (b) partially overlapped pack of spheres, (c) fibrous media of straight cylindrical rods, (d) comparing the absolute permeability of three images obtained by PNM and DeePore, (e) comparing the average pore radius of three images obtained by PNM and DeePore, and (f) comparison of Leveret J function of three porous samples simulated by PNM and estimated by DeePore.

4.4.7 Validation with experimental data

Considering the fact that the dataset of images used in this study have been virtually augmented, a validation with realistic images can provide a better insight towards the applicability of the proposed method for real world problems. In this regard, three tomography images with available pore–scale experiments of absolute permeability have been used. Additionally, we have employed two direct numerical simulation methods of PFVS and LBM (described briefly in Section 4.3.4) to compare the performance of the proposed method. Absolute permeabilities obtained from experiment, Deepore, PFVS and LBM are illustrated in Figure 4.12. Also in this figure we show the segmented images of three samples used namely Bentheimer sandstone [312], Glidehauser sandstone [313], and glass beads [314]. In order to find the permeability of the samples in the cylinder's axial direction, we divide the image into 2–D slices perpendicular to the cylinder main axis. Then using a 256^2–voxels 2-D sliding window we take subsamples to use as DeePore feed. The overal permeability of a slice is determined by arithmetic averaging over all subsamples and this process repeats for all slices of the 3-D image. Next, minimal slice permeability over the whole length of the sample is reported as the sample directional permeability considering the fact that flow capacity is mainly controlled by the tightest openings and bottlenecks. By comparing the three predicted absolute permeabilities with the experimental values it can be concluded that DeePore is predicting the permeability in a good agreement with the direct numerical simulation methods which are considerably more computationally expensive. The average relative error of tested methods compared to the experiment are 13 %, 25 %, and 24%, respectively for DeePore, PFVS, and LBM. Although there could be some sources of uncertainty (such as images' improper segmentation, or experimental and imaging errors), the general conclusion is that based on the tested realistic tomography images, DeePore absolute permeabilities are in good agreement with experimental measurements.

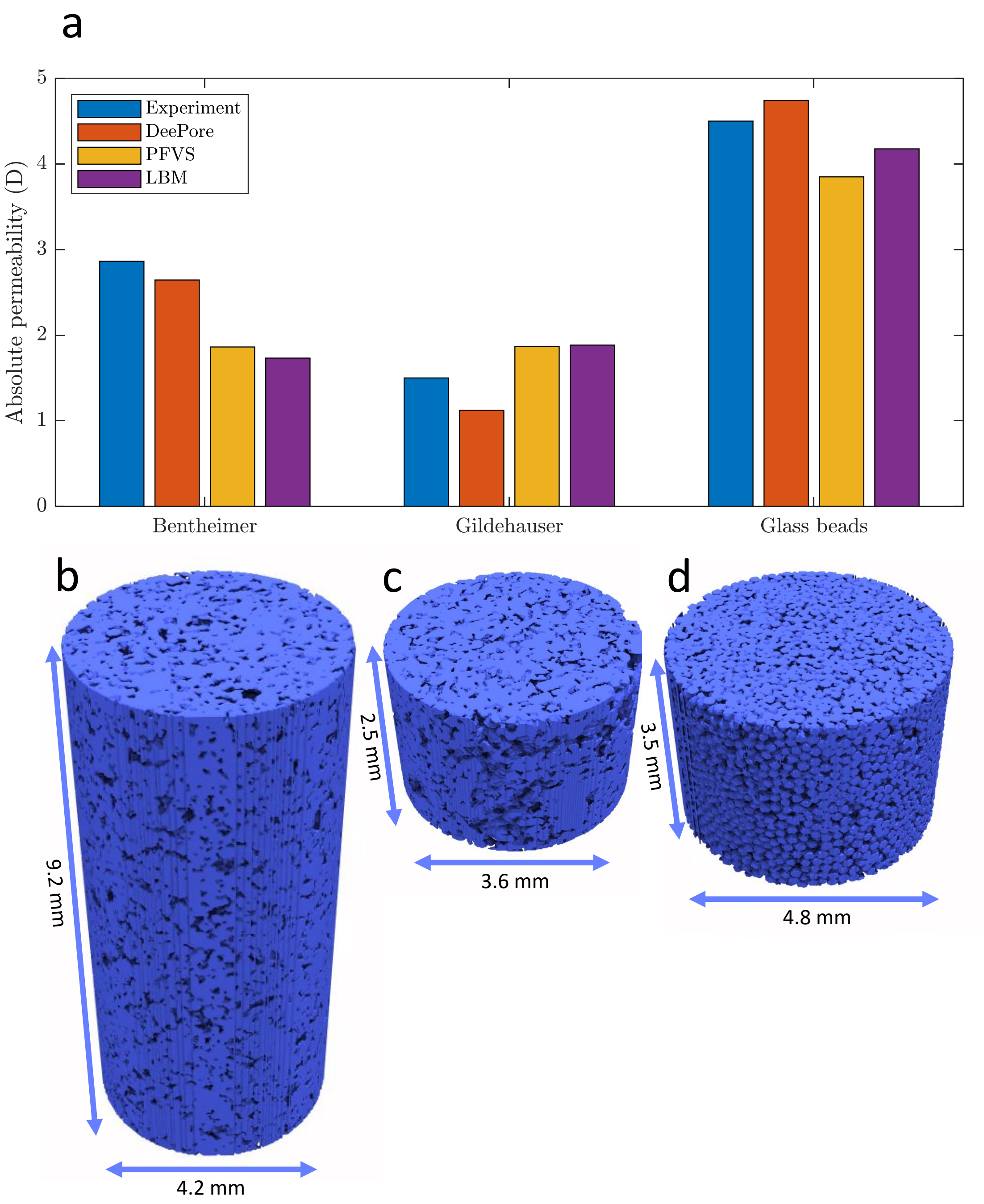

Figure 4.12: Experimental verification of the proposed model by comparing absolute permeabilities with experimental values as well as direct numerical simulation, (a) Absolute permeabilities of Bentheimer sandstone, Glidehauser sandstone, and glass beads obtained from 4 different sources: experiment, DeePore, PFVS, and LBM. (b) Segmented image of the tested Bentheimer sandstone with resolution of 7 $\mu m/voxel$. (c) Segmented image of the tested Glidehauser sandstone with resolution of 4.4 $\mu m/voxel$. (d) Segmented image of the tested glass beads with resolution of 6.5 $\mu m/voxel$.

4.5 Conclusions and Future Studies

In order to deliver the present DeePore package, we have generated a dataset of semi–real 3–D images of porous structures with 17700 samples and 30 features which are physical characteristics of porous material. Using a regression CNN coupled with two dense layers, a fast and comprehensive characterization of 3–D porous material images is implemented. In summary, the following conclusions can be drawn based on the findings of this research:

- A physically diverse dataset of micro–porous structures are generated based on texture transformation and porosity manipulation of 60 original tomography images and a wide range of morphological, hydraulic, electrical and mechanical features are extracted for each sample. The dataset is publicly available and can be used for future studies.
- A dimensionless approach has been presented to extract or predict the porous material features without being affected by the spatial resolution of the images.
- A statistically accurate feature estimation is implemented using a designed feed–forward CNN by training the model for 100 epochs while over–fitting is avoided.
- A cross–correlation heat map of the 15 porous material features are presented that gives a concise but broad insight into the significance of relationships between each pair of the extracted features.
- The average coefficient of determination (R^2) for all 30 extracted features is 0.885 which is significant considering the diverse range of porous morphologies and features.
- Via a GPU–based architecture we are able to predict the above–mentioned features for each 256^3 voxels binary image of porous material in 0.379 ms on average. This high speed of prediction enables us to tackle larger image sizes in future studies.
- To provide an independent model verification, three images outside of the datasets are generated with textures almost unseen in the augmented dataset. The model predictions were almost as good as the testing dataset used to check the model performance in terms of r–squared. This observation indicates that the dataset is diversified enough to avoid false accuracy due to the similarity of the training and test results. Also, considering the novel texture of the verification samples, one can conclude that the model is implicitly learning the physics of the estimated features rather than blindly memorizing the textures.

- In order to provide experimental verification for the proposed method, absolute permeabilities of 3 realistic porous samples have been compared with the measured values in the laboratory and DeePore predictions had around 13% relative error with is reasonable comparing to the accuracy of the direct numerical simulation methods such as PFVS and LBM.

It is noteworthy that each of the physical simulation methods are subject to uncertainty due to some inherent simplification assumptions in pore network modeling. Consequently, it is recommended to use more accurate simulation methods such as direct numerical models to generate the ground truth dataset based on the current set of 3–D images in the future studies.

Acknowledgement

The authors thank the University of Manchester for the President's Doctoral Scholarship Award 2018 awarded to Arash Rabbani to carry out this research. Also, special thanks to Prof. Vahid Niasar for sharing the glass beads image that has been used in the present study.

Chapter 5

Image-based modeling of carbon storage in fractured organic–rich shale with deep learning acceleration

5.1 Abstract

In this study, we present three methods of predicting CO_2 adsorption upon displacing CH_4 in dehydrated fractured shale samples. These methods include a dynamic numerical approach, a steady state numerical approach, and a machine learning (ML)–based approach. We develop a coupled formulation for including the effects of gas competitive adsorption, decompression, Knudsen diffusion, slippage, advection, and Fickian diffusion for multicomponent single-phase CO_2-CH_4 systems. Several stochastic micro–structures of fractured shale samples are generated and processed for pore network extraction. Extracted pore networks contain microporosities as well as mesopores and fractures. Next, we show that the dynamic numerical approach can be substituted with steady state model which is only 2.3% less accurate but 3 to 4 orders of magnitude computationally faster to execute. In order to enhance the computational limits even further, we train a deep learning model on 3982 simulated steady state cases with r–squared greater than 0.93. In addition, we define a storage quality criterion for recognizing suitable shale samples for CO_2 sequestration which depends both on the rate and amount of adsorption. Using this criterion and the developed ML tool, a large number of shale pore–scale images can be ranked based on their suitability in an efficient and accurate manner. The proposed workflow is useful for selection of the proper geological locations for subsurface CO_2 storage by analysing the available image datasets.

5.2 Introduction

Considering, for example the net–zero emission pledge of the UK by 2050 [315, 316], subsurface carbon capture and storage (CCS) is considered more widely to mitigate carbon emissions in upcoming years. There is a great potential of carbon storage in subsurface formations with organic or mineral micro-structures that can adsorb CO_2 molecules in a stable manner. Due to the tight nature and high surface area of some clay–based and organic–rich subsurface deposits, CO_2 molecules can be trapped in micro-structural cages or dissolve in the inter-particle residing water due to its low minimum miscibility pressure [317, 318, 319]. Although, the CCS strategy seems to be an ideal solution to get rid of the excess carbon, there are still practical issues that need to be addressed by researchers. One major issue is the uncertainty and randomness of the subsurface porous structures that make it difficult to find the proper locations for CCS purposes [320]. While running thousands of experiments does not seem a viable solution to screen the appropriate storage spots, machine learning (ML) can be used to deal with the complexity and repetitiveness of this screening process.

Deep machine learning has already proven its enormous capability in medical diagnostics [321] and it can be adopted in an interdisciplinary manner to make predictions regarding the CO_2 adsorption capacity of different micro-structured porous materials.

Data–driven methods such as deep learning heavily rely on diversified and accurate datasets to be trained on. However, due to the limited available experimental data on shale deposits, numerically simulated data can be used as an alternative. A pore network model (PNM) is a simplified version of porous micro-structures designed to speed up the numerical simulations while maintaining a reasonable level of physical accuracy [322]. Consequently, PNMs have been widely employed by researchers to solve coupled physical problems in a wide range of length scales of shaly subsurface deposits [323, 147]. Many different physics have been simulated in shale PNMs during the past decade from Knudsen and surface diffusion to inclusion of mechanical deformation and geo–chemistry [324]. Javadpour *et al.* [324] reported a significant increase in the number of shale PNM papers in the past few years as well as different physics included in the developed PNMs.

The main gas transport mechanisms in shale PNMs is believed to be Knudsen diffusion and gas slippage [148, 325], while some researchers have reported evidences in significance of surface diffusion [326, 327]. Knudsen diffusion and gas slippage have been coupled to give a unified formulation of gas transport in two main schemes of dusty gas models [328] and Knudsen number based models [329, 146]. Knudsen number based models, merge the two mechanisms by assuming weighting coefficients related to the surface roughness and have been more frequently used in the literature [330]. Although, gas flow mechanisms of shale have been significantly discussed by researchers, physical morphology and complexity of the shale PNMs have not been equally attended [324]. In the present study, in order to address this gap we have presented a novel arrangement of the micro and meso pores combined with fractures which has been a shale–tailored version of the triple pore network model (T-PNM) presented by Rabbani *et al.* [218]. As a recent and comprehensive example of dynamic simulation of CO_2 adsorption to CH_4–saturated shale pore networks, the work by Zhang *et al.* [331] is significantly aligned with the PNM methodology of the present study. The authors have included a wide range of physics from changes in pore volume and shape factor to competitive adsorption in a two–component system [331]. Despite of similarities in flow transport and adsorption mechanisms with Zhang *et al.* [331], the PNM section of this chapter is distinguishable due to the more realistic pore network generation and coupling of diversified structural elements of shale samples like clay, kerogen, meso pores and fractures.

Although adding several physics to a geometrically complex and heterogeneous PNM model improves the accuracy, it will significantly expand the computational expense of the model [198, 136]. Deep machine learning has been frequently used by researchers to emulate the results of numerical simulations in porous media and cut the computational costs [251, 252, 256]. As an example Wei *et al.*[253] have used a convolutional neural network (CNN) to estimate the effective thermal conductivity of composite porous materials and reached the coefficient of determination of 0.98 for 100 test samples. Also, porosity and permeability of the porous micro–structures have been popular subjects of CNN prediction [254, 255, 256, 257, 31]. As an example, Alqahtani *et al.*[21] designed a CNN model to estimate features like porosity, specific surface, and average pore size of the porous sandstones based on 2–D binary and gray–scale images. As a more recent attempt, Kamrava *et al.* [251] have studied the link between the morphology of the porous materials and numerically simulated absolute permeability. They have employed a cross–correlation–based method to increase the number of images in a sandstone dataset in addition to adding hundreds of synthetic granular porous structures. As a closely related paper to the ML section of the present study, Rabbani *et al.* [31] presented a comprehensive deep learning model to predict 30 different physical functions and features of the porous materials from network morphology, permeability and conductivity to mechanical elasticity. The main distinguishable feature of the ML section of the present study compared to Rabbani *et al.* [31] is the prediction of gas permeability and adsorption capacity as well as accounting for presence of several mineralogies like clay and kerogen.

5.3 Methodology

In the present study, we aim to make an efficient image–based model which is able to quantify the quality of the fractured organic–rich shale samples for subsurface storage of CO_2. A brief workflow of the model development is presented in Figure 5.1. The process, starts with a set of random numbers as input and continues by generating diversified stochastic shale realizations based on those numbers. Afterwards, using image segmentation and pore network extraction techniques, a multiple porosity network model is prepared. Then using dynamic as well as steady–state simulations of gas adsorption, we can find the ultimate capacity of the generated shale samples for CO_2 storage. Considering the fact that both of these methods are computationally intensive, we have proposed a deep learning approach to mimic the steady–state storage capacity of the shale samples. After generating a large dataset of stochastic images and pore network simulations, we have prepared the required information for training a deep learning model which takes the shale image as input. Finally, after testing the trained model to avoid the over–fitting issues, we have an ML tool which is able to evaluate and rank different shale images based on their quality for underground storage of gaseous CO_2.

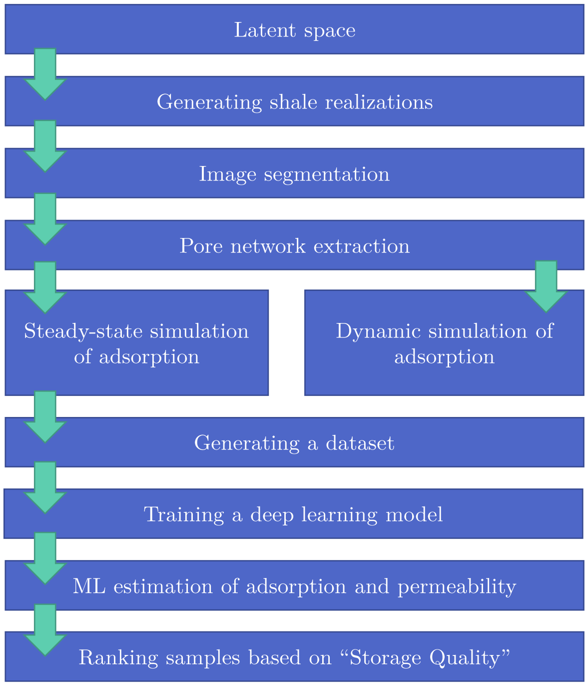

Figure 5.1: Summarized workflow of the present study from input latent space of random numbers to prepare an ML tool for ranking different shale samples based on their quality for CO_2 storage.

5.3.1 Generation of images

3–D imaging of the fractured organic–rich shale samples is challenging due to the mechanical stability issues and technical difficulties in preparing such small size specimens. As an alternative, we have designed a statistical approach to generate stochastic realizations of the shale samples based on a set of random numbers as input which is also called latent space as a data science jargon. Generation of the 3-D shale samples is composed of 5 steps respectively to build pyrite framboids, calcite/silicate, clay, kerogen, and fractures which are principal components of many realistic shale samples. Figure 5.2 illustrates the discussed steps each of which with four sub-steps. In step #1, we have used thresholded distance map of some random points and packed the obtained space with spheres of sizes around 0.2 to 0.7 micron.

The obtained map is assumed to mimic pyrite framboids in the sample. In step #2, we have applied watershed segmentation on thresholded distance map of a binary salt and paper noise to emulate the solid grains of calcite and silicate. Then in step #3, we extract the contour lines of the distance map of the remaining parts of the image after subtracting pyrite and other solid grains. By running a motion blur, thresholding, dilation, and adding spatial noise, a visually similar flake–like texture is achieved which mimics the clay-rich sections of shale samples. In step #4, we fill the remaining space with kerogen while subtracting two randomly generated sets of large and small organic pores. Finally, in step #5, in order to generate a visually reasonable fracture within the sample, we have used watershed segmented map of granular space to cut the geometry from the weaker connections and at the interfaces of different structural elements. More elaborations regarding the fracturing method are provided in [332]. A 2–D slice of the generated fractured shale sample is illustrated in Figure 5.2–g which is visually comparable with the real SEM image in Figure 5.2–f that shows, pyrite framboids, clay flakes, calcite/silicate grains, kerogen, and a fracture at the middle of the sample. The real SEM image shows a cretaceous shale sample from Alberta, Canada, which is available online [333] [1].

---

[1] The courtesy of Fibics Incorporated.

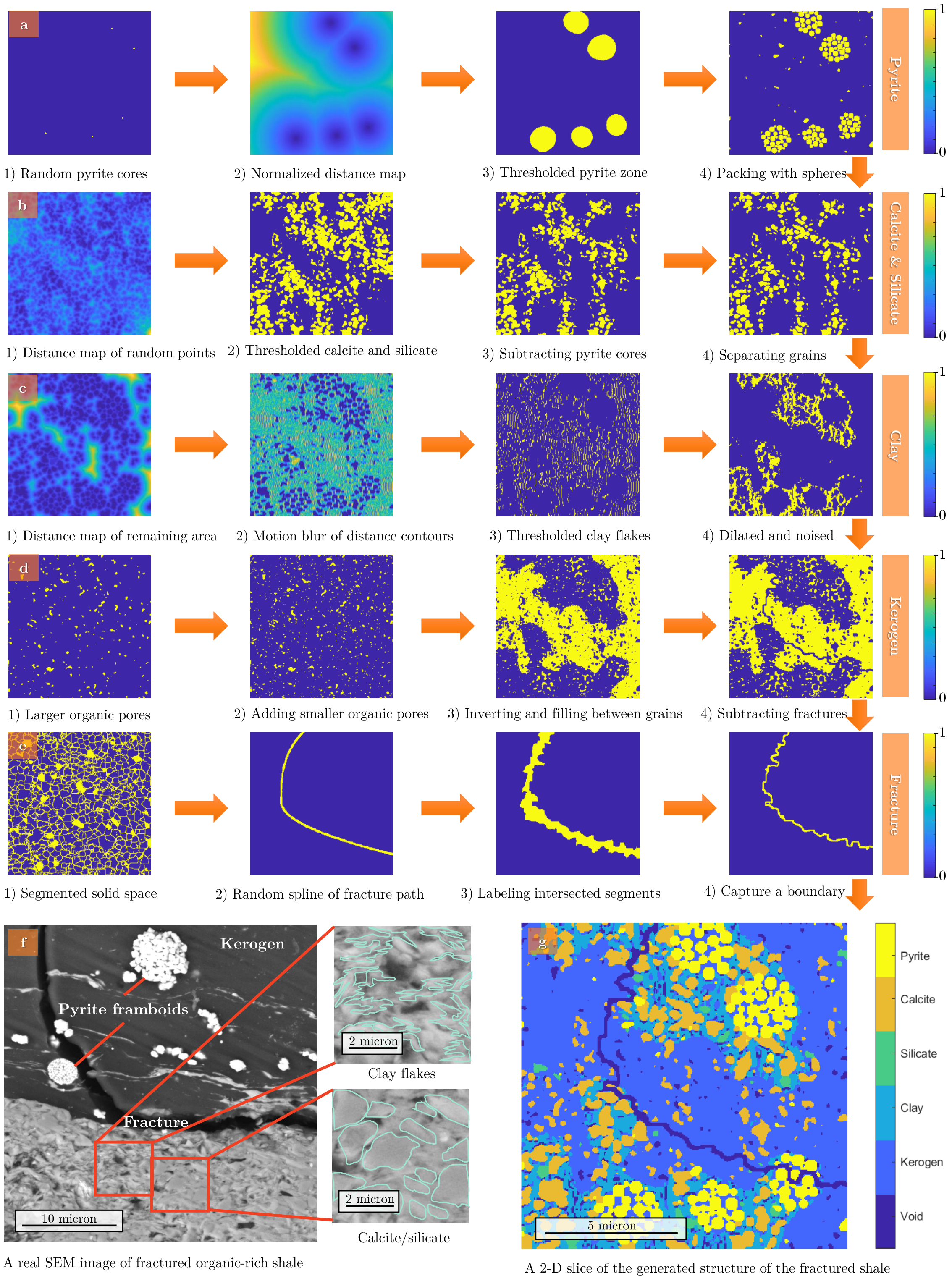

Figure 5.2: Shale sample generation process with 5 main steps and visual comparison of a real SEM image of shale [333] with a stochastically generated image.

5.3.2 Pore Network Modeling

Classic pore network modeling approach is often used for making a simplified mathematical model of porous material with one level of porosity, while in many of the real world cases, multiple scales of porosity are present within the materials. Organic–rich shale deposits are among the well–known examples with the above-mentioned properties. In order to make a simplified mathematical representation of shale samples in this study, we have used triple pore network modeling (T–PNM) introduced by [218] which couples mesopores, micropores, and fractures in a fluid flow simulation problem. As a modification to T–PNM, we have assumed two types of microporosities for kerogen and clay with different pore size distribution (Figure 5.5–c) and adsorption behaviour (Table 5.1). Additionally, we have included solid minerals including pyrite, calcite and silicate that do not contribute to the transport properties in the gas flow system of this study. Figure 5.3 illustrates the pore network structure considered for simulation of gas transport and adsorption. As described by Rabbani *et al.* [218] the absolute permeability (K_p) of meso–throats and fracture links can be estimated using a unified quadratic formula depending on the average distance value of the channels cross-sectional image ($\bar{D}$):

$$K_p = 1.342\bar{D}^2 - 0.913\bar{D} - 0.381 \tag{5.1}$$

where K_p is the absolute permeability of the links with $pixel^2$ unit, and $\bar{D}$ denotes the average distance value with the unit of *pixel*. In addition, the authors calculated the gas permeability of micro-throats as bundle of microtubes with the radius of r_m connected to an arbitrary micropore at the center of semi–porous nodes including clay and kerogen. Gas permeability K_g of these three types of links in the network can be calculated as follows [218]:

$$K_g = \begin{cases} K_n(r) + F(r).K_p(\bar{D}).R_s^2 & \text{meso-throat and frac-link} \\ \int f(r_m).K_n(r_m) + \frac{1}{8} f(r_m).F(r_m).\alpha\phi_m r_m^2 \, dr_m & \text{micro–throat} \end{cases} \tag{5.2}$$

where, r is the equivalent radius of meso–throats and fracture links cross-section, R_s is the spatial resolution of the simulated image in $m/voxel$. ϕ_m is the microporosity of the clay and kerogen nodes. Also, r_m is the radius of the micro–tubes with the size distribution of $f(r_m)$. Here, $f(r_m)$ calculates the void fraction of the microporous nodes occupied by microtubes with the radius equal to r_m. Parameter α is a porosity correction factor which takes values from 0 to 1 and excludes the fraction of the node microporosity which belongs to the isolated pores. The term $K_n(r)$ calculates the link permeability enhancement due to the Knudsen diffusion as a function of gas properties and channel radius (r) and its value is always greater than 1 (refer to [218] for details). Also, the gas slippage term ($F(r)$) for different types of links can be calculated as: [146, 148, 147, 334]:

$$F(r) = 1 + \frac{c}{r}\frac{\mu}{\bar{P}}\sqrt{\frac{8Zk_bT\pi}{M}} \tag{5.3}$$

where, $\bar{P}$ is gas average pressure, Z is real gas compressibility, μ is gas viscosity obtained using an empirical correlation developed by Lee *et al.* [335], r can be replaced by r_m in the case of micro–throats, c is the collision proportionality factor which is commonly set equal to 1.0. It should be noted that the gases are not in the supercritical conditions for the pressure and temperature that are assumed (Table 5.1).

The pore network system we aim to simulate in this study, is a shale specimen initially fully saturated with methane to represent a small element of a dry gas shale reservoir. This assumption may not be fully representative of actual shale gas systems because at most field sites, a large portion of the fracking fluid imbibes into the shale matrix during the fracking process, and thus two-phase flow occurs [217]. Therefore, the model presented here is useful for areas away from two-phase fracking regions of the reservoir. At the beginning of the dynamic simulation of gas adsorption, the bottom face of the shale sample opens to a higher pressure of the CO_2 gas compared to the average pressure of the system and CO_2 starts to penetrate through the network via advection and Fickian diffusion. In order to simulate the advection, we use Eq. 5.2, and for diffusion, Fick's law is used. At the same time, many surface sites in the microporous regions that have been initially occupied by CH_4 will be captured by CO_2 which has experimentally proved to be more adhesive to the microporous portion of shale samples [336, 337, 338, 339, 340]. The competitive adsorption has been described by a two-component Langmuir model [341] with detailed derivation by Zhang *et al.* [331]. The boundary conditions assumed in our pore network modelling is no–flow at the sides and constant pressure at the top of the domain, with the value equal to the initial average pressure. This assumption creates an upward gas flow through the system. The CO_2 concentration of the injected gas is at 100 %. Gradually, over time, a uniform pressure gradient forms between the inlet and outlet of the system and simultaneously CO_2 pushes out the residing CH_4 until the equilibrium is reached. In order to model this dynamic process we start by writing the volume balance of the system with the assumption that the pore volume of each node i remains constant:

$$\Delta V_{ads,i} + \Delta V_{adv,i} + \Delta V_{dif,i} + \Delta V_{cmp,i} = 0 \tag{5.4}$$

Where $\Delta V_{ads,i}$ is the free gas volume change in node i due to adsorption/desorption, $\Delta V_{adv,i}$ is the free gas volume change due to advection which is basically the fluid flow from other pores, $\Delta V_{dif,i}$ is the volume change due to the Fickian diffusion, and $\Delta V_{cmp,i}$ is the free gas volume change due to the compression. Each of these terms can be expressed as a function of system's pressure for each node (P_i) and methane gas saturation (S_i) as follows:

$$\Delta V_{ads,i} = S_{p,i} M_g C (P_i^n - P_i^{n-1})/\rho \tag{5.5}$$

$$\Delta V_{adv,i} = \sum_{j=1}^{N} \left(K_g A_{t,ij} (P_i^{n-1} - P_j^{n-1})/L_{t,ij}\mu \right) \Delta t \tag{5.6}$$

$$\Delta V_{dif,i} = \sum_{j=1}^{N} \left(K_f A_{t,ij} (S_i^{n-1} - S_j^{n-1})/L_{t,ij} \right) \Delta t \tag{5.7}$$

$$\Delta V_{cmp,i} = V_{p,i} (P_i^n - P_i^{n-1})/P_i^{n-1} \tag{5.8}$$

where, in Eq. 5.5, $S_{p,i}$ is the internal surface area of the node, M_g is the mass surface density of the adsorbed gas (kg/m^2), C is a linearization coefficient dependant of Langmuir adsorption coefficient and the range of pressure variation [217], μ is gas viscosity, and ρ is the free gas density. In Eq. 5.6, $A_{t,ij}$ is the interface area between the node i and the adjacent node j, $L_{t,ij}$ is the length between the centers of node i and j, N is the number of the connected nodes to the central node of i, and Δt is the time step of simulation. In Eq. 5.7, K_f is the Fickian coefficient of diffusion for a system of two gases, and S_i is the volumetric proportion of CH$_4$ to the total volume of the free gas present in the node i. Finally, in Eq. 5.8, $V_{p,i}$ is the pore volume of the node that we are writing the material balance for it. By replacing Eq. 5.5 and Eq. 5.8 in Eq. 5.4, we can write the pressure of the time step n explicitly as a function of pressure and the saturation of the previous time step ($n - 1$) as follows:

$$P_i^n = P_i^{n-1} - \frac{\Delta V_{adv,i} + \Delta V_{dif,i}}{S_{p,i} M_g C/\rho + V_{p,i}/P_i^{n-1}} \tag{5.9}$$

This equation needs to be written for both of the gaseous components for which the pressure is interpreted as partial pressure. Additionally, variables such as ρ, C, M_g, and K_p need to be used for the specific components, accordingly. When writing Eq. 5.9 for both of the components, it is noteworthy that the summation of both gas saturations becomes 1. Assigned values for some of the parameters and constants used in this study are presented in Table 5.1.

In order to solve Eq. 5.9 in a dynamic manner, we start from the initial condition of the system and calculate the partial pressures of the second time step. Then saturations of the system will be updated based on the ratio of the partial pressures to the total pressure. In order to select an appropriate time step for simulation, we start with a relatively large time step e.g., 0.01 s, and then check for possible non–physical values such as saturations larger than 1 and pressures outside of the simulation range. In case of observing these abnormalities which are violations of the mass balance in the system, we split the time step to half and recalculate the same time step again. When the time step becomes small enough, the simulation continues. Most of the converging time steps in our simulations were around 10^{-8}s. Additionally, it is expected to reach an equilibrium in the system after few millions of time steps. Considering the high computational burden of the dynamic simulations and many time steps required to achieve an equilibrium, steady state simulation can be valuable, too. Steady state simulation is capable of estimating ultimate CO_2 storage capacity at the equilibrium. In other words, a steady state simulation may show a high storage capacity whereas, in practice, due to low permeability of the sample, injection of CO_2 will become so slow that the operation is impractical. Thus, in addition to the CO_2 storage capacity, gas permeability of the samples should be taken into the account as a measure of the adsorption rate in case we want to use steady state simulations instead of dynamic. In this regards we define a storage quality (Q_s) factor which is equivalent to the multiplication of the storage capacity C_s and total gas permeability (K_t):

$$Q_s = K_t C_s \tag{5.10}$$

Storage capacity (C_s) represents the standard volume of the gas content (m^3) divided by the mass of the shale sample (tonne), and K_t is total gas permeability (Darcy).

In order to solve the problem in the steady state condition, we need to assume that the adsorption and compression volumes are constant at the equilibrium condition and by assuming the full saturation of CH_4 at that point, pressure distribution of the pore network is obtainable by solving the following volume balance equation for all of the nodes at the same time in a system of equations:

$$\Delta V_{adv,i} + \Delta V_{dif,i} = 0 \tag{5.11}$$

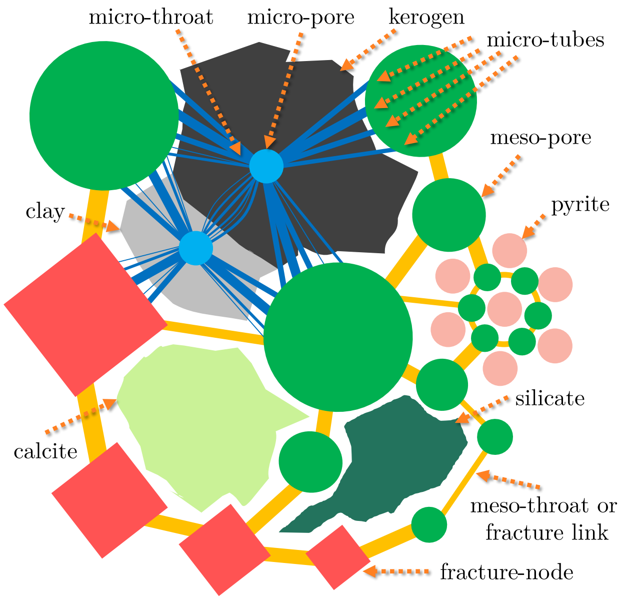

Figure 5.3: Proposed pore network structure for simulation of gas transport within organic-rich shale deposits, including two types of micro porosities (clay and kerogen), meso–pores and fractures entangled with solid minerals such as pyrite, calcite, and silicate.

Parameter	Value
Kerogen density (g/cm^3)	1.21 [342]
Clay density (g/cm^3)	1.75 [343]
Silicate density (g/cm^3)	2.650 [344]
Calcite density (g/cm^3)	2.710 [345]
Pyrite density (g/cm^3)	5.020 [342]
Mass surface density of the adsorbed CH_4 on kerogen (kg/m^2)	2×10^{-7} [217]
Mass surface density of the adsorbed CH_4 on clay (kg/m^2)	1×10^{-7} [346]
Mass surface density of the adsorbed CO_2 on kerogen (kg/m^2)	5.5×10^{-7}
Mass surface density of the adsorbed CO_2 on clay (kg/m^2)	2.75×10^{-7}
Fickian diffusion coefficient of CO_2–CH_4 (m^2/s)	1.5×10^{-8}
Langmuir linearization coefficient	5.18×10^{-10} [217]
Temperature (K)	500
Input pressure (Pa)	$(7 \times 10^6) + 10^4$
Outlet pressure (Pa)	7×10^6
Spatial resolution (μm/voxel)	0.05

Table 5.1: Parameters and constants used in the pore network modeling of the present study and their values.

5.3.3 Machine learning

In order to achieve a higher level of computational efficiency, machine learning can also be used to estimate the steady state results. Although, steady state simulations are fast, they still require traditional image analysis, pore network extraction and solving systems of equations. A sufficiently complex machine learning model can be trained to emulate the whole computational workflow of steady state simulations and estimate the storage capacity and total permeability of the shale samples, by just taking at the images and preliminary physical properties as inputs.

For this purpose we have built a dataset of 4978 stochastic shale 3–D images with the size of $256 \times 256 \times 32$ voxels and steady state simulation of the ultimate gas storage capacity is performed for each of them. In addition to the mineralogy maps, we have assumed a porosity map for the microporous regions of the images by applying a Gaussian smoothing on a random map of uniformly distributed numbers between 0.01 to 0.1. Considering the importance of the microporosities for adsorption capacity, we have stacked the middle 2–D slice of the porosity map into the middle slice of the mineralogy map to both be used as the inputs of the deep learning model (Figure 5.4). Then, four levels of convolutions are performed on the input vector with the filter numbers of 6, 12, 18 and 24, respectively. Also, size of the filters are 8^2, 4^2, 2^2, and 2^2, respectively, and with same–size padding and He Normal [347] kernel initialization. Every convolution is followed by a 2×2 max pooling filter with unit stride and 10% dropout to help avoiding the over–fitting problem. After the 4_{th} dropout, the data vector is flattened into a dense layer of 6144 elements and activated with Rectified Linear Unit (ReLU) [348]. The second dense layer consists of 20 nodes and it is activated using sigmoid function to address the non–linearities. The output layer of the model includes two normalized numbers representing ultimate gas storage capacity and permeability of the shale sample. Suggested optimizer for training the network is RMSprop [310] with learning rate of 10^{-4} and mean squared error as the loss function.

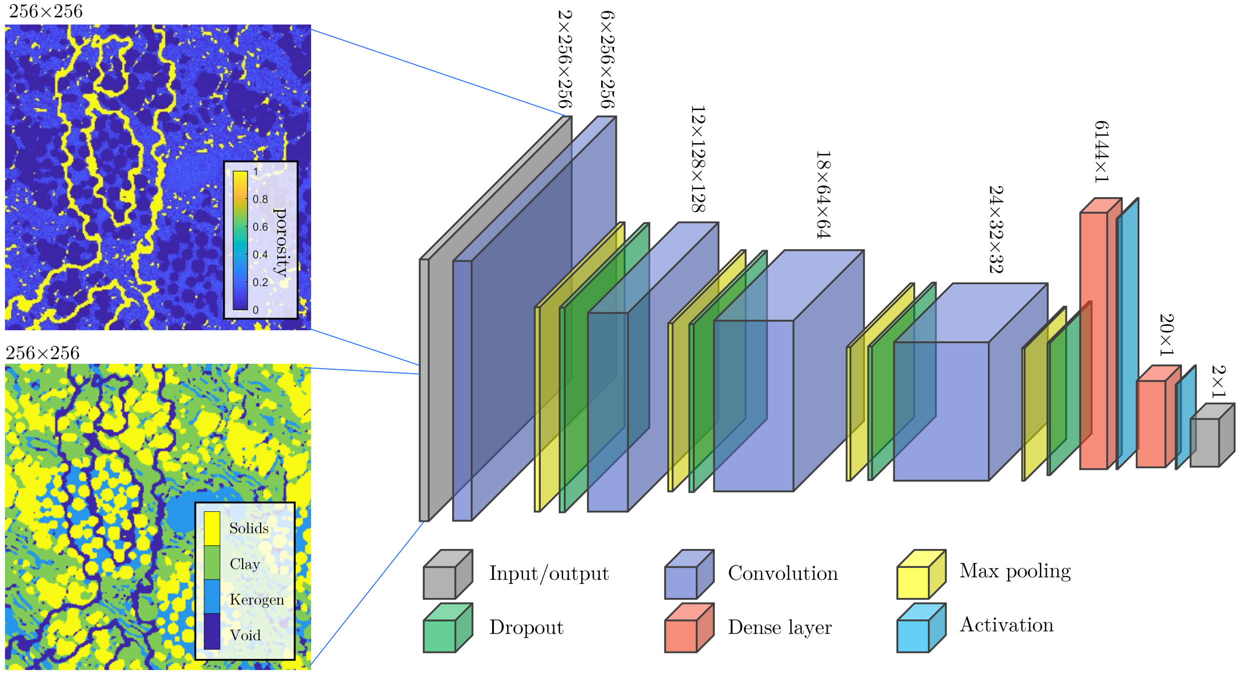

Figure 5.4: Proposed deep learning model structure for estimating the ultimate gas storage capacity, permeability based on the mineralogy, and porosity maps of shale samples.

5.4 Results and Discussions

In this section we present results of the dynamic and steady state simulations of CO_2 adsorption into fully saturated shale samples with CH_4. Then using the results, some of the structural properties of shale will be examined to evaluate their effects on the storage quality of the samples. Finally, the results of the machine learning approach will be presented and the accuracy of the presented methodology is discussed.

5.4.1 Pore network modeling

During the dynamic simulation of the adsorption, gradually CO_2 molecules occupy the surface sites and release the previously adsorbed CH_4 molecules. Figure 5.5–a and b illustrates the changes in the gas content of shale sample during the mentioned process. In the simulated sample, kerogen can contain more than 6 times gas compared to the void space which indicates the suitability of the organic–rich shales for carbon sequestration. As it can be seen, the dynamic amount of gas contents in Figure 5.5–a is converging to the steady state value although a small gap is visible for some of the mineralogies. Considering the fact that in our case the steady state modeling runs around 10^3 to 10^4 times faster than the dynamic simulation, it is valuable to compensate the gap error. For this purpose, we have simulated 50 shale samples with both approaches and plotted the obtained ultimate adsorptions vs. each other in Figure 5.5–d. The mean relative error of the data points from the unit slope line is 12.5% while by fitting a straight line on the data points the amount of error between the dynamic and steady state results reduces to 2.3% which is promising considering the huge difference made in the computational expense.

However, dynamic simulation is still important for the cases we want to have a closer look on the mechanisms of gas transport and adsorption. As an example, Figure 5.6 presents the simulated pore network structure and properties for the same simulation plotted in Figure 5.5–a and b. In this figure, gas pressure distribution, CO_2 mass content, and CH_4 saturation are shown in four snapshots of the process at times of 0 μs, 20 μs, 40 μs, and 50 ms which indicates the equilibrium time. Pressure development occurs mainly after passing only few microseconds of the process due to the high permeability of the fractures, while CO_2 mass content and CH_4 saturation needs to pass 50 milliseconds to reach their final state. This observation is justifiable considering the diffusion dominant nature of the flow transport in micropores. By comparing the regions in the network with the high CO_2 content in Figure 5.6–b–4 and mineralogy map in Figure 5.7–a, it is visible that that kerogen is the main storage site of the gas. Considering the relatively high sub–resolution porosity of the kerogen in the studied sample (Figure 5.7–b) and average pore sizes of few nanometers (Figure 5.5-c), a high surface area and consequently high adsorption are expected. As discussed, the ultimate gas adsorption capacity can be obtained from both dynamic and steady state approaches, which their pressure distributions are visualized in Figures 5.7–c, and d to show the similarities between results of the two methods.

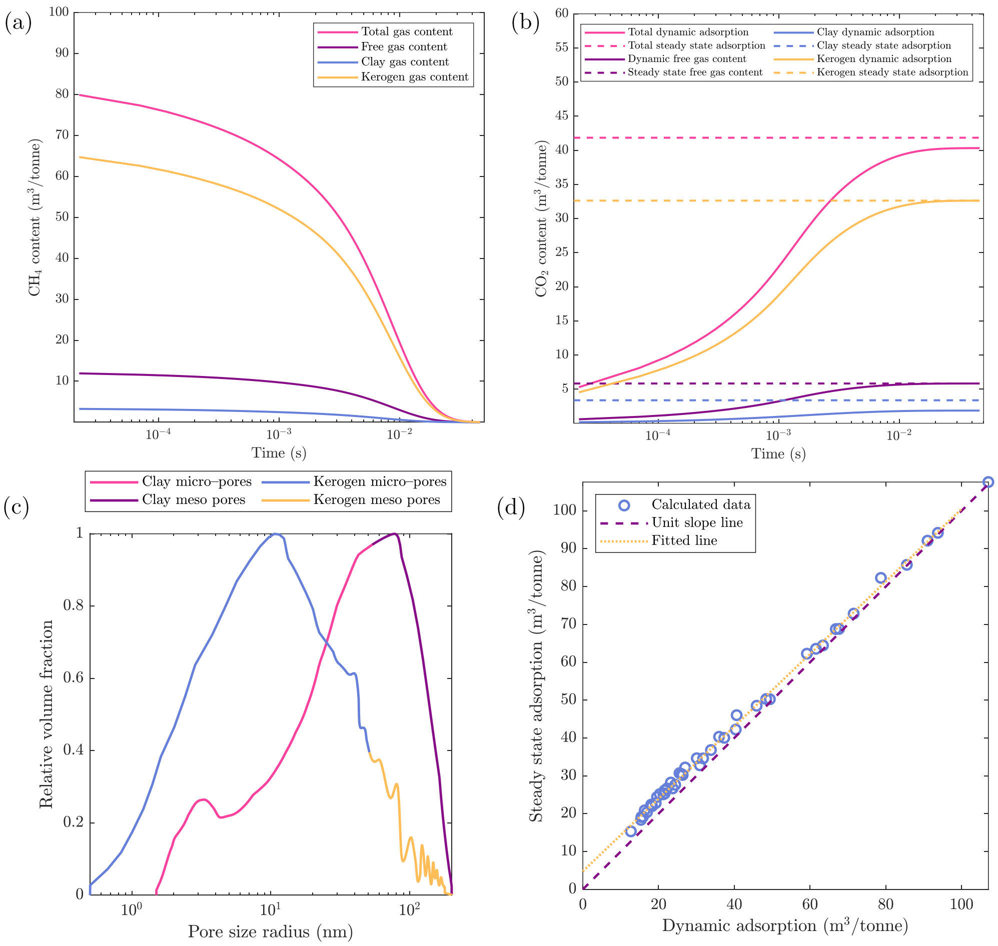

Figure 5.5: Sample results of the dynamic and steady state adsorption in terms of gas content, (a) changes in CH_4 gas content, (b) changes in CO_2 gas content, (c) pore size distribution of clay and kerogen zones of the sample adopted from [349], and (d) comparison of the ultimate adsorption capacity using dynamic and steady state simulations.

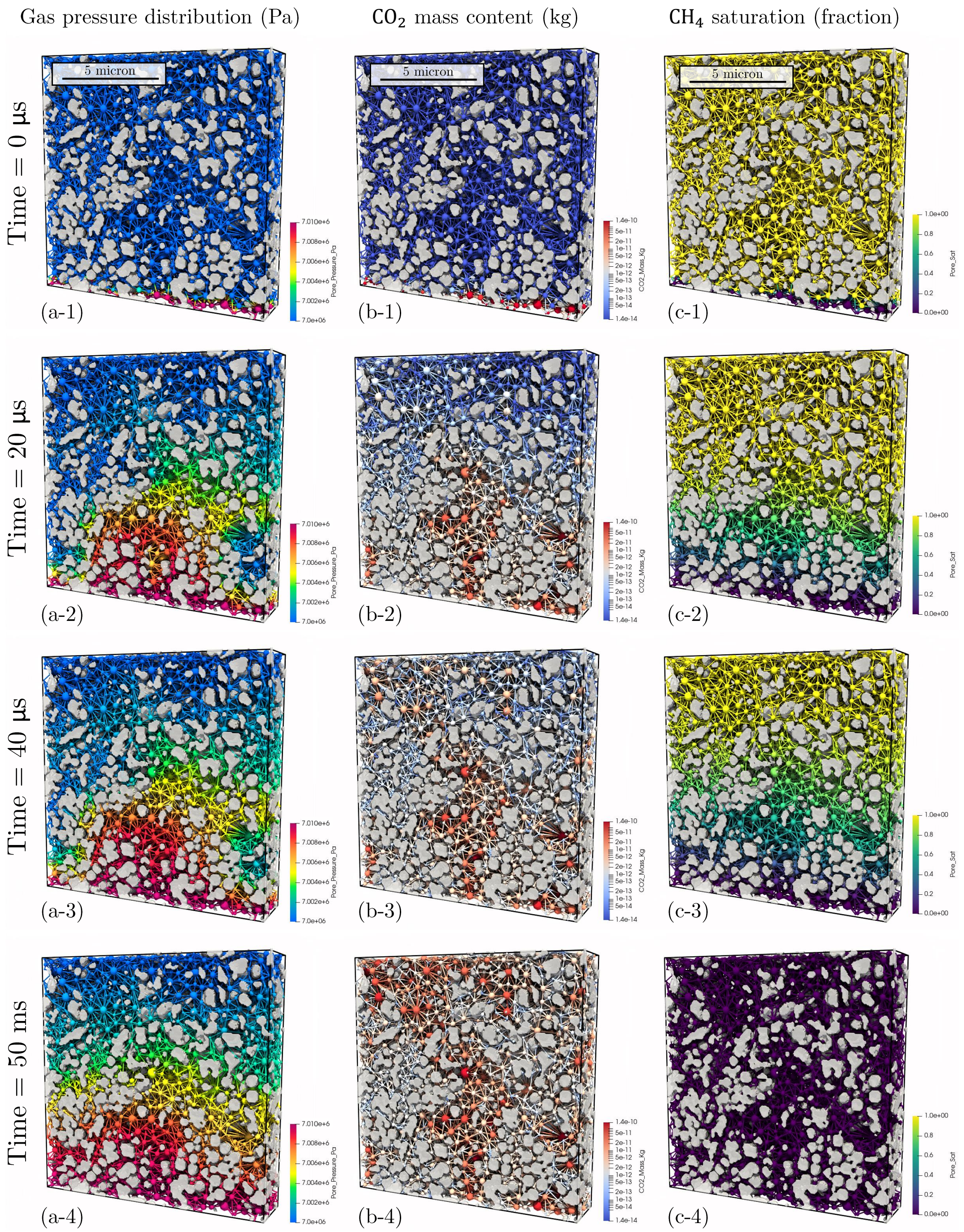

Figure 5.6: (a) Visualization of the gas pressure distribution, (b) CO_2 mass content, and (c) CH_4 saturation for four snapshots of the process at times of 0 μs, 20 μs, 40 μs, and 50 ms.

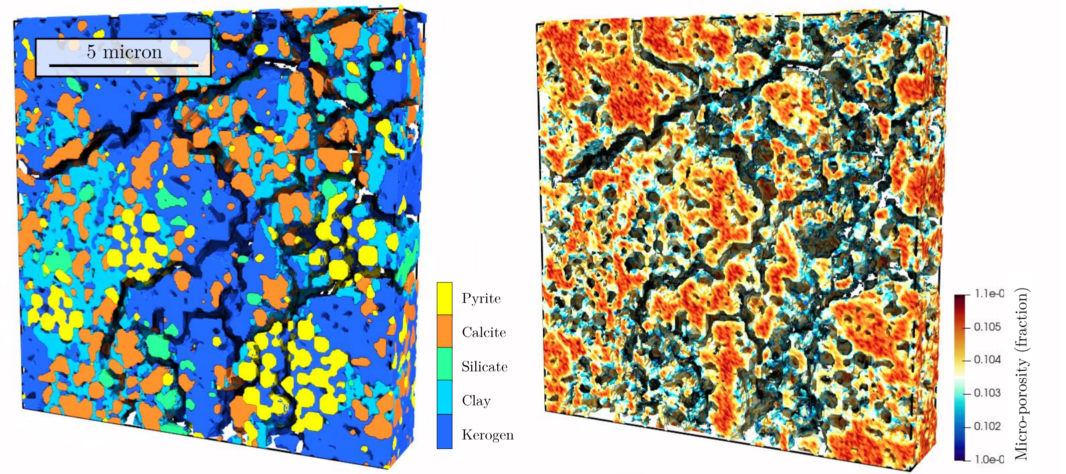

(a) Minerals map

(b) Micro-porosity map

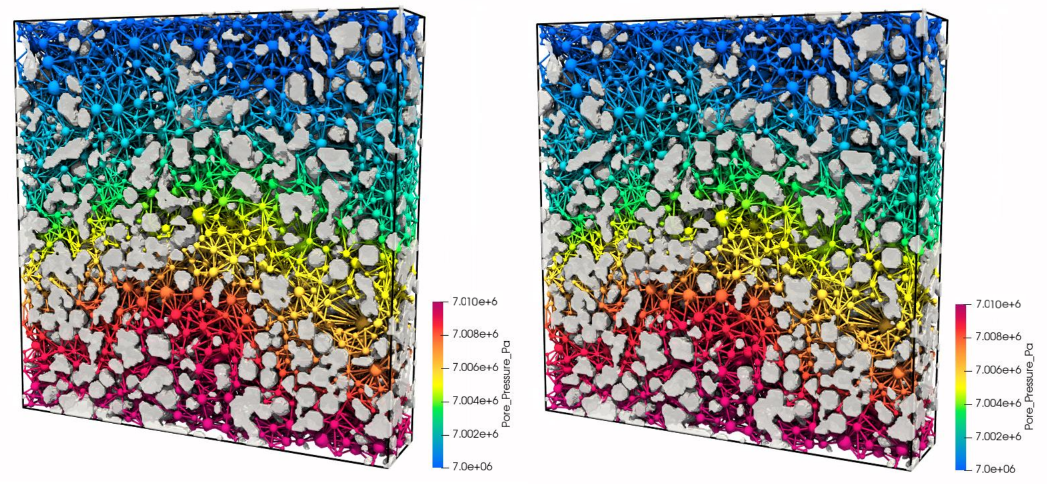

(c) Steady state pressure map

(d) Stabilized dynamic pressure map

Figure 5.7: (a) Minerals map, (b) micro–porosity map, and comparison of the pressure distribution of dynamic simulation (d) at the equilibrium and pressure distribution of the steady state simulation (c).

5.4.2 Shale micro–structural effects on storage

In this section, using the randomly generated dataset of 4978 shale samples, we investigate the interrelations between micro-structural properties of shale and its storage quality. Figure 5.8 illustrates the sensitivity analysis of some parameters like fracture density, fracture aperture, average meso pore and throat sizes, and the fraction of the sample volume occupied by meso pores as well as kerogen. Increasing the fracture density can improve the storage quality up to 6 times, although the storage quality may eventually reach its upper limit due to the fact that a high fracture density causes a reduction in the kerogen portion of the sample. On the other hand, a higher value of fracture aperture improves the absolute permeability quadratically which compensates the absence of kerogen that linearly controls the adsorption capacity (Eq. 5.10). In other words, the growth rate of permeability is greater than the shrinkage rate of the storage capacity, that eventually leads to a higher storage quality as defined in Eq. 5.10. Average size of the meso pores and throats are also presented in Figure 5.8–c. As expected, the correlation coefficient of storage quality with meso throats is greater than the meso pores. According to the definition, a throat is the geometrical bottleneck between two connected pores [108], and it is reasonable that the permeability of a channel will be more controlled by its narrowest opening. Finally, based on Figure 5.8–d it can be stated that increasing the volume fraction of samples occupied by kerogen does not necessarily improve the storage quality since abundance of storage sites without giving the proper access for gas transport such as fractures is not effective.

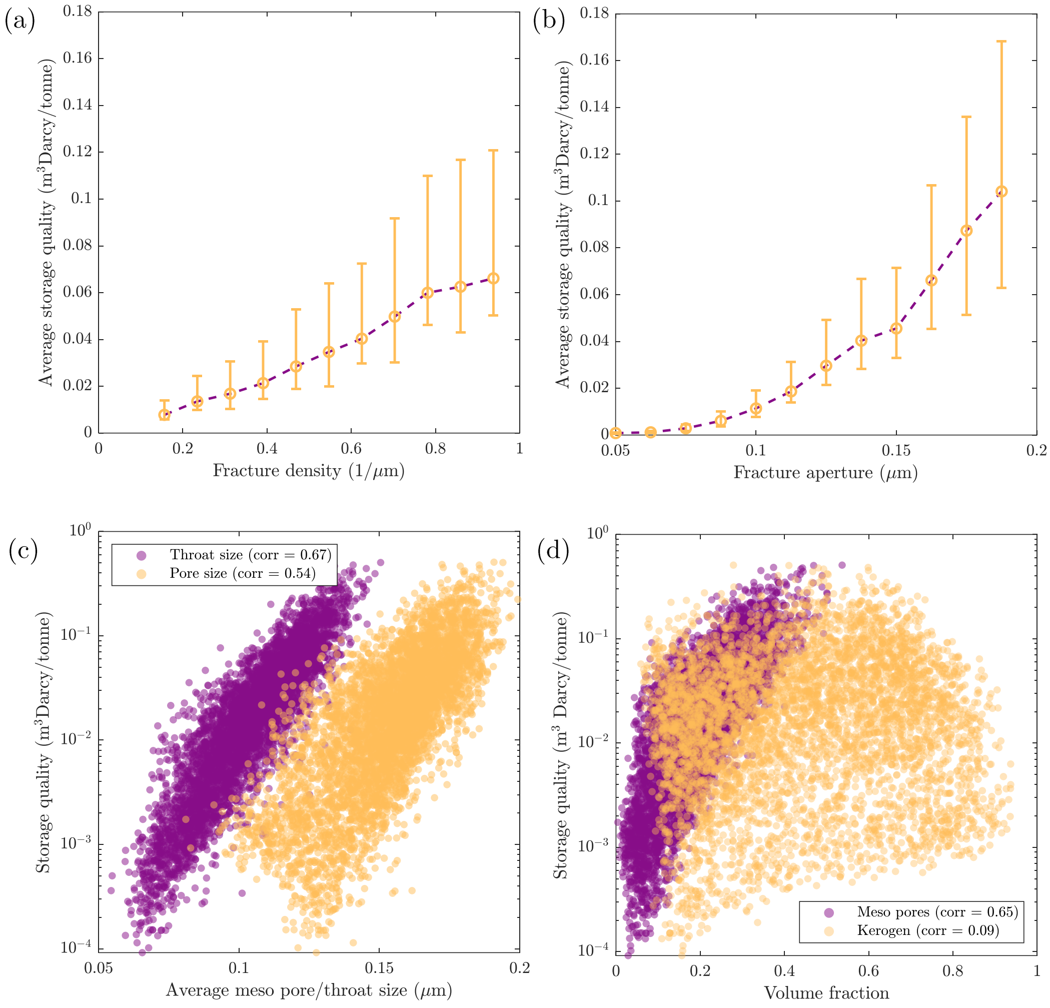

Figure 5.8: Effects of the shale micro–structural features on the storage quality (Eq. 5.10), (a) fracture density with upper and lower quartile bars, (b) fracture aperture with upper and lower quartile bars, (c) average radius of meso–pores and throats, and (d) volume fraction of kerogen and meso–pores.

5.4.3 Deep learning acceleration

We have substituted the dynamic simulation with steady state calculations to speed up the quality measurement of shale samples for carbon storage. To push the computational limits even further, we have used deep machine learning to emulate the steady state calculations and predict the storage quality in a fraction of a second. For this purpose a deep convolutional neural network model is trained on 3982 shale images with the size of 256×256×32 voxels with spatial resolution of 50 nm per voxel. Additionally, two sets of data each with 498 samples have been used for validation and testing purposes. Figure 5.9 illustrates the distribution of the data points in each of the mentioned subsets for two variables of gas adsorption and permeability. In addition, storage quality lines in the figure, segment the data points into different zones based on their suitability for CO_2 storage.

In order to ensure the fitness of the developed deep learning model, we have considered two other alternative models with slight structural changes and then we have recorded the training performance of all three cases. Figure 5.10–a presents the training and validation loss of three deep learning models in terms of mean squared error for 100 epochs. As a rule of thumb, divergence of the training and validation loss is a sign of over–fitting and means that the model is performing very well on the training data while very poorly on the validation set [350]. Consequently, model #2 has shown the best performance considering the gradual decrease of both the training and validation curves up to the epoch 100. The detailed structure of this model has been discussed in Section 5.3.3 as the approved method for ML predictions of the presented paper. Model #1 is structurally similar to model #2 with the difference of having 5 convolutional layers and fixed filter size of 3^3 voxels in all the layers. Loss values of this model starts to diverge from an early point in epoch 15. Model #3 is also mainly similar to model #2, but the number of the filters used remains constant at 6 for all the convolutional layers. This model is a good example of over–fitting with very low loss values on the training dataset and large errors on the validation set. To conclude, increasing the number of filters and decreasing the filter size across the convolutional layers seems to be crucial to obtain a good training performance as we can see for model #2. Finally, we have plotted ML predicted vs. numerically calculated values of gas adsorption and permeability for different subsets of data in Figure 5.10–b and c. Coefficients of determination (R^2) for all the cases are above 0.93 for prediction of the storage qualities. Similarity of the r–squared values for each of the training, validation and test data implies that over–fitting has not occurred in the training process.

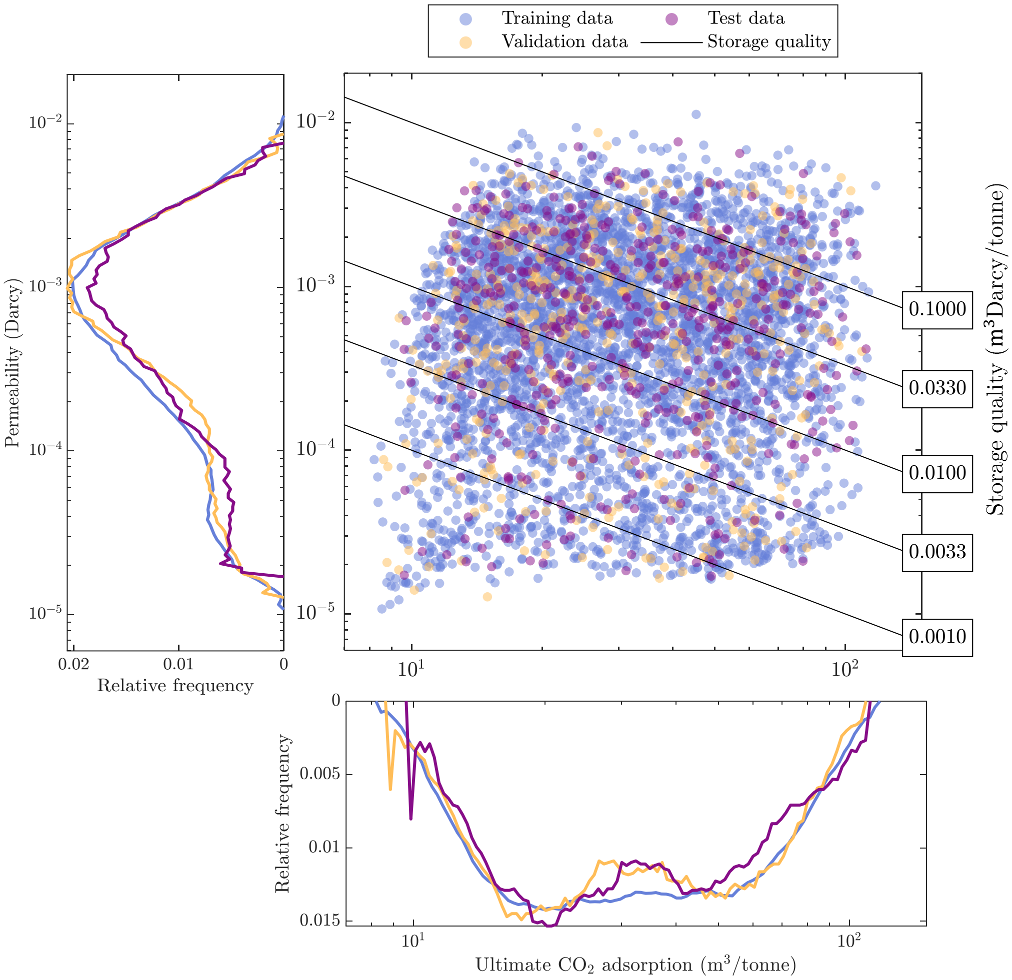

Figure 5.9: Distribution of the ultimate gas adsorption capacity and permeability of the samples in the dataset for each of the training, validation and testing subsets.

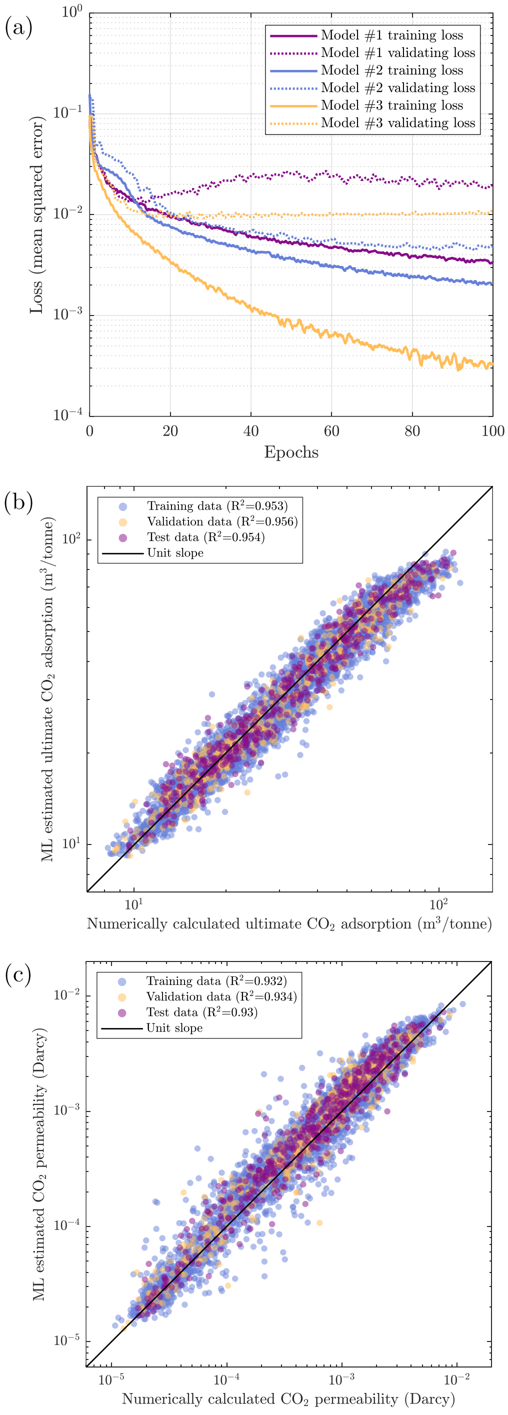

Figure 5.10: Comparing the training and validation loss of three proposed deep learning models in terms of mean squared error (a), comparing CO_2 adsorption values predicted by machine learning and numerical method (b), comparing gas permeability values predicted by machine learning and numerical method.

5.5 Conclusions

In this study, we have developed an image–based numerical tool for simulation of CO_2 storage in CH_4 saturated shale samples that contain fractures. In such systems, CO_2 can easily transport through the fracture network and access the locations with high surface area such as the kerogen–rich zones. Then, due to a higher adsorption tendency compared to the residing gas, CO_2 will occupy the surface sites and starts to accumulate in the sample. In order to accelerate the numerical simulation process, we have utilized deep learning to expand the computational limits. The developed ML model has shown an acceptable performance with less than 7% of error in prediction of gas adsorption and permeability.

In this study, to simplify the selection criteria of a suitable shale sample for carbon storage, we have defined a term as "Storage Quality" that implies the amount and rate of gas adsorption by different shale samples. This criterion, coupled with the developed ML model, can be utilized to help ranking different geological sites based on pore–scale images of their common shale structures. Additionally, the following conclusions can be drawn based on the findings of this study in a summarized manner:

- Numerical simulation of the dynamic gas adsorption through fractured shale samples has shown that pressure profiles converge to their equilibrium state considerably faster than the gas saturations. This is mainly due to the diffusion dominant nature of the gas transport in microporosities.

- Steady state simulation of gas adsorption is able to estimate the dynamic gas content at the equilibrium condition with 2.3% error on 50 studied samples. Thus, it can be alternatively used especially knowing the fact that its computational expense is 3 to 4 orders of magnitude lower than the dynamic numerical simulation. However, dynamic modeling will still be irreplaceable for the cases in which the system's properties change significantly during the simulation.

- A deep convolutional neural network model is developed to predict the steady state simulation results and accelerate the calculations even further. Ultimate gas adsorption capacity and permeability of the shale samples have been predicted based on their mineralogy and microporosity maps with r–squared of 0.95 and 0.93, respectively.

Summary

In this thesis, which has been an amalgamate of four published research papers, a range of fluid flow models in porous material are developed with an approach to machine learning. In the first chapter, a brief introduction to porous material concepts and common machine learning methods is presented. In the second chapter, a hybrid model of Lattice Boltzmann method and pore network modeling is developed to make an surrogate but accurate permeability model which utilizes the realistic geometry of pore–throats instead of a cylindrical simplification. We have used the developed model to make a unified fluid flow equation in chapter 3 which is able to predict the permeability of pore-throats and micro–fractures at the same time. Thus by introducing micro–porosity into such flow model, a triple pore network model is developed which can be used to model heterogeneous porous materials such as tight carbonate rocks and organic–rich shale deposits. In chapter 4, we have used pore scale images for data–driven characterization of the porous material to bypass the need for heavy numerical simulations. The developed model was able to predict some flow based characteristics with a good agreement not only with numerical simulations but also experimental data such as absolute permeability. Finally in the last chapter, we have used the methods developed in the previous chapters to evaluate the suitability of the organic rich shale deposits for subsurface storage of CO_2 based on the pore–scale images. Here, we have summarized the the conclusion sections of each chapter to provide a more comprehensive view on research outcomes:

- In chapter 2, two ANN's and one empirical formula were presented capable of estimating the throat's LBM-based permeabilities with coefficient of determination (R^2) higher than 0.99. Additionally, the "mean distance" was found to be an image-based feature highly correlated with LBM throat permeabilities. In this chapter, throat permeabilities obtained were substituted within the classical pore networks of 12 rock samples and overall network permeabilities were calculated successfully. We compared the PNM-LBM absolute permeabilities with pure LBM-based permeabilities of the samples and found that the proposed model was capable of predicting the overall permeability of the rock samples with coefficient of determination around 0.997 while minimizing the computational cost by two orders of magnitude compared to the full LBM solution.
- In chapter 3, triple pore network models are introduced and constructed based on the semi–real tomography images in order to simulate gas and liquid permeabilities. In this regards, a unified approach is invented to simulate fluid flow within a network with both meso–pores and fractures using the distance map of the channels. In this

chapter, a hypothetical micro–network structure is presented for taking into the account the hydrodynamical effects of micro–porosities in liquid and gas flow through porous samples with dual scales of porosity. In addition, effects of micro–porosities on gas permeability are investigated and operational conditions in which ignoring the presence of micro–porosities make a significant error are discussed.

- In chapter 4, a physically diverse dataset of micro–porous structures are generated based on texture transformation and porosity manipulation of 60 original tomography images and a wide range of morphological, hydraulic, electrical and mechanical features are extracted for each sample. The dataset is publicly available and can be used for future studies. In addition, a dimensionless approach has been presented to extract or predict the porous material features without being affected by the spatial resolution of the images. The average coefficient of determination (R^2) for all 30 extracted features is 0.885 which is significant considering the diverse range of porous morphologies and features. In this chapter, to provide an independent model verification, three images outside of the datasets are generated with textures almost unseen in the augmented dataset. The model predictions were almost as good as the testing dataset used to check the model performance in terms of r–squared. This observation indicates that the dataset is diversified enough to avoid false accuracy due to the similarity of the training and test results. Also, considering the novel texture of the verification samples, one can conclude that the model is implicitly learning the physics of the estimated features rather than blindly memorizing the textures. Additionally, in this chapter, in order to provide experimental verification for the proposed method, absolute permeabilities of 3 realistic porous samples have been compared with the measured values in the laboratory and DeePore predictions had around 13% relative error with is noticeable comparing to the accuracy of the direct numerical simulation methods such as PFVS and LBM.
- Finally, in chapter 5, numerical simulation of the dynamic gas adsorption through fractured shale samples has shown that pressure profiles converge to their equilibrium state considerably faster than the gas saturations. This is mainly due to the diffusion dominant nature of the gas transport in micro–porosities. We have shown that, steady state simulation of gas adsorption is able to estimate the dynamic gas content at the equilibrium condition with 2.3% error on 50 studied samples. As a result, it can be alternatively used especially knowing the fact that its computational expense is 3 to 4 orders of magnitude lower than the dynamic numerical simulation. In order to

push computational limits even further, a deep convolutional neural network model is developed to predict the steady state simulation results. Using the developed deep learning model, ultimate gas adsorption capacity and permeability of the shale samples have been predicted based on their mineralogy and microporosity maps with r–squared of 0.95 and 0.93, respectively.

Appendices

Appendix A: Fracture realization

In each sample we have created 12 fractures which half of them are deviated by 30 degrees and the rest by 60 degrees from y axis and the angle is measured in the xy plane. These angles only indicate the general trend of the fractures, and fracture local curvature changes due to porous media texture. These fractures are generated via a random walk approach which is inspired by the idea used in Mhiri *et al.* [183]. In this approach, we consider some arbitrary walkers that can move to their neighbouring cells/pixel in each time step in a random manner. In 2D, each walker, has 8 neighbouring pixel to travel. In order to control the general trend of the pathway, a bias weight is put on the pixels which are aligned to the desired fracture direction. So, the walkers wobble randomly but in a larger picture they are gradually moving towards the biased direction. Then we run this process for several times and calculate a cost function for each trial. If a walker path cuts hard grains/solid sections of the porous media in which the CT number is higher, the path cost would increase. Finally, in a random search approach, we select the least expensive path to establish a fracture in that area.

Fig. 5.11 illustrates the cost minimization process which is used to generate a horizontal fracture in the Estaillades sample. As can be seen, at the initial generations of the random search, fracture path has a high cost due to hitting many high density zones in the image (Fig. 5.11a). Quickly, the algorithm finds pathways with a lower cost and start to bypass some expensive zones (Fig. 5.11b). And finally, after 1000 generations, a plausible trend for an artificial fracture is obtained in which the sample is cut at the points with the lowest cost while maintaining the optimization limits such as the maximum number of steps (Fig. 5.11c).

It is noteworthy that the cost function is defined as the averaged values of the voxels within the fracture path. Also, the voxel cost of the whole map is normalized to be between 0 and 1 (Fig. 5.11d). A simple version of this fracture approximation code is published in the public domain [2].

---

[2] `https://github.com/ArashRabbani/PaperCodes`

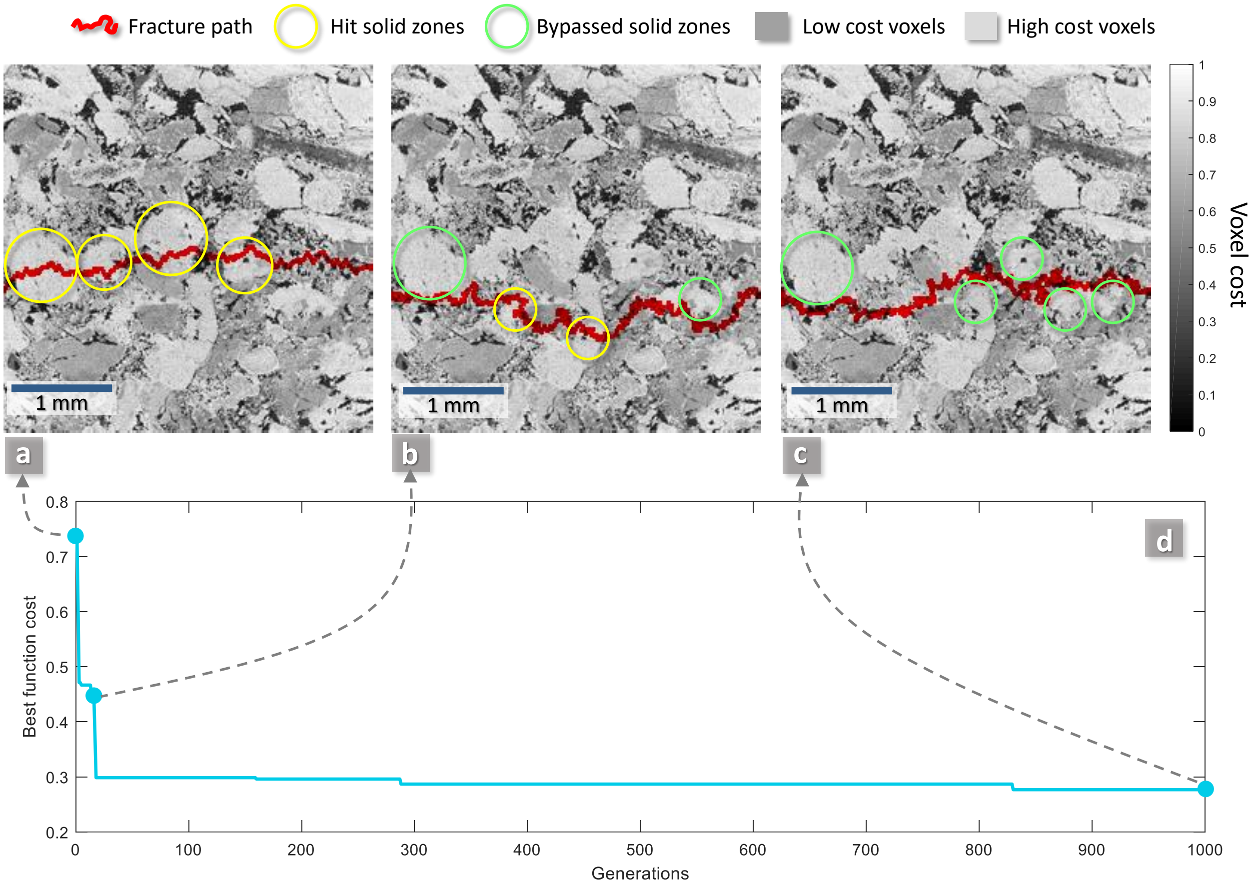

Figure 5.11: Cost minimization process used to generate realizations of fractures within porous material, (a) fracture path at the beginning of optimization with high cost and several solid hits, (b) fracture path at the middle of the optimization with partially passed solids, (c) final fracture path that bypasses most of the solid regions, and (d) best function cost during the optimization process to find the least expensive fracture pathway.

Appendix B: Lattice–Boltzmann simulation

We used LBM to numerically calculate absolute permeability of pores and fractures, and compared it with ITPM results. In order to simulate a steady–state, single–phase, and fully–developed flow in a channel–like link in the network (pore–throat or fracture), we assume it has arbitrary cross–section and a uniform shape along its length. A 2D cross–section of the fluid conductor is taken 6 times and they are stacked upon each other to create the simulation geometry. Image voxels will be simulation grids so if the conductor image is 50 by 50 voxels, the simulation grid is 50 by 50 by 6 grids. The scheme of LBM is D3Q19 which means there will be 18 possible directions for fluid flow within each block. The code that has been modified and used to calculate LBM permeability is originally published by Haslam *et al.* [112]. In this simulation, fluid is assumed to be Newtonian with BGK collision model [103]. Additionally, bounce–back is only in the direction normal to the geometry boundary. The same as the regular formulation of LBM, we have assumed that the particle distribution function f_i evolves in the directions of the distribution vectors e_i at each time step $(t + \Delta t)$ and location (x) as [112]:

$$f_i(x + e_i + \Delta t) - f_i(x, t) = -1/\tau(f_i(x, t) - {f_i}^{eq}(x, t)) \tag{B1}$$

where ${f_i}^{eq}$ is a truncated Maxwell–Boltzmann equilibrium distribution and it can be written as a function of local velocity (v) in 18 directions and τ is equilibrium state time. Also i is the distribution function index for different neighbouring cells. Simulation starts by imposing a fixed flow velocity at the inlet of geometry (first layer) and periodic boundary condition is considered in the direction of flow. We have defined the convergence criteria when calculated permeability value is stabilized and its relative error compared to the previous time step is less than 10^{-6}. More details on LBM permeability calculation is provided in [198].

Appendix C: Gas flow simulation

In this Appendix, we describe the method for gas flow simulation within the modelled T–PNMs. The reason for selecting gas flow to be simulated is that gas flow mechanisms change significantly in different size scales of the pores and channels. In micro–porosities more molecular and diffusive mechanisms such as Knudsen and slip flow are active while in the meso–porosities and fractures, viscous flow regime is dominant [146, 328]. Absolute permeability of the network links is commonly addressed as the liquid permeability. However, gas permeability is partially different than Newtonian liquids due to the molecular interactions with solid walls [351]. In this paper, we calculate the absolute permeability of gas in different temperature–pressure conditions for the whole pore network with a steady–state approach. Due to the assumed small pressure changes from inlet to the outlet of the PNM, gas properties such as viscosity and density are taken constant. Based on Javadpour *et al.* [146, 148] formulation for gas flow in nano to micro size channels, and by assuming three flow mechanisms of Knudsen, slippage and viscous, the gas permeability of a channel can be calculated as [146, 148, 150]:

$$K_g = K_n(r) + F(r)K_a \tag{C1}$$

$$K_n(r) = \frac{2r\mu_g M}{3k_b T\bar{\rho}}\sqrt{\frac{8k_b T}{\pi M}} \tag{C2}$$

where M is molecular mass of the gas, k_b is the gas Boltzmann constant, T is average temperature, $\bar{\rho}$ is the average density of the gas, μ_g is gas dynamic viscosity, r is tube equivalent radius, $F(r)$ is a correction factor to include slip flow in gas permeability as a function of r, and K_a is the absolute or liquid permeability of the channel which is independent to the fluid properties. $K_n(r)$ describes the channel permeability increment due to the Knudsen diffusion. This term is a function of gas properties and channel radius (r) and its presence increases the apparent gas permeability of any type of network links including meso–throats, micro–throats and fracture–links.

We have previously calculated the absolute permeability of meso–throats and fracture links (K_p) in Eq. 5.1, so this value can be replaced in Eq. C1 as K_a. We cannot do the same replacement for the gas permeability of micro–throats since they contain a range of micro–tubes with different sizes and we need to calculate slippage ($F(r_m)$) and Knudsen terms ($K_n(r_m)$) for each size of the tubes, and then integrate the calculated permeabilities over different micro–tube radii (r_m). Thus, the gas permeability of all different links within the T–PNM can be calculated as:

$$K_g = \begin{cases} K_n(r) + F(r)K_p(\bar{D})R_s^2 & \text{meso-throat and fracture-link} \\ \int \left(f(r_m)K_n(r_m) + \frac{1}{8}f(r_m)F(r_m)\alpha\phi_m r_m^2\right)\, dr_m & \text{micro–throat} \end{cases} \tag{C3}$$

where R_s is the spatial resolution of the image in μm/voxel. Additionally, gas slippage term for all types of channels can be calculated as: [146, 148, 147]:

$$F(r) = 1 + \frac{4c\bar{\lambda}}{r} \tag{C4}$$

where r can be replaced by r_m in the case of micro–throats, c is a collision proportionality factor, and is commonly set equal to 1, and $\bar{\lambda}$ is average mean free path of the gas and can be calculated as [334]:

$$\bar{\lambda} = \frac{\mu}{\bar{P}}\sqrt{\frac{k_b T\pi}{2M}} \tag{C5}$$

where $\bar{P}$ is gas average pressure. Eq. C4 and Eq. C5 can be used for all types of network links including micro–tubes with the radius of r_m and meso–throats or fracture–links with the equivalent radius of r. By assuming that gas properties remain constant in a small pressure range of the flow, we can write a steady–state gas flow balance for each pore based on Darcy's law [352, 217]:

$$\sum_{i=1}^{n} \frac{K_{g_i} A_i \Delta P_i}{\mu_g L_i} = 0 \tag{C6}$$

where A_i is the effective surface area of a network link in the direction of flow, ΔP_i is the pressure difference between two sides of the link, L_i is the length of the i_{th} link, and n is the total number of network links connected to the specified node and μ_g is gas viscosity obtained by empirical correlation developed by Lee *et al.* [335] at the average temperature–pressure condition:

$$\mu_g = Z \exp(X \rho^Y) \tag{C7}$$

$$Z = \frac{(7.77 + 0.0063M)T^{1.5}}{122.4 + 12.9M + T} \tag{C8}$$

$$X = 2.57 + 1914.5/T + 0.0095M \tag{C9}$$

$$Y = 1.11 + 0.04X \tag{C10}$$

where X, Y and Z are correlation constants used to estimate the gas viscosity. By writing Eq. C6 for each of the nodes in the network, a set of equations is given in which the only unknown parameter is the node pressure (P_i). In order to solve this set of equations, we apply a small pressure difference of 1 Pa between two opposite faces of the PNM as a boundary condition. Other sides of the geometry are assumed as no–flow boundaries. Then, using the biconjugate gradients method [353] coupled with a lower–upper (LU) factorization [354], we solve the system of equations obtained in an iterative manner to find the pore pressure at the centers of each node. Now, using Darcy's law, we find the volumetric flow rate of each network link as well as the overall flow rate. Finally, writing Darcy's law for the whole network, the equivalent gas permeability of the T–PNM is obtained.

Appendix D: Original samples

Here we have listed the real tomography images of porous material used to generate the dataset using the data augmentation method. The size and spatial resolutions mentioned in this table are modified by resizing/cropping the original images to fit the purpose of this study.

Num.	Name	Resolution ($\mu m/px$)	Modified size (px^3)	Type	DOI
1	Berea #1	11.72	256^3	Sandstone	https://doi.org/10.1016/j.advwatres.2012.03.003
2	Berea #1	8.35	256^3	Sandstone	http://dx.doi.org/10.1103/PhysRevE.80.036307
3	Berea #2	3.25	256^3	Sandstone	https://doi.org/10.1016/j.advwatres.2012.03.003
4	Berea #3	3.25	256^3	Sandstone	https://doi.org/10.1016/j.advwatres.2012.03.003
5	Berea #4	3.25	256^3	Sandstone	https://doi.org/10.1016/j.advwatres.2012.03.003
6	Berea #5	4.33	256^3	Sandstone	https://doi.org/10.1016/j.advwatres.2012.03.003
7	Berea #6	4.33	256^3	Sandstone	https://doi.org/10.1016/j.advwatres.2012.03.003
8	Berea #7	4.33	256^3	Sandstone	https://doi.org/10.1016/j.advwatres.2012.03.003
9	C1	4.45	256^3	Carbonate	http://dx.doi.org/10.1103/PhysRevE.80.036307
10	C2	8.35	256^3	Carbonate	http://dx.doi.org/10.1103/PhysRevE.80.036307
11	Doddington #1	5.41	256^3	Sandstone	https://doi.org/10.1016/j.advwatres.2012.03.003
12	Doddington #2	5.41	256^3	Sandstone	https://doi.org/10.1016/j.advwatres.2012.03.004
13	Doddington #3	5.41	256^3	Sandstone	https://doi.org/10.1016/j.advwatres.2012.03.005
14	Doddington #4	5.41	256^3	Sandstone	https://doi.org/10.1016/j.advwatres.2012.03.006
15	Estaillades #1	10.72	256^3	Carbonate	https://doi.org/10.1016/j.physa.2009.12.006
16	Fontainebleau #1	17.17	256^3	Sandstone	https://doi.org/10.1016/j.physa.2009.12.006
17	Fontainebleau #2	17.17	256^3	Sandstone	https://doi.org/10.1016/j.physa.2009.12.006
18	Fontainebleau #3	17.17	256^3	Sandstone	https://doi.org/10.1016/j.physa.2009.12.006
19	Fontainebleau #4	17.17	256^3	Sandstone	https://doi.org/10.1016/j.physa.2009.12.006
20	Fontainebleau #5	17.17	256^3	Sandstone	https://doi.org/10.1016/j.physa.2009.12.006
21	Fontainebleau #6	17.17	256^3	Sandstone	https://doi.org/10.1016/j.physa.2009.12.006
22	Ketton	10.62	256^3	Carbonate	https://doi.org/10.1016/j.advwatres.2012.03.005
23	S1	10.18	256^3	Sandstone	http://dx.doi.org/10.1103/PhysRevE.80.036307
24	S2	5.81	256^3	Sandstone	http://dx.doi.org/10.1103/PhysRevE.80.036307
25	S3	10.66	256^3	Sandstone	http://dx.doi.org/10.1103/PhysRevE.80.036307
26	S4	10.50	256^3	Sandstone	http://dx.doi.org/10.1103/PhysRevE.80.036307
27	S5	4.68	256^3	Sandstone	http://dx.doi.org/10.1103/PhysRevE.80.036307
28	S6	5.98	256^3	Sandstone	http://dx.doi.org/10.1103/PhysRevE.80.036307
29	S7	5.63	256^3	Sandstone	http://dx.doi.org/10.1103/PhysRevE.80.036307
30	S8	5.73	256^3	Sandstone	http://dx.doi.org/10.1103/PhysRevE.80.036307
31	S9	3.98	256^3	Sandstone	http://dx.doi.org/10.1103/PhysRevE.80.036307
32	F42A	11.72	256^3	Sandpack	http://dx.doi.org/10.1103/PhysRevE.80.036307
33	F42B	11.72	256^3	Sandpack	http://dx.doi.org/10.1103/PhysRevE.80.036307
34	F42C	11.72	256^3	Sandpack	http://dx.doi.org/10.1103/PhysRevE.80.036307
35	LV60A	11.72	256^3	Sandpack	http://dx.doi.org/10.1103/PhysRevE.80.036307
36	LV60B	11.68	256^3	Sandpack	http://dx.doi.org/10.1103/PhysRevE.80.036307
37	LV60C	11.72	256^3	Sandpack	http://dx.doi.org/10.1103/PhysRevE.80.036307
38	A1	4.51	256^3	Sandpack	http://dx.doi.org/10.1103/PhysRevE.80.036307
39	Benthemier #2	4.97	256^3	Sandstone	https://doi.org/10.1016/j.advwatres.2012.03.005
40	Benthemier #3	4.97	256^3	Sandstone	https://doi.org/10.1016/j.advwatres.2012.03.005
41	Benthemier #4	4.97	256^3	Sandstone	https://doi.org/10.1016/j.advwatres.2012.03.005

42	Benthemier #5	4.97	256^3	Sandstone	https://doi.org/10.1016/j.advwatres.2012.03.005
43	Benthemier #6	4.97	256^3	Sandstone	https://doi.org/10.1016/j.advwatres.2012.03.005
44	Benthemier #7	4.97	256^3	Sandstone	https://doi.org/10.1016/j.advwatres.2012.03.005
45	Berea #8	7.11	256^3	Sandstone	https://doi.org/10.1016/j.advwatres.2015.07.012
46	Clashach	10.15	256^3	Sandstone	https://doi.org/10.1016/j.advwatres.2015.07.012
47	Doddington #5	9.50	256^3	Sandstone	https://doi.org/10.1016/j.advwatres.2015.07.012
48	Estaillades #2	10.16	256^3	Carbonate	https://doi.org/10.1016/j.advwatres.2015.07.012
49	Indiana	10.15	256^3	Carbonate	https://doi.org/10.1016/j.advwatres.2015.07.012
50	Ketton #2	10.15	256^3	Carbonate	https://doi.org/10.1016/j.advwatres.2015.07.012
51	Monte Gamb. #1	4.94	256^3	Carbonate	https://doi.org/10.1016/j.advwatres.2012.03.004
52	Monte Gamb. #2	4.94	256^3	Carbonate	https://doi.org/10.1016/j.advwatres.2012.03.004
53	Monte Gamb. #3	4.94	256^3	Carbonate	https://doi.org/10.1016/j.advwatres.2012.03.004
54	Monte Gamb. #4	4.94	256^3	Carbonate	https://doi.org/10.1016/j.advwatres.2012.03.004
55	Monte Gamb. #5	4.94	256^3	Carbonate	https://doi.org/10.1016/j.advwatres.2012.03.004
56	Monte Gamb. #6	4.94	256^3	Carbonate	https://doi.org/10.1016/j.advwatres.2012.03.004
57	Monte Gamb. #7	4.94	256^3	Carbonate	https://doi.org/10.1016/j.advwatres.2012.03.004
58	Monte Gamb. #8	4.94	256^3	Carbonate	https://doi.org/10.1016/j.advwatres.2012.03.004
59	Hollington #1	2.17	256^3	Sandstone	https://doi.org/10.1007/s11242-019-01244-8
60	Hollington #2	2.17	256^3	Sandstone	https://doi.org/10.1007/s11242-019-01244-8

Table 5.2: Sources of the original tomography data and some specifications including original names, size and spatial resolutions.

Appendix E: Statistical test

Feature	Training–validation (K–S distance)	Training–test (K–S distance)
Absolute Perm.	0.025	0.118
Formation Factor	0.013	0.019
Cementation Factor	0.017	0.021
Pore Density	0.013	0.025
Tortuosity	0.018	0.018
Avg. Connectivity	0.022	0.017
Avg. Throat Rad.	0.016	0.014
Avg. Pore Rad.	0.015	0.023
Avg. Throat Length	0.017	0.021
Avg. Pore Inscribed Rad.	0.012	0.023
Specific Surface	0.024	0.020
Avg. Throat Inscribed Rad.	0.014	0.016
Grain Sphericity	0.012	0.020
Avg. Grain Rad.	0.014	0.009
Rel. Young Module	0.013	0.018

Table 5.3: Results of two–sample Kolmogorov–Smirnov (K–S) test to check the similarity/dissimilarity of the training–validation and training–test data, K–S distances close to 1 indicate dissimilarity of the distributions.

Appendix F: Author Contribution Statement

In chapters 2, 3, and 5, Arash Rabbani has developed the idea of research, executed the research by computer code development and written the main body of the article. Masoud Babaei supervised the research and contributed in writing and correction of the article. In chapter 4, Arash Rabbani has developed the idea of research, executed the research by computer code development and written the main body of the article. Reza Shams contributed to execution of research through trouble shooting of the computer codes. Ying Da Wang executed the LBM simulations and contributed in writing the article. Traiwit Chung executed the PFVS simulations and contributed in writing the article. Masoud Babaei supervised the research and contributed in writing and correction of the article.

Appendix G: Nomenclature and terminologies

In this appendix, a list of different variables or parameters used in different chapters of the thesis are provided.

Chapter 2

Variable	Definition
f_i	Particle distribution function
e_i	Particle distribution vectors
Δt	Time step
x	Grid location
${f_i}^{eq}$	Tuncated Maxwell–Boltzmann equilibrium distribution
v	local velocity
τ	equilibrium state time
r	Number of particle density distribution vectors
r_t	Tube radius
k	Absolute fluid permeability
p	Pressure
$\bar{U}$	Averaged velocity vector in the direction of pressure drop
ω	Relaxation frequency used in the LBM simulation
k_{throat}	Pore throat absolute permeability
$\bar{D}$	mean distance of the throat image
A	Throat cross area
P	Wetted perimeter of throat

Chapter 3

Variable	Definition
K_p	absolute permeability of the porous space links such as a meso–throat with $pixel^2$ unit
$\bar{D}$	Mean distance of the channel cross-sectional image
r_m	Radius of the micro–tubes residing within a micro–throat
r	Channel equivalent radius
ϕ_m	Total micro–porosity of the solid element
ϕ_s	Volume fraction of geometry occupied by the partially solid elements
ϕ_f	Volume fraction of the geometry occupied by the fracture
α	Porosity correction factor
K_g	Gas permeability of a network link
$f(r_m)$	Function that gives back the probability of micro–tubes with the radius equal to r_m
K_s	Absolute permeability of a solid element with micro–porosity
K_a	Absolute permeability of the network link
K_n	Knudsen permeability
K_e	Total equivalent analytical permeability of the geometry
K_f	the absolute permeability of the fracture
F_r	Gas slippage correction factor
K_p	Overall permeability of the meso–PNM
$\bar{\lambda}$	Mean free path of gas
A_i	The effective surface area of a network link in the direction of flow
L_i	The length of a network link and its equal to the distance between two connected nodes
M	Molecular mass of gas
$\bar{\rho}$	Average gas density
T	Average temperature
μ_g	Gas viscosity
k_b	gas Boltzmann constant

Additionally, considering the differences between the definition of technical terms in literature and in order to clarify the vocabulary used/defined in chapter 3, the following terminology list is provided:

Term	Definition
Pore	Short way to imply pore–body
Throat	Short way to imply pore–throat
Micro–pore	A hypothetical volume–less joint that connects the micro–throats, unresolved in the tomography images
Micro–throat	A bundle of micro–tubes that connects micro–pores to other elements in the network
Micro–tubes	Capillary tubes with sub–resolution radii that form a micro–throat
Meso–pore	Adequately–resolved pore–body based on the images from tomography
Meso–throat	The interface between two meso–pore–bodies that is the tightest pathway between them
Fracture–node	A similar element to meso–pores but with an elongated structure
Fracture–link	The interface between two fracture–node that is the tightest pathway between them
Throat length	The Euclidean distance between the center of masses of two connecting pore–bodies
Throat area	Cross-sectional area of a throat image which is projected on a 2D surface perpendicular to the throat axis
Throat axis	The straight line that connects the center of masses of two adjacent pore–bodies
Micro–porosity	Existence of a micro–pore and micro–throat system in a partially solid element within a tomography image of porous material
Solid element	A partially solid part of the image that hosts micro–porosities

Chapter 4

Variable	Definition
S	Side size of the image which is 256 voxels in this chapter
$\lfloor x \rfloor$	Floor operator that rounds down the decimal points to the closest smaller integer
f_d	Euclidean distance transform
A	array of a 2–D plane cut through the 3–D volume perpendicular to one of the major axes
$\vec{v}$	Fluid velocity vector
q	Source and sink terms in PFVS
P	Pressure
w	voxel a local conductivity
N_x	the number of voxels in the main flow direction
N_y	the number of voxels in y direction which is perpendicular to the flow direction
N_z	the number of voxels in z direction which is perpendicular to the flow direction
Q	Flow rate (m^3/s)
μ	Fluid viscosity $(Pa.s)$
ΔP	Pressure difference across the image (Pa)
α	Shape factor
R	Spatial resolution of image in PFVS
d_{max}	Largest inscribed radius in pixels
d	Radial distance from the inner wall in pixel
ρ	Fluid density (kg/m^3)
ξ_q	Vector velocity space in LBM
f_q	Velocity distribution in LBM
ξ_q	velocity space vector in LBM
δt	Timestep
J	Collision operation in LBM

Chapter 5

Variable	Definition
K_p	Absolute permeability of the network links
$\bar{D}$	Average distance value with the unit of *pixel*
K_g	Gas permeability
r	Equivalent radius of meso–throats and fracture links cross-section
R_s	Spatial resolution of the simulated image in $m/voxel$
ϕ_m	microporosity of the clay and kerogen nodes
r_m	Radius of the micro–tubes
$f(r_m)$	Size distribution function of micro–tubes
α	porosity correction factor for partially porous elements
$\bar{P}$	Gas average pressure
Z	Real gas compressibility
μ	Gas viscosity
$\Delta V_{ads,i}$	Free gas volume change in node i due to adsorption/desorption
$\Delta V_{adv,i}$	Free gas volume change due to advection
$\Delta V_{dif,i}$	Gas volume change due to the Fickian diffusion
$\Delta V_{cmp,i}$	Free gas volume change due to the compression
P_i	Pressure at each node
S_i	Methane gas saturation
$S_{p,i}$	Internal surface area of the node
M_g	Mass surface density of the adsorbed gas (kg/m^2)
C	Linearization coefficient dependant of Langmuir adsorption coefficient and the range of pressure variation [217]
μ	Gas viscosity
ρ	Free gas density
C_s	Gas storage capacity (m^3/tonne)
K_t	Total gas permeability (Darcy)
Q_s	Gas storage quality

Bibliography

[1] D. Wildenschild, C. Vaz, M. Rivers, D. Rikard, B. Christensen, Using x-ray computed tomography in hydrology: systems, resolutions, and limitations, Journal of Hydrology 267 (3-4) (2002) 285–297.

[2] A. Z. Weber, M. M. Mench, J. P. Meyers, P. N. Ross, J. T. Gostick, Q. Liu, Redox flow batteries: a review, Journal of Applied Electrochemistry 41 (10) (2011) 1137.

[3] C. Brennan, K. Eichholz, D. Hoey, The effect of pore size within fibrous scaffolds fabricated using melt electrowriting on human bone marrow stem cell osteogenesis, Biomedical Materials 14 (6) (2019) 065016.

[4] C. Michler, A. Cookson, R. Chabiniok, E. Hyde, J. Lee, M. Sinclair, T. Sochi, A. Goyal, G. Vigueras, D. Nordsletten, et al., A computationally efficient framework for the simulation of cardiac perfusion using a multi-compartment darcy porous-media flow model, International journal for numerical methods in biomedical engineering 29 (2) (2013) 217–232.

[5] H. Andrä, N. Combaret, J. Dvorkin, E. Glatt, J. Han, M. Kabel, Y. Keehm, F. Krzikalla, M. Lee, C. Madonna, et al., Digital rock physics benchmarks—part i: Imaging and segmentation, Computers & Geosciences 50 (2013) 25–32.

[6] D. Dollimore, G. Heal, An improved method for the calculation of pore size distribution from adsorption data, Journal of applied chemistry 14 (3) (1964) 109–114.

[7] W. Van Der Aalst, Data science in action, in: Process mining, Springer, 2016, pp. 3–23.

[8] V. Dhar, Data science and prediction, Communications of the ACM 56 (12) (2013) 64–73.

[9] D. Conway, J. White, Machine learning for hackers, " O'Reilly Media, Inc.", 2012.

[10] D. Asamoah, D. Doran, S. Schiller, Teaching the foundations of data science: An interdisciplinary approach, arXiv preprint arXiv:1512.04456 (2015).

[11] M. Haider, Getting Started with Data Science: Making Sense of Data with Analytics, IBM Press, 2015.

[12] J.-W. Huang, J.-W. Gao, How could data integrate with control? a review on data-based control strategy, International Journal of Dynamics and Control 8 (4) (2020) 1189–1199.

[13] M. H. Hassoun, et al., Fundamentals of artificial neural networks, MIT press, 1995.

[14] X. Y. Chen, K. W. Chau, A hybrid double feedforward neural network for suspended sediment load estimation, Water resources management 30 (7) (2016) 2179–2194.

[15] I. N. Da Silva, D. H. Spatti, R. A. Flauzino, L. H. B. Liboni, S. F. dos Reis Alves, Artificial neural networks, Cham: Springer International Publishing (2017) 39.

[16] V. Sessions, M. Valtorta, The effects of data quality on machine learning algorithms., ICIQ 6 (2006) 485–498.

[17] I. Bilbao, J. Bilbao, Overfitting problem and the over-training in the era of data: Particularly for artificial neural networks, in: 2017 Eighth International Conference on Intelligent Computing and Information Systems (ICICIS), IEEE, 2017, pp. 173–177.

[18] A. Al-Anazi, I. Gates, Support vector regression to predict porosity and permeability: effect of sample size, Computers & Geosciences 39 (2012) 64–76.

[19] D. B. Das, T. Thirakulchaya, L. Deka, N. S. Hanspal, Artificial neural network to determine dynamic effect in capillary pressure relationship for two-phase flow in porous media with micro-heterogeneities, Environmental Processes 2 (1) (2015) 1–18.

[20] A. Shokrollahi, H. Safari, Z. Esmaeili-Jaghdan, M. H. Ghazanfari, A. H. Mohammadi, Rigorous modeling of permeability impairment due to inorganic scale deposition in porous media, Journal of Petroleum Science and Engineering 130 (2015) 26–36.

[21] N. Alqahtani, F. Alzubaidi, R. T. Armstrong, P. Swietojanski, P. Mostaghimi, Machine learning for predicting properties of porous media from 2D x-ray images, Journal of Petroleum Science and Engineering (2019) 106514.

[22] M. A. Ahmadi, Z. Chen, Comparison of machine learning methods for estimating permeability and porosity of oil reservoirs via petro-physical logs, Petroleum 5 (3) (2019) 271–284.

[23] M. Ali Ahmadi, S. Zendehboudi, A. Lohi, A. Elkamel, I. Chatzis, Reservoir permeability prediction by neural networks combined with hybrid genetic algorithm and particle swarm optimization, Geophysical Prospecting 61 (3) (2013) 582–598.

[24] D. D. Ganji, S. H. H. Kachapi, Application of nonlinear systems in nanomechanics and nanofluids: analytical methods and applications, William Andrew, 2015.

[25] N. Nishiyama, T. Yokoyama, Permeability of porous media: Role of the critical pore size, Journal of Geophysical Research: Solid Earth 122 (9) (2017) 6955–6971.

[26] J. Hommel, E. Coltman, H. Class, Porosity–permeability relations for evolving pore space: a review with a focus on (bio-) geochemically altered porous media, Transport in Porous Media 124 (2) (2018) 589–629.

[27] M. Babaei, H. M. Nick, Performance of low-enthalpy geothermal systems: Interplay of spatially correlated heterogeneity and well-doublet spacings, Applied Energy 253 (2019) 113569.

[28] R. Sander, Z. Pan, L. D. Connell, Laboratory measurement of low permeability unconventional gas reservoir rocks: A review of experimental methods, Journal of Natural Gas Science and Engineering 37 (2017) 248–279.

[29] N. S. Hanspal, B. A. Allison, L. Deka, D. B. Das, Artificial neural network (ann) modeling of dynamic effects on two-phase flow in homogenous porous media, Journal of Hydroinformatics 15 (2) (2012) 540–554.

[30] S. Kamrava, P. Tahmasebi, M. Sahimi, Linking morphology of porous media to their macroscopic permeability by deep learning, Transport in Porous Media 131 (2) (2020) 427–448.

[31] A. Rabbani, M. Babaei, R. Shams, Y. Da Wang, T. Chung, Deepore: a deep learning workflow for rapid and comprehensive characterization of porous materials, Advances in Water Resources 146 (2020) 103787.

[32] A. Rabbani, A. Assadi, R. Kharrat, N. Dashti, S. Ayatollahi, Estimation of carbonates permeability using pore network parameters extracted from thin section images and

comparison with experimental data, Journal of Natural Gas Science and Engineering 42 (2017) 85–98.

[33] J. Sun, J. Zhang, Y. Gu, Y. Huang, Y. Sun, G. Ma, Prediction of permeability and unconfined compressive strength of pervious concrete using evolved support vector regression, Construction and Building Materials 207 (2019) 440–449.

[34] S. Srinivasan, S. Karra, J. Hyman, H. Viswanathan, G. Srinivasan, Model reduction for fractured porous media: a machine learning approach for identifying main flow pathways, Computational Geosciences 23 (3) (2019) 617–629.

[35] R. Sathya, A. Abraham, Comparison of supervised and unsupervised learning algorithms for pattern classification, International Journal of Advanced Research in Artificial Intelligence 2 (2) (2013) 34–38.

[36] E. M. Tzanakou, Supervised and unsupervised pattern recognition: feature extraction and computational intelligence, CRC press, 2017.

[37] M. Moradi, B. Tokhmechi, P. Masoudi, Inversion of well logs into rock types, lithofacies and environmental facies, using pattern recognition, a case study of carbonate sarvak formation, Carbonates and Evaporites 34 (2) (2019) 335–347.

[38] E. E. Baraboshkin, L. S. Ismailova, D. M. Orlov, E. A. Zhukovskaya, G. A. Kalmykov, O. V. Khotylev, E. Y. Baraboshkin, D. A. Koroteev, Deep convolutions for in-depth automated rock typing, Computers & Geosciences 135 (2020) 104330.

[39] M. J. Blunt, B. Bijeljic, H. Dong, O. Gharbi, S. Iglauer, P. Mostaghimi, A. Paluszny, C. Pentland, Pore-scale imaging and modelling, Advances in Water Resources 51 (2013) 197–216.

[40] M. J. Blunt, Multiphase flow in permeable media: A pore-scale perspective, Cambridge University Press, 2017.

[41] J. H. van der Linden, G. A. Narsilio, A. Tordesillas, Machine learning framework for analysis of transport through complex networks in porous, granular media: a focus on permeability, Physical Review E 94 (2) (2016) 022904.

[42] F. E. Bock, R. C. Aydin, C. J. Cyron, N. Huber, S. R. Kalidindi, B. Klusemann, A review of the application of machine learning and data mining approaches in continuum materials mechanics, Frontiers in Materials 6 (2019) 110.

[43] S. Karimpouli, P. Tahmasebi, Segmentation of digital rock images using deep convolutional autoencoder networks, Computers & Geosciences 126 (2019) 142–150.

[44] P. Walker, R. Mason, D. Carrington, Theresa may commits to net zero uk carbon emissions by 2050, The Guardian 11 (6) (2019) 19.

[45] P. C. Slorach, L. Stamford, Net zero in the heating sector: Technological options and environmental sustainability from now to 2050, Energy Conversion and Management 230 (2021) 113838.

[46] M. J. Blunt, B. Bijeljic, H. Dong, O. Gharbi, S. Iglauer, P. Mostaghimi, A. Paluszny, C. Pentland, Pore-scale imaging and modelling, Advances in Water Resources 51 (2013) 197–216. `doi:10.1016/j.advwatres.2012.03.003`.

[47] D. A. Nield, A. Bejan, Convection in porous media, 2013. `doi:10.1007/978-1-4614-5541-7`.

[48] R. Hilfer, Review on scale dependent characterization of the microstructure of porous media, Transport in Porous Media 46 (2-3) (2002) 373–390. `doi:10.1023/A:1015014302642`.

[49] A. Q. Raeini, M. J. Blunt, B. Bijeljic, Direct simulations of two-phase flow on micro-CT images of porous media and upscaling of pore-scale forces, Advances in Water Resources 74 (2014) 116–126. `doi:10.1016/j.advwatres.2014.08.012`.

[50] H. Dong, Micro-CT imaging and pore network extraction, Ph.D. thesis, Department of Earth Science and Engineering, Imperial College London (2008).

[51] S. Jaganathan, H. Vahedi Tafreshi, B. Pourdeyhimi, A realistic approach for modeling permeability of fibrous media: 3-D imaging coupled with CFD simulation, Chemical Engineering Science 63 (1) (2008) 244–252. `doi:10.1016/j.ces.2007.09.020`.

[52] S. Sharma, D. A. Siginer, Permeability Measurement Methods in Porous Media of Fiber Reinforced Composites, Applied Mechanics Reviews 63 (2) (2010) 020802. `doi:10.1115/1.4001047`.

[53] M. J. Blunt, Flow in porous media - Pore-network models and multiphase flow (2001). `doi:10.1016/S1359-0294(01)00084-X`.

[54] A. J. Katz, A. H. Thompson, Quantitative prediction of permeability in porous rock, Physical Review B 34 (11) (1986) 8179–8181. `doi:10.1103/PhysRevB.34.8179`.

[55] A. Szymkiewicz, Modelling water flow in unsaturated porous media: Accounting for nonlinear permeability and material heterogeneity, GeoPlanet: Earth and Planetary Sciences 9 (2013) 1. `doi:10.1007/978-3-642-23559-7`.

[56] G. W. Jackson, D. F. James, The permeability of fibrous porous media, The Canadian Journal of Chemical Engineering 64 (3) (1986) 364–374. `doi:10.1002/cjce.5450640302`.

[57] A. Koponen, M. Kataja, J. Timonen, Permeability and effective porosity of porous media, Physical Review E 56 (3) (1997) 3319–3325. `doi:10.1103/PhysRevE.56.3319`.

[58] Y. S. Song, K. Chung, T. J. Kang, J. R. Youn, Prediction of permeability tensor for three dimensional circular braided preform by applying a finite volume method to a unit cell, Composites Science and Technology 64 (10-11) (2004) 1629–1636. `doi:10.1016/j.compscitech.2003.11.008`.

[59] S. Geiger, S. Roberts, S. K. Matthäi, C. Zoppou, A. Burri, Combining finite element and finite volume methods for efficient multiphase flow simulations in highly heterogeneous and structurally complex geologic media, Geofluids 4 (4) (2004) 284–299. `doi:10.1111/j.1468-8123.2004.00093.x`.

[60] A. Q. Raeini, B. Bijeljic, M. J. Blunt, Modelling capillary trapping using finite-volume simulation of two-phase flow directly on micro-CT images, Advances in Water Resources 83 (2015) 102–110. `doi:10.1016/j.advwatres.2015.05.008`.

[61] A. Munjiza, The combined finite-discrete element method, 2004. `doi:10.1002/0470020180`.

[62] Z. Sun, R. E. Logé, M. Bernacki, 3D finite element model of semi-solid permeability in an equiaxed granular structure, Computational Materials Science 49 (1) (2010) 158–170. `doi:10.1016/j.commatsci.2010.04.042`.

[63] J. A. White, R. I. Borja, J. T. Fredrich, Calculating the effective permeability of sandstone with multiscale lattice Boltzmann/finite element simulations, Acta Geotechnica 1 (4) (2006) 195–209. `doi:10.1007/s11440-006-0018-4`.

[64] C. Sandino, P. Kroliczek, D. D. McErlain, S. K. Boyd, Predicting the permeability of trabecular bone by micro-computed tomography and finite element modeling, Journal of Biomechanics 47 (12) (2014) 3129–3134. `doi:10.1016/j.jbiomech.2014.06.024`.

[65] M. A. A. Spaid, F. R. Phelan, Lattice Boltzmann methods for modeling microscale flow in fibrous porous media, Physics of Fluids 9 (9) (1997) 2468–2474. `doi:10.1063/1.869392`.

[66] L. Hao, P. Cheng, Lattice Boltzmann simulations of anisotropic permeabilities in carbon paper gas diffusion layers, Journal of Power Sources 186 (1) (2009) 104–114. `doi:10.1016/j.jpowsour.2008.09.086`.

[67] L. Chen, L. Zhang, Q. Kang, H. S. Viswanathan, J. Yao, W. Tao, Nanoscale simulation of shale transport properties using the lattice Boltzmann method: permeability and diffusivity, Scientific Reports 5 (2015) 8089. `doi:10.1038/srep08089`.

[68] C. Manwart, U. Aaltosalmi, A. Koponen, R. Hilfer, J. Timonen, Lattice-Boltzmann and finite-difference simulations for the permeability for three-dimensional porous media, Physical Review E - Statistical, Nonlinear, and Soft Matter Physics 66 (1) (2002). `doi:10.1103/PhysRevE.66.016702`.

[69] E. S. Boek, M. Venturoli, Lattice-Boltzmann studies of fluid flow in porous media with realistic rock geometries, Computers and Mathematics with Applications 59 (7) (2010) 2305–2314. `doi:10.1016/j.camwa.2009.08.063`.

[70] Y. Keehm, Permeability prediction from thin sections: 3D reconstruction and Lattice-Boltzmann flow simulation, Geophysical Research Letters 31 (4) (2004) L04606. `doi:10.1029/2003GL018761`.

[71] M. L. Stewart, A. L. Ward, D. R. Rector, A study of pore geometry effects on anisotropy in hydraulic permeability using the lattice-Boltzmann method, Advances in Water Resources 29 (9) (2006) 1328–1340. `doi:10.1016/j.advwatres.2005.10.012`.

[72] M. J. Blunt, M. D. Jackson, M. Piri, P. H. Valvatne, Detailed physics, predictive capabilities and macroscopic consequences for pore-network models of multiphase flow, Advances in Water Resources 25 (8-12) (2002) 1069–1089.

[73] H. Dong, S. Fjeldstad, S. Roth, S. Bakke, P. Øren, Pore Network Modelling on Carbonate: A comparative Study of Different Micro-CT Network Extraction Methods, Proc. International Symp. Society of Core Analysts (2008) 2008–2031.

[74] H. K. Dahle, M. A. Celia, S. M. Hassanizadeh, Bundle-of-tubes model for calculating dynamic effects in the capillary-pressure-saturation relationship, Transport in Porous media 58 (1-2) (2005) 5–22.

[75] E. C. Childs, N. Collis-George, The permeability of porous materials, Proc. R. Soc. Lond. A 201 (1066) (1950) 392–405.

[76] F. A. Dullien, Porous media: fluid transport and pore structure, Academic press, 2012.

[77] Y. Wang, T. Chung, R. Armstrong, J. McClure, P. Mostaghimi, Computations of permeability of large rock images by dual grid domain decomposition, Advances in Water Resources 126 (2019) 1–14.

[78] P. Mostaghimi, R. T. Armstrong, A. Gerami, Y. Hu, Y. Jing, F. Kamali, M. Liu, Z. Liu, X. Lu, H. L. Ramandi, et al., Pore scale characterisation of coal: an unconventional challenge, in: Abu Dhabi International Petroleum Exhibition & Conference, Society of Petroleum Engineers, 2016.

[79] M. Liu, P. Mostaghimi, Pore-scale modelling of CO2 storage in fractured coal, International Journal of Greenhouse Gas Control 66 (2017) 246–253.

[80] A. Rabbani, P. Mostaghimi, R. T. Armstrong, Pore network extraction using geometrical domain decomposition, Advances in Water Resources 123 (2019) 70 – 83. `doi:https://doi.org/10.1016/j.advwatres.2018.11.003`.

[81] M. Liu, P. Mostaghimi, Numerical simulation of fluid-fluid-solid reactions in porous media, International Journal of Heat and Mass Transfer 120 (2018) 194–201.

[82] D. N. Hieu, T. T. Minh, T. Van Quang, B. X. Giang, T. Van Hoai, A Machine Learning-Based Approach for Predicting the Execution Time of CFD Applications on Cloud Computing Environment, in: International Conference on Future Data and Security Engineering, 2016, pp. 40–52.

[83] L. Itu, S. Rapaka, T. Passerini, B. Georgescu, C. Schwemmer, M. Schoebinger, T. Flohr, P. Sharma, D. Comaniciu, A machine-learning approach for computation of fractional flow reserve from coronary computed tomography, Journal of Applied Physiology 121 (1) (2016) 42–52.

[84] J. H. Van Der Linden, G. A. Narsilio, A. Tordesillas, Machine learning framework for analysis of transport through complex networks in porous, granular media: A focus on permeability, Physical Review E 94 (2) (2016). `doi:10.1103/PhysRevE.94.022904`.

[85] U. Frisch, B. Hasslacher, Y. Pomeau, Lattice-gas automata for the Navier-Stokes equation, Physical Review Letters 56 (14) (1986) 1505.

[86] G. R. McNamara, G. Zanetti, Use of the Boltzmann equation to simulate lattice-gas automata, Physical Review Letters 61 (20) (1988) 2332.

[87] S. Chen, G. D. Doolen, Lattice Boltzmann method for fluid flows, Annual review of fluid mechanics 30 (1) (1998) 329–364.

[88] S. Freudiger, J. Hegewald, M. Krafczyk, A parallelisation concept for a multi-physics Lattice Boltzmann prototype based on hierarchical grids, Progress in Computational Fluid Dynamics, an International Journal 8 (1-4) (2008) 168–178.

[89] J. Zhao, Q. Kang, J. Yao, H. Viswanathan, R. Pawar, L. Zhang, H. Sun, The effect of wettability heterogeneity on relative permeability of two-phase flow in porous media: A lattice boltzmann study, Water Resources Research 54 (2) (2018) 1295–1311.

[90] A. Fakhari, Y. Li, D. Bolster, K. T. Christensen, A phase-field Lattice Boltzmann model for simulating multiphase flows in porous media: Application and comparison to experiments of CO2 sequestration at pore scale, Advances in Water Resources 114 (2018) 119–134.

[91] Z. Li, S. Galindo-Torres, G. Yan, A. Scheuermann, L. Li, A Lattice Boltzmann investigation of steady-state fluid distribution, capillary pressure and relative permeability of a porous medium: Effects of fluid and geometrical properties, Advances in Water Resources 116 (2018) 153–166.

[92] D. V. Patil, K. Lakshmisha, Finite volume TVD formulation of Lattice Boltzmann simulation on unstructured mesh, Journal of Computational Physics 228 (14) (2009) 5262–5279.

[93] S. Geller, M. Krafczyk, J. Tölke, S. Turek, J. Hron, Benchmark computations based on Lattice-Boltzmann, finite element and finite volume methods for laminar flows, Computers & Fluids 35 (8-9) (2006) 888–897.

[94] J. Yi, H. Xing, Finite element lattice boltzmann method for fluid flow through complex fractured media with permeable matrix, Advances in Water Resources 119 (2018) 28–40.

[95] C. Manwart, U. Aaltosalmi, A. Koponen, R. Hilfer, J. Timonen, Lattice-boltzmann and finite-difference simulations for the permeability for three-dimensional porous media, Physical Review E 66 (1) (2002) 016702.

[96] S. Bakke, P.-E. Øren, A, 3-D Pore-Scale Modelling of Sandstones and Flow Simulations in the Pore Networks, Society of Petroleum Engineers 2 (June) (1997) 136—-149. `doi:SPE35479`.

[97] V. Joekar-Niasar, M. Prodanović, D. Wildenschild, S. Hassanizadeh, Network model investigation of interfacial area, capillary pressure and saturation relationships in granular porous media, Water Resources Research 46 (6) (2010).

[98] S. R. Stock, Recent advances in X-ray microtomography applied to materials, International Materials Reviews 53 (3) (2008) 129–181. `doi:10.1179/174328008X277803`.

[99] T. Bultreys, M. A. Boone, M. N. Boone, T. De Schryver, B. Masschaele, L. Van Hoorebeke, V. Cnudde, Fast laboratory-based micro-computed tomography for pore-scale research: Illustrative experiments and perspectives on the future, Advances in Water Resources 95 (2016) 341–351. `doi:10.1016/j.advwatres.2015.05.012`.

[100] X. Miao, K. M. Gerke, T. O. Sizonenko, A new way to parameterize hydraulic conductances of pore elements: A step towards creating pore-networks without pore shape simplifications, Advances in Water Resources (2017). `doi:10.1016/j.advwatres.2017.04.021`.

[101] T. B. Costa, K. Kennedy, M. Peszynska, Hybrid three-scale model for evolving pore-scale geometries, Computational Geosciences (2018). `doi:10.1007/s10596-018-9733-9`.

[102] W.-C. Sun, T.-f. Wong, Prediction of permeability and formation factor of sandstone with hybrid Lattice Boltzmann/finite element simulation on microtomographic images, International Journal of Rock Mechanics and Mining Sciences 106 (2018) 269–277.

[103] E. G. Flekkoy, Lattice Bhatnagar-Gross-Krook models for miscible fluids, Physical Review E 47 (6) (1993) 4247–4257. `doi:10.1103/PhysRevE.47.4247`.

[104] J. T. Gostick, Versatile and efficient pore network extraction method using marker-based watershed segmentation, Physical Review E 96 (2) (2017) 23307.

[105] A. Rabbani, S. Ayatollahi, Comparing three image processing algorithms to estimate the grain-size distribution of porous rocks from binary 2d images and sensitivity analysis of the grain overlapping degree, Special Topics & Reviews in Porous Media: An International Journal 6 (1) (2015) 71–89. `doi:10.1615/SpecialTopicsRevPorousMedia.v6.i1.60`.

[106] A. Rabbani, S. Ayatollahi, R. Kharrat, N. Dashti, Estimation of 3-D pore network coordination number of rocks from watershed segmentation of a single 2-D image, Advances in Water Resources 94 (2016) 264–277. `doi:10.1016/j.advwatres.2016.05.020`.

[107] D. Wildenschild, A. P. Sheppard, X-ray imaging and analysis techniques for quantifying pore-scale structure and processes in subsurface porous medium systems, Advances in Water Resources 51 (2013) 217–246.

[108] A. Rabbani, S. Jamshidi, S. Salehi, An automated simple algorithm for realistic pore network extraction from micro-tomography images, Journal of Petroleum Science and Engineering 123 (2014) 164–171.

[109] A. P. Sheppard, R. M. Sok, H. Averdunk, Improved pore network extraction methods, in: International Symposium of the Society of Core Analysts, Vol. 2125, 2005, pp. 1–11.

[110] J.-Y. Arns, A. P. Sheppard, C. H. Arns, M. A. Knackstedt, A. Yelkhovsky, W. V. Pinczewski, Pore-level validation of representative pore networks obtained from micro-ct images, in: Proceedings of the International Symposium of the Society of Core Analysts, 2007, pp. 1–12.

[111] A. Rabbani, T. Baychev, S. Ayatollahi, A. Jivkov, Evolution of Pore-Scale Morphology of Oil Shale During Pyrolysis: A Quantitative Analysis, Transport in Porous Media 119 (1) (2017). `doi:10.1007/s11242-017-0877-1`.

[112] I. W. Haslam, R. S. Crouch, M. Seaïd, Coupled finite element–Lattice Boltzmann analysis, Computer Methods in Applied Mechanics and Engineering 197 (51-52) (2008) 4505–4511.

[113] N. A. Mortensen, F. Okkels, H. Bruus, Reexamination of Hagen-Poiseuille flow: Shape dependence of the hydraulic resistance in microchannels, Physical Review E - Statistical, Nonlinear, and Soft Matter Physics 71 (5) (2005). `doi:10.1103/PhysRevE.71.057301`.

[114] U. Aaltosalmi, Fluid flow in porous media with the Lattice-Boltzmann method, no. 3, 2005.

[115] A. Pazdniakou, P. M. Adler, Dynamic permeability of porous media by the Lattice Boltzmann method, Advances in Water Resources 62 (2013) 292–302. `doi:10.1016/j.advwatres.2013.06.001`.

[116] E. Alpaydın, Introduction to machine learning, Vol. 1107, 2014. `doi:10.1007/978-1-62703-748-8-7`.

[117] M. I. Lourakis, et al., A brief description of the levenberg-marquardt algorithm implemented by levmar, Foundation of Research and Technology 4 (1) (2005) 1–6.

[118] H. Yu, B. M. Wilamowski, Levenberg-marquardt training, Industrial Electronics Handbook 5 (12) (2011) 1.

[119] N. M. Nasrabadi, Pattern recognition and machine learning, Journal of Electronic Imaging 16 (4) (2007) 049901.

[120] N. H. Chen, An explicit equation for friction factor in pipe, Industrial & Engineering Chemistry Fundamentals 18 (3) (1979) 296–297.

[121] H. Dong, M. J. Blunt, Pore-network extraction from micro-computerized-tomography images, Physical Review E - Statistical, Nonlinear, and Soft Matter Physics 80 (3) (2009). `doi:10.1103/PhysRevE.80.036307`.

[122] P. Mostaghimi, M. J. Blunt, B. Bijeljic, Computations of absolute permeability on micro-ct images, Mathematical Geosciences 45 (1) (2013) 103–125.

[123] B. Bijeljic, A. Raeini, P. Mostaghimi, M. J. Blunt, Predictions of non-fickian solute transport in different classes of porous media using direct simulation on pore-scale images, Physical Review E 87 (1) (2013) 013011.

[124] R. B. Bendel, A. A. Afifi, Comparison of stopping rules in forward “stepwise” regression, Journal of the American Statistical Association 72 (357) (1977) 46–53.

[125] A. Raoof, S. M. Hassanizadeh, A new method for generating pore-network models of porous media, Transport in Porous Media 81 (3) (2010) 391–407.

[126] N. Karadimitriou, V. Joekar-Niasar, S. Hassanizadeh, P. Kleingeld, L. Pyrak-Nolte, A novel deep reactive ion etched (drie) glass micro-model for two-phase flow experiments, Lab on a Chip 12 (18) (2012) 3413–3418.

[127] H. Dong, M. J. Blunt, Pore-network extraction from micro-computerized-tomography images, Physical Review E 80 (3) (2009) 036307.

[128] J. T. Gostick, Versatile and efficient pore network extraction method using marker-based watershed segmentation, Physical Review E 96 (2) (2017) 023307.

[129] A. Rabbani, P. Mostaghimi, R. T. Armstrong, Pore network extraction using geometrical domain decomposition, Advances in Water Resources 123 (2019) 70–83.

[130] I. Fatt, The network model of porous media, Petroleum Transactions, AIME 207 (1956) 144–181.

[131] T. G. Baychev, A. P. Jivkov, A. Rabbani, A. Q. Raeini, Q. Xiong, T. Lowe, P. J. Withers, Reliability of algorithms interpreting topological and geometric properties of porous media for pore network modelling, Transport in Porous Media 128 (1) (2019) 271–301.

[132] E. J. Garboczi, Permeability, diffusivity, and microstructural parameters: A critical review, Cement and Concrete Research 20 (4) (1990) 591–601.

[133] V. Joekar-Niasar, S. Hassanizadeh, Analysis of fundamentals of two-phase flow in porous media using dynamic pore-network models: A review, Critical Reviews in Environmental Science and Technology 42 (18) (2012) 1895–1976.

[134] Q. Xiong, T. G. Baychev, A. P. Jivkov, Review of pore network modelling of porous media: experimental characterisations, network constructions and applications to reactive transport, Journal of Contaminant Hydrology 192 (2016) 101–117.

[135] V. Burganos, S. V. Sotirchos, Diffusion in pore networks: effective medium theory and smooth field approximation, AIChE Journal 33 (10) (1987) 1678–1689.

[136] H. Erfani, V. Joekar-Niasar, R. Farajzadeh, Impact of micro-heterogeneity on upscaling reactive transport in geothermal energy, ACS Earth and Space Chemistry (2019).

[137] S. P. Friedman, N. A. Seaton, Critical path analysis of the relationship between permeability and electrical conductivity of three-dimensional pore networks, Water Resources Research 34 (7) (1998) 1703–1710.

[138] F. Plourde, M. Prat, Pore network simulations of drying of capillary porous media. influence of thermal gradients, International Journal of Heat and Mass Transfer 46 (7) (2003) 1293–1307.

[139] R. Millington, J. Quirk, Permeability of porous solids, Transactions of the Faraday Society 57 (1961) 1200–1207.

[140] N. Wakao, J. Smith, Diffusion in catalyst pellets, Chemical Engineering Science 17 (11) (1962) 825–834.

[141] J. W. Beeckman, G. F. Froment, Catalyst deactivation by active site coverage and pore blockage, Industrial & Engineering Chemistry Fundamentals 18 (3) (1979) 245–256.

[142] S. W. Webb, E. Weist, M. Chiovetta, R. Laurence, W. Conner, Morphological influences in the gas phase polymerization of ethylene by silica supported chromium oxide catalysts, The Canadian Journal of Chemical Engineering 69 (3) (1991) 665–681.

[143] M.-O. Coppens, G. F. Froment, Diffusion and reaction in a fractal catalyst pore—I. Geometrical aspects, Chemical Engineering Science 50 (6) (1995) 1013–1026.

[144] D. G. Victor, A. M. Jaffe, M. H. Hayes, Natural gas and geopolitics: From 1970 to 2040, Cambridge University Press, 2006.

[145] F. P. Wang, R. M. Reed, Pore networks and fluid flow in gas shales, in: SPE Annual Technical Conference and Exhibition, Society of Petroleum Engineers, 2009.

[146] F. Javadpour, D. Fisher, M. Unsworth, et al., Nanoscale gas flow in shale gas sediments, Journal of Canadian Petroleum Technology 46 (10) (2007).

[147] P. Zhang, L. Hu, J. N. Meegoda, S. Gao, Micro/nano-pore network analysis of gas flow in shale matrix, Scientific reports 5 (1) (2015) 1–11.

[148] F. Javadpour, et al., Nanopores and apparent permeability of gas flow in mudrocks (shales and siltstone), Journal of Canadian Petroleum Technology 48 (08) (2009) 16–21.

[149] A. Ghanizadeh, C. Clarkson, S. Aquino, O. Ardakani, H. Sanei, Petrophysical and geomechanical characteristics of canadian tight oil and liquid-rich gas reservoirs: I. Pore network and permeability characterization, Fuel 153 (2015) 664–681.

[150] M. E. Naraghi, F. Javadpour, A stochastic permeability model for the shale-gas systems, International Journal of Coal Geology 140 (2015) 111–124.

[151] C. Chen, Multiscale imaging, modeling, and principal component analysis of gas transport in shale reservoirs, Fuel 182 (2016) 761–770.

[152] Y. Wang, Y. Yuan, S. S. Rahman, C. Arns, Semi-quantitative multiscale modelling and flow simulation in a nanoscale porous system of shale, Fuel 234 (2018) 1181–1192.

[153] P. Tahmasebi, Nanoscale and multiresolution models for shale samples, Fuel 217 (2018) 218–225.

[154] W. Song, D. Wang, J. Yao, Y. Li, H. Sun, Y. Yang, L. Zhang, Multiscale image-based fractal characteristic of shale pore structure with implication to accurate prediction of gas permeability, Fuel 241 (2019) 522–532.

[155] D. Chai, G. Yang, Z. Fan, X. Li, Gas transport in shale matrix coupling multilayer adsorption and pore confinement effect, Chemical Engineering Journal 370 (2019) 1534–1549.

[156] Y. Yang, K. Wang, L. Zhang, H. Sun, K. Zhang, J. Ma, Pore-scale simulation of shale oil flow based on pore network model, Fuel 251 (2019) 683–692.

[157] J. Bai, Y. Kang, M. Chen, L. Liang, L. You, X. Li, Investigation of multi-gas transport behavior in shales via a pressure pulse method, Chemical Engineering Journal 360 (2019) 1667–1677.

[158] M. Chen, Y. Kang, T. Zhang, L. You, X. Li, Z. Chen, K. Wu, B. Yang, Methane diffusion in shales with multiple pore sizes at supercritical conditions, Chemical Engineering Journal 334 (2018) 1455–1465.

[159] J. Ma, J. P. Sanchez, K. Wu, G. D. Couples, Z. Jiang, A pore network model for simulating non-ideal gas flow in micro-and nano-porous materials, Fuel 116 (2014) 498–508.

[160] K. Wu, Z. Chen, X. Li, Real gas transport through nanopores of varying cross-section type and shape in shale gas reservoirs, Chemical Engineering Journal 281 (2015) 813–825.

[161] J. T. Gostick, M. A. Ioannidis, M. W. Fowler, M. D. Pritzker, Pore network modeling of fibrous gas diffusion layers for polymer electrolyte membrane fuel cells, Journal of Power Sources 173 (1) (2007) 277–290.

[162] P. K. Sinha, C.-Y. Wang, Pore-network modeling of liquid water transport in gas diffusion layer of a polymer electrolyte fuel cell, Electrochimica Acta 52 (28) (2007) 7936–7945.

[163] M. A. Sadeghi, M. Aghighi, J. Barralet, J. T. Gostick, Pore network modeling of reaction-diffusion in hierarchical porous particles: The effects of microstructure, Chemical Engineering Journal 330 (2017) 1002–1011.

[164] M. J. Blunt, Flow in porous media—pore-network models and multiphase flow, Current Opinion in Colloid & Interface Science 6 (3) (2001) 197–207.

[165] P. Tahmasebi, S. Kamrava, Rapid multiscale modeling of flow in porous media, Physical Review E 98 (5) (2018) 052901.

[166] S. Bekri, C. Laroche, O. Vizika, Pore network models to calculate transport and electrical properties of single or dual-porosity rocks, in: SCA, Vol. 35, 2005, p. 2005.

[167] D. Bauer, S. Youssef, M. Fleury, S. Bekri, E. Rosenberg, O. Vizika, Improving the estimations of petrophysical transport behavior of carbonate rocks using a dual pore network approach combined with computed microtomography, Transport in Porous Media 94 (2) (2012) 505–524.

[168] D. Bauer, S. Youssef, M. Han, S. Bekri, E. Rosenberg, M. Fleury, O. Vizika, From computed microtomography images to resistivity index calculations of heterogeneous carbonates using a dual-porosity pore-network approach: Influence of percolation on the electrical transport properties, Physical Review E 84 (1) (2011) 011133.

[169] Z. A. Khan, T. Tranter, M. Agnaou, A. Elkamel, J. Gostick, Dual network extraction algorithm to investigate multiple transport processes in porous materials: Image-based modeling of pore and grain scale processes, Computers & Chemical Engineering 123 (2019) 64–77.

[170] T. Bultreys, L. Van Hoorebeke, V. Cnudde, Multi-scale, micro-computed tomography-based pore network models to simulate drainage in heterogeneous rocks, Advances in Water Resources 78 (2015) 36–49.

[171] Z. Jiang, M. Van Dijke, K. S. Sorbie, G. D. Couples, Representation of multiscale heterogeneity via multiscale pore networks, Water Resources Research 49 (9) (2013) 5437–5449.

[172] E. T. de Vries, A. Raoof, M. T. van Genuchten, Multiscale modelling of dual-porosity porous media; a computational pore-scale study for flow and solute transport, Advances in Water Resources 105 (2017) 82–95.

[173] P. J. Schmid, D. S. Henningson, Optimal energy density growth in Hagen–Poiseuille flow, Journal of Fluid Mechanics 277 (1994) 197–225.

[174] P. A. Witherspoon, J. S. Wang, K. Iwai, J. E. Gale, Validity of cubic law for fluid flow in a deformable rock fracture, Water Resources Research 16 (6) (1980) 1016–1024.

[175] R. W. Zimmerman, G. S. Bodvarsson, Hydraulic conductivity of rock fractures, Transport in Porous Media 23 (1) (1996) 1–30.

[176] R. G. Hughes, M. J. Blunt, Network modeling of multiphase flow in fractures, Advances in Water Resources 24 (3-4) (2001) 409–421.

[177] S. Erzeybek, S. Akin, Pore network modeling of multiphase flow in fissured and vuggy carbonates, in: SPE Symposium on Improved Oil Recovery, Society of Petroleum Engineers, 2008.

[178] Z. Jiang, M. I. J. Van Dijke, S. Geiger, J. Ma, G. D. Couples, X. Li, Pore network extraction for fractured porous media, Advances in Water Resources 107 (2017) 280–289.

[179] K. Weishaupt, V. Joekar-Niasar, R. Helmig, An efficient coupling of free flow and porous media flow using the pore-network modeling approach, Journal of Computational Physics: X 1 (2019) 100011.

[180] H. Liu, X. Zhang, X. Lu, Q. Liu, Study on flow in fractured porous media using pore-fracture network modeling, Energies 10 (12) (2017) 1984.

[181] H. Taud, R. Martinez-Angeles, J. Parrot, L. Hernandez-Escobedo, Porosity estimation method by x-ray computed tomography, Journal of Petroleum Science and Engineering 47 (3-4) (2005) 209–217.

[182] D. Everett, Manual of symbols and terminology for physicochemical quantities and units, appendix ii: Definitions, terminology and symbols in colloid and surface chemistry, Pure and Applied Chemistry 31 (4) (1972) 577–638.

[183] A. Mhiri, T. Blasingame, G. Moridis, Stochastic modeling of a fracture network in a hydraulically fractured shale-gas reservoir, in: SPE Annual Technical Conference and Exhibition, Society of Petroleum Engineers, 2015.

[184] A. S. Alaboodi, S. Sivasankaran, Experimental design and investigation on the mechanical behavior of novel 3d printed biocompatibility polycarbonate scaffolds for medical applications, Journal of Manufacturing Processes 35 (2018) 479–491.

[185] J. Bryant, N. Drage, S. Richmond, CT number definition, Radiation Physics and Chemistry 81 (4) (2012) 358 – 361.

[186] M. Lagravère, Y. Fang, J. Carey, R. Toogood, G. V. Packota, P. Major, Density conversion factor determined using a cone-beam computed tomography unit newtom qr-dvt 9000, Dentomaxillofacial Radiology 35 (6) (2006) 407–409.

[187] L. F. Athy, Density, porosity, and compaction of sedimentary rocks, AAPG Bulletin 14 (1) (1930) 1–24.

[188] B. Vega, A. Dutta, A. R. Kovscek, CT imaging of low-permeability, dual-porosity systems using high x-ray contrast gas, Transport in Porous Media 101 (1) (2014) 81–97.

[189] H. J. Vala, A. Baxi, A review on Otsu image segmentation algorithm, International Journal of Advanced Research in Computer Engineering & Technology 2 (2) (2013) 387–389.

[190] S. Gibeaux, P. Vázquez, T. De Kock, V. Cnudde, C. Thomachot-Schneider, Weathering assessment under x-ray tomography of building stones exposed to acid atmospheres at current pollution rate, Construction and Building Materials 168 (2018) 187–198.

[191] L. Neveux, D. Grgic, C. Carpentier, J. Pironon, L. Truche, J. Girard, Experimental simulation of chemomechanical processes during deep burial diagenesis of carbonate rocks, Journal of Geophysical Research: Solid Earth 119 (2) (2014) 984–1007.

[192] A. P. Mangan, R. T. Whitaker, Partitioning 3d surface meshes using watershed segmentation, IEEE Transactions on Visualization and Computer Graphics 5 (4) (1999) 308–321.

[193] A. Rabbani, S. Ayatollahi, Comparing three image processing algorithms to estimate the grain-size distribution of porous rocks from binary 2D images and sensitivity analysis of the grain overlapping degree, Special Topics & Reviews in Porous Media: An International Journal 6 (1) (2015) 71–89.

[194] H. Breu, J. Gil, D. Kirkpatrick, M. Werman, Linear time euclidean distance transform algorithms, IEEE Transactions on Pattern Analysis and Machine Intelligence 17 (5) (1995) 529–533.

[195] A. Rabbani, T. G. Baychev, S. Ayatollahi, A. P. Jivkov, Evolution of pore-scale morphology of oil shale during pyrolysis: a quantitative analysis, Transport in Porous Media 119 (1) (2017) 143–162.

[196] L. Shafarenko, M. Petrou, J. Kittler, Automatic watershed segmentation of randomly textured color images, IEEE transactions on Image Processing 6 (11) (1997) 1530–1544.

[197] J. Angulo, D. Jeulin, Stochastic watershed segmentation, in: PROC. of the 8th International Symposium on Mathematical Morphology, 2007, pp. 265–276.

[198] A. Rabbani, M. Babaei, Hybrid pore-network and lattice-boltzmann permeability modelling accelerated by machine learning, Advances in water resources 126 (2019) 116–128.

[199] M. Diepenbroek, A. Bartholomä, H. Ibbeken, How round is round? A new approach to the topic 'roundness' by Fourier grain shape analysis, Sedimentology 39 (3) (1992) 411–422.

[200] C. Juang, R. Holtz, A probabilistic permeability model and the pore size density function, International Journal for Numerical and Analytical Methods in Geomechanics 10 (5) (1986) 543–553.

[201] L. Ma, T. Slater, P. J. Dowey, S. Yue, E. H. Rutter, K. G. Taylor, P. D. Lee, Hierarchical integration of porosity in shales, Scientific Reports 8 (1) (2018) 11683.

[202] D. Luffel, F. Guidry, New core analysis methods for measuring reservoir rock properties of devonian shale, Journal of Petroleum Technology 44 (11) (1992) 1–184.

[203] T. Ahmed, Reservoir engineering handbook, Gulf Professional Publishing, 2018.

[204] A. Peigney, C. Laurent, E. Flahaut, R. Bacsa, A. Rousset, Specific surface area of carbon nanotubes and bundles of carbon nanotubes, Carbon 39 (4) (2001) 507–514.

[205] R. Bacsa, C. Laurent, A. Peigney, W. Bacsa, T. Vaugien, A. Rousset, High specific surface area carbon nanotubes from catalytic chemical vapor deposition process, Chemical Physics Letters 323 (5-6) (2000) 566–571.

[206] R. Liu, Y. C. Yabansu, A. Agrawal, S. R. Kalidindi, A. N. Choudhary, Machine learning approaches for elastic localization linkages in high-contrast composite materials, Integrating Materials and Manufacturing Innovation 4 (1) (2015) 13.

[207] S. R. Kalidindi, J. A. Gomberg, Z. T. Trautt, C. A. Becker, Application of data science tools to quantify and distinguish between structures and models in molecular dynamics datasets, Nanotechnology 26 (34) (2015) 1–15.

[208] P. Steinmetz, Y. C. Yabansu, J. Hötzer, M. Jainta, B. Nestler, S. R. Kalidindi, Analytics for microstructure datasets produced by phase-field simulations, Acta Materialia 103 (2016) 192–203.

[209] S. R. Niezgoda, Y. C. Yabansu, S. R. Kalidindi, Understanding and visualizing microstructure and microstructure variance as a stochastic process, Acta Materialia 59 (16) (2011) 6387–6400.

[210] S. R. Niezgoda, A. K. Kanjarla, S. R. Kalidindi, Novel microstructure quantification framework for databasing, visualization, and analysis of microstructure data, Integrating Materials and Manufacturing Innovation 2 (1) (2013) 54–80.

[211] W. A. M. Fernando, I. Ilankoon, A. Rabbani, M. Yellishetty, Inter-particle fluid flow visualisation of larger packed beds pertaining to heap leaching using x-ray computed tomography imaging, Minerals Engineering 151 (2020) 106334.

[212] T. Fast, S. R. Niezgoda, S. R. Kalidindi, A new framework for computationally efficient structure–structure evolution linkages to facilitate high-fidelity scale bridging in multi-scale materials models, Acta Materialia 59 (2) (2011) 699–707.

[213] M. Knezevic, S. R. Kalidindi, Fast computation of first-order elastic–plastic closures for polycrystalline cubic-orthorhombic microstructures, Computational Materials Science 39 (3) (2007) 643–648.

[214] G. Landi, S. R. Niezgoda, S. R. Kalidindi, Multi-scale modeling of elastic response of three-dimensional voxel-based microstructure datasets using novel DFT-based knowledge systems, Acta Materialia 58 (7) (2010) 2716–2725.

[215] A. Derossi, B. Nicolai, P. Verboven, C. Severini, Characterizing apple microstructure via directional statistical correlation functions, Computers and Electronics in Agriculture 138 (2017) 157–166.

[216] A. Derossi, T. De Pilli, C. Severini, Statistical description of food microstructure. extraction of some correlation functions from 2D images, Food Biophysics 8 (4) (2013) 311–320.

[217] X. Huang, K. W. Bandilla, M. A. Celia, Multi-physics pore-network modeling of two-phase shale matrix flows, Transport in Porous Media 111 (1) (2016) 123–141.

[218] A. Rabbani, M. Babaei, F. Javadpour, A triple pore network model (t-pnm) for gas flow simulation in fractured, micro-porous and meso-porous media, Transport in Porous Media (2020) 1–34.

[219] P. Mohammadmoradi, A. Kantzas, Petrophysical characterization of porous media starting from micro-tomographic images, Advances in Water Resources 94 (2016) 200–216.

[220] M.-R. Rokhforouz, A. Rabbani, S. Ayatollahi, V. Taghikhani, Numerical analysis of heat conduction treated with highly conductive copper oxide nanoparticles in porous media, Special Topics & Reviews in Porous Media: An International Journal 7 (2) (2016).

[221] R. Gholami, A. Shahraki, M. Jamali Paghaleh, Prediction of hydrocarbon reservoirs permeability using support vector machine, Mathematical Problems in Engineering 2012 (2012) 1–18.

[222] S. J. Russell, P. Norvig, Artificial intelligence: a modern approach, Malaysia; Pearson Education Limited, 2016.

[223] M. Bianchini, F. Scarselli, On the complexity of neural network classifiers: A comparison between shallow and deep architectures, IEEE transactions on neural networks and learning systems 25 (8) (2014) 1553–1565.

[224] J. Schmidhuber, Deep learning in neural networks: An overview, Neural Networks 61 (2015) 85–117.

[225] Y. LeCun, Y. Bengio, G. Hinton, Deep learning, Nature 521 (7553) (2015) 436.

[226] Y. LeCun, Y. Bengio, Convolutional networks for images, speech, and time series, The handbook of brain theory and neural networks 3361 (10) (1995) 1995.

[227] Y. LeCun, Generalization and network design strategies, in: Connectionism in perspective, Vol. 19, Citeseer, 1989.

[228] A. Krizhevsky, I. Sutskever, G. E. Hinton, Imagenet classification with deep convolutional neural networks, in: Advances in neural information processing systems, 2012, pp. 1097–1105.

[229] V. Mnih, K. Kavukcuoglu, D. Silver, A. A. Rusu, J. Veness, M. G. Bellemare, A. Graves, M. Riedmiller, A. K. Fidjeland, G. Ostrovski, Human-level control through deep reinforcement learning, Nature 518 (7540) (2015) 529.

[230] K. He, X. Zhang, S. Ren, J. Sun, Deep residual learning for image recognition, in: Proceedings of the IEEE Conference on Computer Vision and Pattern Recognition, 2016, pp. 770–778.

[231] R. Keys, Cubic convolution interpolation for digital image processing, IEEE transactions on acoustics, speech, and signal processing 29 (6) (1981) 1153–1160.

[232] Y.-T. Zhou, R. Chellappa, Computation of optical flow using a neural network, in: IEEE International Conference on Neural Networks, Vol. 1998, 1988, pp. 71–78.

[233] R. Girshick, Fast r-cnn, in: Proceedings of the IEEE International Conference on Computer Vision, 2015, pp. 1440–1448.

[234] Y. Niu, P. Mostaghimi, M. Shabaninejad, P. Swietojanski, R. T. Armstrong, Digital rock segmentation for petrophysical analysis with reduced user bias using convolutional neural networks, Water Resources Research 56 (2) (2020) e2019WR026597.

[235] S. Kamrava, P. Tahmasebi, M. Sahimi, Enhancing images of shale formations by a hybrid stochastic and deep learning algorithm, Neural Networks 118 (2019) 310–320.

[236] X. Li, Y. Zhang, H. Zhao, C. Burkhart, L. C. Brinson, W. Chen, A transfer learning approach for microstructure reconstruction and structure-property predictions, Scientific Reports 8 (2018) 1–13.

[237] Y. Wang, S. S. Rahman, C. H. Arns, Super resolution reconstruction of μ-ct image of rock sample using neighbour embedding algorithm, Physica A: Statistical Mechanics and its Applications 493 (2018) 177–188.

[238] E. Baraboshkin, L. Ismailova, D. Orlov, E. Zhukovskaya, G. Kalmykov, O. Khotylev, E. Y. Baraboshkin, D. Koroteev, Deep convolutions for in-depth automated rock typing, Computers & Geosciences (2019) 104330.

[239] P. J. Kreyenberg, H. H. Bauser, K. Roth, Velocity field estimation on density-driven solute transport with a convolutional neural network, Water Resources Research 55 (8) (2019) 7275–7293.

[240] Y. Wang, C. H. Arns, S. S. Rahman, J.-Y. Arns, Porous structure reconstruction using convolutional neural networks, Mathematical Geosciences 50 (7) (2018) 781–799.

[241] Y. Wang, Q. Teng, X. He, J. Feng, T. Zhang, CT–image super resolution using 3D convolutional neural network, arXiv preprint arXiv:1806.09074 (2018).

[242] Y. Wang, Q. Teng, X. He, J. Feng, T. Zhang, CT–image of rock samples super resolution using 3D convolutional neural network, Computers & Geosciences (2019) 104314.

[243] Y. Da Wang, R. T. Armstrong, P. Mostaghimi, Enhancing resolution of digital rock images with super resolution convolutional neural networks, Journal of Petroleum Science and Engineering 182 (2019) 106261.

[244] Y. Da Wang, R. Armstrong, P. Mostaghimi, Super resolution convolutional neural network models for enhancing resolution of rock micro-ct images, arXiv preprint arXiv:1904.07470 (2019).

[245] L. Mosser, O. Dubrule, M. J. Blunt, Stochastic reconstruction of an oolitic limestone by generative adversarial networks, Transport in Porous Media 125 (1) (2018) 81–103.

[246] L. Mosser, O. Dubrule, M. J. Blunt, Reconstruction of three-dimensional porous media using generative adversarial neural networks, Physical Review E 96 (4) (2017) 043309.

[247] J. Feng, X. He, Q. Teng, C. Ren, H. Chen, Y. Li, Accurate and fast reconstruction of porous media from extremely limited information using conditional generative adversarial network, arXiv preprint arXiv:1905.02135 (2019) 1–11.

[248] R. Shams, M. Masihi, R. B. Boozarjomehry, M. J. Blunt, Coupled generative adversarial and auto-encoder neural networks to reconstruct three-dimensional multi-scale porous media, Journal of Petroleum Science and Engineering 186 (2020) 106794.

[249] B. L. DeCost, T. Francis, E. A. Holm, Exploring the microstructure manifold: image texture representations applied to ultrahigh carbon steel microstructures, Acta Materialia 133 (2017) 30–40.

[250] D. Floriello, A. Ortenzi, M. Idiomi, S. Ricci, A. Amendola, S. Carminati, E. Baralis, P. Garza, A. Pasini, Automatic pore typing classification from 2D images, in: Offshore Mediterranean Conference and Exhibition, Offshore Mediterranean Conference, 2019.

[251] S. Kamrava, P. Tahmasebi, M. Sahimi, Linking morphology of porous media to their macroscopic permeability by deep learning, Transport in Porous Media 131 (2) (2020) 427–448.

[252] P. Tahmasebi, S. Kamrava, T. Bai, M. Sahimi, Machine learning in geo-and environmental sciences: From small to large scale, Advances in Water Resources (2020) 103619.

[253] H. Wei, S. Zhao, Q. Rong, H. Bao, Predicting the effective thermal conductivities of composite materials and porous media by machine learning methods, International Journal of Heat and Mass Transfer 127 (2018) 908–916.

[254] J. Wu, X. Yin, H. Xiao, Seeing permeability from images: fast prediction with convolutional neural networks, Science Bulletin 63 (18) (2018) 1215–1222.

[255] N. Srisutthiyakorn, Deep-learning methods for predicting permeability from 2D/3D binary-segmented images, in: SEG technical program expanded abstracts 2016, Society of Exploration Geophysicists, 2016, pp. 3042–3046.

[256] N. Alqahtani, R. T. Armstrong, P. Mostaghimi, Deep learning convolutional neural networks to predict porous media properties, in: SPE Asia Pacific Oil and Gas Conference and Exhibition, Society of Petroleum Engineers, 2018.

[257] M. Araya-Polo, F. Alpak, S. Hunter, R. Hofmann, N. Saxena, Deep learning-driven pore-scale simulation for permeability estimation, in: ECMOR XVI-16th European Conference on the Mathematics of Oil Recovery, 2018.

[258] Y. Zhang, P. Mostaghimi, R. T. Armstrong, On the challenges of greyscale-based quantifications using x-ray computed microtomography, Journal of Microscopy (2019) 82–96.

[259] R. Cang, H. Li, H. Yao, Y. Jiao, Y. Ren, Improving direct physical properties prediction of heterogeneous materials from imaging data via convolutional neural network and a morphology-aware generative model, Computational Materials Science 150 (2018) 212–221.

[260] S. Karimpouli, P. Tahmasebi, Image-based velocity estimation of rock using convolutional neural networks, Neural Networks 111 (2019) 89–97.

[261] C. Shorten, T. M. Khoshgoftaar, A survey on image data augmentation for deep learning, Journal of Big Data 6 (1) (2019) 60.

[262] E. Castro, J. S. Cardoso, J. C. Pereira, Elastic deformations for data augmentation in breast cancer mass detection, in: 2018 IEEE EMBS International Conference on Biomedical & Health Informatics (BHI), IEEE, 2018, pp. 230–234.

[263] C. Summers, M. J. Dinneen, Improved mixed-example data augmentation, in: 2019 IEEE Winter Conference on Applications of Computer Vision (WACV), IEEE, 2019, pp. 1262–1270.

[264] H. Gao, Z. Shou, A. Zareian, H. Zhang, S.-F. Chang, Low-shot learning via covariance-preserving adversarial augmentation networks, in: Advances in Neural Information Processing Systems, 2018, pp. 975–985.

[265] D. Cohen-Or, A. Solomovic, D. Levin, Three-dimensional distance field metamorphosis, ACM Transactions on Graphics (TOG) 17 (2) (1998) 116–141.

[266] F. Yan, H. Zhang, C. R. Kube, A multistage adaptive thresholding method, Pattern recognition letters 26 (8) (2005) 1183–1191.

[267] A. Herman, Shear-jamming in two-dimensional granular materials with power-law grain-size distribution, Entropy 15 (11) (2013) 4802–4821.

[268] C. Cortés, M. Osorno, D. Uribe, H. Steeb, O. Ruiz-Salguero, I. Barandiarán, J. Flórez, Geometry simplification of open-cell porous materials for elastic deformation fea, Engineering with Computers 35 (1) (2019) 257–276.

[269] D. Wildenschild, A. P. Sheppard, X-ray imaging and analysis techniques for quantifying pore-scale structure and processes in subsurface porous medium systems, Advances in Water Resources 51 (2013) 217–246.

[270] D. Beard, P. Weyl, Influence of texture on porosity and permeability of unconsolidated sand, AAPG Bulletin 57 (2) (1973) 349–369.

[271] N. O. Shanti, V. W. Chan, S. R. Stock, F. De Carlo, K. Thornton, K. T. Faber, X-ray micro-computed tomography and tortuosity calculations of percolating pore networks, Acta Materialia 71 (2014) 126–135.

[272] E. W. Dijkstra, A note on two problems in connexion with graphs, Numerische Mathematik 1 (1) (1959) 269–271.

[273] S. C. Blair, P. A. Berge, J. G. Berryman, Using two-point correlation functions to characterize microgeometry and estimate permeabilities of sandstones and porous glass, Journal of Geophysical Research: Solid Earth 101 (B9) (1996) 20359–20375.

[274] P. H. Valvatne, M. J. Blunt, Predictive pore-scale modeling of two-phase flow in mixed wet media, Water Resources Research 40 (7) (2004) 1–21.

[275] M. Chaouche, N. Rakotomalala, D. Salin, B. Xu, Y. Yortsos, Capillary effects in drainage in heterogeneous porous media: continuum modelling, experiments and pore network simulations, Chemical Engineering Science 49 (15) (1994) 2447–2466.

[276] P.-E. Oren, S. Bakke, O. J. Arntzen, Extending predictive capabilities to network models, SPE Journal 3 (04) (1998) 324–336.

[277] H. Man, X. Jing, Pore network modelling of electrical resistivity and capillary pressure characteristics, Transport in Porous Media 41 (3) (2000) 263–285.

[278] G. E. Archie, The electrical resistivity log as an aid in determining some reservoir characteristics, Transactions of the AIME 146 (01) (1942) 54–62.

[279] P. M. Adler, C. G. Jacquin, J.-F. Thovert, The formation factor of reconstructed porous media, Water Resources Research 28 (6) (1992) 1571–1576.

[280] I. Sevostianov, A. Trofimov, J. Merodio, R. Penta, R. Rodriguez-Ramos, Connection between electrical conductivity and diffusion coefficient of a conductive porous material filled with electrolyte, International Journal of Engineering Science 121 (2017) 108–117.

[281] M. Aminnaji, A. Rabbani, V. J. Niasar, M. Babaei, Effects of pore-scale heterogeneity on macroscopic NAPL dissolution efficiency: A two-scale numerical simulation study, Water Resources Research 55 (11) (2019) 8779–8799.

[282] G. A. Buxton, N. Clarke, "bending to stretching" transition in disordered networks, Physical Review Letters 98 (23) (2007) 1–4.

[283] J. Wallach, L. Gibson, Mechanical behavior of a three-dimensional truss material, International Journal of Solids and Structures 38 (40-41) (2001) 7181–7196.

[284] G. Y. Gor, L. Bertinetti, N. Bernstein, T. Hofmann, P. Fratzl, P. Huber, Elastic response of mesoporous silicon to capillary pressures in the pores, Applied Physics Letters 106 (26) (2015) 261901.

[285] D. Cooper, J. Matyas, M. Katzenberg, B. Hallgrimsson, Comparison of microcomputed tomographic and microradiographic measurements of cortical bone porosity, Calcified Tissue International 74 (5) (2004) 437–447.

[286] M. Menon, T. Mawodza, A. Rabbani, A. Blaud, G. J. Lair, M. Babaei, M. Kercheva, S. Rousseva, S. Banwart, Pore system characteristics of soil aggregates and their relevance to aggregate stability, Geoderma 366 (2020) 114259.

[287] A. Rabbani, S. Ayatollahi, R. Kharrat, N. Dashti, Estimation of 3-D pore network coordination number of rocks from watershed segmentation of a single 2-D image, Advances in Water Resources 94 (2016) 264–277.

[288] Z. Jiang, K. Wu, G. Couples, M. I. J. Van Dijke, K. S. Sorbie, J. Ma, Efficient extraction of networks from three-dimensional porous media, Water Resources Research 43 (12) (2007) 1–17.

[289] A. Rabbani, S. Jamshidi, S. Salehi, Determination of specific surface of rock grains by 2D imaging, Journal of Geological Research 2014 (2014) 1–7.

[290] A. Rabbani, S. Jamshidi, Specific surface and porosity relationship for sandstones for prediction of permeability, International Journal of Rock Mechanics and Mining Sciences 71 (2014) 25–32.

[291] O. Yeheskel, O. Tevet, A new assessment method for the bulk modulus and the poisson's ratio of porous ceramics, Journal of Testing and Evaluation 28 (3) (2000) 189–198.

[292] L. Kong, M. Ostadhassan, C. Li, N. Tamimi, Pore characterization of 3D-printed gypsum rocks: a comprehensive approach, Journal of Materials Science 53 (7) (2018) 5063–5078.

[293] M. Raissi, P. Perdikaris, G. E. Karniadakis, Physics informed deep learning (part i): Data-driven solutions of nonlinear partial differential equations, arXiv preprint arXiv:1711.10561 (2017).

[294] M. J. Gormish, E. L. Schwartz, A. F. Keith, M. P. Boliek, A. Zandi, Lossless and nearly lossless compression for high-quality images, in: very High resolution and Quality Imaging II, Vol. 3025, International Society for Optics and Photonics, 1997, pp. 62–70.

[295] M. Abadi, P. Barham, J. Chen, Z. Chen, A. Davis, J. Dean, M. Devin, S. Ghemawat, G. Irving, M. Isard, Tensorflow: A system for large-scale machine learning, in: 12th USENIX Symposium on Operating Systems Design and Implementation OSDI 16), 2016, pp. 265–283.

[296] J. D. Hunter, Matplotlib: A 2D graphics environment, Computing in Science & Engineering 9 (3) (2007) 90.

[297] M. Riedmiller, H. Braun, A direct adaptive method for faster backpropagation learning: The rprop algorithm, in: Proceedings of the IEEE International Conference on Neural Networks, Vol. 1993, San Francisco, 1993, pp. 586–591.

[298] T. Chung, Y. D. Wang, R. T. Armstrong, P. Mostaghimi, et al., Approximating permeability of microcomputed-tomography images using elliptic flow equations, SPE Journal 24 (03) (2019) 1–154.

[299] J. Aarnes, T. Gimse, K. Lie, Geometrical modeling, numerical simulation, and optimization: Industrial mathematics at sintef, chapter an introduction to the numerics of flow in porous media using matlab (2007).

[300] K.-A. Lie, S. Krogstad, I. S. Ligaarden, J. R. Natvig, H. M. Nilsen, B. Skaflestad, Open-source matlab implementation of consistent discretisations on complex grids, Computational Geosciences 16 (2) (2012) 297–322.

[301] Y. Da Wang, T. Chung, R. T. Armstrong, J. E. McClure, P. Mostaghimi, Computations of permeability of large rock images by dual grid domain decomposition, Advances in water resources 126 (2019) 1–14.

[302] J. E. McClure, J. F. Prins, C. T. Miller, A novel heterogeneous algorithm to simulate multiphase flow in porous media on multicore cpu–gpu systems, Computer Physics Communications 185 (7) (2014) 1865–1874.

[303] Y. Wang, T. Chung, R. T. Armstrong, J. McClure, T. Ramstad, P. Mostaghimi, Accelerated computation of relative permeability by coupled morphological and direct multiphase flow simulation, Journal of Computational Physics 401 (2020) 108966.

[304] M. Rezaee, A. Jafari, E. Kazemzadeh, Relationships between permeability, porosity and pore throat size in carbonate rocks using regression analysis and neural networks, Journal of Geophysics and Engineering 3 (4) (2006) 370–376.

[305] J. Mortensen, F. Engstrom, I. Lind, The relation among porosity, permeability, and specific surface of chalk from the Gorm field, Danish North Sea, SPE Reservoir Evaluation & Engineering 1 (03) (1998) 245–251.

[306] A. Timur, An investigation of permeability, porosity, and residual water saturation relationships for sandstone reservoirs, The Log Analyst 9 (04) (1968) 3–5.

[307] E. D. Pittman, Relationship of porosity and permeability to various parameters derived from mercury injection-capillary pressure curves for sandstone (1), AAPG bulletin 76 (2) (1992) 191–198.

[308] R. Rubinstein, The cross-entropy method for combinatorial and continuous optimization, Methodology and computing in applied probability 1 (2) (1999) 127–190.

[309] D. P. Kingma, J. Ba, Adam: A method for stochastic optimization, arXiv preprint arXiv:1412.6980 (2014).

[310] F. Zou, L. Shen, Z. Jie, W. Zhang, W. Liu, A sufficient condition for convergences of adam and rmsprop, in: Proceedings of the IEEE conference on computer vision and pattern recognition, 2019, pp. 11127–11135.

[311] S. Ruder, An overview of gradient descent optimization algorithms, arXiv preprint arXiv:1609.04747 (2016).

[312] T. Ramstad, N. Idowu, C. Nardi, P.-E. Øren, Relative permeability calculations from two-phase flow simulations directly on digital images of porous rocks, Transport in Porous Media 94 (2) (2012) 487–504.

[313] M. Rücker, S. Berg, R. Armstrong, A. Georgiadis, H. Ott, A. Schwing, R. Neiteler, N. Brussee, A. Makurat, L. Leu, et al., From connected pathway flow to ganglion dynamics, Geophysical Research Letters 42 (10) (2015) 3888–3894.

[314] S. Hasan, V. Niasar, N. K. Karadimitriou, J. R. Godinho, N. T. Vo, S. An, A. Rabbani, H. Steeb, Direct characterization of solute transport in unsaturated porous media using fast x-ray synchrotron microtomography, Proceedings of the National Academy of Sciences 117 (38) (2020) 23443–23449.

[315] A. Millot, A. Krook-Riekkola, N. Maïzi, Guiding the future energy transition to net-zero emissions: Lessons from exploring the differences between france and sweden, Energy Policy 139 (2020) 111358.

[316] S. Pye, F. G. Li, J. Price, B. Fais, Achieving net-zero emissions through the reframing of uk national targets in the post-paris agreement era, Nature Energy 2 (3) (2017) 1–7.

[317] V. Pranesh, Subsurface co2 storage estimation in bakken tight oil and eagle ford shale gas condensate reservoirs by retention mechanism, Fuel 215 (2018) 580–591.

[318] H. Erfani, M. Babaei, V. Niasar, Signature of Geochemistry on Density-Driven CO2 Mixing in Sandstone Aquifers, Water Resources Research 56 (3) (2020) e2019WR026060.

[319] B. Kutchko, S. Sanguinito, S. Natesakhawat, P. Cvetic, J. T. Culp, A. Goodman, Quantifying pore scale and matrix interactions of SCCO2 with the Marcellus shale, Fuel 266 (2020) 116928.

[320] S. T. Brennan, R. C. Burruss, M. D. Merrill, P. A. Freeman, L. F. Ruppert, A probabilistic assessment methodology for the evaluation of geologic carbon dioxide storage, US Geological Survey Open-File Report 1127 (2010) (2010) 31.

[321] D. Shen, G. Wu, H.-I. Suk, Deep learning in medical image analysis, Annual review of biomedical engineering 19 (2017) 221–248.

[322] H. Liu, L. Zhang, N. A. Seaton, Analysis of sorption hysteresis in mesoporous solids using a pore network model, Journal of colloid and interface science 156 (2) (1993) 285–293.

[323] H. Yu, J. Fan, J. Xia, H. Liu, H. Wu, Multiscale gas transport behavior in heterogeneous shale matrix consisting of organic and inorganic nanopores, Journal of Natural Gas Science and Engineering 75 (2020) 103139.

[324] F. Javadpour, H. Singh, A. Rabbani, M. Babaei, S. Enayati, Gas flow models of shale: A review, Energy and Fuels (2021).

[325] J. Yao, W. Song, D. Wang, H. Sun, Y. Li, Multi-scale pore network modelling of fluid mass transfer in nano-micro porous media, International Journal of Heat and Mass Transfer 141 (2019) 156–167.

[326] S. M. Kang, E. Fathi, R. J. Ambrose, I. Y. Akkutlu, R. F. Sigal, et al., Carbon dioxide storage capacity of organic-rich shales, SPE J 16 (4) (2011) 842–855.

[327] K. Wu, X. Li, C. Wang, W. Yu, Z. Chen, Model for surface diffusion of adsorbed gas in nanopores of shale gas reservoirs, Industrial & Engineering Chemistry Research 54 (12) (2015) 3225–3236.

[328] C. Freeman, G. Moridis, T. Blasingame, A numerical study of microscale flow behavior in tight gas and shale gas reservoir systems, Transport in porous media 90 (1) (2011) 253–268.

[329] K. Wu, X. Li, C. Guo, C. Wang, Z. Chen, et al., A unified model for gas transfer in nanopores of shale-gas reservoirs: coupling pore diffusion and surface diffusion, Spe Journal 21 (05) (2016) 1–583.

[330] X. Wang, J. J. Sheng, Pore network modeling of the non-darcy flows in shale and tight formations, Journal of Petroleum Science and Engineering 163 (2018) 511–518.

[331] P. Zhang, M. A. Celia, K. W. Bandilla, L. Hu, J. N. Meegoda, A pore-network simulation model of dynamic co 2 migration in organic-rich shale formations, Transport in Porous Media 133 (3) (2020) 479–496.

[332] A. Singh, A. Rabbani, K. Regenauer-Lieb, R. T. Armstrong, P. Mostaghimi, Computer vision and unsupervised machine learning for pore-scale structural analysis of fractured porous media, Advances in Water Resources 147 (2021) 103801.

[333] D. Schumann, Atlas browser-based viewer (Jun 2014).
URL `https://petapixelproject.com/mosaics/Shale/GF-S28-Region-02/index.html`

[334] G. Bird, Definition of mean free path for real gases, The Physics of fluids 26 (11) (1983) 3222–3223.

[335] A. L. Lee, M. H. Gonzalez, B. E. Eakin, et al., The viscosity of natural gases, Journal of Petroleum Technology 18 (08) (1966) 997–1.

[336] S. Duan, M. Gu, X. Du, X. Xian, Adsorption equilibrium of co2 and ch4 and their mixture on sichuan basin shale, Energy & Fuels 30 (3) (2016) 2248–2256.

[337] T. Wang, S. Tian, G. Li, M. Sheng, Selective adsorption of supercritical carbon dioxide and methane binary mixture in shale kerogen nanopores, Journal of Natural Gas Science and Engineering 50 (2018) 181–188.

[338] O. P. O. Cancino, D. P. Pérez, M. Pozo, D. Bessieres, Adsorption of pure co2 and a co2/ch4 mixture on a black shale sample: Manometry and microcalorimetry measurements, Journal of Petroleum Science and Engineering 159 (2017) 307–313.

[339] S. Rani, B. K. Prusty, S. K. Pal, Adsorption kinetics and diffusion modeling of ch4 and co2 in indian shales, Fuel 216 (2018) 61–70.

[340] J. Zhou, S. Xie, Y. Jiang, X. Xian, Q. Liu, Z. Lu, Q. Lyu, Influence of supercritical co2 exposure on ch4 and co2 adsorption behaviors of shale: implications for co2 sequestration, Energy & Fuels 32 (5) (2018) 6073–6089.

[341] C. R. Clarkson, B. Haghshenas, et al., Modeling of supercritical fluid adsorption on organic-rich shales and coal, in: SPE unconventional resources conference-USA, Society of Petroleum Engineers, 2013.

[342] K. S. Okiongbo, A. C. Aplin, S. R. Larter, Changes in type ii kerogen density as a function of maturity: Evidence from the kimmeridge clay formation, Energy & fuels 19 (6) (2005) 2495–2499.

[343] M. García-Gutiérrez, J. Cormenzana, T. Missana, M. Mingarro, P. Martin, Large-scale laboratory diffusion experiments in clay rocks, Physics and Chemistry of the Earth, Parts A/B/C 31 (10-14) (2006) 523–530.

[344] R. Punturo, H. Kern, R. Cirrincione, P. Mazzoleni, A. Pezzino, P-and s-wave velocities and densities in silicate and calcite rocks from the peloritani mountains, sicily (italy): The effect of pressure, temperature and the direction of wave propagation, Tectonophysics 409 (1-4) (2005) 55–72.

[345] D. Northwood, D. Lewis, Transformation of vaterite to calcite during grinding, American Mineralogist: Journal of Earth and Planetary Materials 53 (11-12) (1968) 2089–2092.

[346] E. Fan, S. Tang, C. Zhang, Q. Guo, C. Sun, Methane sorption capacity of organics and clays in high-over matured shale-gas systems, Energy exploration & exploitation 32 (6) (2014) 927–942.

[347] K. He, X. Zhang, S. Ren, J. Sun, Delving deep into rectifiers: Surpassing human-level performance on imagenet classification, in: Proceedings of the IEEE international conference on computer vision, 2015, pp. 1026–1034.

[348] K. Hara, D. Saito, H. Shouno, Analysis of function of rectified linear unit used in deep learning, in: 2015 International Joint Conference on Neural Networks (IJCNN), IEEE, 2015, pp. 1–8.

[349] U. Kuila, M. Prasad, Surface area and pore-size distribution in clays and shales, in: SPE Annual Technical Conference and Exhibition, Vol. 30, Denver, Colorado, 2011, pp. 1–13.

[350] L. Rice, E. Wong, Z. Kolter, Overfitting in adversarially robust deep learning, in: International Conference on Machine Learning, PMLR, 2020, pp. 8093–8104.

[351] Y.-S. Wu, K. Pruess, Gas flow in porous media with klinkenberg effects, Transport in Porous Media 32 (1) (1998) 117–137.

[352] S. Whitaker, Flow in porous media I: A theoretical derivation of Darcy's law, Transport in Porous Media 1 (1) (1986) 3–25.

[353] R. Fletcher, Conjugate gradient methods for indefinite systems, in: Numerical analysis, Springer, 1976, pp. 73–89.

[354] Y. Saad, ILUT: A dual threshold incomplete lu factorization, Numerical Linear Algebra with Applications 1 (4) (1994) 387–402.